CRISPR-Cas9 gene targeting of human induced pluripotent stem cells to generate a palette of optical reporter cell lines towards investigating hypertrophic cardiomyopathy



Submitted by

Jamie Bhagwan BSc MSc

School of Medicine

Department of Cancer & Stem Cells

The University of Nottingham

March 2018

Thesis submitted to The University of Nottingham for the degree of Doctor of Philosophy

Acknowledgements

I would like to thank my supervisor, Professor Chris Denning, for his patience, support and guidance throughout my studies here at The University of Nottingham. I know that the skills I have developed under your leadership will stand me in good stead for the rest of my career.

I am also grateful to Dr Chris Gell for support and training in the School of Life Sciences Imaging and Microscopy (SLIM) facility, Dr Matt Daniels for the kind gift of R-GECO plasmids and helpful advice, Dr Mine Bakar Dogu for Western blot analysis and generation of the optogenetic cell line, Dr James Smith for generation of the *ACTC1* mutant cell lines, and Dr Diogo Mosqueira for generation of the *MYH7* mutant cell lines.

My gratitude extends to all those, past and present, who I have truly enjoyed working with over the past few years. In particular, I would like to thank members of "The Firm": Drs James Crutchley, Gary Duncan, Luke Flatt, Lazaros Fotopoulos, Jamie Patient, and Alex Popov. I would especially like to thank Jordan Thorpe for countless hungover weekend lab sessions, Dr Liz Scott for being the older sister I thankfully never had, Dr Diogo Mosqueira for hours upon hours of planned jokes as we both embarked on this PhD journey, and Dr James Smith, for being the "wise old man" of the lab and going above and beyond in terms of mentorship.

An enormous thanks go to Peggy Lo, for looking after me throughout the latter stages of my PhD. Many pages of this thesis were fuelled by your incomparable Cantonese cuisine and unwavering love and support.

Finally, I'd like to thank my older brother, Gavin, for setting such high aspirational goals and my Mum, for always believing in me and encouraging me to pursue my goals.

Declaration

I hereby declare that this thesis has been composed by myself and has not been submitted for any other degree previously. Acknowledgements of specific procedures not performed by myself are stated; otherwise, the work described is my own.

Jamie Bhagwan _____

Date:

Abstract

Hypertrophic cardiomyopathy (HCM) is an inherited cardiomyopathy with a variety of causative mutations, largely within sarcomeric proteins. This can result in thickening of the left ventricle of the heart, altered contractility, arrhythmias, and in some cases, sudden cardiac death.

Human induced pluripotent stem cell derived cardiomyocytes (hiPSC-CMs) are a valuable tool for disease modelling cardiomyopathies such as HCM, and screening for potential pharmaceutical interventions. The recent emergence of CRISPR Cas9 has opened new opportunities to carry out precise gene editing to correct disease-causing mutations, as well as providing an accessible method of introducing reporter genes into the genome of hiPSCs.

This project sought to utilise CRISPR-Cas9 to generate a palette of genetically encoded calcium indicator (GECI) hiPSC lines in both healthy and diseased backgrounds to investigate HCM *in vitro*.

Site-specific guide RNAs and targeting vectors were designed to target the *AAVS1* locus, an apparent safe harbour, with the GECIs RGECO or GEM-GECO, using CRISPR Cas9. These reporter lines were generated in three different genetic backgrounds, representing two different mutation backgrounds associated with HCM, two *ACTC1* G301A isogenic pairs of healthy and heterozygous mutant hiPSCs and an *MYH7* C9123T isogenic trio of healthy, heterozygous and homozygous mutant hiPSCs. These lines were validated with PCR, immunostaining and live imaging microscopy.

By utilising confocal line scan microscopy and repurposing software to quantify and measure calcium transients, an arrhythmic phenotype was found in *MYH7* C9123T mutant hiPSC-CMs. This arrhythmic phenotype was also seen in P1 *ACTC1* G301A mutant hiPSC-CMs, but not P2 *ACTC1* G301A mutant hiPSC-CMs, suggesting that this particular mutation is necessary yet not sufficient to cause an arrhythmic phenotype.

Based on the observation that *MYH7* mutants were resistant to calcium channel blockers and the arrhythmic phenotype was rescued in low extracellular calcium conditions, a focused drug screen was performed which identified the late sodium current inhibitor ranolazine, and the ryanodine receptor antagonist dantrolene, as viable drug treatments for phenotypic rescue in mutant hiPSC-CMs.

Through this study, new insights into the mechanisms underlying HCM and the variability between mutations and within individuals have been elucidated.

Table of Contents

Acknowledgements ..... **i**

Declaration ..... **ii**

Abstract ..... **iii**

Table of Contents ..... **iv**

List of Figures ..... **ix**

List of Tables ..... **xiii**

Abbreviations ..... **xiv**

Gene names ..... **xvii**

1 Introduction **1**

1.1 Thesis rationale 1

1.2 Hypertrophic cardiomyopathy 2

1.2.1 Mutation of the *MYH7* gene encoding β-myosin heavy chain 8

1.2.2 Mutation of the *ACTC1* gene encoding α-cardiac actin 10

1.3 Human induced pluripotent stem cell-derived cardiomyocytes 11

1.3.1 Derivation of human embryonic stem cells 12

1.3.2 Derivation of human induced pluripotent stem cells 12

1.3.3 Human pluripotent stem cell culture and maintenance 13

1.3.4 Differentiation of human induced pluripotent stem cells towards a cardiomyocyte fate 14

1.3.5 Human induced pluripotent stem cell-derived cardiomyocytes as tools for disease modelling 18

1.3.6 Human induced pluripotent stem cell-derived cardiomyocytes as tools for drug screening 19

1.3.7 Challenges associated with the use of human induced pluripotent stem cell-derived cardiomyocytes 21

1.4 Harnessing site-specific nucleases for precise genome engineering 23

1.4.1 DNA damage response pathways 23

1.4.2 Zinc finger nucleases 26

1.4.3 Transcription activator-like effector nucleases 28

1.4.5 CRISPR-Cas9 30

1.5 Hypothesis & Aims 34

2 Materials and Methods **35**

2.1 Molecular Biology 35
2.1.1 Construct design and sequence analysis 35
2.1.2 Cloning and vector construction 35
2.1.3 Design and assembly of single guide RNA plasmids 36
2.1.4 DNA extraction from cultured mammalian cells 37
2.1.5 PCR genotyping 37
2.1.6 Reverse-transcriptase PCR analysis of RNA expression 38
2.1.7 Immunocytochemistry 38
2.2 Cell culture 40
2.2.1 Human induced pluripotent stem cell maintenance in E8 medium 40
2.2.2 Cardiac differentiation and dissociation 40
2.2.3 293T BL15 cell maintenance 41
2.2.4 Transfection of live cells 41
2.2.5 Time-course assay 42
2.2.6 Cell viability assay 43
2.2.7 Precise gene targeting of human induced pluripotent stem cells 43
2.2.8 Generation of ChR2-EYFP optogenetic line 44
2.3 Microscopy 45
2.3.1 Operetta™ high content image analysis 45
2.3.2 DeltaVision widefield epifluorescence microscopy for live imaging of hiPSC-CMs expressing GECIs 45
2.3.3 Confocal line-scan microscopy as a method to generate calcium transient traces 45
2.3.4 Optogenetic pacing of hiPSC-CMs on the CellOPTIQ™ platform 48
2.3.5 Statistical analysis 48
3 Engineering reporter hiPSC lines to express genetically encoded calcium indicators 49
3.1 Introduction 49
3.1.1 Selecting an engineered nuclease delivery system for precise gene targeting 49
3.1.2 Safe harbour loci within the human genome 51
3.1.3 Calcium handling in cardiomyocytes 58
3.1.4 Calcium imaging 62
3.1.5 Selecting a palette of genetically encoded calcium indicators for cardiac applications 66
3.2 Chapter Aims and objectives 71
3.3 Results 71

3.3.1 Initial *AAVS1* EF1α targeting vector and sgRNA design 71

3.3.2 Optimisation of culture conditions for high efficiency CRISPR/Cas9 targeting 77

3.3.3 Initial genotyping 83

3.3.4 Troubleshooting the failure of EF1α constructs to fluoresce 85

3.3.5 Generating isogenic sets of cell lines harbouring sarcomeric gene mutations 92

3.3.6 Targeting and genotyping isogenic sets of clones 96

3.3.7 Refinement of clone selection for robust GECI expression..... 106

3.4 Discussion..... 113

3.4.1 Modular cloning 113

3.4.2 Functional failure of *AAVS1*-EF1α-Myc constructs upon targeting 114

3.4.3 Characterisation of clones..... 116

3.4.4 Refinement of clone selection 117

4 Engineered reporter lines and their application to assess calcium transients in human induced pluripotent stem cell derived cardiomyocytes 119

4.1 Introduction 119

4.1.1 Calcium handling in human induced pluripotent stem cell derived cardiomyocytes 119

4.2 Chapter Aims and Objectives..... 127

4.3 Results 128

4.3.1 A comparison between genetically encoded calcium indicators and chemical calcium dyes 128

4.3.2 Developing a microscopy technique to capture and analyse calcium transients in targeted GECI hiPSC-CMs..... 132

4.3.3 Interrogating the calcium handling machinery of hiPSC-CMs with a panel of drugs of known response 139

4.4 Discussion..... 151

4.4.1 GECIs offer increased experimental flexibility compared to chemical calcium indicator dyes 151

4.4.2 Confocal line scans are more suited to data acquisition from ratiometric calcium indicators 152

4.4.3 The calcium handling machinery of hiPSC-CMs is functional 154

5 The application of engineered calcium reporter lines for modelling hypertrophic cardiomyopathy and screening potential pharmacological interventions *in vitro*.....158

5.1 Introduction 158

5.1.1 Current approaches for treatment of hypertrophic cardiomyopathy.. 158

5.1.2 Optogenetics and the advent of optical pacing in hiPSC-CMs 167
5.2 Chapter Aims and Objectives 169
5.3 Results 170
5.3.1 Isogenic sets of hiPSC-CMs that express GECIs reveal an arrhythmic phenotype in mutated HCM cell lines 170
5.3.2 The application of drugs to targeted hiPSC-CMs in an attempt to alleviate aberrant calcium transient events associated with HCM 183
5.3.3 The use of optogenetics in hiPSC-CMs towards optical pacing 198
5.4 Discussion 202
5.4.1 The severity of the *MYH7* C9123T phenotype compared to the *ACTC1* G301A phenotype 203
5.4.2 Mechanistic insights into *MYH7*-associated HCM 204
6 General discussion 207
6.1 Fulfilment of thesis objectives 208
6.1.1 Objective 1: Utilise CRISPR/Cas9 to generate GECI-expressing hiPSC lines in an HCM background, with healthy isogenic controls 208
6.1.2 Objective 2: Develop a method to optically analyse calcium transients and quantify changes in response to drugs or disease-causing mutations 209
6.1.3 Objective 3: Validate the utility of hiPSC-CMs to model disease *in vitro* and demonstrate their ability to recapitulate hallmarks of calcium handling .. 210
6.1.4 Objective 4: Use GECI-expressing hiPSC-CMs as a tool to detect HCM phenotypes and compare phenotypes between different gene mutations 211
6.1.5 Objective 5: Use drugs in an attempt to alleviate the HCM phenotype 212
6.2 Calcium and its role in HCM progression 213
6.2.1 Phenotyping HCM *in vitro* 213
6.2.2 Hypertrophic pathway and potential drug targets 217
6.3 Limitations and Improvements 220
6.3.1 *ACTC1* mutant phenotype 220
6.3.2 Genetically encoded calcium indicators 221
6.3.3 Drug screening improvements 221
6.4 Future perspectives 222
6.5 Final remarks 223
References 225
Appendix I – Publications 252
Articles 252
Conference abstracts 252

Appendix II – Predicted off-target locations for *AAVS1* targeting 253

List of Figures

Figure 1.1. Morphological changes to a heart with hypertrophic cardiomyopathy. 3

Figure 1.2. Location of sarcomeric proteins involved in causing hypertrophic cardiomyopathy. 4

Figure 1.3. Calcium handling, the cross-bridge cycle and the energy depletion model. 7

Figure 1.4. *In silico* modelling of β-MHC R453C interactions. 9

Figure 1.5. Generation of human induced pluripotent stem cell-derived cardiomyocytes for *in vitro* phenotyping of cardiomyopathies. 11

Figure 1.6. Stepwise specification of the cardiomyocyte lineages.....15

Figure 1.7. Morphological immaturity of hiPSC-CMs compared to adult CMs. 22

Figure 1.8. DNA damage repair pathways exploited for site-specific genome engineering.....25

Figure 1.9. Zinc finger nucleases. 27

Figure 1.10. Transcription activator-like effector nucleases. 29

Figure 1.11. CRISPR Cas9 for site-specific DNA cleavage.....32

Figure 1.12. Summary of genome editing approaches using site-directed nucleases. 33

Figure 3.1. The CRISPR Cas9 D10A nickase approach for reduced off-target cleavage of DNA.....51

Figure 3.2 Schematic of commonly used genomic safe harbour loci and their location. 53

Figure 3.3. Calcium handling in adult cardiomyocytes. 59

Figure 3.4. The cross-bridge cycle mediates cardiac muscle contraction. 61

Figure 3.5. FRET and cpFP based methods of calcium sensing by GECIs. 64

Figure 3.6. The interrelationship between the cardiac action potential, calcium transient and contraction traces.....66

Figure 3.7. Crystal structures and spectral properties of selected GECO variants. ...70

Figure 3.8. Location of AAVS1 safe harbour locus and site-specific single guide RNA design. 72

Figure 3.9. Modular cloning of AAVS1 EF1α constructs. 75

Figure 3.10. Efficiency of GeneJammer™-mediated transfection of REBL-PAT hiPSCs after 24 hours. 78

Figure 3.11. Transfection efficiency optimisation of Amaxa™ 4D nucleofection of REBL PAT hiPSCs. 79

Figure 3.12. Antibiotic titration on REBL PAT hiPSCs over 48 hours to optimise colony selection conditions. 81

Figure 3.13. CRISPR/Cas9 workflow for targeting the *AAVS1* locus of hiPSCs. 82

Figure 3.14. Polymerase chain reaction and reverse-transcriptase polymerase reaction genotyping to identify targeted clones. 84

Figure 3.15. Ligation of non-compatible ends with small phosphorylated linkers to clone CAG promoter into targeting constructs. 86

Figure 3.16. Transient transfection of 293T BL15 cells to compare promoter efficiencies. 88

Figure 3.17. Inefficient P2A cleavage between genes leads to poor expression in CRISPR/Cas9 targeted clones. 91

Figure 3.18. CRISPR/Cas9 editing of REBL PAT hiPSCs to generate an isogenic trio of *MYH7* C9123T hiPSCs for disease modelling hypertrophic cardiomyopathy *in vitro*. ..93

Figure 3.19. Footprint-free CRISPR/Cas9 editing of patient-derived *ACTC1* G301A hiPSCs to generate isogenic pairs of HCM disease models *in vitro*. 95

Figure 3.20. PCR genotyping of healthy REBL PAT R-GECO and REBL PAT GEM-GECO clones. 97

Figure 3.21. PCR genotyping of isogenic *MYH7* C9123T R-GECO clones. 100

Figure 3.22. PCR genotyping of isogenic P2 *ACTC1* G301A GEM-GECO clones. 102

Figure 3.23. Immunocytochemistry-based screening for targeted isogenic P1 *ACTC1* G301A hiPSCs. 104

Figure 3.24. Assessing cardiac differentiation efficiency in targeted clones. 107

Figure 3.25. Puromycin enrichment of poorly expressing *MYH7* C1923T clones and immunocytochemistry-based selection of robustly expressing clones. 109

Figure 3.26. Selected R-GECO clones and their expression status. 112

Figure 4.1. The L-type Ca^{2+} channel. 121

Figure 4.2. Crystal structure of SERCA inhibition by thapsigargin. 123

Figure 4.3. Calcium handling in cardiomyocytes and interacting compounds. 125

Figure 4.4. hiPSC-CM calcium transient response to reference compounds. 126

Figure 4.5. A comparison between GECIs and existing chemical calcium indicator dyes - evidence of dye leakage using time-course live imaging. 129

Figure 4.6. A comparison between GECIs and existing chemical calcium indicator dyes - evidence of toxicity using a luminescence-based viability assay. 131

Figure 4.7. Application of DeltaVision widefield epifluorescence microscopy to detect fluorescent changes in targeted hiPSC-CMs. 133

Figure 4.8. Use of confocal laser line scan microscopy to simultaneously detect fluorescence from two separate wavelengths. 135

Figure 4.9. ClampFit event detection of calcium transients recorded using confocal laser line scan microscopy. 138

Figure 4.10. Caffeine induces Ca^{2+} release from sarcoplasmic reticulum of hiPSC-CMs. 140

Figure 4.11. Thapsigargin, a non-competitive inhibitor of the sarco/endoplasmic reticulum ATPase, prevents Ca^{2+} re-uptake into the sarcoplasmic reticulum of hiPSC-CMs. 143

Figure 4.12. Micromolar concentration of ryanodine cause decreased beat rate and an increased frequency of arrhythmic events in targeted hiPSC-CMs. 145

Figure 4.13. Isoprenaline, a non-selective ß-adrenoreceptor agonist, increases calcium transient frequency and beating rate of hiPSC-CMs. 147

Figure 4.14. Nifedipine, an L-type Ca^{2+} channel blocker, reduces calcium transient frequency and beating rate of healthy hiPSC-CMs. 149

Figure 4.15. Inhibition of the Na^{+}/Ca^{2+} exchanger by nickel chloride. 150

Figure 4.16. Principle of confocal line scan kymographs to assess cardiomyocyte maturity. 153

Figure 4.17. The cardiac ryanodine receptor and store overload-induced Ca^{2+} release. 156

Figure 5.1. Drug mechanisms within hiPSC-CMs for the treatment of HCM. 162

Figure 5.2. MYK-461 inhibition of myosin ATPase reduces contractile force by slowing actin binding. 164

Figure 5.3. An illustration of the light-gated cation channel channelrhodopsin-2 (ChR2). 168

Figure 5.4. Targeted GEM-GECO hiPSC-CMs harbouring *ACTC1* G301A mutation display decreased systolic calcium and increased beat rate. 171

Figure 5.5. Targeted RGECO hiPSC-CMs harbouring *ACTC1* G301A mutation display arrhythmic events. 173

Figure 5.6. Targeted RGECO hiPSC-CMs harbouring *MYH7* C9123T mutation display arrhythmic events, increased systolic calcium and increased beat rate. 176

Figure 5.7. Targeted hiPSC-CMs harbouring an *MYH7* C9123T mutation display a delayed response to the L-type calcium channel blocker nifedipine. 179

Figure 5.8. The response of targeted hiPSC-CMs harbouring an *MYH7* C1923T mutation to varying extracellular calcium concentrations. 181

Figure 5.9. Calcium transient changes in *MYH7* C1923T RGECO hiPSC-CMs treated with the ß–adrenergic antagonist propranolol. 184

Figure 5.10. Calcium transient changes in *ACTC1* G301A and *MYH7* C1923T RGECO hiPSC-CMs treated with the ß-MHC ATPase MYK-461..... 187

Figure 5.11. Calcium transient changes in *MYH7* C1923T RGECO hiPSC-CMs treated with the angiotensin II receptor antagonist valsartan. 189

Figure 5.12. Reduced arrhythmic calcium transient event frequency in *MYH7* C1923T RGECO hiPSC-CMs treated with the late sodium current inhibitor ranolazine. 191

Figure 5.13. Reduced systolic calcium peak amplitude in *MYH7* C9123T RGECO hiPSC-CMs treated with the ryanodine receptor antagonist dantrolene is not reflected in *ACTC1* G301A RGECO hiPSC-CMs. 194

Figure 5.14. Reduced arrhythmic calcium transient event frequency in *MYH7* C1923T RGECO hiPSC-CMs in response to combined dantrolene and ranolazine treatment is not reflected in *ACTC1* G301A RGECO hiPSC-CMs. 197

Figure 5.15. Random integration of ChR2, a light-gated ion channel, into P1 hiPSCs allows for optogenetic pacing of hiPSC-CMs on the CellOPTIQ™ platform. 201

Figure 5.16. Both calcineurin and CaMKII are involved in hypertrophic remodelling and calcium dysfunction in HCM. 206

Figure 6.1. Ca^{2+} related signalling pathways associated with HCM progression and potential pharmacological interventions. 220

List of Tables

Table 1.1. Abridged list of genes associated with hypertrophic cardiomyopathy 4

Table 1.2. Selected monolayer cardiac differentiation protocols. 17

Table 1.3. Characteristics of hiPSC-CMs compared to adult CMs reveal a lack of maturity in hiPSC-CMs. 22

Table 2.1. Primers used for genotyping.....37

Table 2.2. Antibodies used for immunocytochemistry.....39

Table 2.3. Table of drugs and concentrations used. 46

Table 3.1 Successful fluorescent gene knock-in at safe harbour loci.....54

Table 3.2. Overview of genetically-encoded calcium indicators and their properties. 68

Table 3.3. Primer sequences for stepwise modular cloning of *AAVS1* EF1α constructs 76

Table 3.4. Summary of cell lines engineered to express genetically encoded calcium indicators..... 118

Table 5.1. Approved drugs for the treatment of symptoms associated with hypertrophic cardiomyopathy. 160

Table 5.2. Experimental drugs for the treatment of symptoms associated with hypertrophic cardiomyopathy. 165

Table 6.1. Studies where hiPSC-CMs have been used to investigate HCM and changes to calcium handling properties. 216

Table 1. Guide RNA sequences and predicted off-target locations 253

Table 2. Guide RNA sequences and predicted off-target locations 254

Table 3. Guide RNA sequences and predicted off-target locations 255

Abbreviations

Abbreviation	Description
AAV	Adeno-associated virus
AM	Acetoxymethyl ester
ANOVA	Analysis of variance
BL15	Biotin-lenti clone 15
bp	Base pairs
bpm	Beats per minute
ß-MHC	Beta myosin heavy chain
BMP	Bone morphogenic protein
BSD	Blasticidin-S deaminase
CAG	CMV early enhancer/chicken ß-actin promoter
CaM	Calmodulin
CaMKII	Ca^{2+}/calmodulin-dependent kinase II
CCD	Charge-coupled device
cDNA	Complementary DNA
ChR2	Channelrhodopsin-2
CICR	Calcium-induced calcium release
CM	Cardiomyocyte
CPVT	Catecholaminergic polymorphic ventricular tachycardia
CRISPR	Clustered Regularly Interspaced Short Palindromic Repeats
crRNA	CRISPR RNA
DAD	Delayed after-depolarisation
DAPI	Di-amino phenyl-indole
DMEM	Dulbecco's (Modified Eagle's) minimal essential medium
DMSO	Dimethyl sulfoxide
DNA	Deoxyribonucleic acid
dNTP	Deoxyribonucleotide triphosphate
DSB	Double-strand break
DPBS	Dulbecco’s Phosphate Buffered Saline
E8	Essential 8 medium
EMCCD	Electron-multiplying CCD
EDTA	Ethylene diamine tetra-acetic acid
ESPT	Excited state proton transfer
F/F_0	Fluorescence intensity signal-to-noise ratio

FP	Fluorescent protein
FRET	Förster resonance energy transfer
FRT	Flippase recombinase target
FWD	Forward
gDNA	Genomic DNA
GECI	Genetically encoded calcium indicator
GECO	Genetically encoded calcium indicator for optical imaging
GEVI	Genetically encoded voltage indicator
GFP	Green fluorescent protein
HBSS	Hank's Buffered Salt Solution
HCM	Hypertrophic Cardiomyopathy
HDR	Homology-directed repair
hESC	Human embryonic stem cell
hESC-CM	Human embryonic stem cell derived cardiomyocyte
hiPSC	Human induced pluripotent stem cell
hiPSC-CM	Human induced pluripotent stem cell derived cardiomyocyte
hPSC	Human pluripotent stem cell
hPSC-CM	Human pluripotent stem cell derived cardiomyocyte
iPSC	Induced pluripotent stem cell
IRES	Internal ribosome entry site
kb	Kilobases
mESC	Mouse embryonic stem cell
mRNA	Messenger RNA
MW	Molecular weight marker
MUT	Mutant
NTC	No template control
NEAA	Non-essential amino acids
NHEJ	Non-homologous end joining
NpHR	Halorhodopsin from Natronomonas
P2A	Porcine teschovirus-1 2A
PAM	Protospacer adjacent motif
PBS	Phosphate buffered saline
PCR	Polymerase chain reaction
Puro	Puromycin
RB	RPMI 1640 with B27 supplement
REV	Reverse
RFP	Red fluorescent protein

RGEN	RNA-guided endonuclease
RLU	Relative luminescence units
RNA	Ribonucleic acid
ROCKi	Rho-associated kinase inhibitor
RT	Room temperature
RT-PCR	Reverse transcriptase PCR
SCD	Sudden cardiac death
SD	Standard deviation of the mean
SEM	Standard error of the mean
SERCA	Sarcoplasmic reticulum Ca^{2+}-ATPase
sgRNA	Single guide RNA
SNP	Single nucleotide polymorphism
SR	Sarcoplasmic reticulum
T2A	Thoseaasigna virus 2A
TALEN	Transcription activator-like effector nuclease
TAE	Tris-acetate-EDTA
tracrRNA	Transactivating CRISPR RNA
VTN	Vitronectin-N truncated protein
WT	Wild-type
ZFN	Zinc finger nuclease
%	Percentage
^0C	Degree Celsius

Gene names

Abbreviation	Full name
ACTC1	Alpha Cardiac Actin
BMP4	Bone Morphogenic Protein 4
CASQ2	Calsequestrin 2
CCR5	C-C Motif Chemokine Receptor 5
CLYBL	Citrate Lyase Beta Like
FGF4	Fibroblast Growth Factor 4
KLF4	Kruppel-Like Factor 4
LIN28	Protein lin-28 homolog A
MYBPC3	Myosin Binding Protein C
MYH7	Myosin Heavy Chain Beta-Subunit
NANOG	From Tir Na Nanog (= land of the ever young)
NODAL	Nodal homolog precursor
OCT4	Octamer 4 (aka POU5F1: POU class 5 forkhead box 1
PPP1R12C	Protein Phosphatase 1 Regulatory Subunit 12C
RYR2	Ryanodine receptor 2
SOX2	Sex-determining region Y (SRY) - related high mobility group (HMG) box 2
TRDN	Triadin
TGF	Transforming Growth Factor
WNT	Wingless type

1 Introduction

1.1 Thesis rationale

Hypertrophic cardiomyopathy (HCM) is an inherited cardiac disease that can lead to thickening of the heart muscle, irregular heartbeat and, in some cases, sudden cardiac death in young adults and professional athletes. However, HCM has a wide range of causative mutations, and a similarly wide range of phenotype severity.

Human induced pluripotent stem cell-derived cardiomyocytes (hiPSC-CMs) offer an opportunity to model this complex disease *in vitro*. Key questions surround the severity of specific HCM-causing mutations, and the underlying mechanisms behind some of the harmful phenotypes expressed.

Calcium is known to play a key role in excitation-contraction coupling of cardiomyocytes, as well as being a crucial messenger in intracellular signalling pathways. Calcium imaging has therefore been used as a tool to phenotype cardiomyopathies, but has often relied on commercially-available dyes which are prone to dye leakage and toxicity. The use of genetically encoded calcium indicators (GECIs) can circumvent some of these issues.

Incorporating GECIs into the genome of hiPSCs can be achieved with genome engineering techniques. CRISPR Cas9 has rapidly developed as a tool for SNP correction and reporter gene knock-in.

This thesis aimed to investigate the calcium handling properties of hiPSC-CMs as well as compare and contrast two mutations associated with HCM, using optical imaging of calcium transients to obtain insights into disease mechanisms.

Chapter 3 outlines how CRISPR Cas9 components were designed and constructed so that isogenic sets of hiPSCs harbouring gene mutations that are associated with HCM could be targeted to introduce GECIs into a safe harbour locus of the genome.

In chapter 4, these GECI-expressing cell lines were differentiated to cardiomyocytes and validated by comparing them to commercially-available dyes. A method for measuring and quantifying calcium transients was then developed. To address concerns that the calcium handling machinery of hiPSC-CMs is not mature enough to be used for

disease modelling, a panel of drugs of known action were applied to activate or inhibit key channels and receptors involved in cardiomyocyte calcium cycling.

In chapter 5, hiPSC-CMs with mutations that are implicated in HCM were phenotyped using GECIs, and compared to healthy isogenic controls. The insights gained from these experiments led to a focussed drug screen which revealed compounds that can stifle the HCM phenotype through a calcium-dependent mechanism.

1.2 Hypertrophic cardiomyopathy

Hypertrophic cardiomyopathy (HCM) is a prevalent genetic disease that occurs in roughly 1 in 500 individuals (Maron and Maron, 2013). It is a leading cause of sudden cardiac death in young adults, including athletes (Jacoby et al., 2013). Patients with HCM have a diverse clinical presentation, although may commonly be identified by thickening of the left ventricle detected by echocardiogram (Marian and Braunwald, 2017) (**Figure 1.1A**). Other clinical manifestations include cardiomyocyte hypertrophy, myofibrillar disarray, interstitial fibrosis and left ventricular outflow tract (LVOT) obstruction (Houston and Stevens, 2014) (**Figure 1.1B**).

HCM can be an inherited cardiomyopathy, and several causative genes have been identified (**Table 1.1**) (**Figure 1.2**). Of the roughly 1400 mutations that have been found to be involved in HCM, the majority affect sarcomeric proteins. Indeed, 71% of all HCM-linked mutations occur in the myofilament proteins ß-myosin heavy chain (encoded by *MYH7*) and myosin binding protein c (encoded by *MYBPC3*) (Roma-Rodrigues and Fernandes, 2014) (**Table 1.1**).

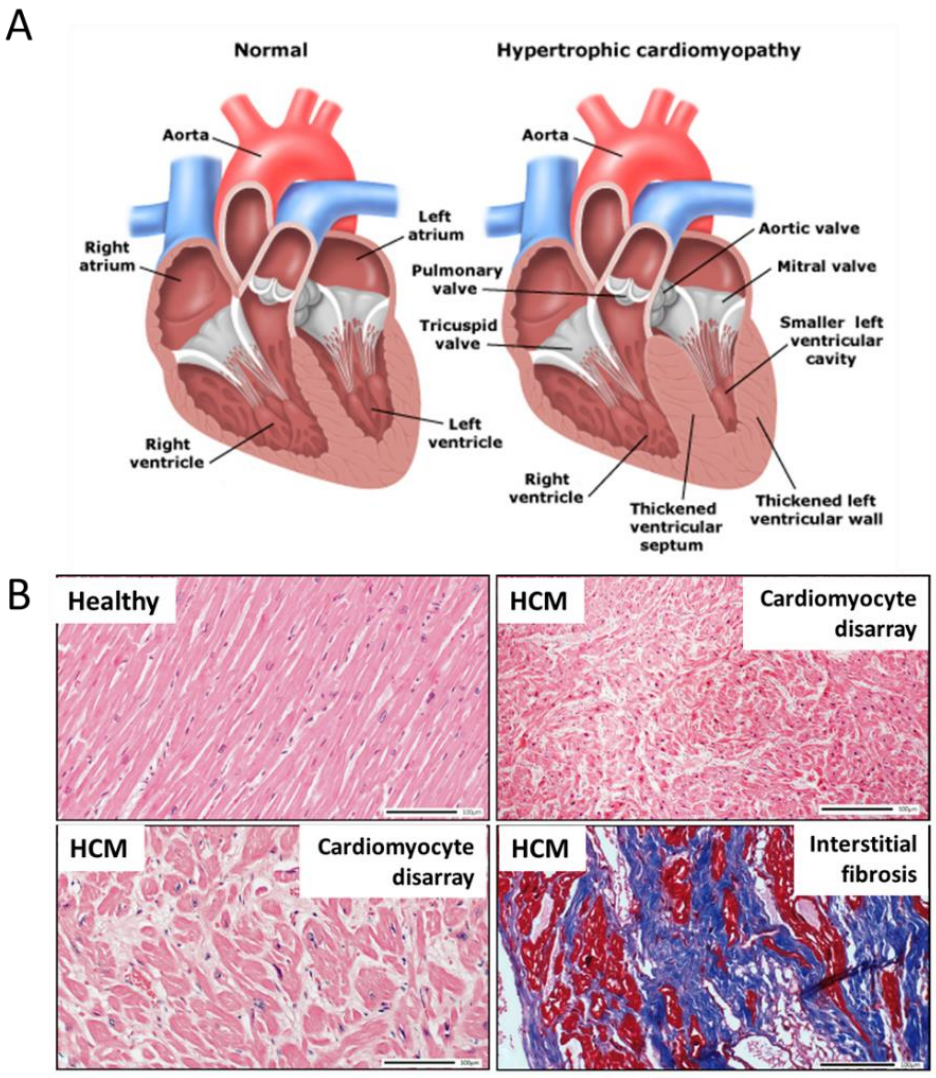


Figure 1.1. Morphological changes to a heart with hypertrophic cardiomyopathy.

(A) HCM is generally categorised by thickening of the left ventricle. **(B)** Histology sections of hearts with HCM demonstrate cardiomyocyte disarray. Masson trichrome staining (blue) shows interstitial fibrosis in HCM hearts. Adapted from (Nishimura et al., 2003, Marian and Braunwald, 2017)

Table 1.1. Abridged list of genes associated with hypertrophic cardiomyopathy

Gene	Protein	HCM-associated mutations	Frequency in patients with HCM	Location/ Function
MYH7	**ß-myosin heavy chain**	**491**	**35 – 45%**	**Sarcomere**
MYBPC3	Myosin-binding protein C (cardiac type)	503	20 – 30%	Sarcomere
TNNT2	Troponin T (cardiac muscle)	90	3 - 5%	Sarcomere
TNNI3	Troponin I (cardiac muscle)	70	<5%	Sarcomere
TPM1	Tropomyosin 1α	38	<5%	Sarcomere
ACTC1	**α-cardiac actin**	**25**	**<5%**	**Sarcomere**
MYL2	Regulatory myosin light chain 2	20	<5%	Sarcomere
MYL3	Essential myosin light chain 3	16	<1%	Sarcomere
PLN	Phospholamban	7	<1%	Regulates sarcoplasmic reticulum Ca^{2+}-ATPase

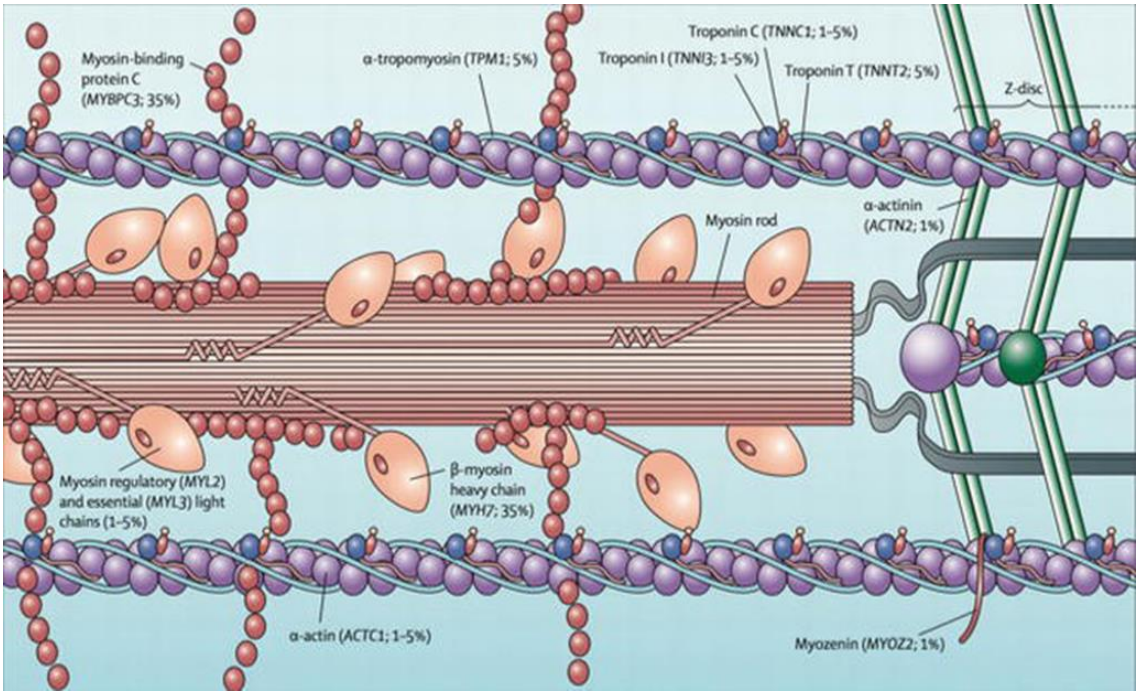


Figure 1.2. Location of sarcomeric proteins involved in causing hypertrophic cardiomyopathy.

Illustration of proteins within the cardiac sarcomere commonly implicated in hypertrophic cardiomyopathy including; α-cardiac actin (purple) and ß-myosin heavy chain (pink). Adapted from (Liu et al., 2017a).

However, HCM has variable penetrance, expressivity and severity (Roma-Rodrigues and Fernandes, 2014). Some individuals may harbour gene mutations associated with HCM, but not exhibit any phenotypic abnormalities. This is known as “variable penetrance”. In addition, individuals with an identical mutation associated with HCM, even within the same family, can show different degrees of phenotypic expression ranging from mild to severe. This is known as “variable expressivity”.

Due this phenotypic variability in HCM, animal models and *in vitro* models have been used to gain a deeper understanding of this complex disease. Some mouse models of HCM have displayed myofilament calcium sensitivity, where lower concentrations of calcium are capable of eliciting contraction (Huke and Knollmann, 2010, Song et al., 2011). However, skinned myofilaments from patients with different β-MHC mutations have shown both increased and decreased sensitivity to calcium (Kirschner et al., 2005).

In addition, altered contractility is often seen in HCM, with some models showing reduced force generation, or a hypo-contractile phenotype (Witjas-Paalberends et al., 2013). Alternatively, some models show a hyper-contractile phenotype (Lowey, 2002, Sommese et al., 2013, Song et al., 2011). Calcium handling abnormalities and arrhythmias have also been seen in various models harbouring gene mutations associated with HCM (Lan et al., 2013, Han et al., 2014, Fatkin et al., 2000, Ren et al., 2017).

There is not yet a unifying theory or mechanism underlying HCM. One theory is the “compensatory model” which states that sarcomeric mutations lead to a decrease in contractility, causing a mechanical response from HCM hearts which in turn results in compensatory hypertrophy (Harvey and Leinwand, 2011). However, this model fails to explain how some forms of HCM have a hyper-contractile phenotype, or involve non-sarcomeric proteins (Landstrom et al., 2011, Song et al., 2011). An alternative “energy-depletion” model states that mutant sarcomeric and regulatory proteins lead to inefficient ATP usage during cross-bridge cycling (**Figure 1.3B**). This in turn leads to an increased energetic cost of force production and a hypertrophic response to an intracellular calcium signalling pathway (**Figure 1.3B**) (Ashrafian et al., 2003).

Calcium plays a vital role in mediating excitation-contraction coupling between sarcomeric proteins (**Figure 1.3A**). The role of calcium sensitivity, potential calcium-dependent signalling pathways and calcium handling abnormalities in HCM are particularly interesting in the context of this thesis. Indeed, calcium handling

abnormalities have been shown to precede other phenotypes of HCM such as hypertrophy in an hiPSC-CM model of ß-MHC R663H HCM (Lan et al., 2013). The investigation of calcium handling in further models of HCM is therefore warranted.

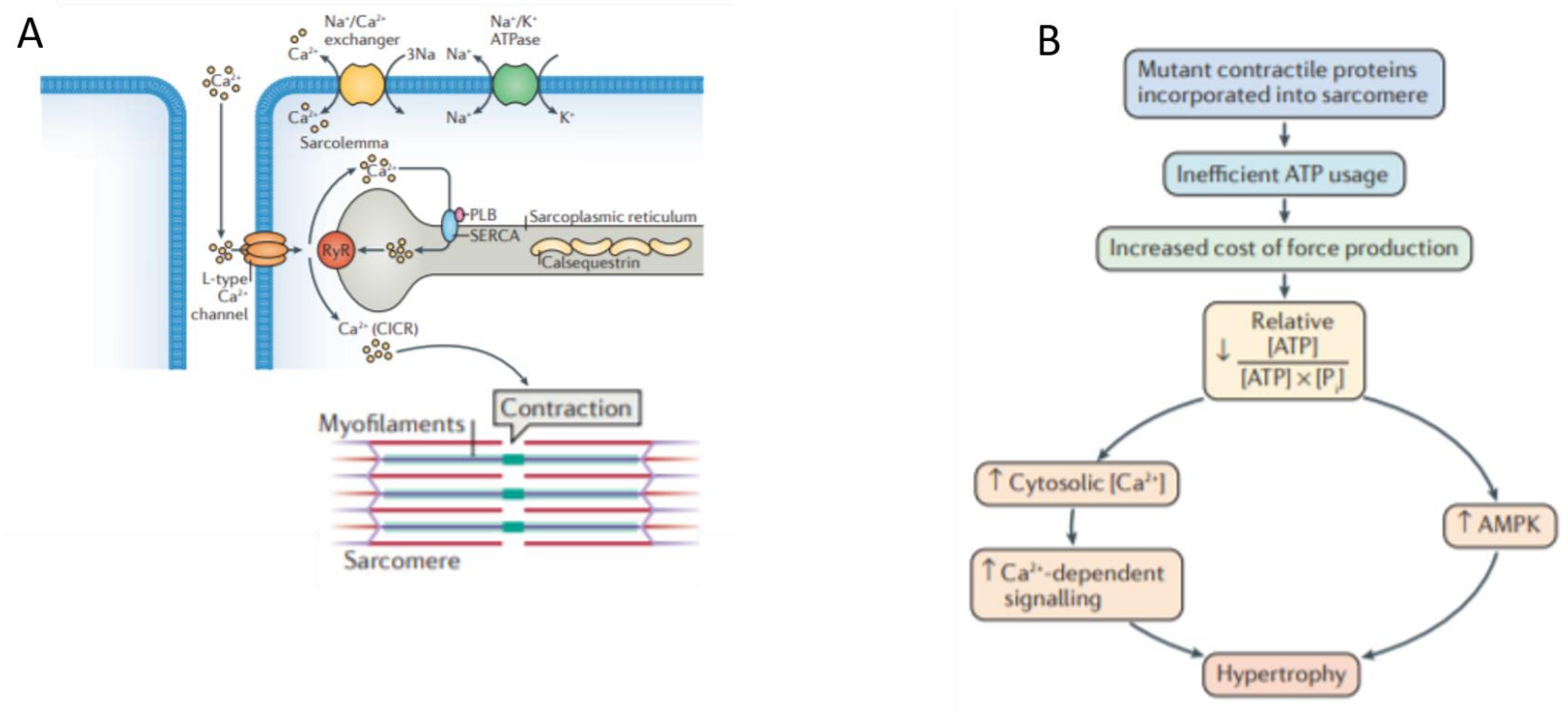


Figure 1.3. Calcium handling, the cross-bridge cycle and the energy depletion model.

(A) Calcium cycling in cardiomyocytes is essential for excitation-contraction coupling. **(B)** The energy depletion model states that sarcomeric mutations cause inefficient ATP usage during the cross-bridge cycle, which in turn leads to hypertrophy via intracellular Ca^{2+}-signalling pathways. Adapted from (Sen-Chowdhry et al., 2016).

1.2.1 Mutation of the *MYH7* gene encoding ß-myosin heavy chain

ß-myosin heavy chain (ß-MHC) is a sarcomeric protein involved in cardiac contractility and mutations to the encoding gene *MYH7* are heavily implicated in HCM (**Table 1.1**). Mutations to ß-MHC are severe and the incidence of sudden cardiac death is particularly high in those with ß-MHC mutations R403Q, R453C, G716R and R719W (Ackerman et al., 2002). Indeed, patients with these mutations generally have a poor prognosis and an average life expectancy of 33 years old (Watkins et al., 1992).

Much of the disease modelling in this thesis focuses on the ß-MHC R453C mutation, caused by a C9123T substitution in the *MYH7* gene. Our own *in silico* structural homology models, together with others, predict that this mutation directly interferes with the interaction between ß-MHC and MyBPC through the C1 binding domain (**Figure 1.4A**). The C2 and M domains, which are also associated with the interaction between ß-MHC and MyBPC remain unaffected (Sadayappan and de Tombe, 2012). In addition, the ß-MHC R453C mutation is shown to alter the flexibility of the loop between the motor domain and the actin binding site (**Figure 1.4B**) (Colegrave and Peckham, 2014, Mosqueira et al., 2018).

To date, this specific ß-MHC R453C mutation has only been modelled using mouse myofilament models, with a specific focus on contractility and force generation (Sommese et al., 2013, Palmer et al., 2004). However, mice are known to express higher levels of the α-MHC isoform in cardiac muscle (Ng et al., 1991). It is therefore appropriate to use a physiologically relevant hiPSC-CM model to investigate other phenotypes of HCM, such as calcium handling.

Whilst some studies have shown abnormal calcium handling in hiPSC-CMs with ß-MHC mutations R663H and R442G (Lan et al., 2013, Han et al., 2014), this thesis seeks to investigate the calcium handling properties of hiPSC-CMs with the ß-MHC R453C (*MYH7* C9123T) mutation.

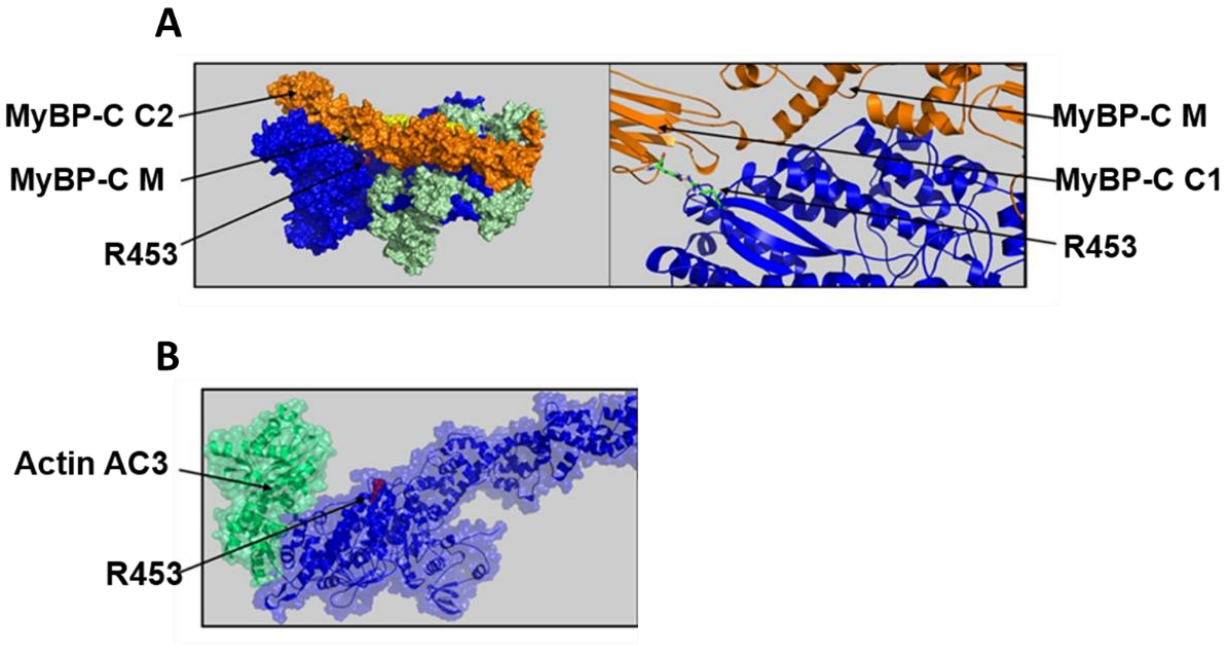


Figure 1.4. *In silico* modelling of ß-MHC R453C interactions.

(A) The interaction between ß-MHC (blue) and MYBPC (orange) is directly influenced by the R453C mutation and is seen to form interactions with the C1 domain in molecular dynamics simulations. C2 and M domains of MYBPC, which are also associated with ß-MHC binding, remain unaffected. **(B)** The R453C mutation occurs away from the actin binding site (AC3, turquoise), but alters the flexibility of the loop between the myosin binding head. Adapted from (Mosqueira et al., 2018).

1.2.2 Mutation of the *ACTC1* gene encoding α-cardiac actin

The *ACTC1* gene encodes the thin myofilament protein α-cardiac actin. Although mutations to this gene are relatively rare in HCM compared to *MYH7*, there are still 25 known mutations which contribute to HCM (Liu et al., 2017a) (**Table 1.1**). Of these, perhaps the most extensively studied is *ACTC1* G301A, which causes a Glu101Lys substitution. Although this mutation occurs at codon 101, it is often referred to as the E99K mutation, because two N-terminal amino acids are lost during post-translational modification (Rubenstein and Martin, 1983).

Patients harbouring the *ACTC1* G301A mutation present with a range of phenotypes including apical remodelling, left ventricular non-compaction, septal defects and ventricular arrhythmias (Olson et al., 2000, Arad et al., 2005, Monserrat et al., 2007). However, the expressivity of these phenotypes varies, even within related patient cohorts.

The mechanism by which *ACTC1* G301A causes such diverse phenotypes has not been elucidated. Structural modelling has shown that the mutation occurs near to the myosin binding site and may impair sarcomere function by altering the cross-bridge interaction (Mogensen et al., 2004).

Mouse models of *ACTC1* G301A have revealed calcium sensitivity and hypercontractility as noticeable phenotypes (Song et al., 2011). In addition, human protein has been expressed in baculovirus and used to populate the thin filament of bovine myofilaments to show a hyper-contractile phenotype (Bai et al., 2015).

As yet, there are no reports of hiPSC-CM models of the *ACTC1* G301A mutation, and this offers an opportunity to gain new insights into this disease-causing mutation in a physiologically relevant model. Furthermore, the opportunity to cross-compare the *ACTC1* G301A mutation to the *MYH7* C9123T mutation may help to add to the knowledge of why such diverse phenotypes can be seen in HCM.

1.3 Human induced pluripotent stem cell-derived cardiomyocytes

Human induced pluripotent stem cell-derived cardiomyocytes (hiPSC-CMs) offer a unique opportunity for *in vitro* disease modelling of cardiomyopathies and drug screening. The ability to derive cell samples from patients with cardiomyopathies, reprogram these cells to pluripotent stem cells, and then differentiate them to cardiomyocytes, provides a readily available resource for phenotyping cardiomyopathies and investigating potential therapeutic interventions (**Figure 1.5**). The genetic profile of these hiPSC-CMs is identical to patients, and a human model recapitulates the disease *in vitro* in a way that animal models may not. However, the maturity of hiPSC-CMs needs to improve in order to truly recreate certain disease phenotypes in the laboratory.

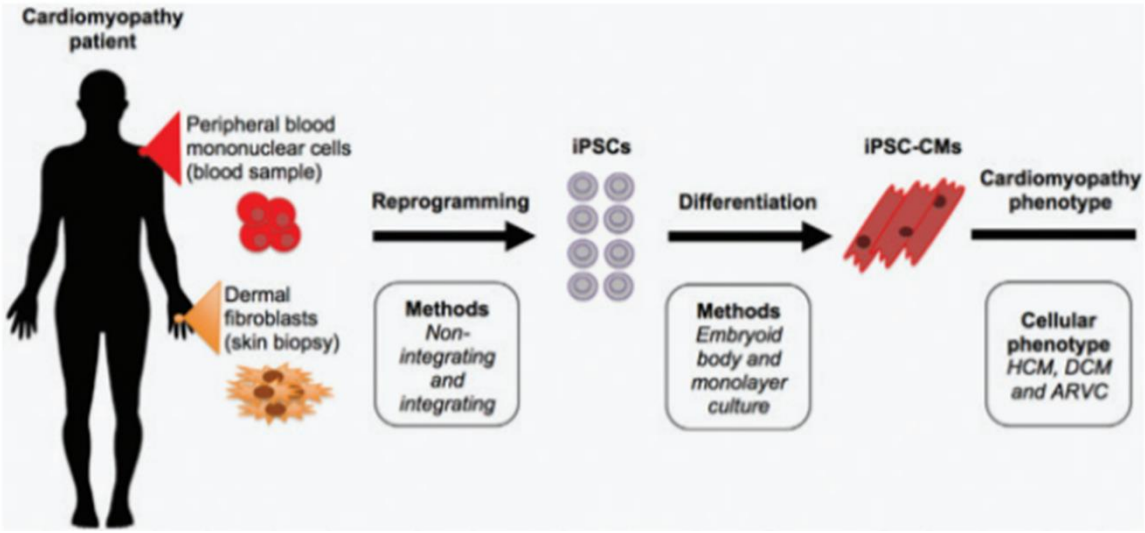


Figure 1.5. Generation of human induced pluripotent stem cell-derived cardiomyocytes for *in vitro* phenotyping of cardiomyopathies.

Somatic cells are taken from a patient and reprogrammed back to a pluripotent stem cell state (hiPSCs). These hiPSCs can then be differentiated to a cardiomyocyte fate (hiPSC-CMs) which can be used for *in vitro* phenotyping and drug screening experiments. Adapted from (Liu et al., 2017a).

1.3.1 Derivation of human embryonic stem cells

Pluripotent stem cells are defined as cells that are self-replicating and capable of developing into cells and tissues of the three primary germ layers; endoderm, ectoderm and mesoderm (Yu and Thomson, 2008). These two properties mean that human pluripotent stem cells provide a readily expandable resource for studying cells and tissues of the human body.

Human embryonic stem cells (hESCs) are derived from the blastocyst of pre-implantation embryos, and are capable of self-renewal *in vitro* for 5 months whilst retaining differentiation potential (Thomson et al., 1998). However, the use of these cells is controversial due to their origin, and regulatory hurdles to their use still exist in some countries such as Germany (Dederer, 2006).

1.3.2 Derivation of human induced pluripotent stem cells

These issues were overcome with the emergence of human induced pluripotent stem cells (hiPSCs) that were generated by reprogramming somatic cells. Utilising integrating retroviruses to deliver four key transcription factors; *OCT3/4*, *SOX2*, *KLF4*, and *c-MYC*, the ability to reprogram adult human fibroblasts to a pluripotent state was demonstrated (Takahashi et al., 2007). This technique has been further developed with the use of non-integrating Sendai virus (Fusaki et al., 2009) and mRNA delivery of pluripotency factors (Warren et al., 2010) to offset the risk of insertional mutagenesis.

Our laboratory, and others, favour Sendai virus reprogramming of skin punch biopsies from patients to provide a self-renewing resource to study complex diseases *in vitro* (Denning et al., 2016, Duncan et al., 2017, Kondrashov et al., 2018). Reprogramming somatic cells and differentiating them to cardiomyocytes provides an almost unlimited supply of cells for studying cardiac diseases that abrogates the need to source cadaveric tissue or use non-human cells. Crucially, by deriving cells from patients, we can investigate potential therapies that are tailor-made for individuals, and begin to explore the fields of pharmacogenomics and personalised medicine.

1.3.3 Human pluripotent stem cell culture and maintenance

Since the initial derivation of hPSCs, the methods for continuous culture of these cells has gradually improved, streamlining the number of factors required for their maintenance.

Feeder cells, such as irradiated mouse embryonic fibroblasts (MEFs) have been used to support self-renewal of hPSCs through the secretion of essential growth factors such as TGF-ß and extracellular matrices (ECM) such as laminin (Eiselleova et al., 2008). However, these animal cells are a potential source of immunogenic pathogens and mycoplasma which can alter growth rate, karyotype or differentiation efficiency of hPSCs (Martin et al., 2005, Villa-Diaz et al., 2013).

Feeder-free culture methods initially relied on tissue culture plates coated with Matrigel™ in combination with MEF-conditioned medium. Matrigel™ is derived from mouse sarcoma tissue and is composed of a mixture of ECM proteins including laminin, collagen IV and heparin sulphate proteoglycans (Ghasemi-Dehkordi et al., 2015). A drawback of using Matrigel™ is that it suffers from batch-to-batch variability, and must be carefully tested before application in established differentiation protocols. Furthermore, the risk of xenogeneic contamination persists with the use of a MEF-conditioned culture medium.

To fully realise the potential of hPSCs for regenerative medicine and disease modelling, the use of xenogeneic factors must be kept to a minimum. Defined hPSC culture has been achieved with the discovery of eight essential factors for hPSC maintenance. This “essential 8” (E8) medium contains; L-ascorbic acid, selenium, transferrin, insulin, FGF2, TGFß1 and sodium bicarbonate dissolved in DMEM/F12 (Chen et al., 2011c). There are seemingly no deleterious effects on differentiation efficiency or hPSC survival by using E8 medium, although it must be combined with the Rho-associated kinase inhibitor Y-27632 in the first 24 hours after passaging to prevent anoikis caused by a lack of cell adhesion (Watanabe et al., 2007). For truly xeno-free culture of hPSCs, defined substrates such as laminin, vitronectin or fibronectin should be used to support maintenance (Rajala et al., 2010, Fan et al., 2015).

Despite its expense (£340 per litre) and short shelf-life of 2 weeks, E8 medium is now widely used for hPSC maintenance, and paves the way for chemically-defined, GMP-compliant culture of hPSCs for regenerative medicine or drug screening applications.

1.3.4 Differentiation of human induced pluripotent stem cells towards a cardiomyocyte fate

In order to apply hiPSCs to study cardiac diseases *in vitro*, efficient differentiation protocols are required to reproducibly generate large number of cardiomyocytes. By using biological cues discovered in the field of developmental biology, several approaches for generating human induced pluripotent stem cell-derived cardiomyocytes (hiPSC-CMs) have been established.

1.3.4.1 Recapitulating *in vivo* development

The *in vitro* generation of hiPSC-CMs relies heavily on recapitulating *in vivo* embryonic heart development. Broadly, this consists of; mesoderm induction, cardiac specification and cardiomyocyte maturation.

In vivo, a process called epithelial-to-mesenchymal transition (EMT) occurs during gastrulation to form the mesoderm. This process is induced by NODAL, which encourages BMP4 and WNT3 expression in surrounding germ layers (Burridge et al., 2012).

Once the cardiac mesoderm has been specified, proximal migration and the formation of the first and second heart fields occurs. Here, inhibitory WNT signalling keeps cells in a cardiac progenitor state. Active Wnt/ß-catenin signalling is required for primitive streak and pre-cardiac mesoderm formation, whereas its inhibition is required for cardiac progenitor formation (**Figure 1.6**) (Spater et al., 2014). This highlights the intricacies involved in these complex spatiotemporal growth factor gradients during development. Finally, cardiomyocytes develop from the first and second heart fields with the expression of key transcription factors such as *NKX2.5*, *GATA4* and *MEF2*.

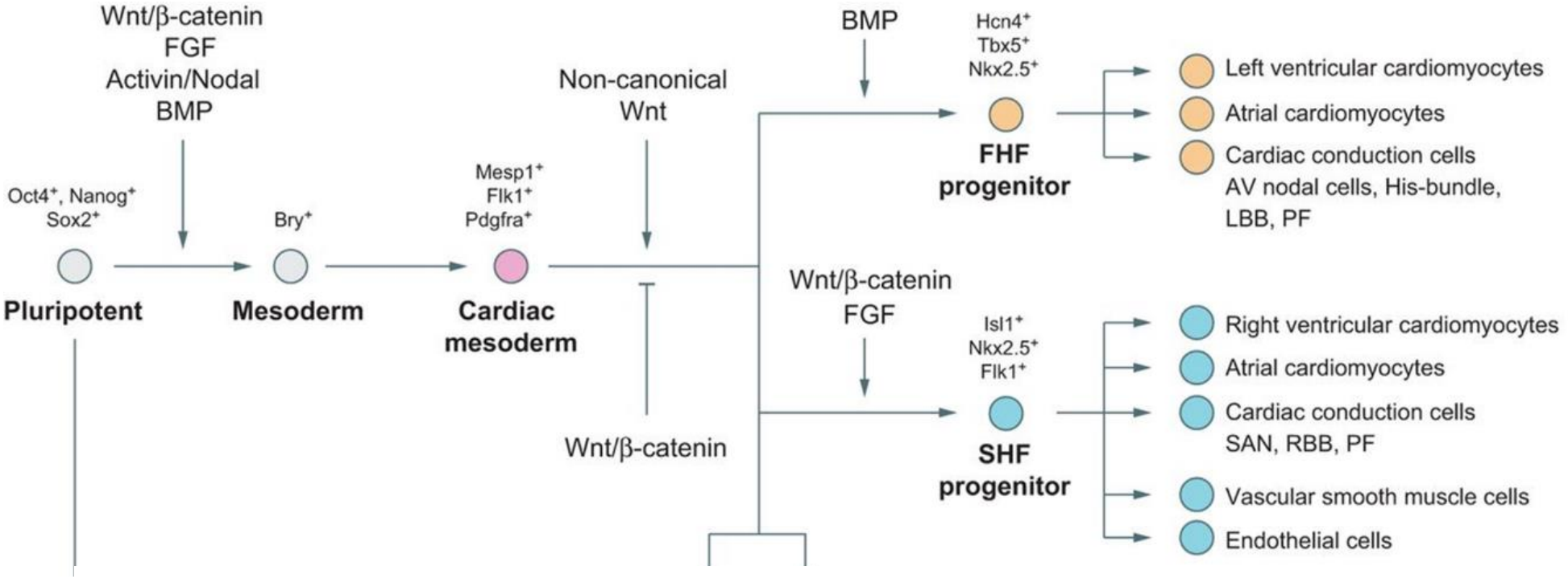


Figure 1.6. Stepwise specification of the cardiomyocyte lineages.

During development pluripotent cells are coaxed towards a cardiomyocyte fate through various signalling pathways. The spatiotemporal regulation of development is complex. Whilst Wnt/β-catenin signalling is essential for mesoderm induction, it is later inhibitory to cardiomyocyte development, and maintains a progenitor state. FHF – first heart field, SHF – second heart field. Adapted from (Spater et al., 2014).

1.3.4.2 Differentiation protocols

In vivo cardiomyocyte production shows that stage-specific activation/inhibition of developmental pathways and growth factor concentration gradients are essential. This has been exploited *in vitro* to generate cardiomyocytes in several ways. These can be largely grouped into; embryoid body (EB), monolayer, subtype-specific and suspension culture based differentiation protocols.

EB based protocols are based on the formation of three dimensional aggregates of pluripotent stem cells. These aggregates can be made by a 'hanging drop' method of suspending hiPSCs in a drop of fluid that hangs from a coverslip, or by forced aggregation in V-bottom wells. The aggregation into EBs helps to provide the concentration gradients required for differentiation, and can generate cardiomyocytes through spontaneous differentiation (Itskovitz-Eldor et al., 2000). However, these protocols were initially inefficient, yielding around 50% cardiomyocyte purity (Anderson et al., 2007). Additionally, EB based methods rely on EB transfer techniques which are time-consuming and not amenable to high throughput cardiomyocyte generation.

Monolayer protocols allow the diffusion of key growth factors and small molecules to guide hiPSCs towards a cardiomyocyte fate. One of the first such protocols utilised Activin A to mimic NODAL signalling, followed by BMP4 treatment to generate hESC-CMs at a purity of 30% (**Table 1.2**) (Laflamme et al., 2007). Another protocol utilises a matrigel-sandwich method to simulate EMT *in vitro*, generating average yields of approximately 60% troponin-T positive cardiomyocytes (Zhang et al., 2012).

Our own laboratory has modified these protocols and developed a monolayer protocol capable of routinely generating cardiomyocytes of >80% purity as measured by α-actinin staining (**Table 1.2**) (Celiz et al., 2015, Duncan et al., 2017, Kondrashov et al., 2018).

In the push towards more xeno-free protocols, a chemically-defined differentiation protocol has been developed which can produce cardiomyocyte purities of >90% (Burridge et al., 2014). However, the use of such a lean medium can lead to frequent differentiation failures (personal observation).

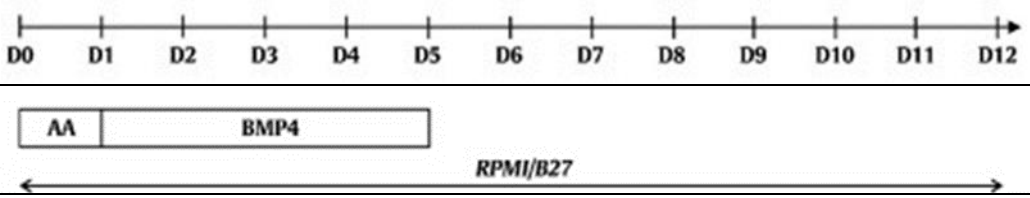
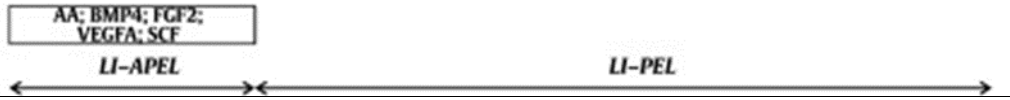
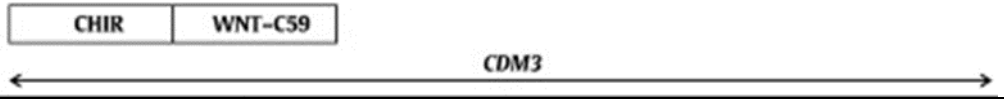
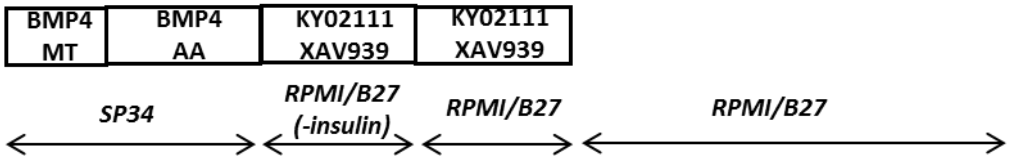
Medium	Substrate	Differentiation protocol	Efficiency	Subtypes	References
MEF-CM	Matrigel™		30%	V, A	(Laflamme et al., 2007)
MEF-CM	Matrigel™		40%	V, A	(Elliott et al., 2011)
E8	Matrigel™		90%	V, A	(Burridge et al., 2014)
MEF-CM, mTESR, E8	Matrigel™, Laminin, Vitronectin		80%	V, A	(van den Berg et al., 2016)
mTESR, E8	Matrigel™, synthetic polymer		80%	V, A	(Celiz et al., 2015, Duncan et al., 2017, Kondrashov et al., 2018)

Table 1.2. Selected monolayer cardiac differentiation protocols.

AA – Activin A, BMP4 – Bone morphogenetic protein 4, CDM3 – 3-component chemically defined medium, FGF2 – basic fibroblast growth factor, VEGFA – vascular endothelial growth factor, SCF – stem cell factor, LI-APEL – low insulin albumin polyvinylalcohol essential lipids medium, LI-PEL – low insulin polyvinylalcohol essential lipids medium, CHIR – CHIR99021 GSK-3β inhibitor, WNT-C59 – Wnt inhibitor, XAV939 – Wnt inhibitor, SP34 – Stem Pro 34 medium, MT – Matrigel™. MEF-CM – MEF-conditioned medium. V – ventricular cardiomyocyte, A – atrial cardiomyocyte Adapted from (Denning et al., 2016).

The aforementioned monolayer protocols tend to generate a heterogeneous mixture of different cardiomyocyte subtypes. However certain disease models or drug screens, such as those involving atrial fibrillation, may require subtype specification with tailored differentiation protocols.

Advances have been made towards generating mostly atrial cardiomyocytes, with the addition of retinoic acid (Devalla et al., 2015). Alternatively, pacemaker-like cardiomyocytes can be generated by modulating the activity of the transcription factors *SHOX2* and *TBX3* (Birket et al., 2015b, Protze et al., 2017). These advances will provide the field with the tools necessary to study cardiac diseases that are restricted to certain areas of the heart.

In order to enhance the scalability of cardiac differentiation protocols and make them amenable to industrial and clinical use, 3D suspension protocols are beginning to emerge. One such protocol uses a bioreactor to generate cardiomyocyte spheroids through temporal modulation of FGF, Wnt and TGF-β pathways. As a result over 90% of the spheroids are positive for the cardiomyocyte marker troponin-T (Fonoudi et al., 2015).

In summary, the past decade has seen a rapid evolution in the quest for efficient, scalable and reproducible cardiac differentiation protocols. However, there are still challenges of batch to batch variation, inter-lab variability and, crucially, maturity (section 1.2.5) of these hiPSC-CMs. Nevertheless, current approaches allow the generation of sufficient quantities of cardiomyocytes to model cardiac diseases and screen drugs *in vitro*.

1.3.5 Human induced pluripotent stem cell-derived cardiomyocytes as tools for disease modelling

Cardiovascular diseases are the leading cause of death worldwide, accounting for a staggering 33% of all deaths in 2015 (Roth et al., 2017). The financial impact of heart failure alone is roughly $45bn, which is set to rise to $90bn by 2030 (Denning et al., 2016). There is consequently an acute need to better understand cardiac diseases.

A wealth of information about disease progression and underlying mechanisms has been uncovered with the use of animal models. However, species differences can confuse matters. For example, the heart rate of mice is approximately 5 times faster than that of humans, due to differences in ion channel expression (Edwards and Louch, 2017).

Sarcomeric protein expression can also be species-dependent, with mouse hearts predominantly expressing α-myosin heavy chain in the ventricle, compared to the predominantly ß–myosin heavy chain expression in human ventricles (Lyons et al., 1990, Reiser et al., 2001).

Ideally, human primary cardiomyocytes would be used for understanding disease mechanisms in the laboratory, however their large-scale use is hindered by poor availability, poor consistency and a lack of proliferation capacity (Pavlova et al., 2013).

On the other hand, hiPSC-CMs can be derived from patients with cardiac diseases, provide an almost unlimited supply of cells, and generate functional readouts *in vitro* to model complex cardiac pathophysiology.

Several genetic heart conditions including; catecholaminergic ventricular tachycardia (CPVT) (Jung et al., 2012), Long QT syndrome type 2 (LQTS2) (Matsa et al., 2011), Barth syndrome (Wang et al., 2014) and LEOPARD syndrome (Carvajal-Vergara et al., 2010) have been successfully modelled *in vitro* using patient-specific hiPSC-CMs.

This demonstrates the value that hiPSC-CMs can provide to the field for gaining insights into complex genetic diseases.

1.3.6 Human induced pluripotent stem cell-derived cardiomyocytes as tools for drug screening

Predicting the cardiac safety profile of new drug candidates remains a critical part of the drug development pipeline. Of the 38 new drugs withdrawn from the market by the US FDA between 1996 and 2004, 45% were due to unforeseen cardiotoxicity (Dykens and Will, 2007). This costs the pharmaceutical industry billions of pounds, and therefore the ultimate goal is to be able to identify potentially cardiotoxic compounds early in the drug development process.

Established methods for assessing cardiac safety pharmacology include the use of animal models such as rodents and rabbits, or overexpression of the hERG channel in HEK or CHO cells (Heijman et al., 2014).

However, there are clear species-dependent differences in cardiac electrophysiology. For example, during calcium cycling in the cardiomyocyte, rodent models such as mice and rats only utilise NCX extrusion for approximately 7% of the calcium cycled during

diastole, with the majority of the remaining calcium re-sequestered into the SR. In larger mammals such as rabbits and humans NCX clearance of calcium is responsible for 28% of calcium extrusion (Edwards and Louch, 2017).

In addition, mice express higher levels of repolarising K^+ currents such as I_{Kur} compared to humans. This means that the murine APD is 4 times shorter than the human (50 ms compared to 200 ms in human) and the action potential is more triangular in shape (Ahrens-Nicklas and Christini, 2009).

Furthermore, studying overexpression of a single repolarising K^+ channel, such as hERG alone is not sufficient to predict more complex arrhythmogenic mechanisms (Killeen, 2009).

This is highlighted by the fact that cardiotoxic drugs such as the serotonin agonist cisapride or the antipsychotic drug sertindole have made it to market before being withdrawn after QT prolongation and sudden cardiac deaths (Quigley, 2011, Nielsen et al., 2015).

Cardiac drug safety assessment has therefore turned to hiPSC-CMs, which provide an advantage over previous models as they are scalable, amenable to high-throughput drug screening, and are physiologically relevant and complex. Consequently, the comprehensive *in vitro* proarrhythmia assay (CiPA) initiative has been set up. This is a consortium of academic and industrial partners which seek to use hiPSC-CMs and emerging technologies to more accurately predict arrhythmia risk of candidate drugs (Colatsky et al., 2016).

Within this framework, the contract research organisation Quintiles has already shown that the cardiotoxic effects of Ponatinib, a withdrawn anticancer drug, could have been detected if hiPSC-CMs had been used for screening (Talbert et al., 2015).

In terms of basic research, hiPSC-CMs can give insights into disease mechanisms and therefore allow potential drugs to be tested *in vitro*. For example, the RYR2 antagonist dantrolene was found to rescue the arrhythmic phenotype of hiPSC-CMs derived from a patient with CPVT (Jung et al., 2012). In addition, hiPSC-CMs derived from patients with Timothy syndrome were shown to exhibit QT prolongation and arrhythmias caused by a mutation in the $Ca_V1.2$ subunit of L-type calcium channels. These phenotypes were rescued with the L-type channel ($Ca_V1.2$) inhibitor roscovitine (Yazawa et al., 2011).

1.3.7 Challenges associated with the use of human induced pluripotent stem cell-derived cardiomyocytes

The application of hiPSC-CMs for drug screening and disease modelling must proceed with caution due to differentiation protocols producing cardiomyocytes with a somewhat immature phenotype.

Differentiated hiPSC-CMs are known to exhibit several hallmarks of immaturity including; rounded shape, disorganised sarcomere, slower conduction velocity and a negative force-frequency relationship (**Table 1.3**) (**Figure 1.7**) (Denning et al., 2016). Calcium handling is also thought to be immature in hiPSC-CMs, with a lack of ultrastructural transverse tubules (T-tubules) and low expression of key sarcoplasmic reticulum accessory proteins such as calsequestrin, junctin and triadin (Liu et al., 2007).

Current differentiation protocols seek to mimic developmental cues, hiPSC-CMs therefore resemble foetal cardiomyocytes rather than adult cardiomyocytes. This remains a major challenge in the field. However, efforts are progressing towards achieving a more mature hiPSC-CM phenotype. Protocols have been developed that employ; mechanical stimulation (Jung et al., 2016), 3D culture (Tiburcy et al., 2017), or co-treatment with triiodothyronine and dexamethasone on a Matrigel™ "mattress" (Parikh et al., 2017). These studies have shown improvements in fully recapitulating adult CM ultrastructure, electrophysiology, calcium handling and gene expression. As the field gradually overcomes the hurdles presented by incomplete maturity, more accurate *in vitro* disease models will be achieved.

Table 1.3. Characteristics of hiPSC-CMs compared to adult CMs reveal a lack of maturity in hiPSC-CMs.

		hiPSC-CMs	Adult CMs
Structure	Shape	Round, polygonal	Rod-shaped
	Sarcomere alignment	Unaligned	Aligned
	T-tubules	No	Yes
Calcium handling	Sarcoplasmic reticulum	Mixed response to caffeine, thapsigargin and ryanodine.	Well developed
	SR proteins	Lower expression	Calsequestrin, triadin, junctin
Energy & force	Beating	Spontaneous	Quiescent
	Metabolism	Fatty acids	Glucose, lactate, fatty acids
	Force-frequency relationship	Negative	Positive
	Conduction velocity	10 – 20 cm/s	60 cm/s
Kinetics	APD90	300 – 700 ms	260 ms
	Calcium transient duration	800 – 2000 ms	800 – 1000 ms
	T-rise	3.5 – 10 ms	2.5 ms

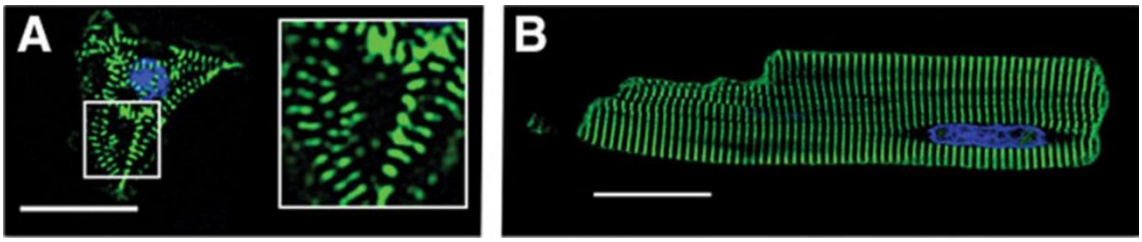


Figure 1.7. Morphological immaturity of hiPSC-CMs compared to adult CMs.

Immunocytochemistry of CMs for the myofibrillar protein α-actinin (green) and nuclear DAPI staining (blue) **(A)** hiPSC-CM with rounded shaped and disorganised sarcomere indicate a lack of maturity. **(B)** Adult rodent CM with rod shape and clearly aligned sarcomere anticipated in mature CMs. Scale bars = 25 μm. Adapted from (Yang et al., 2014).

1.4 Harnessing site-specific nucleases for precise genome engineering

The delivery of a reporter gene into the genome of hPSCs can be achieved in many ways. For example, adeno-associated viral (AAV) and lentiviral transduction of a luciferase reporter gene has been attempted in hESCs, hiPSCs and their derived cardiomyocytes (Rapti et al., 2015). However, viral delivery of genes does not always result in stable integration into the genome, and transgene expression can be lost over successive cell divisions (Wang et al., 2007). Even if stable integration does occur; retroviral or lentiviral techniques risk insertional mutagenesis, as important genes can be disrupted by random integration of the transgene (Vasileva and Jessberger, 2005).

In addition, the likelihood of multiple integration events could result in differential transgene expression between cells. If a transgene has been randomly integrated into the genome, a phenomenon called position effect variegation (PEV) can occur (Williams et al., 2008, Yin et al., 2012). This is when a transgene that is usually found in euchromatin is inserted adjacent to an area of heterochromatin. Methylation can expand across this border and silence the transgene (Elgin and Reuter, 2013). This results in heterogeneous clones with highly variable expression of the transgene.

To overcome these issues, site-specific genome engineering techniques have been developed. Recent advances have moved toward the use of nucleases directed to specific areas of the genome where they initiate double strand breaks (DSBs) to activate endogenous repair pathways. DNA damage response is highly conserved, so these nuclease-based methods of genome engineering can be applied to plants, invertebrates, fish, mammals and human induced pluripotent stem cells (Mao et al., 2008, Gupta and Musunuru, 2014).

1.4.1 DNA damage response pathways

The two main DNA damage response pathways to DSBs are non-homologous end joining (NHEJ) and homology-directed repair (HDR) (**Figure 1.8**).

In NHEJ, broken segments of DNA are directly ligated together, without the use of a homologous template. NHEJ is therefore very fast, taking just 30 minutes to complete in an immortalised human cell line (Mao et al., 2008). However, this speed comes at the expense of fidelity, making NHEJ highly mutagenic. If the error-prone NHEJ pathway is utilised for genome engineering, insertions/deletions (indels) are likely to

take place. In this way, knockout alleles are easily generated by disruption of target genes (Ran et al., 2013b) (**Figure 1.8**).

HDR uses a homologous region of DNA as a template for repair, making it a much more accurate repair pathway. HDR tends to occur during late S and G2 phases of the cell cycle, when sister chromatids are available to serve as templates (Lin et al., 2014). In addition, it is a relatively slow process, taking up to 7 hours to complete (Mao et al., 2008). This means that although HDR accurately restores the DNA sequence, it can be an inefficient process.

By providing an exogenous template for DNA repair to occur via homology-directed repair (HDR), desired sequences can be inserted into the host genome (Kim and Kim, 2014) (**Figure 1.8**). The exogenous template can include large reporter genes, or single SNPs, typically using double-stranded DNA delivered on targeting plasmid vectors. Single stranded oligodeoxynucleotides (ssODNs) can also be used as templates, and are sometimes preferred for their ease of construction and ability to perform plasmid-free targeting by combining with nuclease-encoding mRNA or recombinant nuclease protein (Chen et al., 2011b, Kim et al., 2014b).

The genome engineering presented in this thesis relies heavily on HDR to alter SNPs or insert genes into target locations. To ensure its use as a template for HDR, donor DNA must have adequate homology arms of around 1 kilobases each side of the desired insert. In addition, the low efficiency of HDR will require a selection cassette to locate and isolate targeted cells.

DSBs can be induced at specific locations using a range of site-specific nucleases. These approaches include; zinc finger nucleases (ZFNs), transcription activator-like effector nucleases (TALENS) and RNA-guided endonucleases (RGENs) (Gupta and Musunuru, 2014).

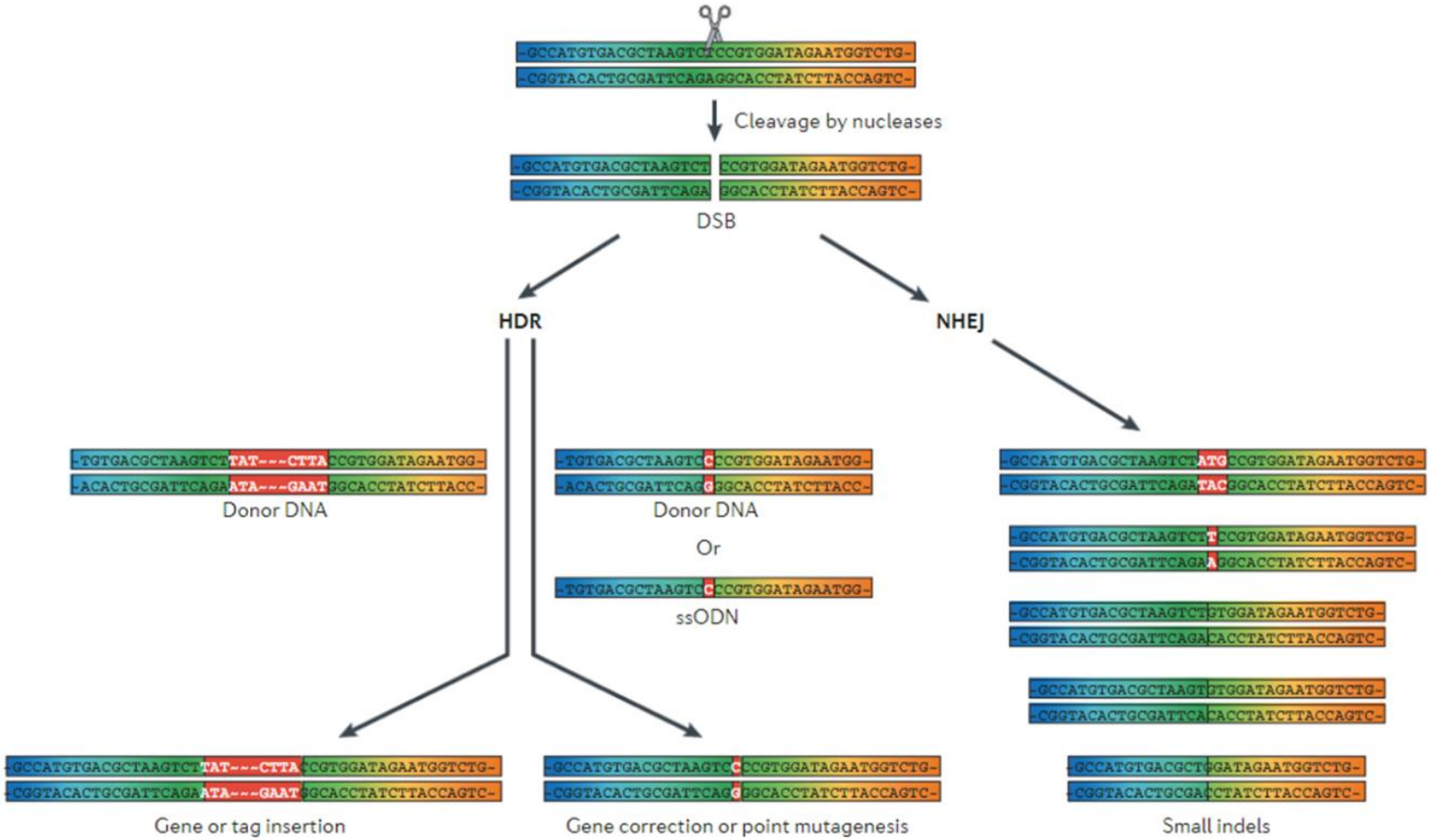


Figure 1.8. DNA damage repair pathways exploited for site-specific genome engineering.

Cleavage by site-specific nucleases induce a double-strand break (DSB) in DNA which can be repaired via homology-directed repair (HDR) or non-homologous end joining (NHEJ). Donor DNA or a single stranded oligodeoxynucleotide donor (ssODN) can be used as a template to achieve gene knock-in or alter single base pairs in the target genome. In the absence of a template, NHEJ is favoured, which often results in small insertions/deletions for target gene knock-out. Adapted from (Kim and Kim, 2014).

1.4.2 Zinc finger nucleases

ZFNs consist of multiple zinc finger motifs that each recognise a specific 3 base pair DNA sequence. Therefore, a zinc finger array consisting of three zinc finger motifs is capable of recognising and binding 9 DNA base pairs.

Zinc finger arrays are often designed using modular assembly, whereby the zinc finger array is gradually extended as zinc finger motifs are added and optimised based on target DNA specificity (Bae et al., 2003). This approach often relies on yeast or *E. coli* to screen plasmid libraries that encode zinc fingers encoded by the human genome. However, this approach has an efficiency of less than 6% (Ramirez et al., 2008). In addition, these approaches require enormous randomised libraries (>10^8 in size), which are outside the reach of many labs (Maeder et al., 2008).

Zinc finger motifs are associated with a FokI endonuclease which require nuclease dimerisation to initiate cleavage of target DNA sequences. This adds to the complication of ZFN design, as cleavage requires the design of two ZFNs to bind to each adjacent half-site (**Figure 1.9**) (Miller et al., 2007).

In addition, dimerisation of ZFNs is weak as FokI remains monomeric at concentrations up to 15 μM, and are only likely to dimerise once bound to a target (Vanamee et al., 2001). Whilst it can be argued that this enhances the specificity of ZFNs, off-target cleavage can occur as a result of poorly designed or insufficient zinc finger motifs. Off-target cleavage has been shown to be highly toxic, with multiple DNA double strand breaks (DSBs) overwhelming the repair mechanisms of the cell (Cornu and Cathomen, 2010).

Despite these drawbacks, ZFNs have been widely exploited for their ability to initiate DSBs and allow an exogenous template to be used for DNA repair by homologous recombination. ZFNs have been used to induce site-specific modifications at an efficiency of up to 50% in a variety of applications (Perez et al., 2008, Lombardo et al., 2007, Beumer et al., 2006). For example, ZFNs have been used to confer resistance to HIV-1 in haematopoetic stem cells by deleting a 32 base pair region of the HIV-1 co-receptor gene, *CCR5* (Holt et al., 2010).

However, due to the modular construction of ZFNs and lack of extensive zinc finger libraries, ZFNs are time-consuming and costly to construct and suffer from reduced

specificity (Urnov et al., 2005). As a result, the field of genome engineering has explored other site-directed nucleases.

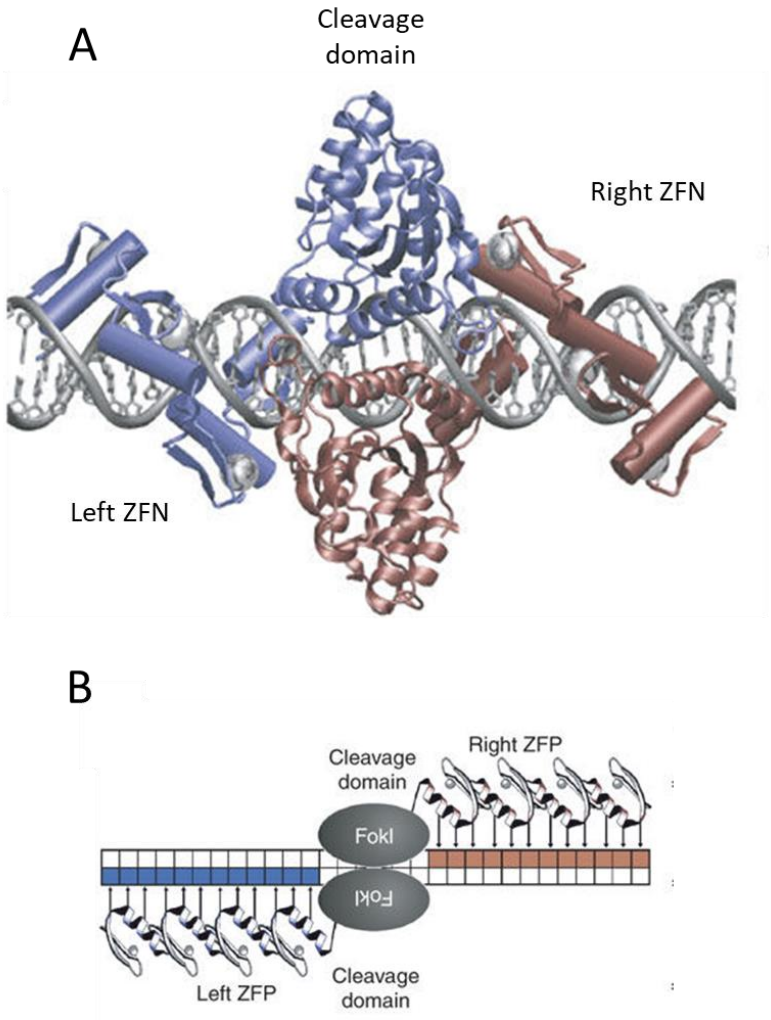


Figure 1.9. Zinc finger nucleases.

(A) Crystal structures of two zinc finger nuclease complexes (blue and red) bound to a DNA helix (grey). Dimerisation of the FokI nuclease monomers allows cleavage of the DNA to occur. **(B)** Schematic of two zinc finger nuclease complexes mediating DNA cleavage. Each zinc finger array consists of four zinc finger motifs, which are each capable of recognising a 3 base pair sequence of DNA. Adapted from (Miller et al., 2007).

1.4.3 Transcription activator-like effector nucleases

Transcription activator-like effector nucleases (TALENs) have also been used in the field of genome engineering. TALE proteins were discovered within pathogens of the *Xanthomonas* genus of plants (Boch et al., 2009, Moscou and Bogdanove, 2009).

TALE proteins have a central DNA binding domain that contains several conserved repeats. However, within this repeat domain lies a polymorphic pair of residues known as repeat variable di-residues (RVDs) (**Figure 1.10A**). RVDs that preferentially bind to each of the four DNA bases have been identified, enabling the ability to design arrays of multiple TALEs to target specific DNA sequences (Hockemeyer et al., 2011) (**Figure 1.10**). Similarly to ZFNs, TALENs utilise the FokI nuclease, and require the design of flanking targeting arrays for dimerisation to mediate DNA cleavage.

Each TALE DNA binding domain can recognise and bind a single base pair, which is more specific than the three base pairs recognised by zinc finger domains in ZFNs. This abrogates the need for vast screening libraries and reduces the likelihood of off-target cleavage. The reduced off-target activity of TALENs make them less cytotoxic than ZFNs in side-by-side comparisons (Mussolino et al., 2011). In addition, the overall gene editing efficiency is similar to ZFNs, and can be as high as 45% (Mussolino et al., 2011).

Nevertheless, TALENS still require unwieldy modular assembly that is expensive and labour-intensive.

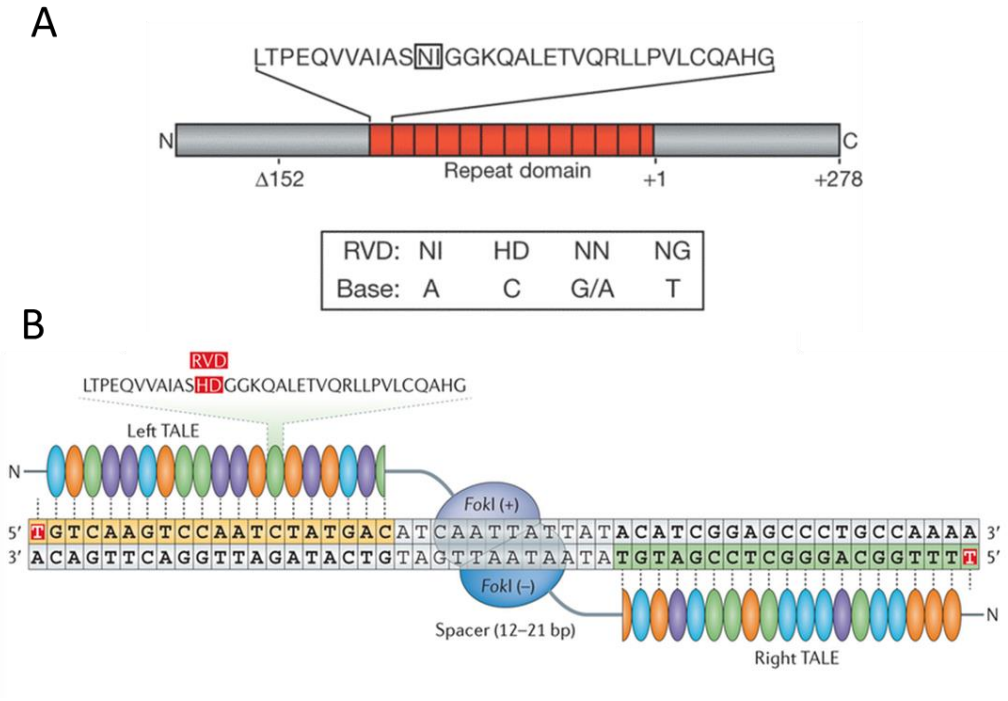


Figure 1.10. Transcription activator-like effector nucleases.

(A) Each TALE DNA binding domain contains a conserved region of repeating amino acid residues. Within this repeat region, polymorphisms can be found in repeat variable di-residues (RVDs). These RVDs confer specificity to each of the four bases found in DNA. **(B)** The ability to produce TALE proteins that are specific to DNA bases means that TALE arrays can be made to direct a FokI nuclease to a target DNA site. Dimerisation of two FokI monomers is necessary to initiate a DSB. Adapted from (Miller et al., 2011, Kim and Kim, 2014)

1.4.5 CRISPR-Cas9

Rather than employing large modular proteins for genome engineering, RNA-guided endonucleases (RGENs) such as the clustered, regularly interspersed, short palindromic repeats (CRISPR) – CRISPR-associated protein (CRISPR-Cas9), instead use small RNA sequences to direct a Cas9 nuclease to the recombination site (Cong et al., 2013).

The CRISPR-Cas9 genome engineering technique is based on the bacterial/archaeal response to phage infection whereby the cleavage of foreign DNA and the incorporation of protospacer repeat elements allows the rapid recognition of future infection. Foreign DNA transcripts containing protospacer adjacent motif (PAM) sequences of –NGG are known as CRISPR-RNA (crRNA). Upon infection, crRNA binds to the invading sequence and transactivating CRISPR RNA (tracrRNA) recognises the associated PAM sequences, recruiting the Cas9 nuclease to cleave the target DNA (Bhaya et al., 2011) (**Figure 1.11A**).

This mechanism can be elegantly exploited for precise genome engineering. By generating single-chain guide RNAs (sgRNAs) that consist of a scaffold and a 20 nucleotide guide sequence that is specific to host chromosomal DNA, Cas9 nuclease can be recruited to the desired site to induce a DSB (**Figure 1.11B**). Exogenously supplied template DNA can then be used for HDR to incorporate a genomic change.

The design of a 20 nucleotide guide sequence is relatively straightforward, but limited by the requirement for an -NGG PAM sequence in the host genome (**Figure 1.11C**). However, these sequences occur at a high frequency of roughly every 8 bp in the human genome (Cong et al., 2013). It is also important to mutate the PAM sequence in any donor DNA construct, to prevent Cas9 cleavage of the template.

Although the requisite PAM sequence for *S. pyogenes* Cas9 occurs relatively frequently throughout the genome, some studies have used Cas9 derived from *Neisseria meningitidis* which has a different PAM site recognition sequence to further improve the flexibility of CRISPR Cas9 (Esvelt et al., 2013, Hou et al., 2013). In addition, a recent xCas9 variant is said to recognise a broad range of PAM sequences including –NG, -GAA and –GAT (Hu et al., 2018).

One area of concern with the use of CRISPR Cas9 for genome engineering is the occurrence of off-target events. Indeed, the specificity of guide sequences need to be carefully considered, as mismatches are more tolerated at the 5' end of sgRNAs,

compared to the 3' end (Hsu et al., 2013). These issues can be addressed in a number of ways. Large libraries of sgRNAs for targeting the human genome have been developed and validated (Shalem et al., 2014). In addition, *in silico* guide design enables researchers to search for guide sequences with high specificity and identify any potential off-target sites (Shalem et al., 2014, Ran et al., 2013b).

Specificity can also be enhanced with the use of a mutant Cas9 nickase. By mutating aspartate to alanine (D10A) in the RuvC catalytic domain of Cas9, the nuclease causes a nick in the DNA rather than a DSB (Ran et al., 2013a). By combining two Cas9 nickases, with guide sequences that are within 100 bp of each other, an offset DSB can be created, improving specificity and reducing the likelihood of off-target events by at least 50-fold in human cell lines (Ran et al., 2013a) (**Figure 1.12D-E**).

As mentioned in section 1.7.1, HDR can be inefficient, and NHEJ is the preferred DNA damage response pathway. As such, the incidence of successful targeting events using CRISPR Cas9 can vary from 0.5% to 20% in human cultured cells (Mali et al., 2013, Byrne and Church, 2015). These efficiencies can be marginally improved with the use of small molecules such as L755507 which enhance HDR (Yu et al., 2015). Alternatively the NHEJ enzyme DNA ligase IV can be inhibited with SCR7, a small molecule inhibitor (Chu et al., 2015). However, the downstream effects of such small molecules has not been investigated thoroughly, particularly in hiPSC cell lines required for drug screening and disease modelling.

The delivery of CRISPR Cas9 components to a host cell has been achieved using lipid-based transfection, electroporation, and nucleofection (Sander and Joung, 2014, Mali et al., 2013). These approaches typically rely on plasmid DNA as a vector and the transient expression of sgRNAs and Cas9 nuclease. This approach was suitable for the study described in this thesis, however, advances using ssODNs, and delivery of ribonucleoprotein (RNP) complexes of sgRNA and Cas9 mRNA can reduce the likelihood of plasmid integration into the host genome (Kim et al., 2014b).

Nevertheless, the ease of construction, flexibility of target site, and ongoing efforts to reduce off-target effects make CRISPR Cas9 a valuable tool for genome engineering. It has been used to induce SNPs, insert transgenes, knock-out genes, or transcriptionally activate/repress genes in a range of organisms and model systems from mouse (Wang et al., 2013), Drosophila (Yu et al., 2013) and yeast (DiCarlo et al., 2013) to hiPSCs (Yang et al., 2016, Li et al., 2015, Kondrashov et al., 2018).

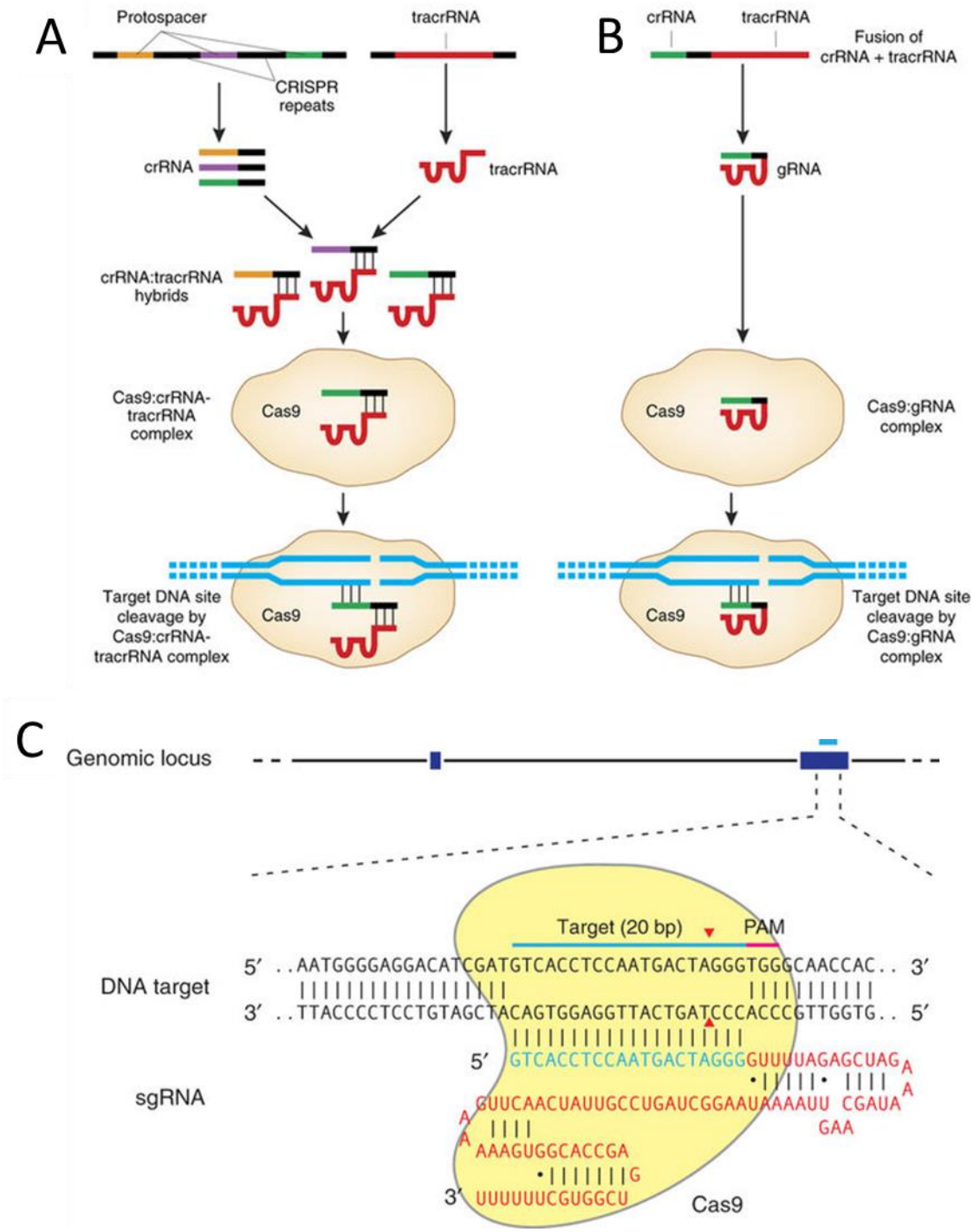


Figure 1.11. CRISPR Cas9 for site-specific DNA cleavage.

(A) CRISPR Cas9 is derived from a bacterial defence mechanism where foreign DNA transcripts are arranged into CRISPR RNA (cRNA) fragments. A transactivating crRNA (tracrRNA) then combines with crRNA to direct Cas9 nuclease cleavage of any more foreign DNA sequences that are discovered. **(B)** Application of CRISPR Cas9 for genome engineering. Fusion of tracrRNA and crRNA is referred to as single guide RNA (sgRNA). This sgRNA directs Cas9 nuclease to target site. Adapted from (Sander and Joung, 2014). **(C)** 20 nt sgRNA (blue) attached to scaffold (red) directs Cas9 to a specific area of genome upstream of an -NGG PAM site. Cas9 initiates a DSB at this location (red arrowhead). Adapted from (Ran et al., 2015).

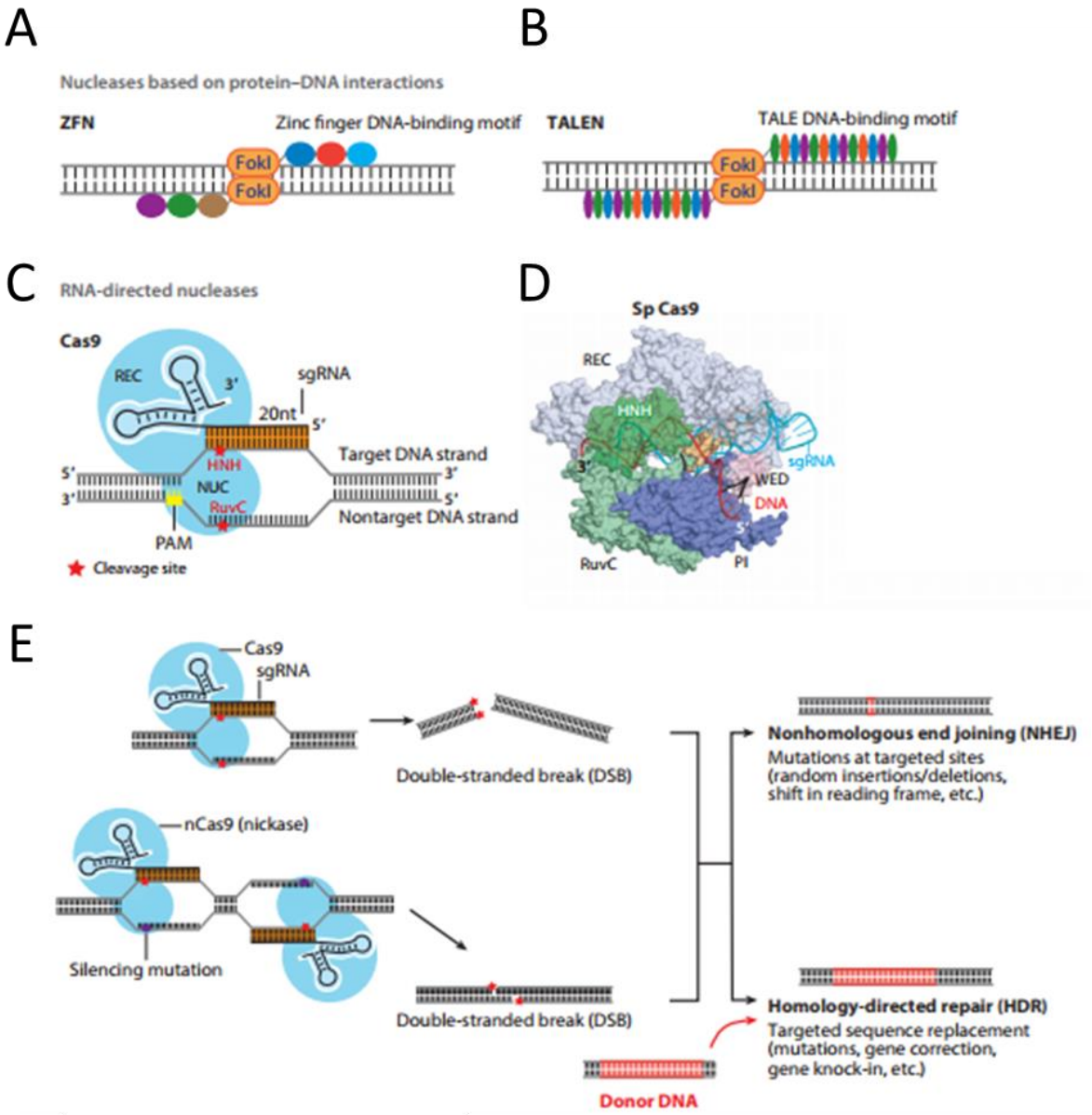


Figure 1.12. Summary of genome editing approaches using site-directed nucleases.

(A) Zinc finger nucleases require the construction of unwieldy modular proteins which are only capable of recognising a 3 bp sequence. DNA cleavage is mediated by the FokI nuclease. **(B)** TALENs have greater specificity than ZFNs because each modular protein is capable of recognising a single base pair. **(C)** CRISPR Cas9 does not require the modular construction of proteins to be able to direct a nuclease to a specific area of the genome. **(D)** Structure of Cas9 nuclease from *Streptococcus pyogenes*. The RuvC domain is responsible for DNA cleavage. **(E)** Nickase Cas9 is produced by mutating the Cas9 RuvC domain. This reduces the likelihood of off-target events. Adapted from (Wang et al., 2016a).

1.5 Hypothesis & Aims

The central hypothesis of this thesis is that calcium handling abnormalities can be detected in HCM hiPSC-CMs using GECIs. The generation of isogenic controls and the use of two different gene mutations should provide a novel way to investigate the mechanisms of HCM, and screen potential drug treatments *in vitro*.

In order to test the hypothesis, the following objectives will need to be achieved:

- Utilise CRISPR/Cas9 to generate GECI-expressing hiPSC lines in an HCM background, with healthy isogenic controls.
- Validate the utility of hiPSC-CMs to model disease *in vitro* and demonstrate their ability to recapitulate hallmarks of calcium handling.
- Develop a method to optically analyse calcium transients and quantify changes in response to drugs or disease-causing mutations.
- Use GECI-expressing hiPSC-CMs as a tool to understand whether the HCM phenotype can be detected. Investigate whether any differences in phenotype depend on the gene mutated.
- Use drugs in an attempt to alleviate the HCM phenotype.

2 Materials and Methods

2.1 Molecular Biology

2.1.1 Construct design and sequence analysis

Constructs were designed and sequences analysed using SnapGene software (GSL Biotech). Primers were designed online using Primer-BLAST (NCBI).

2.1.2 Cloning and vector construction

The parent *AAVS1* EF1α-ChR2-NpHR-BSD targeting construct that formed the backbone for the *AAVS1* GECO targeting constructs was a bespoke plasmid manufactured by a commercial vendor (Eurofins).

CMV-GEM-GECO1 was a kind gift from Prof Robert Campbell (Addgene: 32442), pON1 G-GECO1.0 and pShuttle Myc R-GECO1.0 were a kind gift from Dr Matthew Daniels.

2.1.2.1 Transformation

Transformation of E. coli to generate large amounts of plasmid DNA was performed in One Shot™ TOP10 competent *E. coli* (ThermoFisher: C404010). Ligation products were incubated on ice with the *E. coli* for 30 minutes before a 30 second heat-shock at 42°C in a water bath. *E. coli* were allowed to grow for 1 hour in SOC medium at 37°C before plating out onto antibiotic selection LB agar plates. Re-transformations were performed using JM109 competent *E. coli* (Promega: L2005) and a 30 second heat shock before immediately being plated onto antibiotic selection LB agar plates.

2.1.2.2 DNA miniprep and midiprep

DNA miniprep extractions from *E. coli* cultures were performed using the Wizard® Plus SV miniprep DNA purification kit (Promega: A1460) according to manufacturer's instruction. DNA was eluted in nuclease-free water.

DNA midiprep extractions from *E. coli* to generate large amounts of plasmid DNA for transfection into mammalian cells was performed using the NucleoBond® Xtra Midi kit (Macherey-Nagel: 740420) according to manufacturer's instructions. DNA was eluted in endotoxin-free water.

DNA concentrations were obtained using a NanoDrop-1000 spectrophotometer (ThermoFisher).

2.1.2.3 Restriction enzyme digest

All DNA restriction enzymes were purchased from NEB and used according to manufacturer's instructions. Restriction enzyme DNA digests were incubated at 37°C in a water bath for at least one hour. Vector backbones were treated with Calf Intestinal Phosphatase (CIP) (NEB: M0290) for a further hour to prevent self-ligation.

2.1.2.4 Gel electrophoresis and extraction of digested DNA

Gel electrophoresis was carried out in 1% (w/v) agarose (Sigma: A7431) gels, in TAE buffer at 100 mV unless otherwise stated. Gels were imaged with a LAS-4000 image analyser (Fujifilm). Restriction enzyme-digested products were isolated from gels using a QIAquick gel extraction kit (Qiagen: 28706).

2.1.2.5 Generation of phosphorylated DNA linker sequences

5'-phosphorylated linker oligonucleotides were ordered from Sigma-Aldrich and annealed by heating to 95°C and cooling to room temperature in the presence of 1x T4 DNA ligase buffer (NEB: M0202). Non-phosphorylated oligonucleotides were phosphorylated by incubation at 37°C with T4 Polynucleotide Kinase (NEB: M0201).

2.1.3 Design and assembly of single guide RNA plasmids

Single guide RNA sequences for the AAVS1 locus were designed using http://crispr.mit.edu and chosen according to their predicted quality score (section 3.3.1.). Guide RNAs were ordered as complementary oligonucleotides from Sigma-Aldrich. Equimolar amounts of each complementary oligonucleotide were annealed by heating to 95°C and cooling to room temperature in the presence of 1x T4 DNA ligase buffer (NEB: M0202). Annealed guides were then cloned into a pU6 vector containing an sgRNA scaffold sequence (Shan et al., 2013), by BsaI restriction enzyme digest (NEB: R0535) and ligation using T4 DNA ligase. High-yield, endotoxin-free preparations of guide RNA plasmids were produced using the NucleoBond® Xtra Midi kit (Macherey-Nagel: 740420).

2.1.4 DNA extraction from cultured mammalian cells

Extraction of genomic DNA from cultured mammalian cells was performed with the DNeasy extraction kit (Qiagen: 69504) according to manufacturer's instructions and eluted in nuclease-free water.

Alternatively, mammalian cell pellets were lysed with DirectPCR lysis reagent (VWR: 31-302-C) supplemented with 5% proteinase K. After incubation at 55°C for 5 hours, the proteinase K was inactivated by incubation at 85°C for 45 minutes. The resulting cell lysates were diluted 1:10 with nuclease-free water before being used for PCR.

2.1.5 PCR genotyping

Genotyping of clones was performed by PCR using 100 ng template gDNA, or 1 µl diluted cell lysate with Phusion® polymerase (NEB:M0530). PCR cycle parameters were 95°C for 2 min, 60-64°C for 30 sec and 72°C for 60 sec, with a final elongation step of 72°C for 10 min. Primers and annealing temperatures used are set out in **Table 2.1**. PCR products were purified using a QIAquick PCR purification kit (Qiagen: 28104), and sent to an external Sanger sequencing service (Source Bioscience).

Screen	**Forward primer (5' → 3')**	**Reverse primer (5' → 3')**	**Annealing Temp.**
5' screen (Outside *AAVS1* Left Arm – EF1α promoter)	TCCCCTCTTCCGATGTTGAG	ACCCGTTGCGAAAAAGAACG	64°C
5' screen (Outside *AAVS1* Left Arm – CAG promoter)	TCCCCTCTTCCGATGTTGAG	TGGGCTATGAACTAATGACCCCG	64°C
3' screen (Blasticidin – Outside *AAVS1* Right Arm)	GCTGGCAACCTGACTTGTATCGT	ACCCCGAAGAGTGAGTTTGCC	64°C
3' screen (IRES/Puromycin – Outside *AAVS1* Right Arm)	AGCGTATTCAACAAGGGGCT	ACCCCGAAGAGTGAGTTTGCC	62°C
Het/Hom screen (Inside *AAVS1* Left Arm – Inside *AAVS1* Right Arm)	ATGCCGTCTTCACTCGCTGG	GGGGCTTTTCTGTCACCAATCC	64°C

Table 2.1. Primers used for genotyping

2.1.6 Reverse-transcriptase PCR analysis of RNA expression

RNA was isolated from homogenised hiPSCs and derived cardiomyocytes using the RNeasy Mini Kit (Qiagen: 74104). The optional DNase I treatment was performed to limit genomic DNA contamination.

Synthesis of cDNA was achieved using SuperScript™ III Reverse Transcriptase (ThermoFisher: 18080093) according to manufacturer's instructions.

Each PCR reaction used 250 ng of cDNA with Phusion® polymerase for 35 cycles. PCR cycle conditions were 95°C for 2 min, 63-64°C for 30 sec and 72°C for 60 sec, with a final elongation step of 72°C for 10 min. Gels were imaged with a LAS-4000 image analyser.

Gene	Forward primer (5' → 3')	Reverse Primer (5' → 3')	Annealing temp.
GGECO /GEM-GECO	TCGCCTACCACTACCAGCAGA	TTGTGCCCCAGGATGTTGCC	63°C
RGECO	TAAGGCAGGTCACGCAGTCAG	ATGGTGTAGTCCTCGTTGTGGG	63°C
B-actin	CAAGAGATGGCCACGG	CTTGATCTTCAT	64°C

2.1.7 Immunocytochemistry

Mammalian cells were prepared for immunocytochemistry by enzymatic dissociation and plated onto 96-well plates. Cells were allowed to recover or grow for at least two days before being washed with DPBS or HBSS and fixed with 4% paraformaldehyde (PFA) for 15 minutes. Cells were then washed again and stored at 4°C until staining.

For staining, fixed cells were first washed once with DPBS for 5 minutes. The cells were then permeabilised with 100 µl/well 0.1% Triton-X for 15 minutes at room temperature. Once permeabilised, cells were washed again with DPBS. Non-specific epitope binding was prevented by applying a blocking solution for one hour (10% goat serum in DPBS for antibodies raised in mouse or rabbit, 10% rabbit serum for antibodies raised in goat or 10% donkey serum for double-stained samples). Cells were once again washed with DPBS as above. Primary antibodies were diluted in 1% goat serum or 1%

rabbit serum according to **Table 2.2** and staining was performed by adding 50 µl/well and incubating the fixed cells overnight at 4°C.

The following day, cells were washed 3 times with 0.1% Tween diluted in DPBS (DPBS-T). Secondary antibodies were diluted according to **Table 2.2** in DPBS and staining was performed by adding 50 µl/well and incubating at room temperature for 1 hour. Once again the cells were washed three times with DPBS-T. Cells were then countertained with the DAPI nuclear stain (Sigma: D9542) at a dilution of 1:500 in DPBS for 30 minutes at room temperature. Finally the cells were washed once with DPBS and stored at 4C until imaging on the Operetta™ high content imaging system (PerkinElmer).

Target	Primary antibody	Primary antibody dilution	Secondary antibody	Secondary antibody dilution
Cardiac α-actinin	Monoclonal mouse anti-alpha actinin (Sigma: A7811)	1:800	Goat anti-mouse AlexaFluor 488 (ThermoFisher: A11001)	1:400
			Goat anti-mouse AlexaFluor 633 (ThermoFisher: A21050)	1:400
RGECO	Polyclonal rabbit anti-RFP (Abcam: ab124754)	1:1000	Goat anti-rabbit AlexaFluor 647 (ThermoFisher: A21244)	1:400
			Donkey anti-rabbit AlexaFluor 488 (ThermoFisher: A21206)	1:400
OCT4	Monoclonal mouse anti-Oct3/4 (Santa Cruz: sc5279)	1:200	Goat anti-mouse AlexaFluor 488 (ThermoFisher: A11001)	1:400
			Goat anti-mouse AlexaFluor 633 (ThermoFisher: A21050)	1:400

Table 2.2. Antibodies used for immunocytochemistry.

2.2 Cell culture

All cell culture was performed in a type II Biological Safety Cabinet. Cells were maintained at 37°C in a humidified atmosphere with 5% CO_2.

2.2.1 Human induced pluripotent stem cell maintenance in E8 medium

Human induced pluripotent stem cells were cultured and maintained on matrigel™-coated tissue culture plastic in E8 medium as previously described (Chen et al., 2011c). Coating was performed by diluting matrigel™ (Corning: 354234) 1:100 in DMEM medium, and adding 4 ml per 25cm^2 flask. Matrigel™ was left to polymerise on the culture surface for 45 mins at room temperature. Coated flasks were stored at 4°C for no longer than two weeks. E8 medium was manufactured in-house using a previously described formulation (Burridge et al., 2014).

To passage hiPSCs, the cells were washed with Dulbecco's Phosphate Buffered Saline (DPBS) without calcium or magnesium (ThermoFisher: 14190250) and dissociated using TrypLE Select 1X enzyme (ThermoFisher: 12563029). Cells were manually counted using a haemocytometer and seeded at a density of 20,000 cells/cm^2 in the presence of 10 μM Y-27632 ROCK inhibitor (Tocris: 1254) for the first 24 hours.

2.2.2 Cardiac differentiation and dissociation

Cardiac differentiation of hiPSCs was performed using an in-house monolayer method (Duncan et al., 2017, Kondrashov et al., 2018). Cells were passaged as above but seeded at a density of 30,000 – 50,000 cells/cm^2. The following day the medium was replaced with fresh E8 medium. The day after, cells were again fed with E8 medium. 8 hours later a pre-conditioning step was carried out by adding a matrigel™ overlay (Matrigel™ diluted 1:100 in StemPro™-34 medium (ThermoFisher: 10639011)), supplemented with 1 ng/ml recombinant human BMP4 (R&D: 314-BP-050). Approximately 16 hours later (day 0 of differentiation), the medium was changed to StemPro™-34 supplemented with 10 ng/ml recombinant human BMP4 and 8 ng/ml recombinant human Activin A (ThermoFisher: PHC9564). After 48 hours (day 2), medium was changed to RPMI 1640 basal medium (ThermoFisher: 21875034) with B27 minus insulin (ThermoFisher: A1895601) (RB Ins-), supplemented with 10 μM KY02111 (R&D: 4731) and 10 μM XAV 939 (R&D: 3748). After another 48 hours (day 4), medium was changed to RPMI 1640 without phenol red (ThermoFisher: 11835030) with B27 (ThermoFisher: 17504-044) (RB), supplemented with both KY02111 and XAV 939 at 10 μM. From day 6 onwards, cells were fed with RB every two days until day 15.

In order to dissociate hiPSC-CMs for downstream applications including live imaging and immunocytochemistry on fixed cells, a previously described protocol (Breckwoldt et al., 2017) was used. Beating hiPSC-CMs were washed twice with calcium- and magnesium-free Hank's Balanced Salt Solution (HBSS) (ThermoFisher: 14170112). The cells were then dissociated using 200 units/ml collagenase II (Worthington: LS004176), supplemented with 30 nM *N*-Benzyl-*p*-toluenesulphonamide (BTS) (TCI chemicals: B3082), 10 µM Y-27632 and 1 mM HEPES (Sigma: H4034), all dissolved in HBSS. Cells were left in dissociation solution in a humidified incubator at 37°C, 5% CO_2 for 3 hours. Cells were then harvested and the enzyme quenched with RPMI basal medium supplemented with 24 µg/ml DNaseII (Sigma: D8764), followed by centrifugation at 100 xg for 15 minutes. Cells were then resuspended in RPMI basal medium and passed through a 100 µm cell mesh (VWR: 89508-840). Cells were then counted using a haemocytometer and centrifuged at 100 xg for 15 minutes again before being seeded in RB medium or resuspended in freezing medium - 90% Fetal Bovine Serum (ThermoFisher: 26140079), 10% DMSO (Sigma: D2650) and cryopreserved.

2.2.3 293T BL15 cell maintenance

HEK 293T BL15 cells were maintained in medium containing: 78% 1x DMEM basal medium, 20% FBS, 1% Non-essential amino acids (NEAA), 1% GlutaMAX™ (ThermoFisher: 35050061) and 100 µM ß-mercaptoethanol. Cells were passaged using 0.05% Trypsin-EDTA and seeded at a density of 50,000 cells/cm^2 on uncoated tissue culture flasks.

2.2.4 Transfection of live cells

2.2.4.1 Transfection of hiPSCs

Lipid-based transfection of hiPSCs was achieved using GeneJammer® (Agilent: 204130) reagent. The day prior to transfection, 30,000 cells/cm^2 were seeded onto a matrigel™-coated tissue culture flask (250,000 cells for single well of a 6-well plate). 3 pg/cell of plasmid DNA was then mixed and sterilised at 65°C for 15 minutes (750 ng DNA for a single well of a 6-well plate). Separately, 9 µl GeneJammer® reagent was then mixed with 91 µl of sterile-filtered optiMEM™ serum-free medium and incubated at room temperature for 5 minutes (If transfecting a single well of a 6-well plate). The mixed DNA was subsequently added to the mixture and incubated at room temperature for 15 minutes to allow DNA-lipid complexes to form. The entire transfection mixture was then gently added dropwise to the cells containing the standard volume of E8 medium for regular culture. The next day, media was changed as usual.

Nucleofection of hiPSCs was achieved using an Amaxa 4D nucleofector and P3 primary cell solution (Lonza: V4XP-3024). The following conditions were used for nucleofection of hiPSCs to be seeded onto a single well of a 6-well plate.

On the day of nucleofection, 800,000 cells were resuspended in 100 µl P3 solution in the presence of 1 µg sterile DNA and placed in a nucleocuvette. Using the X unit of the Amaxa 4D and the appropriate nucleofection program (optimised to program DN-100), hiPSCs were nucleofected. Cells were left to recover for 5 minutes at 37°C, 5% CO2 before being carefully added dropwise to a matrigel™-coated tissue culture flask with the standard volume of E8 medium for regular culture.

2.2.4.2 Transfection of 293T BL15 cells

Transfection of 293T BL15 cells was achieved using GeneJammer® reagent as described above.

2.2.4.3 Transfection of hiPSC-CMs

Transfection of hiPSC-CMs was achieved using Lipofectamine™ 3000 (ThermoFisher: L3000001), largely following the manufacturer's instructions, with some minor alterations to reagent volume as follows:

0.3 µl Lipofectamine™ reagent, 0.4 µl P3000 reagent and 100 ng DNA were added per well of a 96-well plate. This 10 – 15 µl reaction was added onto day 20 hiPSC-CMs containing 40 µl/well RPMI B27 medium and left for 5 hours. This was subsequently topped up to 100 µl/well. Imaging of transfected cells was performed 48 hours after transfection.

2.2.5 Time-course assay

To assess dye leakage in hiPSC-CMs, a time-course assay was performed. Day 15 REBL PAT hiPSCs-CMs and REBL PAT RGECO R12 hiPSC-CMs were plated onto a VTN-coated 96-well plate at a density of 50,000 cells/well. A concentration range of 100 nM - 100 µM Fluo-4 AM (ThermoFisher: F14217) was then loaded onto day 21 untargeted REBL PAT hiPSC-CMs for one hour. The hiPSC-CMs were then washed with DPBS and fed with 100 µl/well warm RB medium. The plate was immediately assayed using the live cell chamber of the Operetta™ high content imaging system, with conditions maintained at 37°C, 5% CO_2. An image was captured once every 30 minutes for a total of 12 hours.

2.2.6 Cell viability assay

The CellTiter-Glo® luminescent cell viability assay (Promega: G7570) was used to assess the toxicity of Fluo-4 AM and Calcium Crimson™ AM (ThermoFisher: C3018) cell permeant dyes.

For the standard curve, day 15 REBL PAT hiPSC CMs were seeded at different densities on VTN-coated white-walled 96-well plates. On day 20, 100 µl of CellTiter-Glo® reagent was placed in each well using a multichannel pipette, and left to generate luminescent signal in the dark for 15 min at room temperature. A white adhesive bottom was placed onto the plate, and it was assayed using the luminescence function of the EnVision 2105 (PerkinElmer) plate reader.

For the cytotoxicity assay, day 15 REBL PAT hiPSC CMs were seeded at a density of 50,000 cells per well. On day 20, a 1 mM stock solution of each AM dye was made up in DMSO solvent. A range of concentrations of the AM dyes were then made by diluting the stock in DPBS. Cells were loaded with dye and then returned to the incubator at 37°C, 5% CO_2 for 1 hour. The hiPSC-CMs were then washed with DPBS, which was replaced with 100 µl/well CellTiter-Glo® reagent and the plate assayed using the EnVision plate reader as above.

2.2.7 Precise gene targeting of human induced pluripotent stem cells

2.2.7.1 Transfection

CRISPR-Cas9 targeting was carried out by transfecting hiPSCs with the following plasmid vectors: 1 µg Cas9 D10A nickase, 1 µg *AAVS1* targeting vector and 500 ng each single guide RNA.

For *AAVS1* EF1α-driven targeting constructs, GeneJammer® was used for transfection as described above.

For *AAVS1* CAG-driven targeting constructs, the Amaxa 4D nucleofection program DN-100 was used as described above.

2.2.7.2 Antibiotic selection

To select for targeted clones, E8 medium was supplemented with 2.5 µg/ml blasticidin (ThermoFisher: A1113903) or 0.3 µg/ml puromycin (ThermoFisher: A11138) for between six to ten days, until clearly defined colonies were visible.

2.2.7.3 Colony isolation

In order to isolate colonies, cells were incubated with 50 µM EDTA (ThermoFisher: 15575020) diluted in DPBS for 3 minutes. Using a microscope inside a sterile biological safety cabinet, colonies were picked using a P20 pipette set to 10 µl. The colonies were then transferred to a matrigel™-coated 96-well plate containing 100 µl warm E8 medium. Once transferred, colonies were mechanically triturated using the pipette to ensure even attachment of cells within the well.

2.2.8 Generation of ChR2-EYFP optogenetic line

Generation of the optogenetic ChR2-EYFP hiPSC line was accomplished by co-transfecting a target vector containing the ChR2-EYFP-T2A-BSD cassette flanked with PB repeats with an excision-incompetent Super PiggyBac transposase (System Biosciences: PB210PA-1) as described in (Wang et al., 2017). Antibiotic selection and colony selection was performed as above. Frame-scan confocal microscopy was used to select colonies with the highest EYFP expression evenly distributed across membrane for expansion and banking.

2.3 Microscopy

2.3.1 Operetta™ high content image analysis

Imaging of immunostained samples and live imaging of transiently transfected 293T BL15 cells or hiPSC-CMs was performed on the Operetta™ high content image analysis system (PerkinElmer). Data was analysed using Columbus™ software (PerkinElmer).

2.3.2 DeltaVision widefield epifluorescence microscopy for live imaging of hiPSC-CMs expressing GECIs

To prepare hiPSC-CMs for live imaging analysis on the DeltaVision widefield epifluorescence microcope, targeted GECI hiPSCs were differentiated as previously described in RPMI B27 without phenol red and dissociated on day 15.

hiPSC-CMs were seeded at a density of 150,000 cells per well in vitronectin-N (ThermoFisher: A14700) coated MatTek dishes. Vitronectin-N coating was performed by diluting 1:100 in DPBS and coating the surface for at least one hour at room temperature.

hiPSC-CMs were assayed no earlier than day 24 and no later than day 30. Fluorescence was imaged in a temperature-controlled environment at 37°C, 5% CO_2. Images were captured with a CoolSnap HQ2 CCD camera and processed in FiJi software, a version of ImageJ (National Institute of Health).

2.3.3 Confocal line-scan microscopy as a method to generate calcium transient traces

2.3.3.1 hiPSC-CM preparation

Targeted GECI hiPSCs were differentiated as previously described in RPMI B27 without phenol red and dissociated on day 15. hiPSC-CMs were seeded at a density of 150,000 cells per well in vitronectin-N coated MatTek dishes. hiPSC-CMs were then used for imaging and drug addition experiments between day 24 and day 30 of differentiation.

2.3.3.2 Drug preparation

The test drugs were dissolved so that the amount of vehicle was kept consistent across all concentrations of drug tested as per (Lu et al., 2017). The test drugs were dissolved in DMSO, H_2O or RPMI B27 (RB) according to **Table 2.3**. The maximum final DMSO concentration added to the cells was 0.1%; stock solutions of compounds were

prepared in DMSO at 1000 times the highest concentration to be tested to maintain final DMSO concentrations at 0.1%. For cell treatment, 10% of the well volume was replaced with 10% of the drug solution prepared in RB media at a concentration ten times that of the final well concentration. Parallel vehicle controls were made using DMSO, H_2O or RB as necessary.

Drug	Supplier: Cat no.	Final well concentrations used	Solvent
Caffeine	Sigma: C0750	10 mM	RB
Dantrolene	VWR: CAYM14326	1 µM, 10 µM	DMSO
Isoprenaline	Sigma: I5627	100 nM, 300 nM, 1 µM	H_2O
MYK 461	ApexBio: A8720	1 µM	DMSO
Nickel Chloride	Sigma: 339350	10 µM, 100 µM, 500 µM, 1 mM, 5 mM, 10 mM	RB
Nifedipine	Sigma: N7634	100 nM, 300 nM, 1 µM, 3 µM	DMSO
Propanolol	Sigma: P0884	200 nM	DMSO
Ranolazine	Seleckchem: S1425	1 µM, 10 µM	DMSO
Ryanodine	Tocris: 1329	100 nM, 300 nM, 1 µM, 3 µM	DMSO
Thapsigargin	Sigma: T9033	100 nM, 1 µM	DMSO
Valsartan	Stratech Scientific: S1894	1 µM	DMSO
Verapamil	Sigma: V4629	1 µM	DMSO

Table 2.3. Table of drugs and concentrations used.

2.3.3.3 Image acquisition

Intracellular calcium transient measurements were made using an LSM 880C confocal microscope (Carl Zeiss) in the line-scan mode as previously described (Yazawa et al., 2011). Cardiomyocytes were located using a 40x oil objective and a longitudinal line was drawn across a single CM. The R-GECO fluorophore was excited with a 561 nm laser at 0.8% power, with a detection range of 579 – 639 nm. The GEM-GECO fluorophore was excited with a 405 nm laser. Blue emission was detected in the range 451 – 495 nm, green emission was detected in the range 528 – 566 nm. Line-scan images were taken every 75 milliseconds, with a pixel dwell time of 4.12 µsec, for a total of 4000 cycles resulting in a 5 minute scan. CMs were kept at 37°C and 5% CO_2 throughout data acquisition.

2.3.3.4 Data analysis

Confocal line scan images were analysed in FiJi software, a version of ImageJ (National Institute of Health). The average fluorescence intensity of each line was calculated against time to give a confocal line-scan trace. Using the 'multi kymograph' function, a corresponding kymograph image was produced. In order to calculate beat rate and arrhythmic events, data was fed into pClamp software (Molecular Devices). Baselines were adjusted to account for photobleaching and calcium transients were counted and analysed using the 'event detection' function. Using the event viewer, any calcium transients that did not return to baseline and gave a 'double peak' were considered 'abnormal'. Interevent interval, T_{rise}, T_{decay} and peak height amplitude for each calcium transient event were also calculated in event detection mode. In order to determine abnormal DAD-like calcium transients, median peak height analysis was performed using Excel (Microsoft). Briefly, the median peak height for a line-scan image was calculated and any calcium transient events that were below 75% of the peak height were considered 'abnormal'.

2.3.4 Optogenetic pacing of hiPSC-CMs on the CellOPTIQ™ platform

hiPSC-CMs for optogenetic pacing were dissociated and plated onto a VTN-N coated 96-well plate at a seeding density of 150,000 cells/cm^2 to generate a confluent monolayer as previously described.

After four days, optogenetic pacing experiments were carried out on the CellOPTIQ™ (Clyde Biosciences) platform at 37C, 5% CO2. Using the OptoLED light source (Cairn Research), pulses of 480 nm blue light were applied at varying frequencies with blue light illumination occurring for 50% of the cycle. Images were captured for a ten-second period using an ORCA-Flash4.0 digital CMOS camera (Hamamatsu: C11440). Contraction analysis was performed using a proprietary ImageJ macro (Clyde BioSciences).

2.3.5 Statistical analysis

All data presented as mean with standard deviation unless otherwise stated. Statistical analysis of multiple data sets was performed using GraphPad software.

For multiple comparisons between data sets a one-way ANOVA with Tukey's multiple comparison test was chosen. For comparing multiple data sets to a single control column, one-way ANOVA with Dunnett's multiple comparison test was chosen. Significance tests were based on p-values as follows: * $p < 0.05$; ** $p < 0.01$; *** $p < 0.001$; **** $p < 0.0001$.

3 Engineering reporter hiPSC lines to express genetically encoded calcium indicators

3.1 Introduction

This chapter seeks to outline the generation of a palette of genetically encoded calcium indicator hiPSC lines, in a variety of genetic backgrounds, by site-specific CRISPR/Cas9 knock-in. In order to ensure adequate expression from the GECI, a safe harbour locus had to be chosen and specific sgRNAs designed to target this genomic location. Furthermore, targeting constructs with homology to this locus flanking a constitutively-driven GECI had to be designed and validated. These two components, together with a Cas9 nuclease were capable of generating the desired cell lines once transfection conditions were optimised. This chapter explores how these DNA-based components were designed, engineered and applied to hiPSCs to generate several potentially useful clones. The chapter concludes with molecular analyses to select clones with optimal GECI expression in order to generate cell lines capable of being differentiated to cardiomyocytes and used to optically analyse calcium transients.

3.1.1 Selecting an engineered nuclease delivery system for precise gene targeting

One of the few restrictions of CRISPR-Cas9 is the requirement for an –NGG PAM sequence in the target sequence, following the sgRNA sequence to induce the cut site (Cong et al., 2013, Hsu et al., 2014). The relatively short (~20 nucleotides) length of sgRNAs can tolerate some mismatch and increase the possibility of off-target effects (Cho et al., 2013), which is why the nickase strategy will be employed in this thesis. Paired nicking on each strand induces a slightly offset DSB for homologous recombination to occur (**Figure 3.1C**) (**Section 1.4.5**). This approach increases the number of specifically recognised bases for target cleavage by a modified Cas9 – Cas9 D10A. The nickase strategy can therefore reduce off-target activity by 50- to 1500-fold (Ran et al., 2013a). There are an abundance of online software packages for designing sgRNAs, with 'off-target scores' associated with each design (Mali et al., 2013). These sgRNA sequences can then be easily cloned into vectors or generated by in vitro transcription (Kim et al., 2014b), circumventing the bulky protein engineering processes associated with ZFNs and TALENS. In addition, dependent on locus, targeting vector size, and growth rate of cells; CRISPR-Cas9 can display a ~20% mutation rate,

increasing the likelihood of finding biallelic targeting events compared to ZFNs and TALENS (Kim et al., 2014a, Cho et al., 2013).

In addition to targeted knock-in of reporter genes, CRISPR-Cas9 nickase has been employed in this chapter to introduce or correct SNPs that cause sarcomeric gene dysfunction. Again, this involves the core principle of providing a DNA template for endogenous repair mechanisms to incorporate the desired sequence. Similarly to targeted knock-in, a selection cassette is often inserted alongside to facilitate the isolation of positively targeted clones. However, in the case of gene editing, the selection cassette should be removed after editing has taken place to avoid interference with the host gene. In this chapter, this has been achieved using flippase-mediated recombination (FLP-FRT) (Denning et al., 2016). Other methods of removing a selection cassette include the use of the PiggyBac (PB) transposon. Our group have refined this system by utilising endogenous TTAA sites for PB excision, and using a thymidine kinase negative selection gene in order to target loci and excise the cassette without an intermediate screening step (Kondrashov et al., 2018). This has reduced a typical gene editing experiment from 38 to 24 days.

The ability to perform footprint-free gene editing in patient-derived hiPSCs allows for the generation of isogenic sets of cell lines in which the only difference between cell lines is a single base pair change. This enables research projects such as the one described in this thesis to focus on how the SNP itself affects a phenotype, leaving the genetic background unchanged.

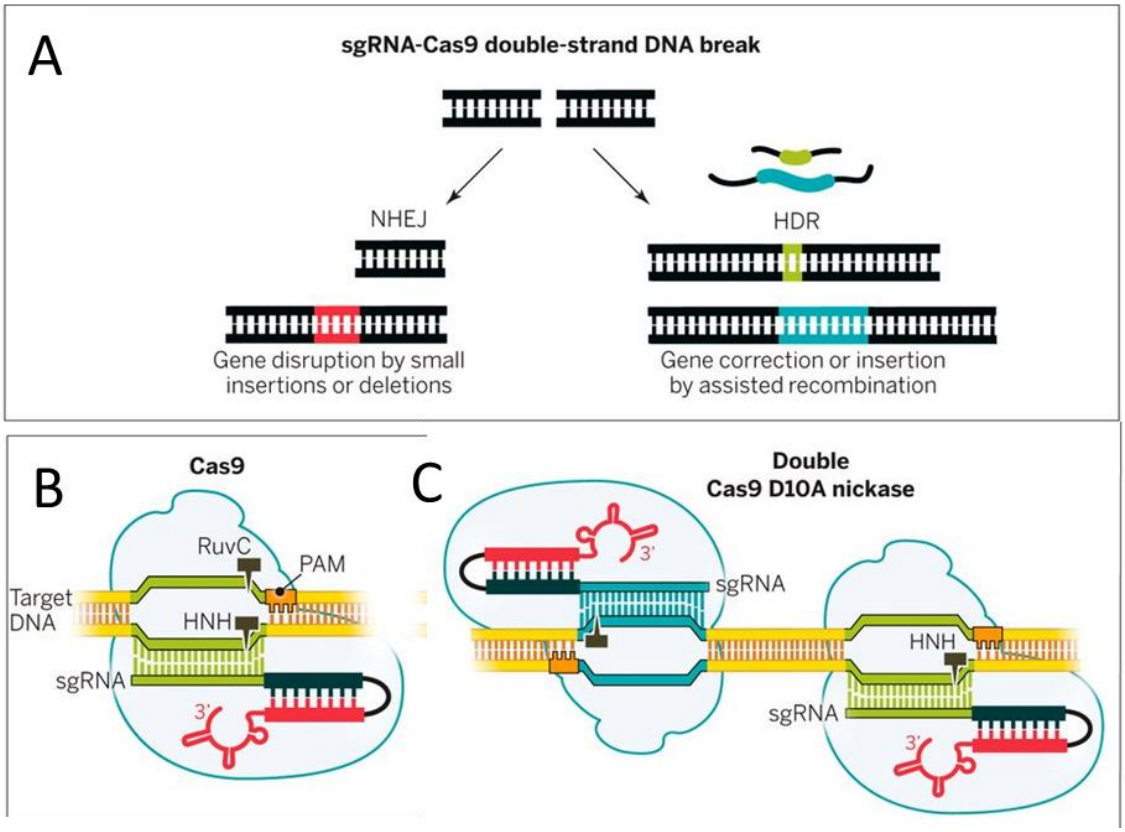


Figure 3.1. The CRISPR Cas9 D10A nickase approach for reduced off-target cleavage of DNA.

(A) A CRISPR Cas9 induced double-stranded break (DSB) in the genome can be repaired via non-homologous end joining (NHEJ) to knock out genes with small indels or homology directed repair (HDR) to induce SNPs or insert transgenes. **(B)** Wild-type Cas9 directed to a site by an sgRNA can induce a DSB at the desired location. **(C)** Mutation of the RuvC domain in Cas9 generates a mutant Cas9 D10A, capable of nicking a single strand. Combination of two sgRNAs and two Cas9 D10A nickases, can induce an off-set DSB. The use of two sgRNAs reduces the likelihood of off-target cleavage. Adapted from (Doudna and Charpentier, 2014).

3.1.2 Safe harbour loci within the human genome

A key consideration for targeted gene delivery is the genomic location at which to insert the exogenous DNA sequence to maximise transgene expression and limit disruption of critical endogenous genes and their function. To this end, a number of chromosomal locations that are amenable to integration have been exploited. These areas of the genome are often referred to as safe harbour loci, and often share some common properties. In order to avoid insertional oncogenesis, oncogene disruption must of course be avoided. However, it is also important to consider that transgene insertion close to adjacent oncogenes can cause problems by interfering with the enhancer/promoter regions. It is therefore advised to avoid regions of the genome

within 50 kb of genes known to play a role in cancer (Papapetrou and Schambach, 2016).

The chemokine (C-C motif) receptor 5 (*CCR5*) gene, located on chromosome 3, is a chemokine receptor gene heavily involved in the pathogenesis of HIV-1 (Dragic et al., 1996). It was discovered as a potential genomic safe harbour when homozygous deletion of this gene was found in supposedly healthy individuals (Liu et al., 1996). This complete deletion of *CCR5* conferred resistance to HIV-1 infection with seemingly no adverse effects. Human pluripotent stem cells have since been successfully targeted at exon 3 of this locus using ZFNs (Lombardo et al., 2007, Lombardo et al., 2011). However, CCR5 has been criticised for a chromatin structure prone to silencing (van Rensburg et al., 2013).

The human orthologue of the mouse *Rosa26* locus has also been explored as a potential safe harbour insertion site. Several studies in the mouse model have shown a propensity for transgenes to incorporate at the *Rosa26* locus at high efficiency (Soriano, 1999, Zambrowicz et al., 1997), leading to the successful targeting of *hROSA26* in hESCs (Irion et al., 2007). Despite this, no further studies have focused on the hROSA26 locus.

A more recently discovered location on chromosome 13 is within intron 2 of the Citrate Lyase Beta-Like (*CLYBL*) gene (Liu et al., 2009b). This gene-deficient region of the human genome has been targeted with TALENs with claims of robust transgene expression (Cerbini et al., 2015), although very few subsequent studies have attempted to target this location.

The *AAVS1* locus is an area of chromosome 19 (position 19q13.42) that has been found to be a common integration site for exogenous DNA delivered to cultured cells with adeno-associated virus AAV (Samulski et al., 1991, Heister et al., 2002). Integration into this site is associated with only limited disruption of endogenous genes. The phosphatase 1 regulatory subunit 12C (*PPP1R12C*) gene codes for a protein with a poorly defined function, and its first intron is disrupted by integration into the AAVS1 site, with no observed deleterious consequences in targeted hPSCs (Hockemeyer et al., 2009, Sadelain et al., 2011). DNA sequences inserted at this location are protected by endogenous insulator regions (Ogata et al., 2003). These insulators contribute to maintaining an open chromatin conformation at the *AAVS1* locus, reducing the likelihood of transgene silencing compared to other safe harbour loci such as *CCR5* (Smith et al., 2008, van Rensburg et al., 2013). However, some reports of DNA

methylation dampening transgene expression in hESC-derived hepatocytes suggest there is no such thing as a perfect safe harbour locus (Ordovas et al., 2015). Despite this, the multitude of direct comparisons between *AAVS1* and previously mentioned safe harbours has time and again demonstrated the superiority of *AAVS1* (**Table 3.1**) (Lombardo et al., 2011, Wang et al., 2016b). This has made the *AAVS1* locus the preferred destination for researchers seeking to incorporate reporter genes into the human genome at high efficiency, with few detrimental effects and limited silencing. For these reasons, the *AAVS1* locus was chosen as the destination for insertion of a genetically encoded calcium indicator in this chapter.

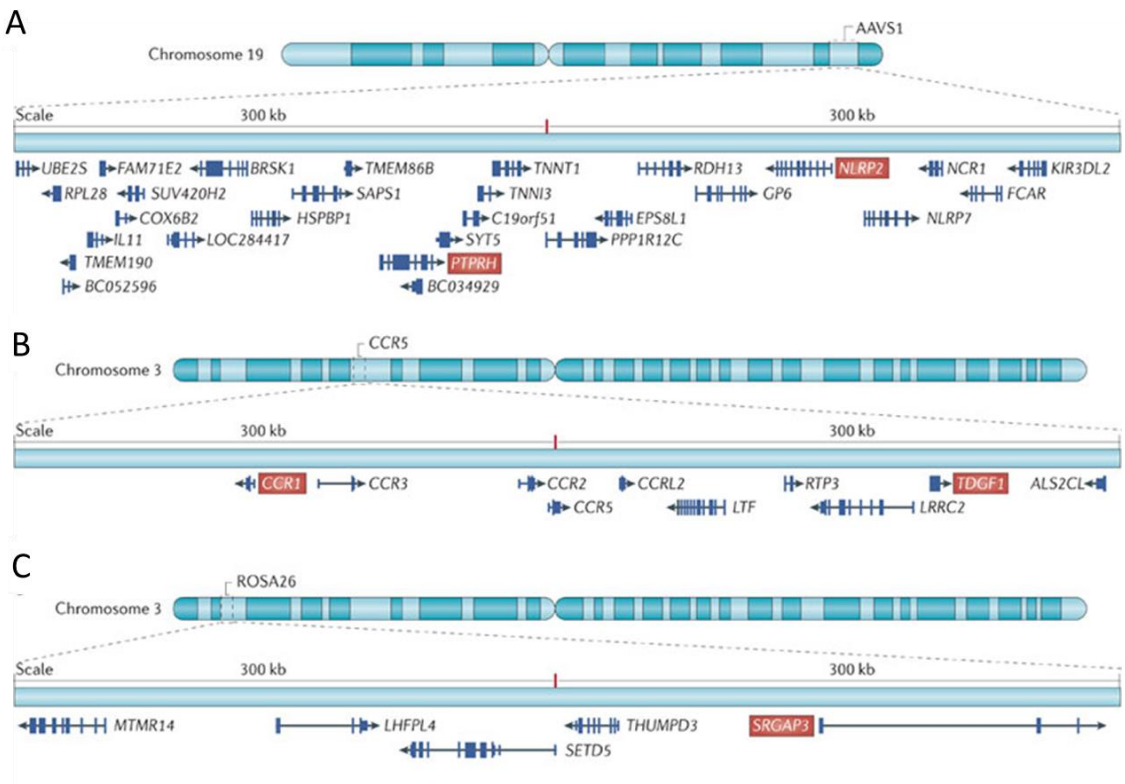
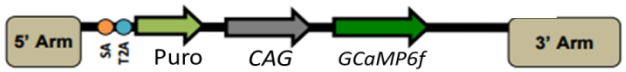
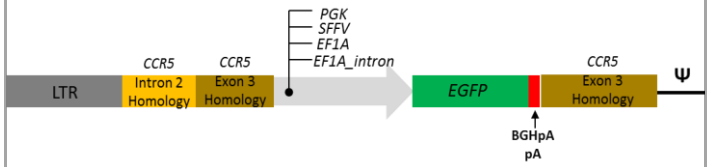


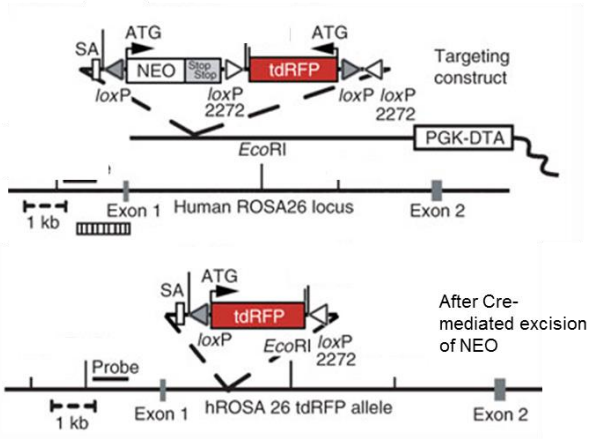
Figure 3.2 Schematic of commonly used genomic safe harbour loci and their location.

Integration sites identified with a vertical red line. Genes associated with cancer highlighted in red boxes. Transcript orientation displayed as arrows. Dark blue boxes indicate exons **(A)** In the gene-rich *AAVS1* locus, integration occurs in the first intron of the *PPP1R12C* gene. **(B)** In the *CCR5* locus integration occurs in the third exon of the *CCR5* gene. **(C)** The human orthologue of the *Rosa26* safe harbour locus discovered in mice. Adapted from (Sadelain et al., 2011).

Table 3.1 Successful fluorescent gene knock-in at safe harbour loci

AAVS1 safe harbour locus						
Integration site & orientation	**Promoter**	**Fluorescent gene**	**Construct schematic**	**Genome targeting method**	**Success**	**Reference**
First intron of *PPP1R12C* (*AAVS1* locus) in same orientation as endogenous gene transcript	PGK SFFV EF1α EF1α_intron	eGFP	 LTR:self-inactivating long terminal repeat BGHpA pA: poly(A) site from bovine growth hormone gene Ψ:packaging signal	ZFNs	All promoter variations result in 8-12% eGFP positive lymphoblast cells or 0.7% eGFP positive iPSCs. Although integration efficiency was unaffected by the promoter, mean fluorescence intensity was affected by the promoter and integration site.	(Lombardo et al., 2011)
First intron of *PPP1R12C* (*AAVS1* locus) in reverse orientation to endogenous gene transcript	CAG	GCaMP3	 Neo: Mammalian neomycin resistance gene	ZFNs	Targeted hESC-CMs successfully used to assess host-graft coupling in guinea pig hearts.	(Shiba *et al.*, 2012)

"*AAVS1* TALEN cut site" (assumed first intron of *PPP1R12C*, in same orientation as transcript)	CAG	GCaMP6f	 SA: Splice acceptor T2A: *Thoseaasigna* virus 2A cleavage peptide Puro: promoterless puromycin resistance gene	TALENS	hiPSC-CMs displayed expected response to sotalol, quinidine, nifedipine, verapamil & cisapride	(Maddah *et al.*, 2015)
***CCR5* safe harbour locus**						
Integration site & orientation	**Promoter**	**Fluorescent gene**	**Construct schematic**	**Genome targeting method**	**Success**	**Reference**
Exon 3 of *CCR5* in same orientation as endogenous transcript	PGK SFFV EF1α EF1α_intron	eGFP	 LTR:self-inactivating long terminal repeat BGHpA pA: poly(A) site from bovine growth hormone gene Ψ:packaging signal	ZFNs	Similar number of integration events as *AAVS1* targeted lymphoblasts (7-11%), but lower mean fluorescence intensity (MFI). EGFP MFI for *EF1A* construct in *CCR5* was 36 arbitrary units (a.u.) compared to 140 a.u. in *AAVS1*.	(Lombardo et al., 2011)

hROSA26 (Human orthologue of mouse *Rosa26*)						
Integration site & orientation	**Promoter**	**Fluorescent gene**	**Construct schematic**	**Genome targeting method**	**Success**	**Reference**
Overlaps first exon and following intron of *ROSA26*	Endogenous *hROSA26*	tdRFP	 tdRFP expression is driven by the endogenous *hROSA26* promoter once Cre-mediated removal of Neomycin-resistance cassette occurs SA: Splice acceptor	Homologous recombination and recombinase-mediated cassette exchange	Targeting efficiency of 1.5%. tdRFP expression observed in each of three germ layer differentiations	(Irion et al., 2007)

3.1.3 Calcium handling in cardiomyocytes

3.1.3.1 Excitation-contraction coupling

The presence of calcium is essential for contraction in cardiomyocytes. Its absence allows the cardiomyocyte to relax. Calcium cycling is therefore vital for working cardiomyocytes, and this process is known as excitation-contraction (E-C) coupling.

Cardiac E-C coupling is initiated by the influx of calcium ions (Ca^{2+}) into the cardiomyocyte through the L-type calcium channels. An increase in cytosolic Ca^{2+} results in the further release of calcium from sarcoplasmic reticulum (SR) stores, via the ryanodine receptors (RyR2) (**Figure 3.3**). This process is known as calcium-induced calcium release (CICR).

The released calcium then binds to troponin C (TnC) and initiates cross-bridge cycling between actin and myosin contractile filaments (Landesberg and Sideman, 1994) (**Figure 3.4**). This contraction phase of the heartbeat is known as systole. In order for relaxation (diastole) to occur, the sarcoplasmic reticulum Ca^{2+}-ATPase (SERCA2a) will also mediate re-uptake of calcium into the SR, where the auxiliary SR protein calsequestrin (CASQ2) will sequester excess Ca^{2+} (**Figure 3.3**).

CASQ2 also forms a complex with RYR2, junctin (JCN) and triadin (TRDN) to inhibit opening of the RYR2 channel at low luminal calcium concentrations (Györke et al., 2004). At high luminal Ca^{2+} concentrations, CASQ2 will dissociate from RYR2, allowing it to open.

Excess cytosolic Ca^{2+} can also be extruded from the cell through the sodium/calcium exchanger (NCX). This entire process of increased intracellular Ca^{2+}, followed by decreased intracellular Ca^{2+}, is known as a calcium transient.

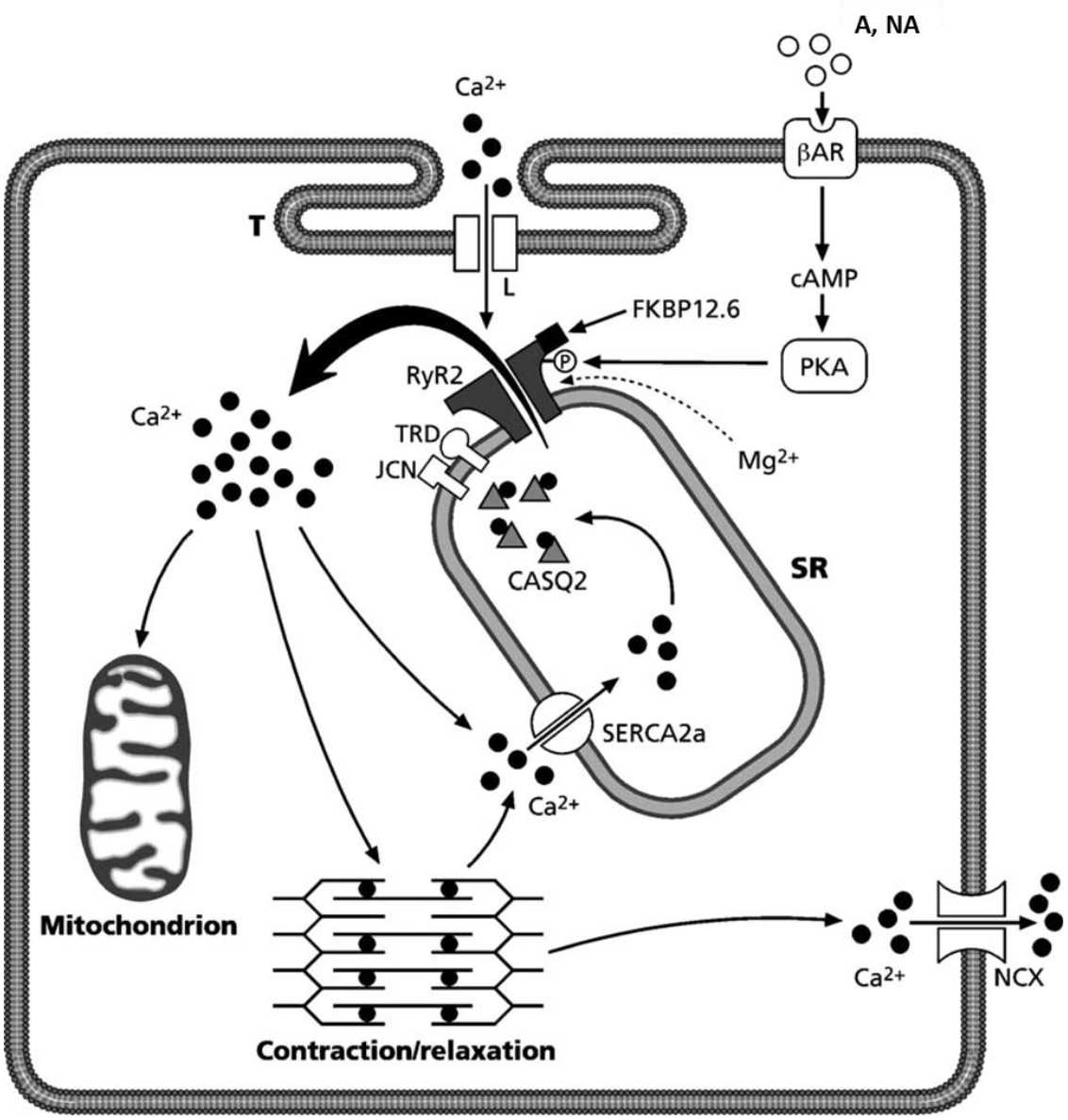


Figure 3.3. Calcium handling in adult cardiomyocytes.

Calcium ions (Ca^{2+}) enter the cardiomyocyte through L-type calcium channels (L) and cause further calcium release from the sarcoplasmic reticulum (SR) via the ryanodine receptors (RyR2). High intracellular Ca^{2+} levels initiate cardiac contraction of the sarcomere. During relaxation, Ca^{2+} re-uptake into the SR occurs, mediated by the sarcoplasmic reticulum Ca^{2+}-ATPase (SERCA). Ca^{2+} within the SR is sequestered by calsequestrin (CASQ2). Intracellular Ca^{2+} can also be released in exchange for two Na^{+} ions through the electrogenic sodium-calcium exchanger (NCX). Adrenaline (A), and noradrenaline (NA), can also modulate Ca^{2+} release from the SR by binding to the ß-adrenergic receptor (ß-AR) and causing phosphorylation of ryanodine receptors via protein kinase A (PKA). T – transverse tubules, TRD – triadin, JCN – junctin. Adapted from (van der Werf and Wilde, 2013).

3.1.3.2 The cross-bridge cycle

Contraction involves thick and thin myofilaments sliding past one another. This process is known as the cross-bridge cycle and can be broken down into three main events; cross-bridge formation, the power stroke and cross-bridge detachment (**Figure 3.4**).

The binding of Ca^{2+} to troponin C exposes the myosin-binding sites on actin filaments. Cross-bridge formation occurs when myosin heads are "energised" by the hydrolysis of ATP into ADP + P and bind actin. The power stroke involves the pivoting of the myosin heads, and the sliding of the thin filament past the thick filament. ADP + P molecules then diffuse away from the myosin head. Finally, in cross-bridge detachment, a new ATP molecule is required for the myosin head to release the actin filament, ready for the cycle to repeat (**Figure 3.4**) (McConnell and Hull, 2010).

Crucially, at low intracellular Ca^{2+} concentration, Ca^{2+} dissociates from troponin C and contraction is not possible because tropomyosin shields the myosin binding sites.

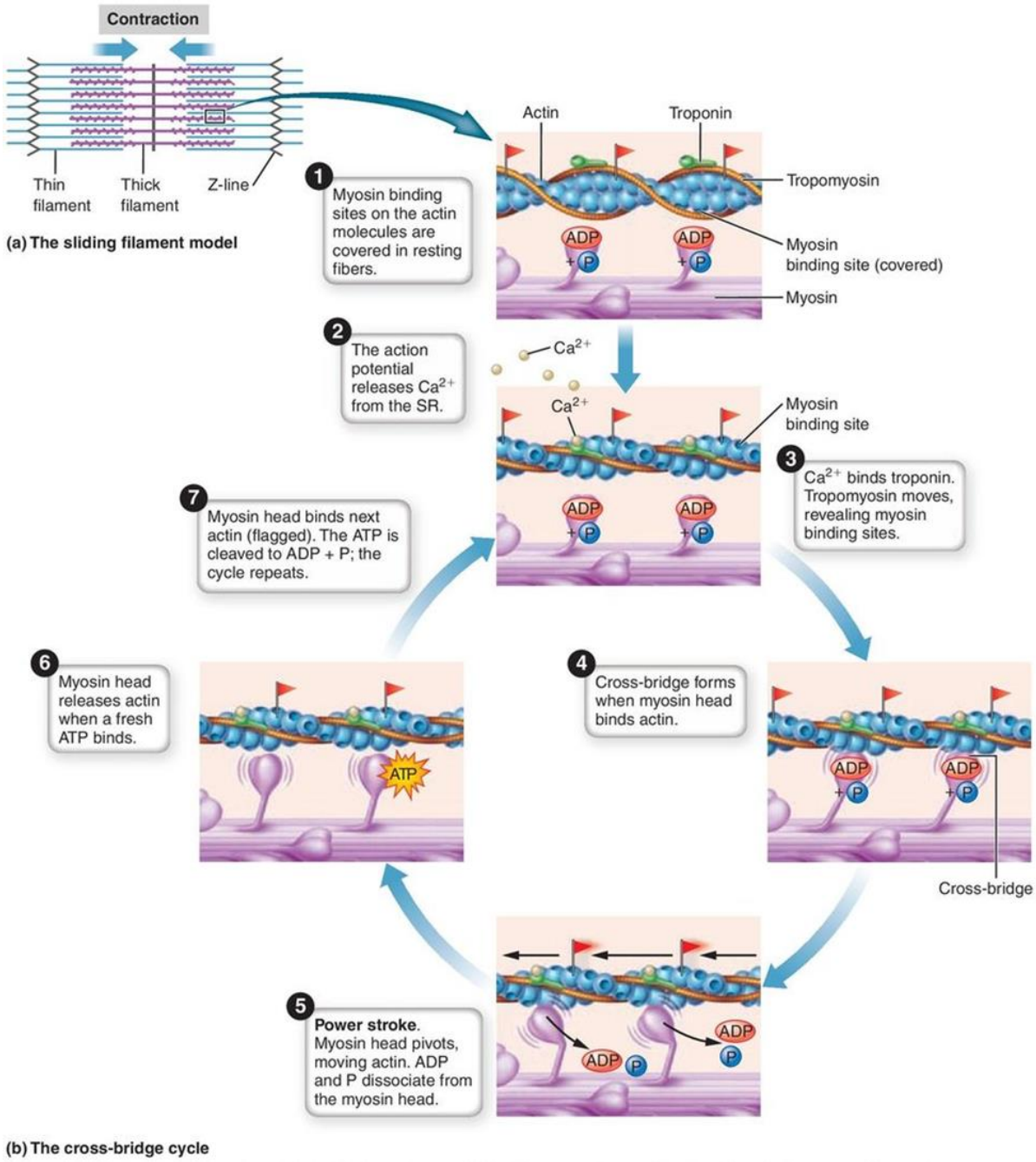


Figure 3.4. The cross-bridge cycle mediates cardiac muscle contraction.

(A) Thick filaments pull thin filaments toward each other during cardiac contraction. **(B)** Steps involved in cross-bridge cycling. Ca^{2+} binds to troponin inducing a conformational change which allows myosin to bind actin. The myosin head pivots causing the filaments to slide past each other. Hydrolysis of ADP + P is followed by ATP binding, which releases the myosin head. ATP is hydrolysed to ADP + P and the cycle continues. Adapted from (McConnell and Hull, 2010).

3.1.4 Calcium imaging

3.1.4.1 Fluorescent calcium indicators

The measurement of calcium flux in cells can be achieved in a number of ways. Whilst patch-clamp can be used to measure influx and efflux of Ca^{2+} through L-type channels and NCX, respectively, it is invasive and cannot be used to detect whole-cell Ca^{2+} transients, Ca^{2+} wave propagation or small Ca^{2+} sparks. In order to detect intracellular calcium transients, fluorescent calcium dyes such as Fluo-4 AM, Fura-2 or Indo-1 are often used to image calcium (Guatimosim et al., 2011, Herron et al., 2012).

These dyes have the advantage of being commercially available in a wide variety of excitation/emission wavelengths and exist across a broad range of calcium dissociation constants (K_d) (Paredes et al., 2008). Furthermore these dyes are relatively easy, although time-consuming, to load into cells and have been successfully applied in a number of hiPSC-CM phenotyping studies (Yazawa et al., 2011, Cerignoli et al., 2012, Sirenko et al., 2013, Clay et al., 2015).

However, calcium dyes are unable to cross the plasma membrane of cells unless acetoxymethyl (AM) ester bonds are used to mask the charged carboxylic groups (Whitaker, 2010). These ester bonds help to confine the dye within the cell, but can also lead to the dye becoming compartmentalised in the endoplasmic reticulum (ER) due to its higher calcium concentration (Thompson et al., 2012). This can distort results when attempting to measure cytoplasmic Ca^{2+}. Moreover, the cleavage of these ester bonds by esterases leads to the release of cytotoxic formaldehyde and acetic acid, albeit at low levels (Schultz et al., 1993).

Yet another drawback of AM calcium dyes is the need to delay calcium imaging once the dye has been loaded in order to allow de-esterification of the dye. Calcium dyes in general often suffer from uneven dye loading; as well as gradual dye extrusion which limits the time-frame of calcium imaging experiments to a few hours and increases the background fluorescence level (Paredes et al., 2008).

3.1.4.2 Genetically encoded calcium indicators

Many of the drawbacks and obstacles associated with chemical calcium indicator dyes can be addressed with the use of genetically encoded calcium indicators (GECIs). As the name suggests, these calcium indicators are coded for by exogenous DNA and fluoresce in response to Ca^{2+} ions. GECIs typically consist of a calcium-sensing domain such as calmodulin (CaM), a linker sequence such as the M13 peptide, and at least one fluorescent protein (FP) domain.

There are two main classes of GECI: Förster-resonance energy transfer (FRET)-based sensors and circularly permutated fluorescent protein (cpFP) based sensors.

FRET is a phenomenon that occurs between two closely associated fluorescent proteins with overlapping emission and excitation spectra. During FRET, one of the fluorescent proteins is excited and acts as a donor that transfers energy to a second, adjacent fluorescent protein (Perez Koldenkova and Nagai, 2013) (**Figure 3.5A**). The efficiency of FRET depends on a number of factors including, the spectral overlap between the two FPs, their orientation and, crucially, the distance between the two FPs (Suzuki et al., 2016). The inclusion of two FPs mean that most FRET-based GECIs such as the CFP-YFP cameleon can emit at different wavelengths in the Ca^{2+} free and Ca^{2+} bound states (Miyawaki et al., 1999) (**Figure3.5A**). This enables ratiometric Ca^{2+} imaging, which can be used to more accurately assess intracellular Ca^{2+} concentrations (Mank and Griesbeck, 2008).

GECIs based that are based on circularly permutated FPs rely on a Ca^{2+}-dependent conformational change to induce de-protonation, and thus activation of the fluorophore (Nagai et al., 2001, Whitaker, 2010) (**Figure 3.5B**). GECIs consisting of cpFPs, such as GCaMP, have advantages over FRET-based GECIs as they often have a higher dynamic range. Dynamic range is defined as the maximum change in fluorescence ratio or intensity (Perez Koldenkova and Nagai, 2013). In addition, as cpFPs are based on a single FP, they often have a narrow excitation/emission spectra, allowing them to be used in conjunction with other fluorescent indicators. As cpFPs are based on a single FP, they are often intensiometric, however, some mutations have generated ratiometric cpFP GECIs, such as the ratiometric emission GEM-GECO and ratiometric excitation GEX-GECO (Zhao et al., 2011b).

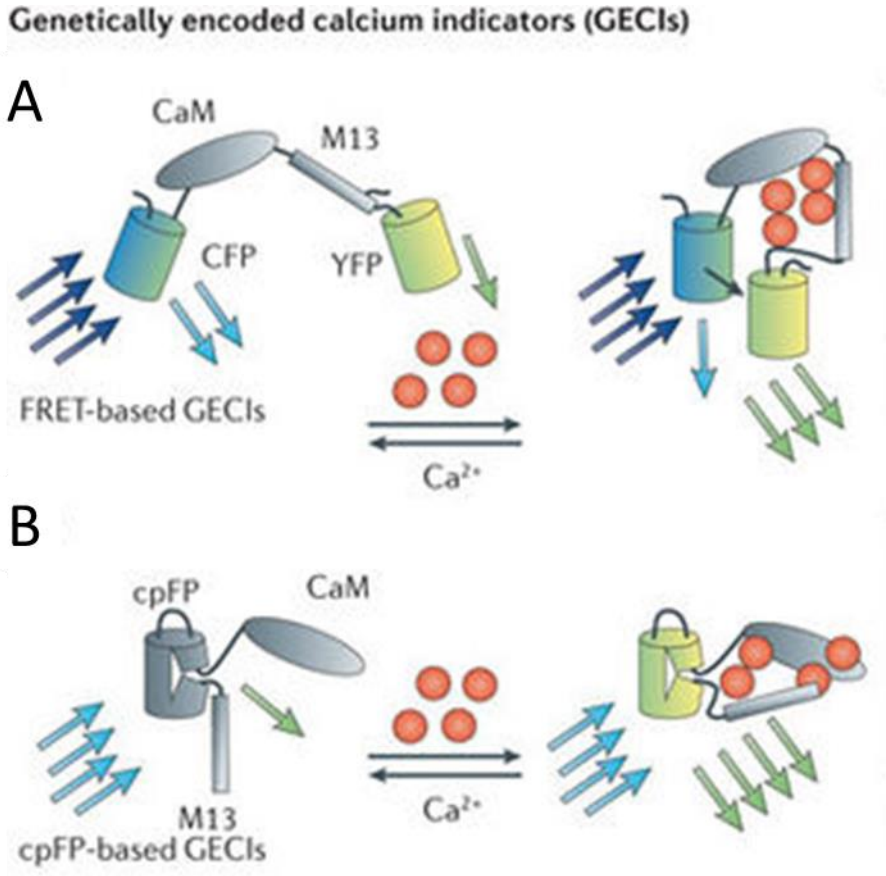


Figure 3.5. FRET and cpFP based methods of calcium sensing by GECIs.

Schematic of genetically encoded calcium indicators. **(A)** Forster resonance energy transfer (FRET)-based GECIs often rely on the close association of CFP and YFP with an intervening calmodulin (CaM) calcium-binding domain and M13 linker peptide sequence. Excitation of CFP causes emission at a wavelength that can excite YFP. Upon calcium binding, YFP is brought into close proximity to CFP and is excited. **(B)** Circularly permuted fluorescent protein (cpFP)-based GECIs rely on a single fluorescent protein, and upon calcium binding to CaM, undergo protonation and excitation of the fluorophore. Excitation wavelengths depicted with blue arrows, emission wavelengths depicted with green arrows. Red circles indicate Ca^{2+} ions. Adapted from (Knopfel, 2012).

Overall, GECIs provide a number of advantages over fluorescent calcium indicator dyes. GECIs do not need to be loaded onto cells, rather the genes encoding them must be expressed in the target cell type (Whitaker, 2010). They also offer advantages in terms of their application in experiments of long duration, and reduced toxicity. In addition, as a result of being genetically encoded, GECIs can be localised to subcellular compartments such as the endoplasmic reticulum (Suzuki et al., 2014); membrane-tethered (Shigetomi et al., 2013); or be driven by tissue-specific promoters such as the cardiac-specific myosin light chain 2v promoter (Kaestner et al., 2014). However, GECIs still suffer from some phototoxicity, photobleaching and slow kinetics (Rose et

al., 2014). Furthermore, the generation of GECI cell lines is time-consuming and labour-intensive.

Nevertheless these promising calcium indicator tools have tremendous utility in the context of optically analysing calcium transients in cardiomyocytes and are further reviewed in **section 3.1.3**.

3.1.4.3 Mechanistic insights

Analysis of calcium transient parameters such as; calcium transient duration (CTD), time to rise (T_{rise}) and calcium transient amplitude have been used to assess drug action on hiPSC-CMs. Calcium transient analysis has been performed using high throughput kinetic plate readers to assess arrhythmogenicity and cardiotoxicity of drug candidates (Grimm et al., 2015, Pointon et al., 2015, Abi-Gerges et al., 2017).

However, these studies rely on potentially toxic chemical calcium indicator dyes and calcium transient analysis alone is not sufficient for fully predicting proarrhythmia risk in new drug candidates (Abi-Gerges et al., 2017).

To address these issues, simultaneous optical pacing, calcium imaging and voltage imaging for cardiotoxicity screening has been achieved with the use of a dual-function calcium/voltage indicator – CaViar (Dempsey et al., 2016). However, these studies rely on viral transduction of the genetically encoded indicator and co-culture with a distinct cell population for optical pacing.

Nevertheless, studies such as this highlight the interplay between the calcium transient and the action potential. Dysfunctional calcium or sodium handling can lead to arrhythmic events that can be detected in the action potential (**Figure 3.6**).

Early afterdepolarisations (EADs) occur when the action potential duration (APD) is prolonged, and reactivation of L-type Ca^{2+} channels occurs during systole. This leads to depolarisation event during the plateau phase (**Figure 3.6B**).

Delayed afterdepolarisations (DADs) are secondary depolarisations that occur after repolarisation is fully complete. DADs are known to occur during intracellular calcium overload (Wagner et al., 2015). Diastolic Ca^{2+} leak from the sarcoplasmic reticulum can cause an increase in inward transient current, resulting in a DAD event (**Figure 3.6C**).

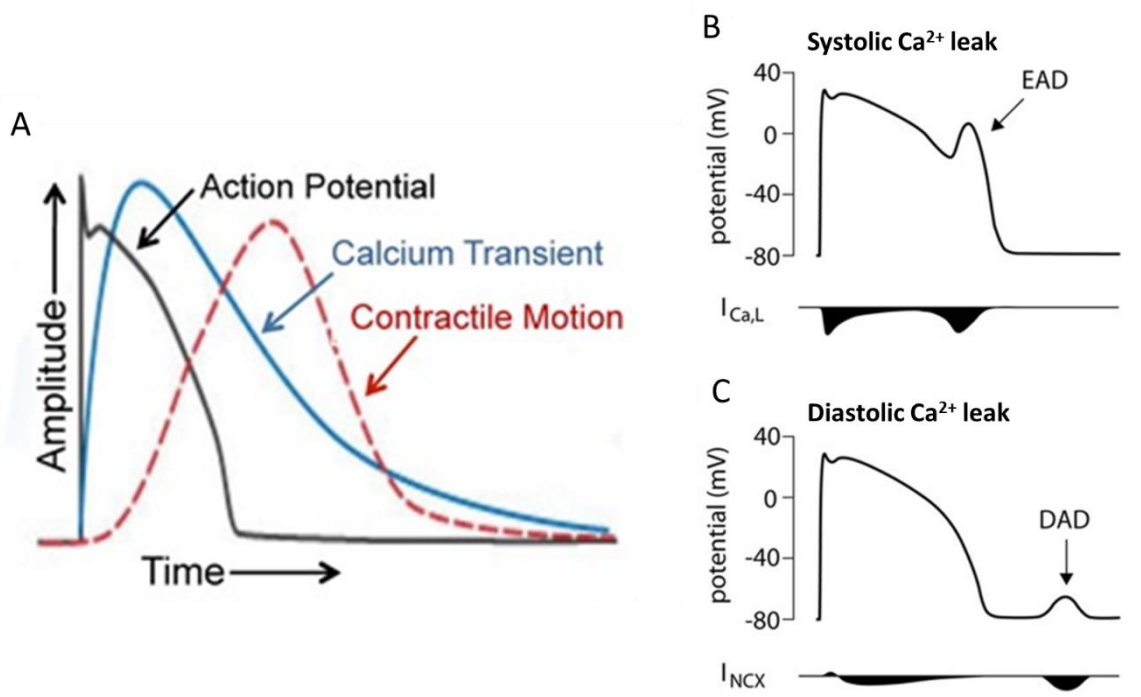


Figure 3.6. The interrelationship between the cardiac action potential, calcium transient and contraction traces.

(A) Schematic representation of the simultaneous action potential (black), calcium transient (blue) and contractile (red) traces. **(B)** Early afterdepolarisation (EAD). A prolonged action potential duration (APD) can result in the reactivation of L-type Ca^{2+} channels and subsequent spontaneous Ca^{2+} release during the plateau phase of the action potential. **(C)** Delayed afterdepolarisation (DAD). Calcium overload in the sarcoplasmic reticulum can lead to diastolic Ca^{2+} release. The resulting inward transient current can induce a depolarisation event. Adapted from (Hoekstra et al., 2012).

3.1.5 Selecting a palette of genetically encoded calcium indicators for cardiac applications

Although originally utilised in the field of neuroscience for imaging neural circuits (Tsien and Miyawaki, 1998, Miyawaki et al., 1997), GECIs have been applied both *in vivo* (Tallini et al., 2006) and *in vitro* (Maddah et al., 2015) to study calcium transients in cardiomyocytes. They are favoured over dyes because they allow for long-term study of calcium transients over several days, without loss of stability (Kotlikoff, 2007). In addition, as a result of being genetically encoded, GECIs can be localised to subcellular compartments such as the endoplasmic reticulum (Suzuki et al., 2014); membrane-tethered (Shigetomi et al., 2013); or be driven by tissue-specific promoters such as the cardiac-specific myosin light chain 2v promoter (Kaestner et al., 2014). An assortment

of different GECIs exists, each with different calcium affinities, kinetics, and spectral properties. A non-exhaustive list of these is provided in **Table 3.2**.

To bind Ca^{2+} GECIs require a calcium-binding domain. The vast majority of GECIs rely on calmodulin (CaM). However, some GECIs with a high K_d for Ca^{2+}, such as camgaroo-2 (**Table 3.2**), have been shown to buffer calcium via this domain (Miyawaki et al., 1999). Furthermore, there are concerns that the reliance on CaM for calcium detection may interfere with host cell signal transduction pathways (Pologruto et al., 2004). This drawback can be addressed with the TN-XL GECI, which uses troponin C (TnC) as the calcium sensor (Mank et al., 2006). However, for the purposes of this project, the use of TnC-based calcium sensors could interfere with the contraction-relaxation cycle of cardiomyocytes, as TnC is heavily involved in cardiac cross-bridge cycling. Consequently, we sought a CaM-based GECI that had an affinity for Ca^{2+} in the nanomolar range, could be applied to cardiac applications, had a detectable dynamic range, and that existed across a wide spectral range for potential combination with other optical reporter genes. The genetically encoded calcium indicators for optical imaging (GECO) series of GECIs met these requirements (**Table 3.2**).

GECI	Excitation/Emission wavelengths	K_d' for Ca^{2+} (nM)	Intensity change $\pm Ca^{2+}$ (Dynamic range)	Comments	References
GCaMP3	399nm/513nm	542	12x	Circularly permutated GFP which forms basis of the GECO series of GECIs	(Nakai *et al.*, 2001)
GCaMP6f	400nm/510nm	375		Calcium indicator with fast kinetics for detection of calcium sparks	(Chen *et al.*, 2013, Shang *et al.*, 2014)
G-GECO1.0	398nm/496nm	749	25x	Green intensiometric GECO	(Zhao et al., 2011a)
R-GECO1.0	561nm/589nm	482	16x	Red intensiometric GECO	(Zhao et al., 2011a)
B-GECO1.0	378nm/446nm	164	7x	Furthest blue-shifted GECO	(Zhao et al., 2011a)
CAR-GECO1	565nm/620nm	490	27x	Furthest red-shifted GECO for use in conjunction with blue-shifted optogenetic actuators	(Wu *et al.*, 2013)
GEM-GECO	397nm/511nm (Ca^{2+}-bound)390nm/455nm (Ca^{2+}-free)	340	110x	Blue-green emission ratiometric (blue when calcium-bound, green when calcium-free) GECO	(Zhao et al., 2011a)
GEX-GECO	397nm/512nm (Ca^{2+}-bound) 390nm/506nm (Ca^{2+}-free)	318	26x	Green excitation, ratiometric GECO	(Zhao et al., 2011a)
Camgaroo-2	480nm/528nm	5300		FRET-based, cameleon series of GECIs. Yellow	(Griesbeck *et al.*, 2001)
TN-XL	440nm/535nm	2500	5x	Troponin-C is the calcium sensor, so no unwanted interaction with calmodulin	(Mank et al., 2006)

Table 3.2. Overview of genetically-encoded calcium indicators and their properties.

The dissociation constant (K_d) for calcium corresponds to the concentration of Ca^{2+} at which half the indicator molecules are bound with Ca^{2+} at equilibrium. The dynamic range is defined as the intensity or ratio change in fluorescence in response to Ca^{2+}. A dynamic range of 1x would be equivalent to a 100% change of fluorescence intensity upon binding Ca^{2+}. Selected GECIs for this thesis highlighted in bold.

The GECO series were generated by error-prone polymerase chain reaction (PCR) mutagenesis of the GECI GCaMP3. GCaMP3 and, by extension, the entire GECO series, are based on the circularly permutated fluorescent protein (cpFP) enhanced green fluorescent protein (EGFP) (Nagai et al., 2001). These GECIs consist of cpEGFP fused to the calmodulin (CaM)-binding region of chicken myosin light chain kinase (M13) at the N-terminus, and a vertebrate CaM at the C-terminus (**Figure 3.7A-C**). Upon binding Ca^{2+}, CaM and M13 interact and the fluorescent protein changes conformation (Wang et al., 2008).

The structural basis for Ca^{2+}-dependent changes in fluorescence is poorly understood which is why the development of new variants requires extensive mutagenesis and screening. Despite this, a wide range of GECOs exist in different colours and with different properties (**Table 3.2**). One such GECO is the green G-GECO1.0 which, through successive rounds of directed evolution, exhibits approximately double the dynamic range of its GCaMP3 predecessor (**Figure 3.7D**) (Zhao et al., 2011a). The red GECO, R-GECO1.0, was generated by using a circularly permutated mApple red FP and is useful because red fluorescent probes possess greater tissue penetration and lower phototoxicity (Wu et al., 2013).

The blue-green emission GEM-GECO was discovered when Zhao *et al*. were attempting to generate a blue B-GECO variant. In the Ca^{2+}-free state, it is thought that the chromophore undergoes excited state proton transfer (ESPT) and emits from the lower energy form (green). Upon Ca^{2+} binding, ESPT is blocked and it emits from higher energy form (blue). Because of this, GEM-GECO is ratiometric and two-photon microscopy can be used to calculate the ratio between Ca^{2+}-bound and Ca^{2+}-free states, allowing the quantification of intracellular Ca^{2+}. GEM GECO is valued because it has an exceptionally high dynamic range of 110x (11,000%) change in signal in response to calcium (Zhao et al., 2011a) (**Table 3.2**). This is important because many fluorescent calcium indicators, whether genetically encoded or chemical in nature, suffer from dynamic range compression when expressed in living cells. Fluorescent probes such as camgaroo-2, inverse pericam and the dye Fluo-3, have all been shown to suffer from this phenomenon (Miyawaki, 2005, Diez-Garcia et al., 2005, Thomas et al., 2000). There is not yet a clear indication as to why this occurs, although it has been postulated that it may be a result of CaM-protein interactions in the cytosol (Kaestner et al., 2014).

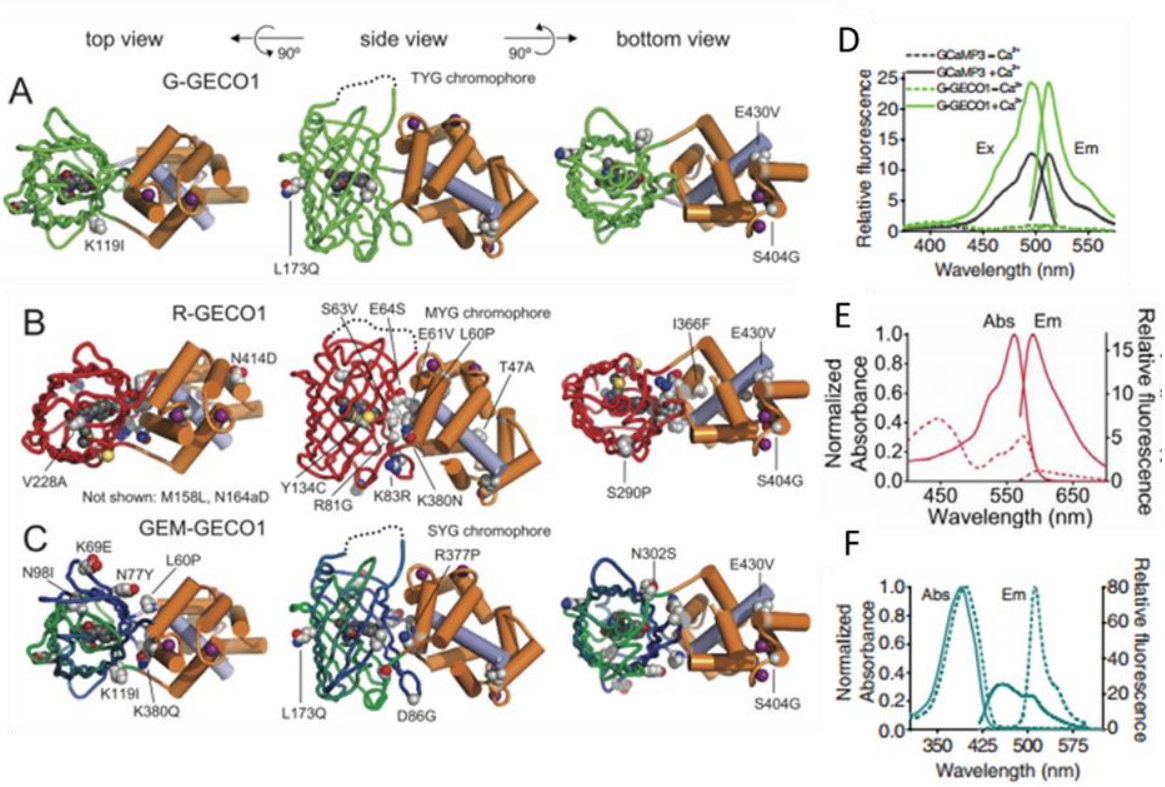


Figure 3.7. Crystal structures and spectral properties of selected GECO variants.

(A-C) GECO crystal structures with annotated amino acid changes from GCaMP3, showing the cpFP ß-barrel (left) fused to CaM-M13 (right) **(D)** Plot illustrating the excitation/emission wavelengths of G-GECO1.0 and GCaMP3. Note the twofold increase in dynamic range of G-GECO1.0 compared to GCaMP3. **(E)** Fluorescence plot illustrating the spectral properties of R-GECO1.0 **(F)** Fluorescence plot for GEM-GECO illustrating spectral properties. Note the two emission peaks for the calcium-free state at 455nm (green), and calcium-bound state at 511nm (blue). Adapted from Figs S3 & S4, (Zhao et al., 2011a).

For the purposes of this thesis, R-GECO1.0, G-GECO1.0 and GEM-GECO should all have sufficient dynamic range to allow the detection of changes in intracellular calcium in beating cardiomyocytes. These indicators should also be compatible with both wide-field and confocal microscopes available. Their different spectral properties should also provide some flexibility in downstream applications. For example, GEM-GECO is a dual-emission ratiometric indicator capable of more accurately quantifying intracellular Ca^{2+}. In contrast, R-GECO1.0 is an intensiometric indicator with a longer excitation wavelength, more suited to combination with optical indicators and actuators with short wavelengths.

3.2 Chapter Aims and objectives

The aim of this chapter was to generate a suite of hiPSC lines that were precisely targeted in a safe genomic location with genetically encoded calcium indicators. In this way, the hiPSCs could be differentiated to cardiomyocytes and used to optically analyse calcium transients in hiPSC-CMs in later chapters. The following objectives had to be met to fulfil this aim:

1. Design and produce sgRNAs specific to the *AAVS1* safe harbour locus.
2. Design and generate targeting constructs to deliver GECIs to the target location.
3. Test a range of methods and conditions for delivering sgRNAs, targeting vector and Cas9 nuclease to hiPSCs with the highest efficiency.
4. Perform CRISPR/Cas9 on both healthy and diseased isogenic sets of hiPSCs.
5. Genotype and characterise clones to select the optimally expressing GECI cell lines.

3.3 Results

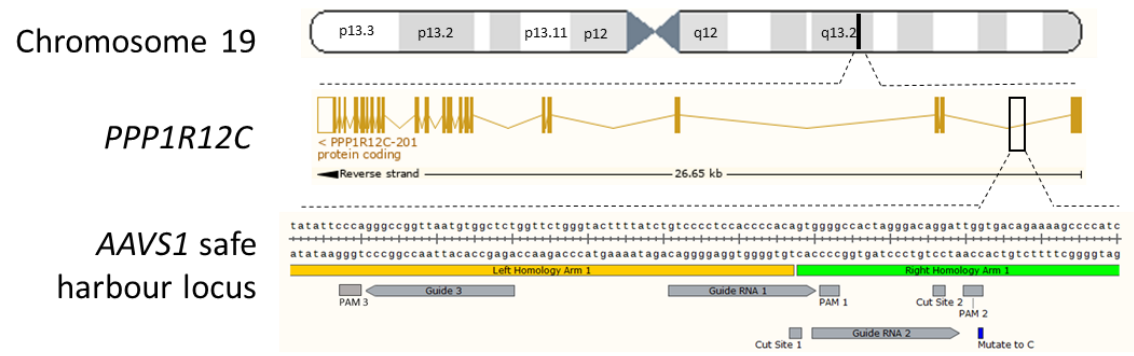
3.3.1 Initial *AAVS1* EF1α targeting vector and sgRNA design

The *AAVS1* safe harbour locus, located within the first intron of *PPP1R12C* on chromosome 19 (**Figure 3.8A**), was chosen as the destination for GECI targeting. To direct a Cas9 nuclease to this locus a several potential single guide RNA (sgRNA) sequences were designed using an online tool (http://crispr.mit.edu). Using any of the top three selected guides on their own in conjunction with a Cas9 nuclease would have initiated a DSB at the target location, but would also have led to several off-target events (**Figure 3.8B**). The top 20 off-target locations for each of these guides is listed in **Appendix II**. Each of these ~20 bp guide sequences were ordered as complementary oligonucleotides, annealed and cloned into a host vector. These sequences were then confirmed by Sanger sequencing (**Figure 3.8C**). By using pairs of bidirectional sgRNAs with a mutant Cas9 D10A nickase, offset DSBs could be generated (**Figure 3.8D**). By using sgRNA pairs of either 1&3 or 2&3, the predicted occurrence of off-target events was reduced to zero. Given that sgRNAs 2&3 gave the highest quality score of 68, they were chosen to direct the nuclease to the target site using a nickase strategy (**Figure 3.8D**).

Figure 3.8. Location of AAVS1 safe harbour locus and site-specific single guide RNA design.

(A) Schematic illustrating the chromosomal location of the *AAVS1* safe harbour locus. Targeting this safe harbour locus disrupts the first intron of *PPP1R12C* with no deleterious effects. The top three selected sgRNAs and their binding sites within *AAVS1* are indicated. Note that the PAM site for guide 2 was silently mutated (G→C) in the targeting construct to prevent it being cut by Cas9 nuclease during targeting. **(B)** Guide sequences were designed using an online sgRNA program developed by MIT. A single sgRNA can direct a conventional Cas9 nuclease to the target site and induce a double-strand break. Potential off-target events were predicted by the software. **(C)** The guide sequences were cloned into the pU6 plasmid backbone containing an sgRNA scaffold and sequenced to confirm homology with *AAVS1*. **(D)** By using sgRNA pairs and utilising a mutant Cas9 D10A, offset double strand breaks can be made using the 'nickase' approach. In silico predictive algorithms suggested that a combination of guides 2 and 3 would be most efficient, with no off-target cleavage.

A

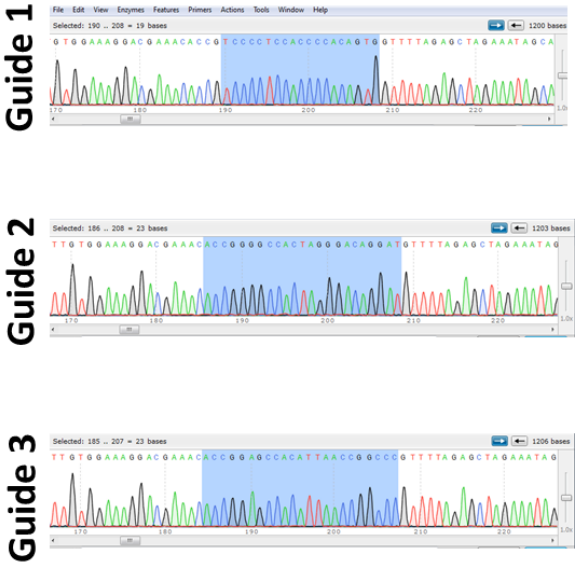


B

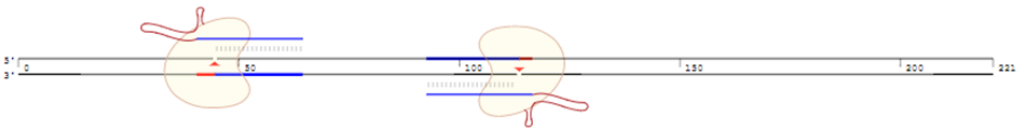


sgRNA	MIT quality score	Sequence	# offtargets	# genic offtargets
Guide 1	61	GTCCCCTCC ACCCCACA GTGGGG	258	25
Guide 2	56	GGGGCCAC TAGGGACA GGATTGG	293	44
Guide 3	89	AGAGCCAC ATTAACCG GCCCTGG	78	16

C



D



sgRNA pair	MIT pair quality score	Number offtargets	Number of genic offtargets
Guide 1 & 3	59	0	0
Guide 2 & 3	68	0	0

In order to precisely target the *AAVS1* locus, a set of targeting constructs were designed. Initially, a channelrhodopsin-2 (ChR2)/halorhodopsin (NpHR3.0) construct designed for a related project, was ordered from a commercial supplier containing the genes of interest flanked on each side by homology to 1kb of the *AAVS1* locus (**Figure 3.9A**). However, this construct was costly to engineer and lacked restriction enzyme sites for the replacement or addition of further genes of interest.

We sought to clone our own set of G-GECO and R-GECO targeting constructs by using the ChR2/NpHR3.0 construct as a parent plasmid (**Figure 3.9A**). The desired GECO constructs consisted of a Myc tag sequence separated from the GECO genes by a P2A site. The constructs also contained the gene conferring resistance to blasticidin, for effective selection of targeted cells (**Figure 3.9B**). In this arrangement, the three elements would be targeted to the *AAVS1* locus under the control of the EF1α promoter. These plasmids were constructed in a modular fashion by first removing the entire cassette downstream of the EF1α promoter by restriction enzyme digest (**Figure 3.9A**). Both the Myc and GECO sequences were PCR amplified from donor vectors originally designed for AAV transduction, and were amplified with primers that included specific restriction enzyme sequences (**Table 3.3**). In this way, the targeting constructs could be cloned in a three-step process (**Figure 3.9A**), and retain the flexibility of future modifications if needed.

A diagnostic digest of the final targeting plasmid (P3), and the intermediate plasmids (P1 and P2) with XhoI and NotI enzymes flanking the cassette, illustrated the stepwise addition of the three gene components (**Figure 3.9D**). These targeting constructs, designated *AAVS1* EF1a Myc G-GECO and *AAVS1* EF1a Myc R-GECO, were further confirmed by sanger sequencing analysis (**Figure 3.9C**), and HpaI diagnostic digests (**Figure 3.9E**). Interestingly, when preparing the bacterial pellet of *AAVS1* Myc R-GECO prep 3 (R3) for plasmid extraction, the pellet was red in colour (**Figure 3.9E**), suggesting an ability for the bacteria to transcribe and express the R-GECO gene.

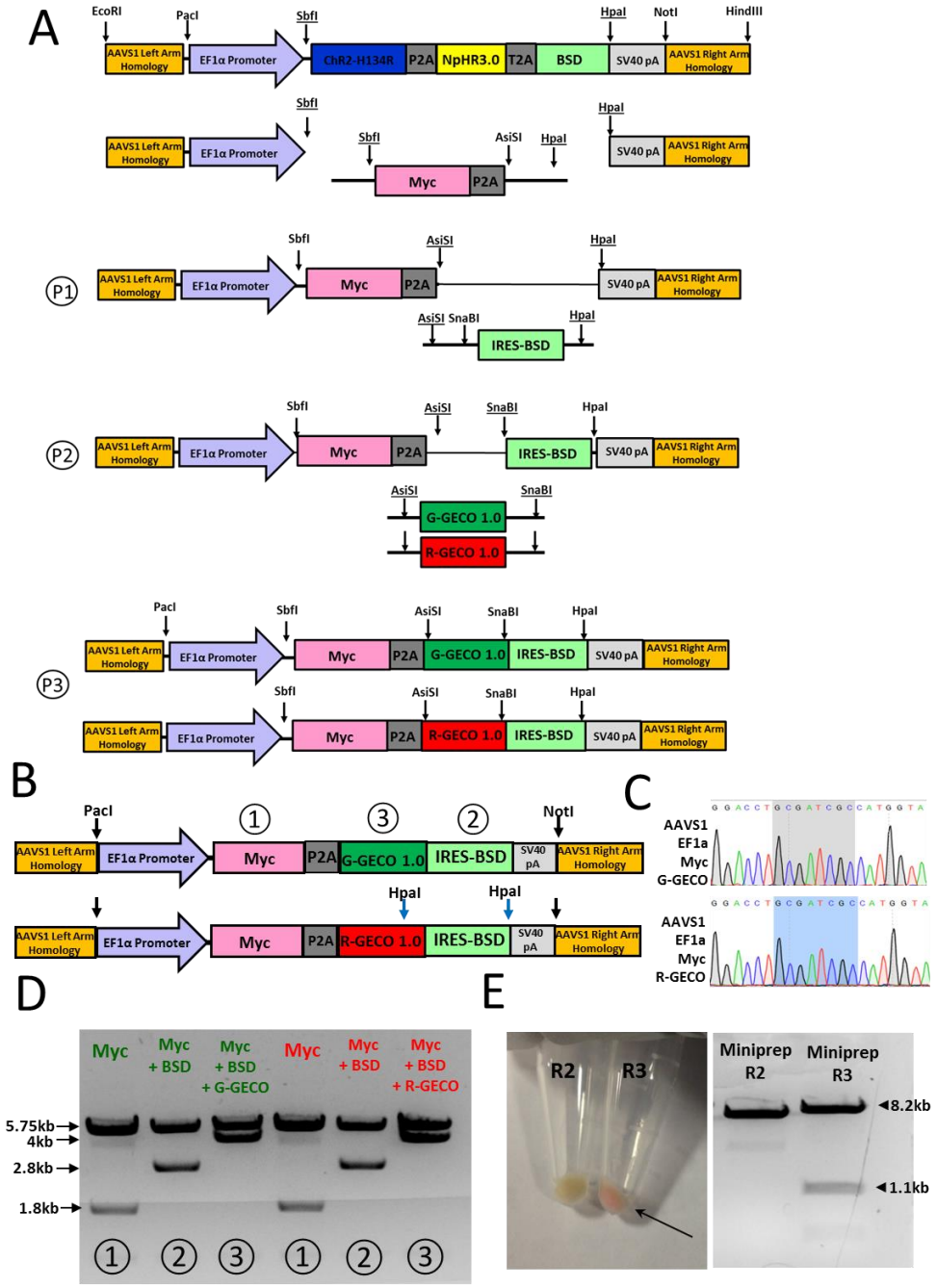


Figure 3.9. Modular cloning of AAVS1 EF1α constructs.

(A) Schematic illustrating stepwise cloning of targeting constructs in three parts (P1-P3). Each constituent section has been PCR amplified with the addition of specific restriction enzyme sites for ligation (underlined – see table 3.1.). **(B)** Resulting EF1α GECO targeting constructs. **(C)** Sanger sequencing to confirm plasmid sequences, showing introduced AsiSI site (highlighted) and ATG start codon of G-/R-GECO. **(D)** PacI/NotI diagnostic digest of intermediate plasmids (P1-P3), showing an increase in the cassette size from 1.8kb to 4kb as each component is cloned into the construct. **(E)** Sample R3 (arrow), showing a red bacterial pellet of E. Coli transformed with EF1α-Myc-RGECO-BSD DNA, which gave the desired band pattern of 8.2kb + 1.1kb upon DNA extraction and diagnostic digest by HpaI.

Table 3.3. Primer sequences for stepwise modular cloning of *AAVS1* EF1α constructs

Primer	Sequence (5' → 3')	Restriction sites
MYC P1 FWD	GCTAGACCTGCAGGACCACCATGGATTATGGAGGCG	Addition of SbfI restriction site
MYC P1 REV	GAGTCTGTTAACGCGATCGCAGGTCCAGGGTTCTCCTCCAC	Addition of AsiSI and HpaI restriction sites
Green GECO P2 FWD	CGGCCCGCGATCGCCATGGTAGACTCATCACGTCGTAAGTG	Addition of AsiSI restriction site
Green GECO P2 REV	ATCCTCTACGTACTACTTCGCTGTCATCATTTGTACAAACTCT	Addition of SnaBI restriction site
Red GECO P2 FWD	GGACCTGCGATCGCCATGGTAGACTCATCACGTCGTAAGTG	Addition of AsiSI restriction site
Red GECO P2 REV	CTTAGGTACGTACTACTTCGCTGTCATCATTTGGACAAACT	Addition of SnaBI restriction site
BLAST P3 FWD	ACAAGTGCGATCGCTACGTATAGATAACTGAGCCCCTCTCCC	Addition of SnaBI and AsiSI restriction sites
BLAST P3 REV	CATGCAGTTAACTTAGCCCTCCCACACATAACCAGA	Addition of HpaI restriction site

3.3.2 Optimisation of culture conditions for high efficiency CRISPR/Cas9 targeting

Transfection efficiency into hiPSCs was first optimised using the lipid-based GeneJammer™ transfection reagent. Transient expression of a pSIN-GFP-BSD plasmid after 48 hours was used to assess the efficiency of transfection in REBL PAT hiPSCs that had been seeded at densities varying from 100,000 cells/cm^2 to 20,000 cells/cm^2 (**Figure 3.10**). Using Operetta high content image analysis, transfection efficiency was calculated as the percentage area of cells that were GFP positive. A seeding density of 33,333 cells/cm^2 was found to have the greatest area of GFP in the cell population (20.37% ±9.28%), which was significantly greater than the highest seeding density of 100,000 cells/cm^2 (n = 3, One-way ANOVA with Tukey's test, *p = 0.032) (**Figure 3.10A**). The next best condition was a seeding density of 20,000 cells/cm^2, giving a transfection efficiency of 17.13% ±6.24%; however, such a low seeding density is likely to result in subsequent cell death or karyotypic abnormalities.

To determine whether greater transfection efficiencies could be achieved in subsequent targeting experiments, nucleofection with an Amaxa-4D™ was tested using a range of program settings. Transiently transfected hiPSCs were live imaged for GFP expression after 24 and 48 hours (**Figure 3.11A**). After 24 hours, each program setting had outperformed the results obtained by using the lipid-based transfection reagent. Indeed, the highest transfection efficiency at 24 hours was achieved with program DN-100 (90.38% ±0.64%) (**Figure 3.11B**). Program DN-100 was the only program to generate an extremely significant increase in GFP expression compared to no DNA control (n = 3, One-way ANOVA with Dunnett's test, **** p < 0.0001). Consequently, Amaxa-4D nucleofection using program DN-100 was the preferred method of transfection for plasmids when attempting CRISPR/Cas9 targeting of hiPSCs.

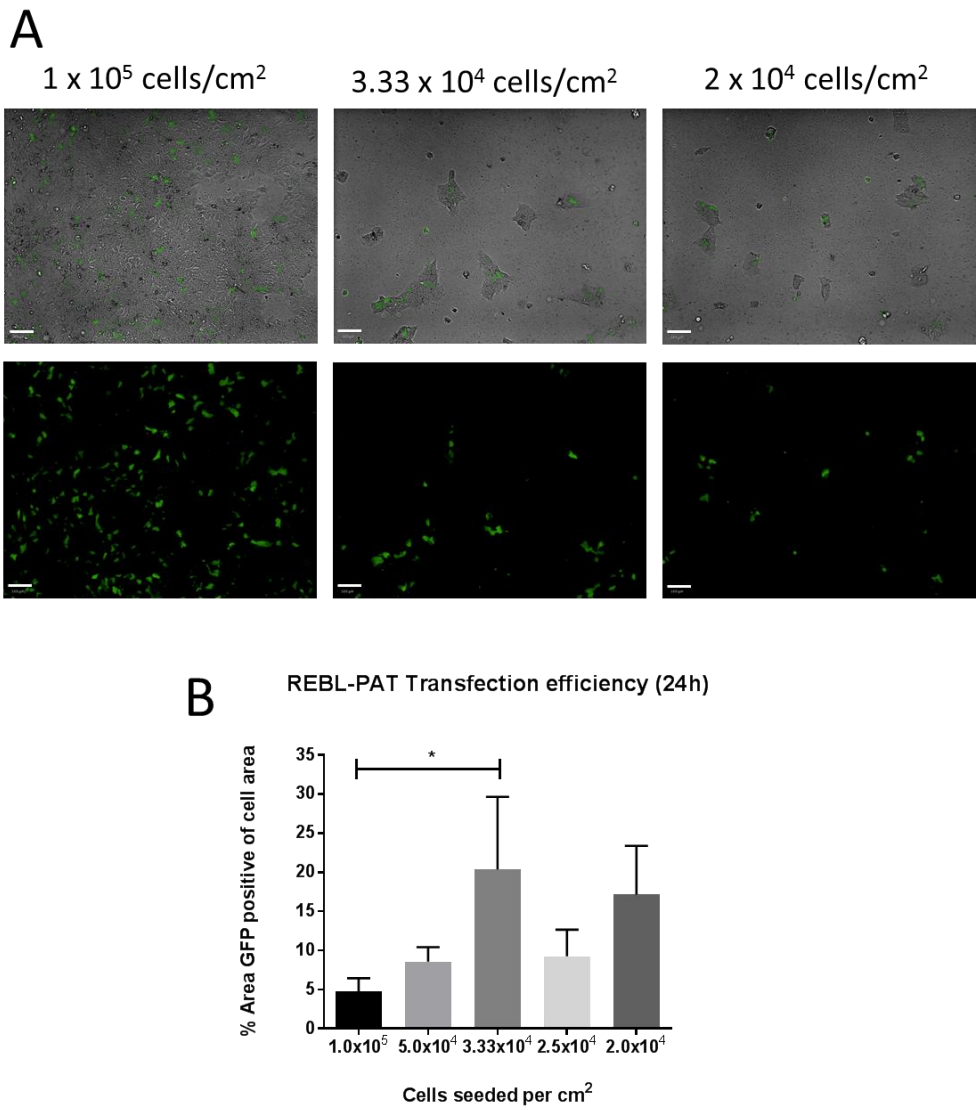


Figure 3.10. Efficiency of GeneJammer™-mediated transfection of REBL-PAT hiPSCs after 24 hours.

(A) Live imaging of transfected REBL-PAT hiPSCs at different densities taken 24 hours after lipid-based transfection of 3pg/cell pSIN-GFP-BSD plasmid. Magnification = 20x. Scale bars = 100 µm. **(B)** Comparison of transfection efficiency across five seeding densities. Transfection efficiency percentage calculated as area of cells that were GFP positive compared to untransfected control using Operetta™ high content image analysis. Data presented as mean ±SD (n = 3 transfections). One-way ANOVA with Tukey's multiple comparison test, * p=0.0322.

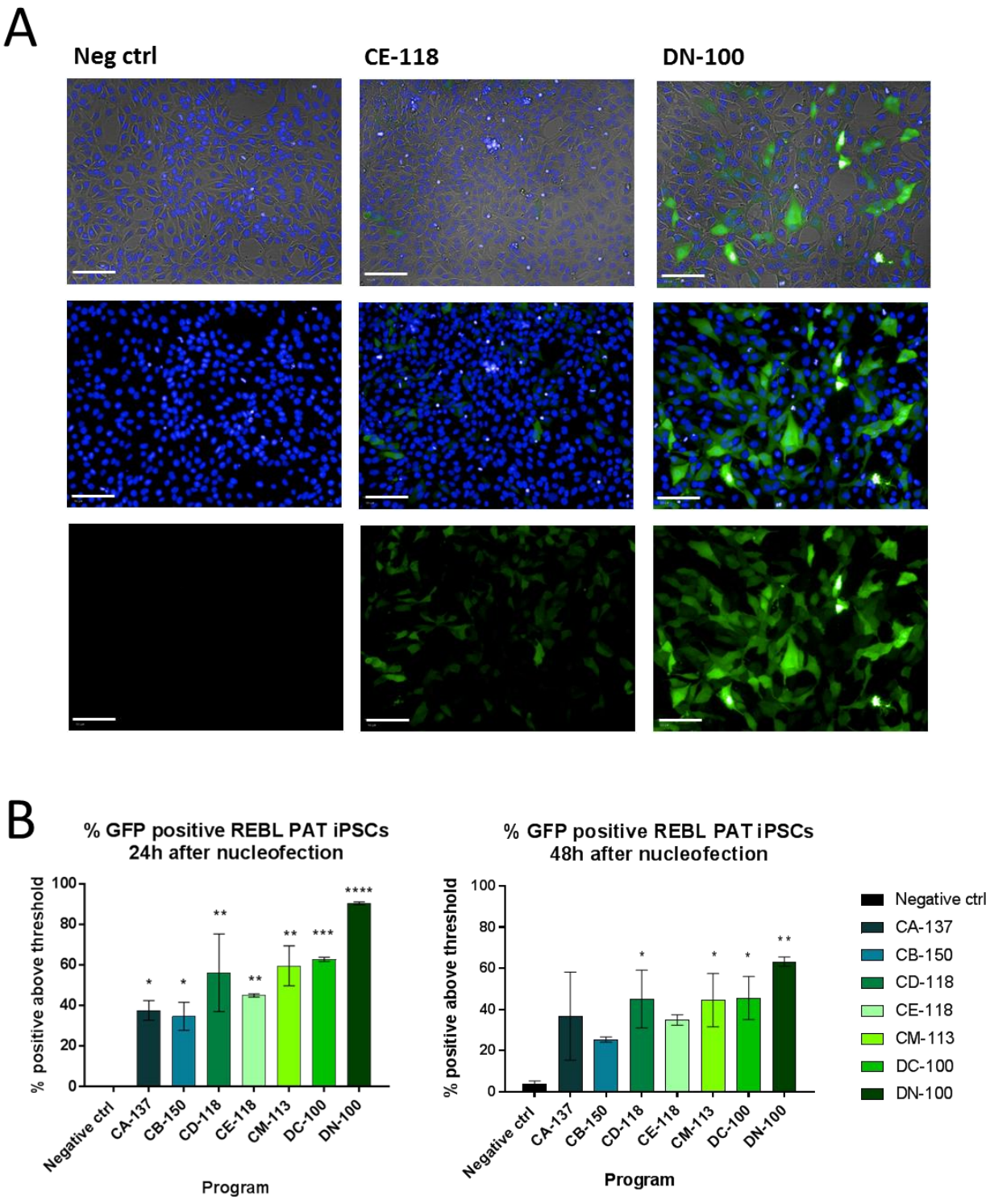


Figure 3.11. Transfection efficiency optimisation of Amaxa™ 4D nucleofection of REBL PAT hiPSCs.

(A) Live imaging of REBL PAT hiPSCs 48 hours after nucleofection with 3pg/cell pSIN-GFP-BSD plasmid using various program settings available on the Amaxa™ 4D. Magnification = 20x. Scale bars = 100 µm. **(B)** Transfection efficiency percentage calculated as number of cells that were GFP positive compared to no plasmid control using Operetta™ high content image analysis. Threshold set using untransfected hiPSCs at 24 hour time-point. Mean ±SD (n = 3 nucleofections). One-way ANOVA with Dunnett's multiple comparison test * $p<0.05$; ** $p<0.01$; ***$p<0.005$; ****$p<0.0001$.

The concentration used for antibiotic selection of successfully targeted clones was optimised by performing blasticidin- or puromycin-based dose response kill curves. The minimum required antibiotic dose required to kill untargeted hiPSCs was found by Operetta™ high content image analysis of confluency (**Figure 3.12A**). By training the software to identify areas containing cells, confluence could be assessed at different antibiotic concentrations at 24 and 48 hours after addition (**Figure 3.12C, E**).

At a concentration of 1.5 µg/ml, blasticidin caused a significant reduction in cell confluence (** p = 0.0011). Although blasticidin showed an almost complete eradication of cells at a concentration of 2.5 µg/ml after 48 hours (**Figure 3.12B**). Confluency was reduced from 33.28% ±4.77% at the beginning of the experiment, to 4.61% ±3.04% after 48 hours (**Figure 3.12C**).

At a concentration of 0.2 µg/ml, puromycin caused a significant reduction in cell confluence (*** p = 0.0003). However, Puromycin killed the majority of hiPSCs after 48 hours at a concentration of 0.3 µg/ml (**Figure 3.12C**). Despite cell debris deceiving the software in some instances, confluency reduced from 27.68% ±0.49% at 0 hours to 21.47% ±1.95% at 48 hours (**Figure 3.12E**). These kill curve experiments informed us that 2.5 µg/ml blasticidin or 0.3 µg/ml puromycin would be more than sufficient to enrich for targeted hiPSCs.

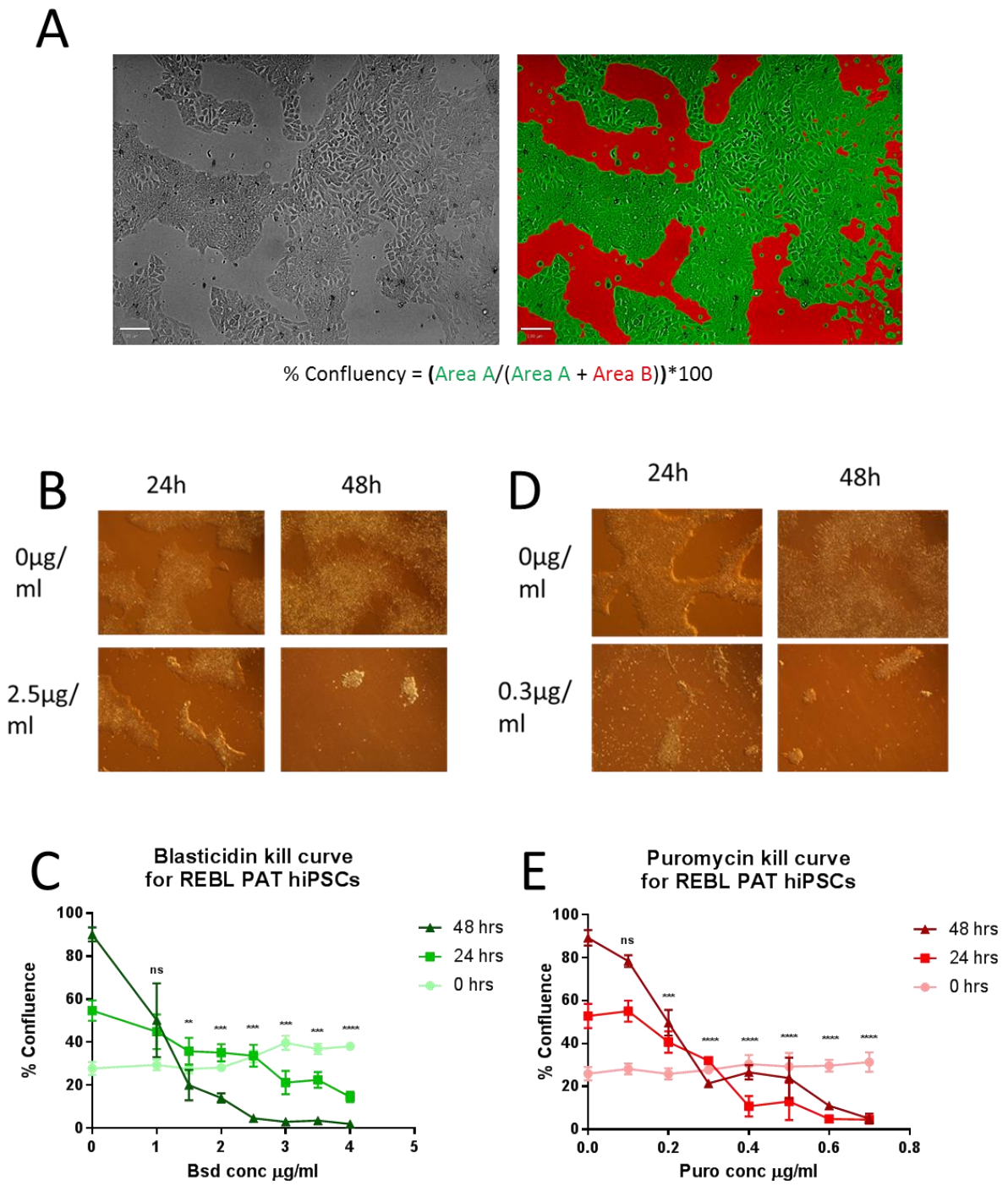


Figure 3.12. Antibiotic titration on REBL PAT hiPSCs over 48 hours to optimise colony selection conditions.

(A) Operetta™ high content image analysis was used to calculate percentage confluence at each timepoint by training the software to identify areas containing cells (Area A – green), or areas without cells (Area B – red). Magnification = 10x, scale bars = 100 µm. **(B, C)** Representative images and corresponding kill curve graph showing reduction in confluence at 2.5 µg/ml blasticidin. Mean ±SD (n = 3 plates). **(D, E)** Representative images and corresponding kill curve graph showing reduction in confluence at 0.3 µg/ml puromycin. Mean ±SD (n=3). Two-way ANOVA with Dunnett's multiple comparison test, ** $p = 0.0011$; *** $p < 0.0005$; **** $p < 0.0001$.

Once the optimal transfection and selection conditions were elucidated, CRISPR/Cas9 targeting of the *AAVS1* locus was carried out using a plasmid-based approach (**Figure 3.13**). Antibiotic selection for at least 6 days was carried out until clearly defined colonies were visible. These were then individually picked and expanded for genotyping.

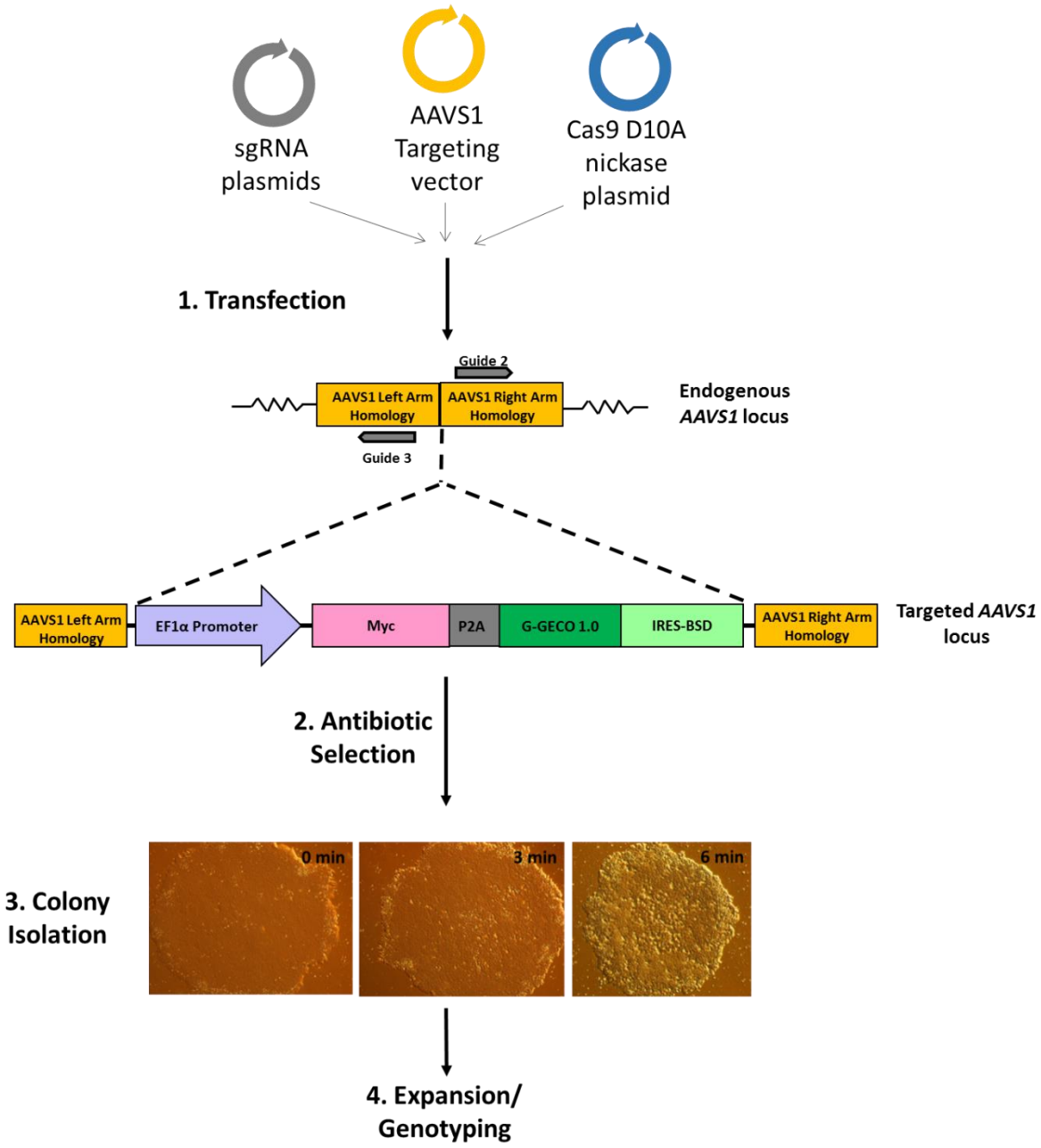


Figure 3.13. CRISPR/Cas9 workflow for targeting the *AAVS1* locus of hiPSCs.

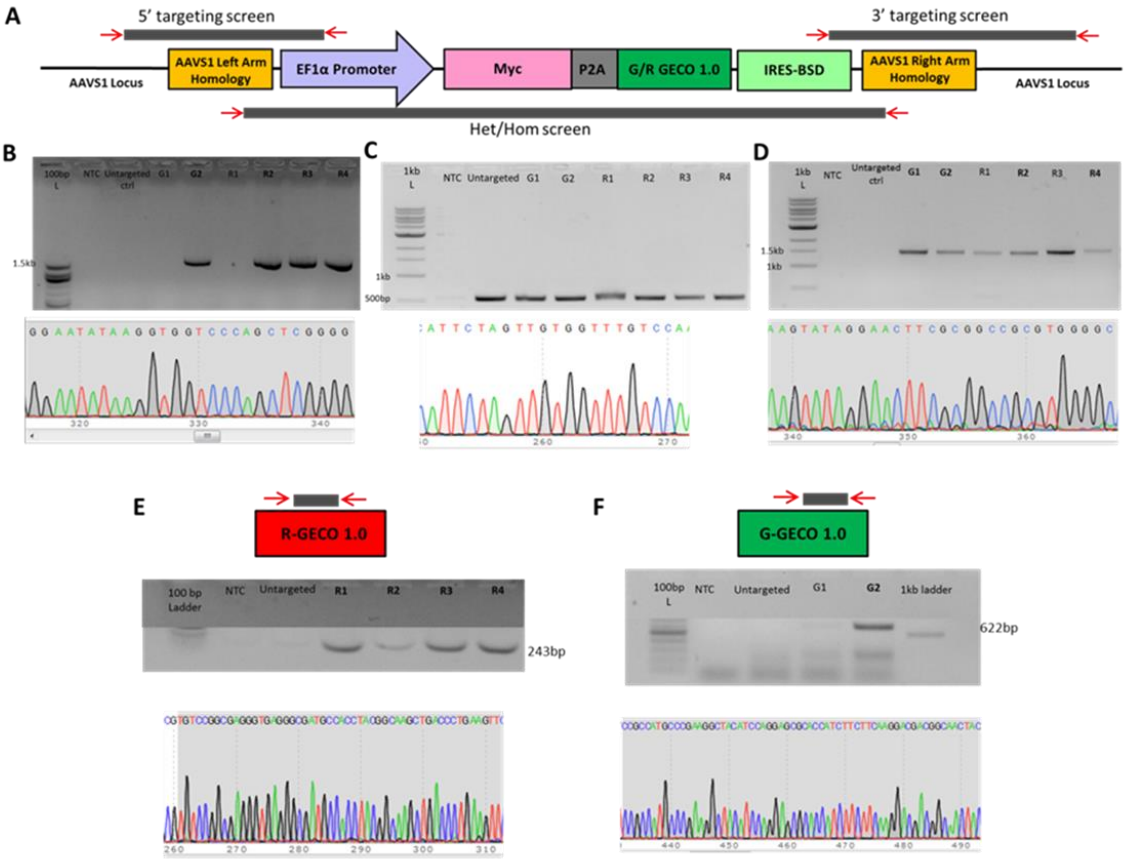
Diagram to illustrate the workflow for CRISPR/Cas9 targeting of the *AAVS1* locus. 1) sgRNAs, targeting vector and Cas9 D10A nickase were transfected into hiPSCs at high efficiency to initiate targeting. 2) Successfully targeted clones were enriched by antibiotic selection. 3) Colonies were isolated by enzymatic dissociation and 4) picked for expansion and downstream genotyping.

3.3.3 Initial genotyping

Cassette integration to the *AAVS1* locus was assessed by PCR on genomic DNA (gDNA) extracted from antibiotic-resistant clones (**Figure 3.14A**). Integration of the 5' end of the insert into the genome was assessed by performing a PCR from outside the *AAVS1* left arm of homology into the EF1α promoter. A total of 3 R-GECO colonies and 1 G-GECO colony were positive for this 5' PCR screen (**Figure 3.14B**). Similarly, 3' integration was assessed by PCR from the BSD-IRES gene to outside of the *AAVS1* right arm of homology. A total of 4 R-GECO colonies, and 2 G-GECO colonies, were positive (**Figure 3.14D**). Notably, colonies G-GECO Guides 2/3 A (G1), and R-GECO Guides 1/3 C (R1), showed integration at the 3' end, but not the 5' end.

In addition, the presence of any biallelic targeting events was evaluated with a PCR spanning the *AAVS1* locus. If both alleles had been targeted, a PCR failure would be expected due to the large 5.6kb size of the inserted cassette. Unfortunately, no biallelic targeting events were observed (**Figure 3.14B**), with each colony screened showing a positive band for the untargeted allele. However, 3 R-GECO (R2, R3, R4) and 1 G-GECO (G2) heterozygotes were identified, all with full integration of the cassette. All PCR products were sequenced and were as expected (**Figure 3.14B-D**). GECO mRNA expression was assessed by generating cDNA and performing RT-PCR for the relevant GECO gene. R-GECO colonies R1, R2, R3 and R4 all gave a positive band at the expected size of 243bp (**Figure 3.14E**). Despite lacking 5' integration of the cassette into the *AAVS1* locus, colony R1 was still capable of expressing both R-GECO1.0 mRNA and blasticidin-S deaminase (BSD) protein. G-GECO colony G2 also demonstrated mRNA expression of G-GECO1.0 (**Figure 3.14F**). Positive RT-PCR products were sequenced and verified that the GECO genes were being transcribed into mRNA (**Figure 3.14E, F**). Accordingly, G-GECO colony G2 and R-GECO colony R2 were chosen for further expansion and banking.

Overall, a targeting efficiency of 12% was attained for R-GECO1.0 using sgRNA guides 2 and 3 (**Figure 3.14G**). A targeting efficiency of 4% was achieved using sgRNA guides 2 and 3 and the *AAVS1* EF1a G-GECO targeting construct (**Figure 3.14G**), suggesting that this sgRNA combination is more effective at targeting the *AAVS1* locus. However, as previously mentioned, a low survival rate of just 19% of picked colonies survived transfer and expansion.



G

Construct & sgRNA combination	Colonies picked	Survived & PCR screened	% Survival	Targeted	% of survivors targeted	Overall targeting efficiency
R-GECO G1/G3	25	8	32%	0	0%	0%
R-GECO G2/G3	25	3	12%	3	100%	12%
G-GECO G1/G3	25	3	12%	0	0%	0%
G-GECO G2/G3	25	5	20%	1	20%	4%

Figure 3.14. Polymerase chain reaction and reverse-transcriptase polymerase reaction genotyping to identify targeted clones.

(A) Schematic showing the locations of PCR screens **(B-D)** within a targeted AAVS1 locus **(B)** 5' PCR screen from outside of the left arm of homology to the beginning of the EF1α promoter. A positive band is seen at 1.5kb. **(C)** Heterozygous/homozygous screen across the expression cassette. An untargeted allele will give a 588bp band, whereas a targeted allele will give a 5.6kb band or PCR failure. **(D)** 3' PCR screen from outside of the right arm of homology to the BSD gene. Positive clones give a band at 1.5kb. All positive clones identified by PCR were fully sequenced for aberrant integration events. **(E-F)** RT-PCR on potentially targeted hiPSC cDNA using primers specific for R-GECO1.0. or G-GECO1.0. Clones that express R-GECO RNA give a product at 243 bp whilst clones that express G-GECO produce a 622 bp product. RT-PCR products were sequenced to confirm their identity. **(G)** Targeting efficiencies using different sgRNA combinations.

3.3.4 Troubleshooting the failure of EF1α constructs to fluoresce

Despite correct targeting of the EF1α GECO cassette to the *AAVS1* locus and RNA expression confirmed by RT-PCR, targeted clones failed to fluoresce upon cardiac differentiation. We hypothesised that this may have been caused by the EF1α promoter being functionally weak once integrated in the *AAVS1* locus, as had been previously described (Luo et al., 2014). We therefore sought to replace the EF1α promoter with the CAG promoter. Initial efforts to PCR amplify the CAG sequence with added restriction sites were unsuccessful, so the promoter was ligated to incompatible cohesive ends with the aid of 5'-phosphorylated linker DNA sequences (**Figure 3.15A**). The *AAVS1* CAG targeting plasmids were successfully generated, retaining the modular nature of the constructs with unique restriction sites between each component (**Figure 3.15B**). Sanger sequencing of the promoter region illustrated that the reason for prior PCR failure was the highly GC-rich nature of the CAG promoter (**Figure 3.15C**).

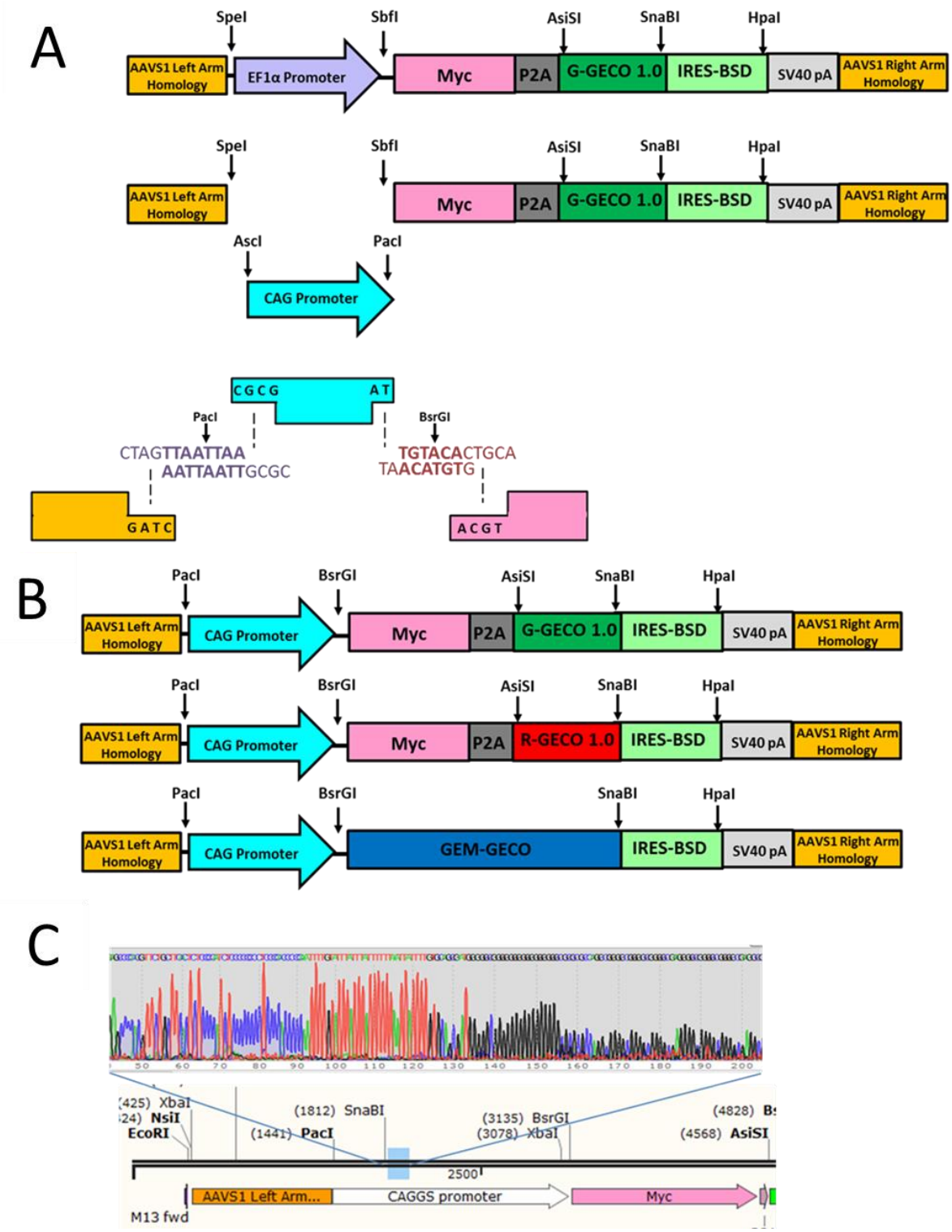


Figure 3.15. Ligation of non-compatible ends with small phosphorylated linkers to clone CAG promoter into targeting constructs.

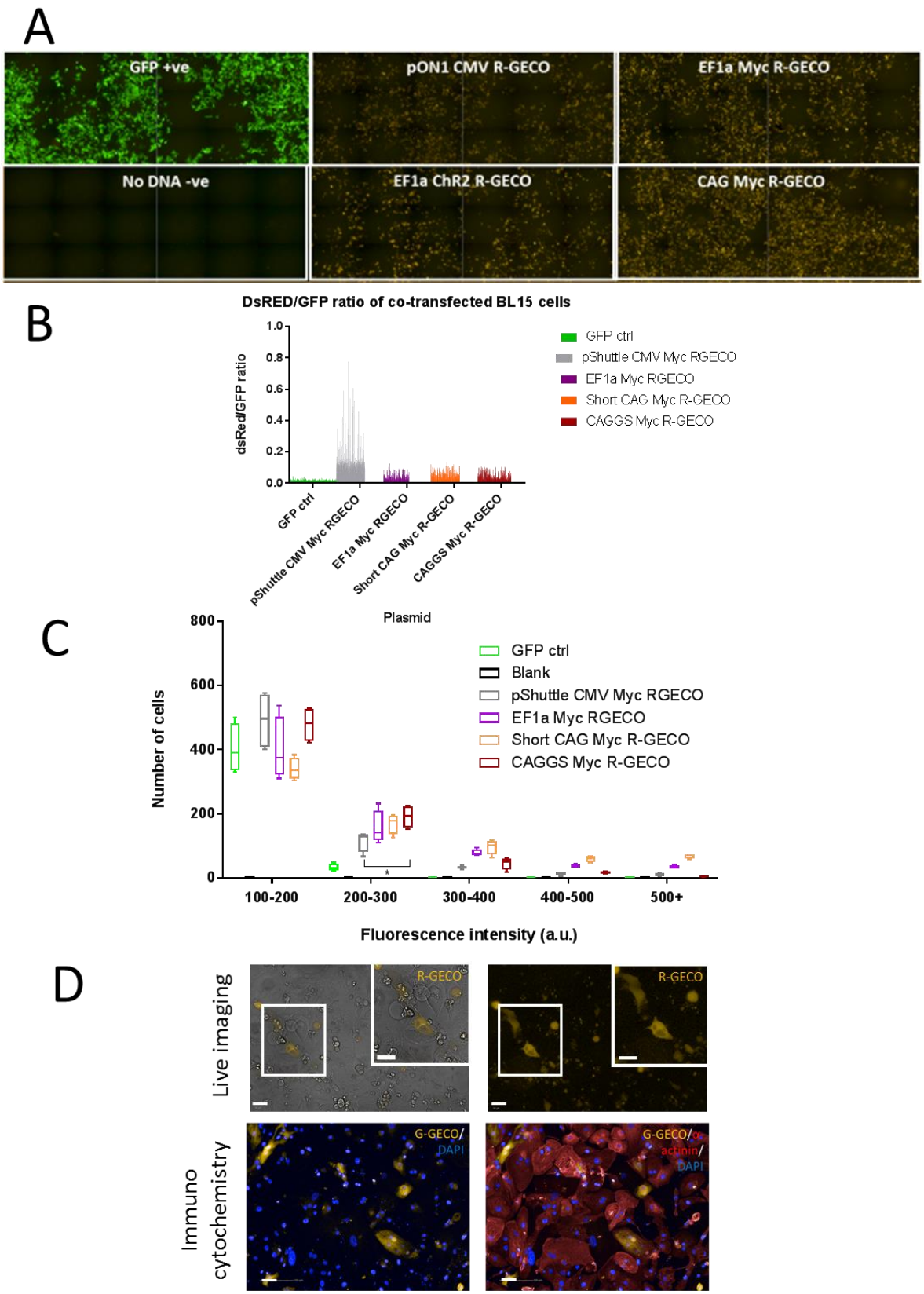
(A) *AAVS1* EF1α targeting constructs were used as a basis for the *AAVS1* CAG targeting constructs. Non-compatible sticky ends were ligated together (dashed line) by using 5' phosphorylated linker sequences with unique restriction sites added (bold). **(B)** Three new *AAVS1* CAG targeting plasmids were constructed, to deliver Myc G-GECO1.0, Myc R-GECO1.0 and GEM-GECO to the *AAVS1* locus. **(C)** Sequencing revealed that the CAG promoter was refractory to conventional PCR with restriction site overhangs for cloning due to highly GC-rich regions. Black peaks = guanine, blue peaks = cytosine, red peaks = thymidine, green peaks = adenine.

In an attempt to compare promoter fidelity before undertaking more targeting work, transient transfection of GECO constructs driven by different promoters in 293T BL15 cells was tested. Modified human embryonic kidney 293T were chosen as they are highly amenable to transfection. Comparisons between R-GECO driven by CMV; EF1α; intronless CAG and CAGGS (containing first intron of chicken beta-actin gene), were made (**Figure 3.16A**). Co-transfection of each plasmid with a control GFP plasmid was performed to account for untransfected cells. The theory was that if a cell was transfected with the GFP plasmid, it should also uptake the R-GECO plasmid. The ratio of R-GECO to GFP signal was calculated using high content image analysis, and single cell results were plotted (**Figure 3.16B**).

These results seemed to show that the CMV-driven construct gave the highest ratio and therefore the greatest R-GECO expression intensity. However, re-analysing this same data and data binning to assess fluorescence intensity showed a significant increase (*$p < 0.05$) in the number of fluorescent cells in the 200 – 300 a.u. bracket with the CAGGS construct compared to the CMV construct (**Figure 3.16C**). This suggests that the higher R-GECO/GFP ratio for the CMV promoter may have been due to low intensity GFP signal rather than high intensity R-GECO signal. Indeed, images stitched together to give a well overview seem to show greater R-GECO intensity in CAG compared to CMV (**Figure 3.16A**). Given that the CAGGS promoter containing the intron performed well from 100 – 300 a.u. fluorescence, CAGGS-MYC-RGECO-IRES-BSD and CAGGS-MYC-GGECO-IRES-BSD were validated in cardiomyocytes. Transient transfection into REBL PAT hiPSC-CMs using a lipid-based transfection reagent showed that R-GECO signal could be detected with both live imaging and immunocytochemistry on fixed cells (**Figure 3.16D**). For the sake of simplicity, CAGGS retaining the intron will continue to be referred to as CAG.

Figure 3.16. Transient transfection of 293T BL15 cells to compare promoter efficiencies.

(A) Well overview image of 293T BL15 cells transiently transfected with R-GECO constructs being driven by different promoters. **(B)** Each construct was co-transfected with GFP to account for differential transfection efficiency between constructs. Single cell results for the ratio between R-GECO signal (dsRed) and control plasmid (GFP) show the highest ratio with the CMV-driven construct. ($n \geq 436$ cells). **(C)** Fluorescence intensity comparison between constructs driven by different constitutive promoters. Data was binned into intervals of 100 arbitrary units (a.u.) of fluorescence. Significantly more cells expressed R-GECO in the 100-200 a.u. range when the CAGGS promoter was used to drive expression rather than the CMV promoter. At higher fluorescence intensities, the intron-free short CAG performed gave more expressing cells. Two-way ANOVA with Tukey's multiple comparison test, * $p < 0.05$. **(D)** Live imaging R-GECO in REBL PAT hiPSC-CMs and immunocytochemistry on fixed REBL PAT hiPSC-CMs transiently transfected with CAGGS Myc R/G-GECO to validate the function of the construct in the desired cell type. Scale bar = 50 µm.


A
GFP +ve
pON1 CMV R-GECO
EF1a Myc R-GECO
No DNA -ve
EF1a ChR2 R-GECO
CAG Myc R-GECO
B
DsRED/GFP ratio of co-transfected BL15 cells
dsRed/GFP ratio
1.0
0.8
0.6
0.4
0.2
0.0
GFP ctrl
pShuttle CMV Myc RGECO
EF1a Myc RGECO
Short CAG Myc R-GECO
CAGGS Myc R-GECO
C
Plasmid
Number of cells
800
600
400
200
0
GFP ctrl
Blank
pShuttle CMV Myc RGECO
EF1a Myc RGECO
Short CAG Myc R-GECO
CAGGS Myc R-GECO
100-200
200-300
300-400
400-500
500+
Fluorescence intensity (a.u.)
D
Live imaging
R-GECO
R-GECO
Immuno cytochemistry
G-GECO/ DAPI
G-GECO/ α actinin/ DAPI

Despite the detection of R-GECO protein in transiently transfected cardiomyocytes, there were still concerns about whether or not the *AAVS1* CAG Myc GECO constructs would work with only single/double copy number in targeted CMs. In a parallel project, colleagues discovered that the *AAVS1*-CAG-ChR2-P2A-NpHR-T2A-BSD parent construct was non-functional in targeted CMs. These targeted clones were assessed by Western blot to visualise protein expression. Surprisingly, it seemed as though the P2A cleavage peptide had failed to cleave between the ~30 kDa ChR2 and NpHR genes, resulting in a fusion protein of ~60 kDa (**Figure 3.17A**).

Given that the Myc gene in the GECO targeting constructs was largely redundant, and wary of the apparently flawed P2A sequence, the Myc-P2A section was removed from the R-GECO construct (**Figure 3.17B**). In addition, the blasticidin selection cassette was replaced by puromycin. This was achieved by restriction enzyme digest of the modular components of the targeting cassette, and ligation of compatible ends. In order to ensure robust expression from R-GECO1.0, the non-compatible BsrGI and AsiSI sites were ligated together with 5'-phosphorylated linker sequences, containing the Kozak consensus sequence for efficient initiation of the translation process (**Figure 3.17B**). The resulting *AAVS1*-CAG-GEMGECO-IRES-PURO and *AAVS1*-CAG-RGECO-IRES-PURO constructs were then used for all downstream targeting applications (**Figure 3.17C**).

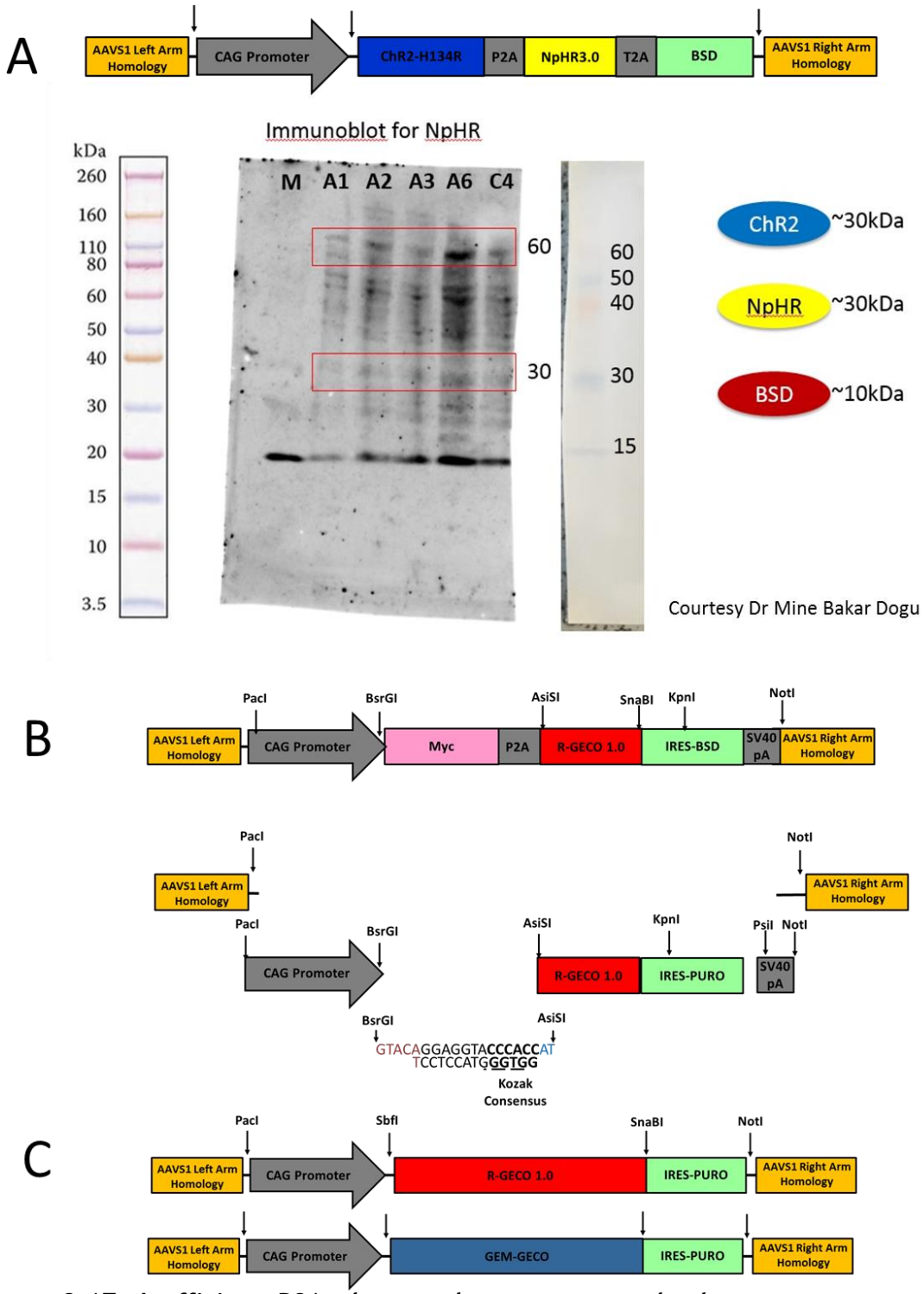


Figure 3.17. Inefficient P2A cleavage between genes leads to poor expression in CRISPR/Cas9 targeted clones.

(A) Western blot for targeted clones made using the parent ChR2-P2A-NpHR-T2A construct used to generate GECO constructs. Inefficient cleavage between ChR2 (30 kDa) and NpHR3.0 (30 kDa) leads to a fused protein (60 kDa) that is non-functional. This inefficient cleavage also leads to poor fluorescence expression in Myc-P2A-GECO targeted clones. (Courtesy Dr Mine Bakar Dogu). **(B)** Schematic showing the replacement of the Myc-P2A sequence with a kozak consensus sequence by restriction enzyme digest and complementary 5'-phospho-linker oligonucleotide sequences. The selection cassette was also swapped from BSD to Puro **(C)** Final CAG-driven AAVS1 targeting constructs used for generation of GECO-expressing cell lines.

3.3.5 Generating isogenic sets of cell lines harbouring sarcomeric gene mutations

To apply GECIs and use them as tools in the context of hiPSC-derived cardiomyocytes, we focused on hiPSC resources with cardiac mutations of interest generated by Dr Diogo Mosqueira and Dr James Smith.

One mutation of interest was a resource developed by Dr Diogo Mosqueira, whereby the *MYH7* C9123T mutation was introduced to the REBL PAT hiPSC line. This SNP results in an Arg453Cys substitution in the sarcomeric protein beta myosin heavy chain (β-MHC) (**Figure 3.18A**). Mutation of this protein is also known to lead to HCM. The *MYH7* locus was edited using a CRISPR/Cas9 nickase approach, with the selection cassette being inserted adjacent to exon 14. The cassette was then removed using FLP/FRT recombination (**Figure 3.18B**). As well as introducing the C9123T mutation, successful editing also mutated the upstream PAM site, resulting in an XhoI restriction site being introduced. This was exploited to perform an allele-specific screen for heterozygous or homozygous *MYH7* mutation (**Figure 3.18C**). In contrast to the 'shortcut' editing method mentioned previously, clones had to be screened for the mutation before the cassette was removed by FLP/FRT recombination. Using primers outside of the 2.2 kb cassette, it is clear to see the presence (2.8 kb) or absence (0.6 kb) of the cassette after Flippase treatment (**Figure 3.18D**). Primers within the cassette fail to give a product after successful excision of the cassette (**Figure 3.18D**). These editing experiments made an isogenic trio of wild-type, heterozygous and homozygous mutant hiPSC lines available for targeting with GECIs to study the *MYH7* C9123T mutation in hiPSC-CMs.

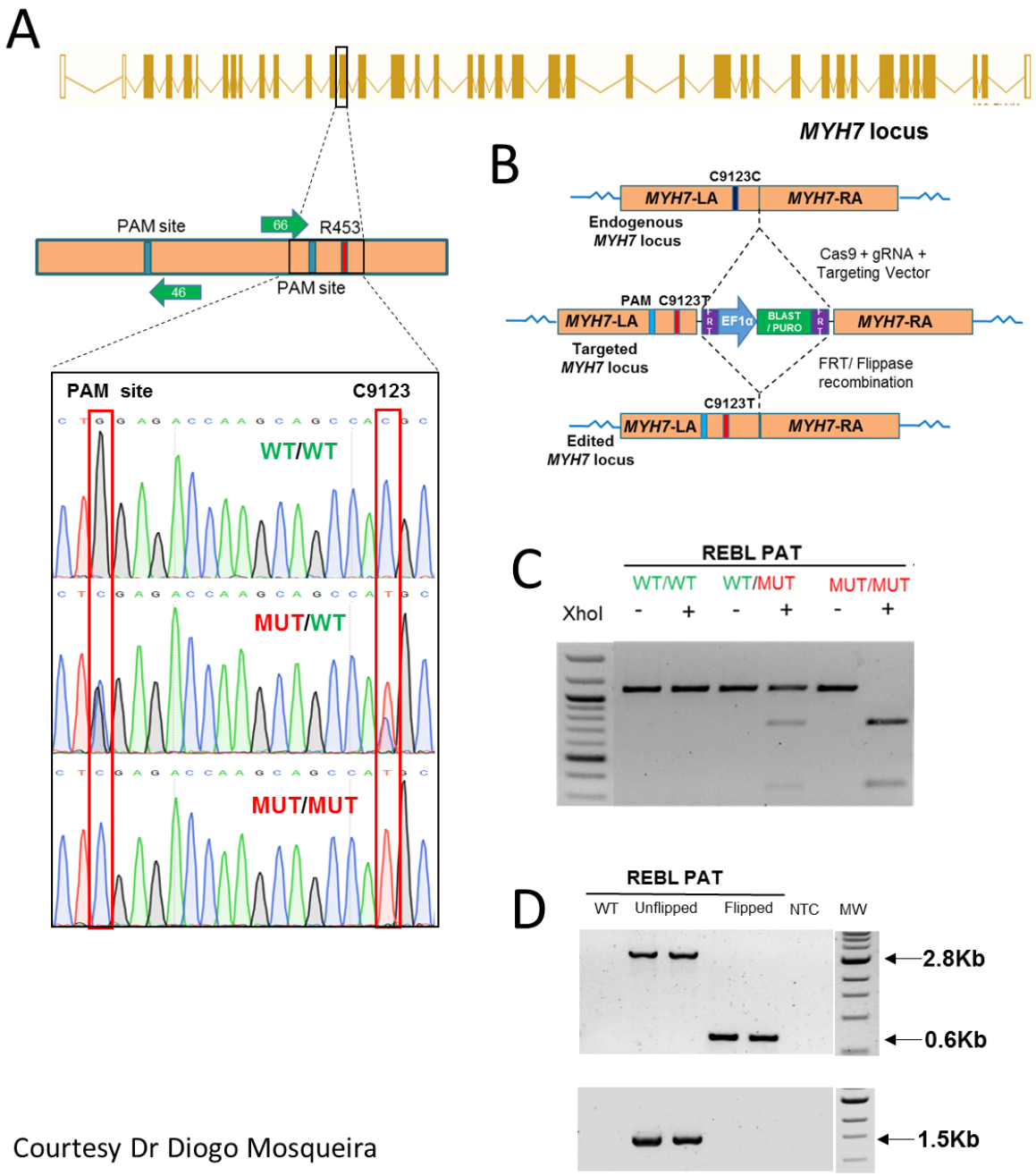


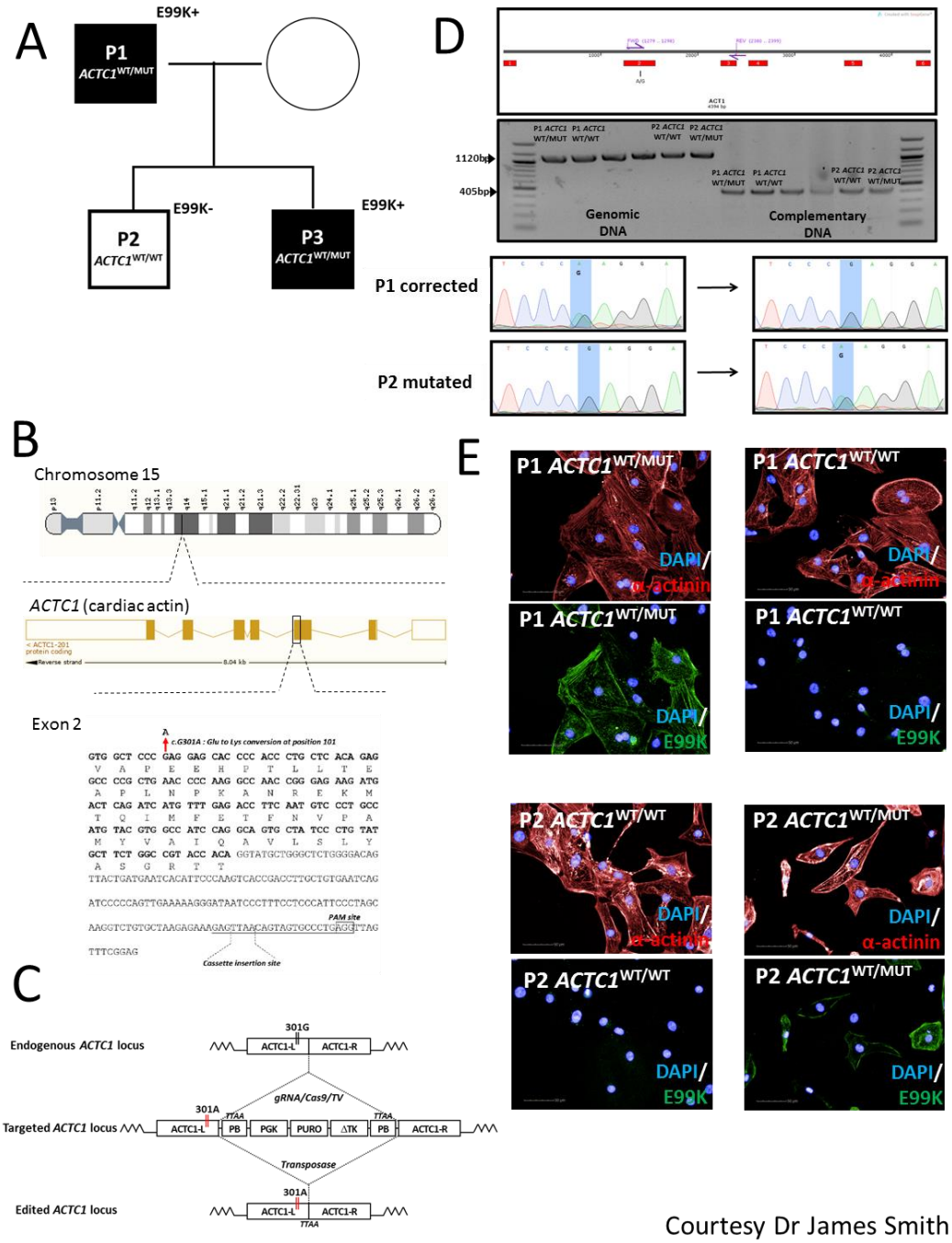
Figure 3.18. CRISPR/Cas9 editing of REBL PAT hiPSCs to generate an isogenic trio of *MYH7* C9123T hiPSCs for disease modelling hypertrophic cardiomyopathy *in vitro*.

(A) Location of C1923T mutation within exon 14 of the *MYH7* locus. Nucleotide 9123 is mutated from C to C/T in the heterozygote and C to T in the homozygote. This results in an Arg453Cys (R453C) substitution in β-MHC. Upstream PAM site is also mutated G to C. **(B)** Schematic showing the approach used for CRISPR/Cas9 gene editing of *MYH7*. The locus is targeted and a SNP occurs in the desired location. The selection cassette is then removed by FRT/Flippase recombination. L/RA – left/right homology arm. **(C)** XhoI digestion of *MYH7* RT-PCR product demonstrating allele-specific expression of mutant *MYH7*. The XhoI site is introduced upon successful mutation of the PAM site. Undigested DNA is used as the negative control. **(D)** PCR genotyping of positive clones before and after flippase-mediated cassette excision. A 2.8kb product is formed if the cassette is still present, a 0.6kb product is formed once the cassette has been excised (top panel). PCR primers that bind within the cassette give a 1.5kb product if the cassette remains, and no product once the cassette has been removed (bottom panel). MW – Molecular weight marker; NTC- non template control.

The second resource of interest was a family harbouring a mutation in the cardiac actin gene, *ACTC1*. Specifically, a G to A base pair change (G301A) causes an amino acid substitution of glutamic acid to lysine (E to K; abbreviated to E99K) in this sarcomeric protein, resulting in a condition known as hypertrophic cardiomyopathy (HCM). The family comprised a father with the mutation (P1-*ACTC1*$^{WT/MUT}$) and two sons, one with (P2-*ACTC1*$^{WT/MUT}$) and one without (P3-*ACTC1*$^{WT/WT}$) the mutation. (**Figure 3.19A**). Dr James Smith was able to successfully derive iPSCs from skin-punch biopsies from these patients.

Single guide RNAs were designed to target this specific region of exon 2 of *ACTC1*, in order to either correct (P1 and P2) or introduce (P3) the mutation to the patient-derived iPSCs (**Figure 3.19B**). The strategy employed was a novel, footprint-free, 'shortcut' method of CRISPR/Cas9 gene editing (Kondrashov et al., 2018). The *ACTC1* gene was edited using sgRNAs, Cas9 and a targeting vector, and edited clones enriched by puromycin selection contained in the cassette. Subsequently endogenous TTAA sites were employed to enable a PiggyBac transposon to excise the selection cassette in a footprint-free manner (**Figure 3.19B, C**). Any clones that retained the cassette were destroyed by negative selection using thymidine kinase to process the cytotoxic drug ganciclovir (**Figure 3.19C**). Clones were genotyped by PCR and RT-PCR using isolated genomic and complementary DNA, respectively, and Sanger sequencing confirmed the presence of the mutation with a 'double peak' in the chromatogram (**Figure 3.19D**). Due to RNA splicing, the cDNA gave a smaller PCR product of 405 bp, compared to 1120 bp for the gDNA (**Figure 3.19D**).

These clones were successfully differentiated to cardiomyocytes, as evidenced by α-actinin staining (**Figure 3.19E**). In conjunction, these sets of cardiomyocytes were stained with a custom α-cardiac actin E99K antibody, showing the correction of P1 *ACTC1*$^{WT/MUT}$ to P1 *ACTC1*$^{WT/WT}$, and the introduction of the mutation to P2 *ACTC1*$^{WT/WT}$ to produce P2 *ACTC1*$^{WT/MUT}$ (**Figure 3.19E**). In this way, two isogenic pairs of hiPSCs could be used to study the *ACTC1* G301A mutation by targeting them with GECIs.



Courtesy Dr James Smith

Figure 3.19. Footprint-free CRISPR/Cas9 editing of patient-derived *ACTC1* G301A hiPSCs to generate isogenic pairs of HCM disease models *in vitro*.

(A) Family tree of the donors used to generate hiPSCs indicating patient initials, age and disease status. **(B)** Chromosomal location of *ACTC1* gene and location of the G301A mutation within exon 2 of *ACTC1*. **(C)** Schematic illustrating the use of an endogenous TTAA site and the PiggyBac (PB) transposon system to introduce the G301A mutation to a healthy donor. Upon transposase treatment the selection cassette is removed, leaving the desired mutation and no footprint. TV – targeting vector; PGK – phosphoglycerate kinase promoter; ΔTK – thymidine kinase. **(D)** PCR and RT-PCR on gene edited isogenic hiPSC pairs with primers spanning exons 2-3. Genomic DNA (gDNA) gives an 1120bp product whereas complementary DNA (cDNA) gives a 405bp product. These samples were sequenced to prove the introduction or removal of the E99K mutation. A double peak of G/A indicates a heterozygous G301A mutation. **(E)** Immunocytochemistry on differentiated isogenic pairs of *ACTC1* G301A hiPSC-CMs for the cardiac marker α-actinin (red) and the E99K mutant α-cardiac actin protein (green).

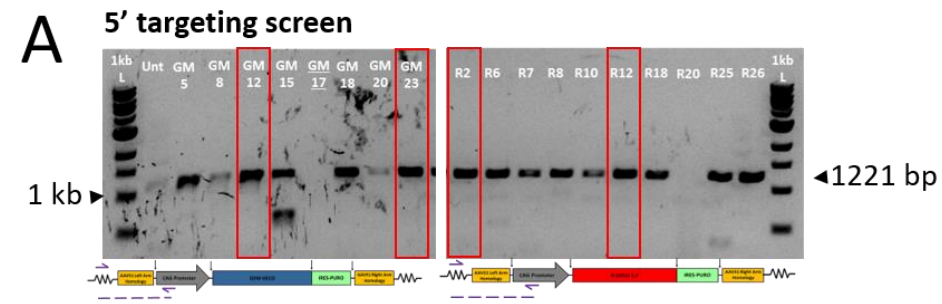
3.3.6 Targeting and genotyping isogenic sets of clones

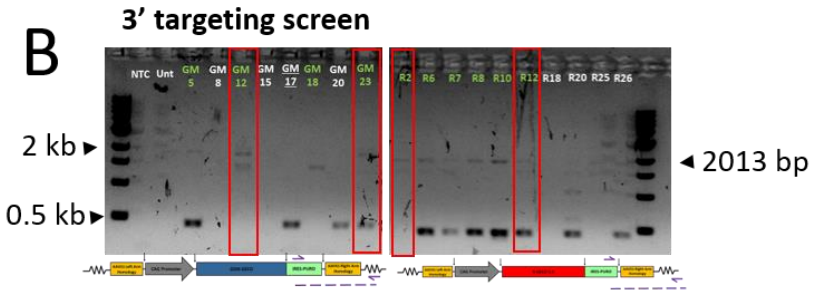
As PCR genotyping experiments progressed for multiple isogenic lines, a more efficient and high-throughput approach was required. Rather than using column extraction to isolate gDNA from each clone individually, DirectPCR Lysis™ was used. In this way, harvested cells could be lysed and immediately used in PCR genotyping reactions. This improved throughput and efficiency at the expense of producing 'clean' gels without ladder-like artefact.

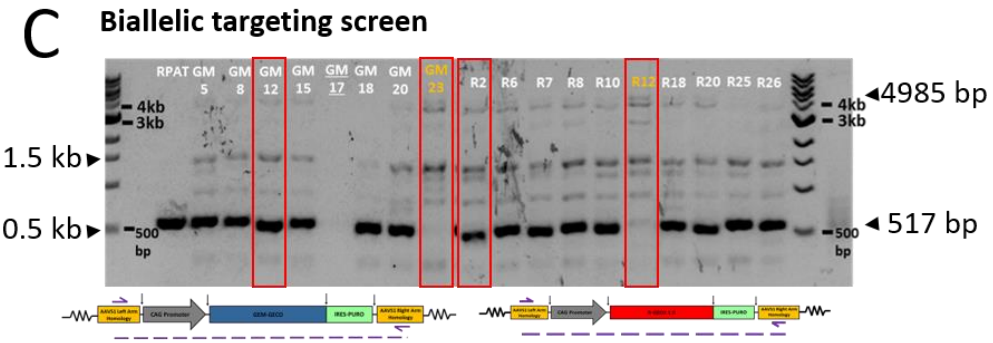
To screen for GEM-GECO or R-GECO cassette insertion at the *AAVS1* locus, primers spanning the endogenous genome into the 5' (**Figure 3.20A**) and 3' (**Figure 3.20B**) side of the cassette were used in PCR screens on cell lysate. These cell lysates were also used to perform a biallelic PCR screen with primers spanning the inserted cassette. Homozygous targeted clones failed to give a 517bp product and, in some cases, produced the higher 4985bp product (**Figure 3.20C**). The selected heterozygous clones GM12 and R2 were expanded and banked, as were the homozygous clones GM23 and R12. A biallelic targeting efficiency of 4.1% was achieved for GEM-GECO, and an efficiency of 3.57% was achieved for R-GECO (**Figure 3.20D**). RT-PCR on these four selected hiPSC clones was carried out to confirm RNA expression of the appropriate GECO (**Figure 3.20E**). The previously created EF1α cell lines acted as a positive control.

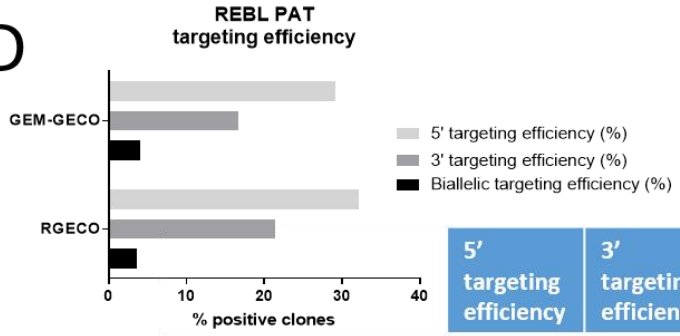
Figure 3.20. PCR genotyping of healthy REBL PAT R-GECO and REBL PAT GEM-GECO clones.

(A) 5' targeting screen on colony lysates with primers from outside the *AAVS1* left arm of homology (endogenous *AAVS1*) to the CAG promoter. Positive targeting is indicated with a 1221bp product. **(B)** 3' targeting screen on colony lysates with primers spanning the IRES-Puro cassette to outside the *AAVS1* right arm of homology (endogenous *AAVS1*). Positive targeting is indicated with a 2013bp product. **(C)** Biallelic targeting screen on colony lysates using primers spanning the entire cassette. Homozygous clones will give a 4985bp product or PCR failure. Heterozygous or negative clones will give a 517 bp product. Red boxes indicate selected clones for expansion and banking. GM# – REBL PAT AAVS1 GEM GECO clone number; R# - REBL PAT *AAVS1* RGECO clone number. **(D)** Targeting efficiencies for both lines including incidence of biallelic targeting events. **(E)** RT-PCR on hiPSC cDNA to confirm expression of GEM-GECO/R-GECO in selected heterozygous and homozygous CAG-GECO clones. RT-PCR product identities were confirmed by Sanger sequencing.

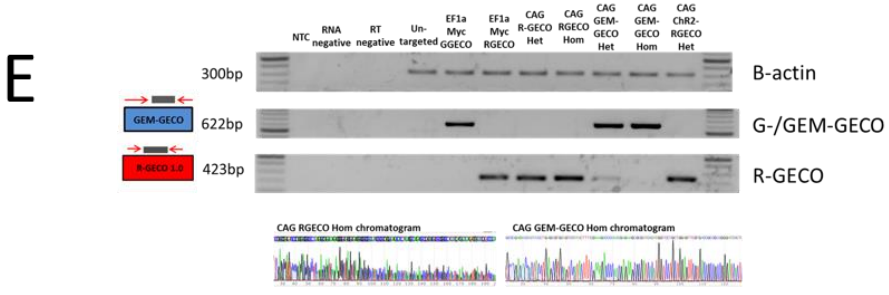




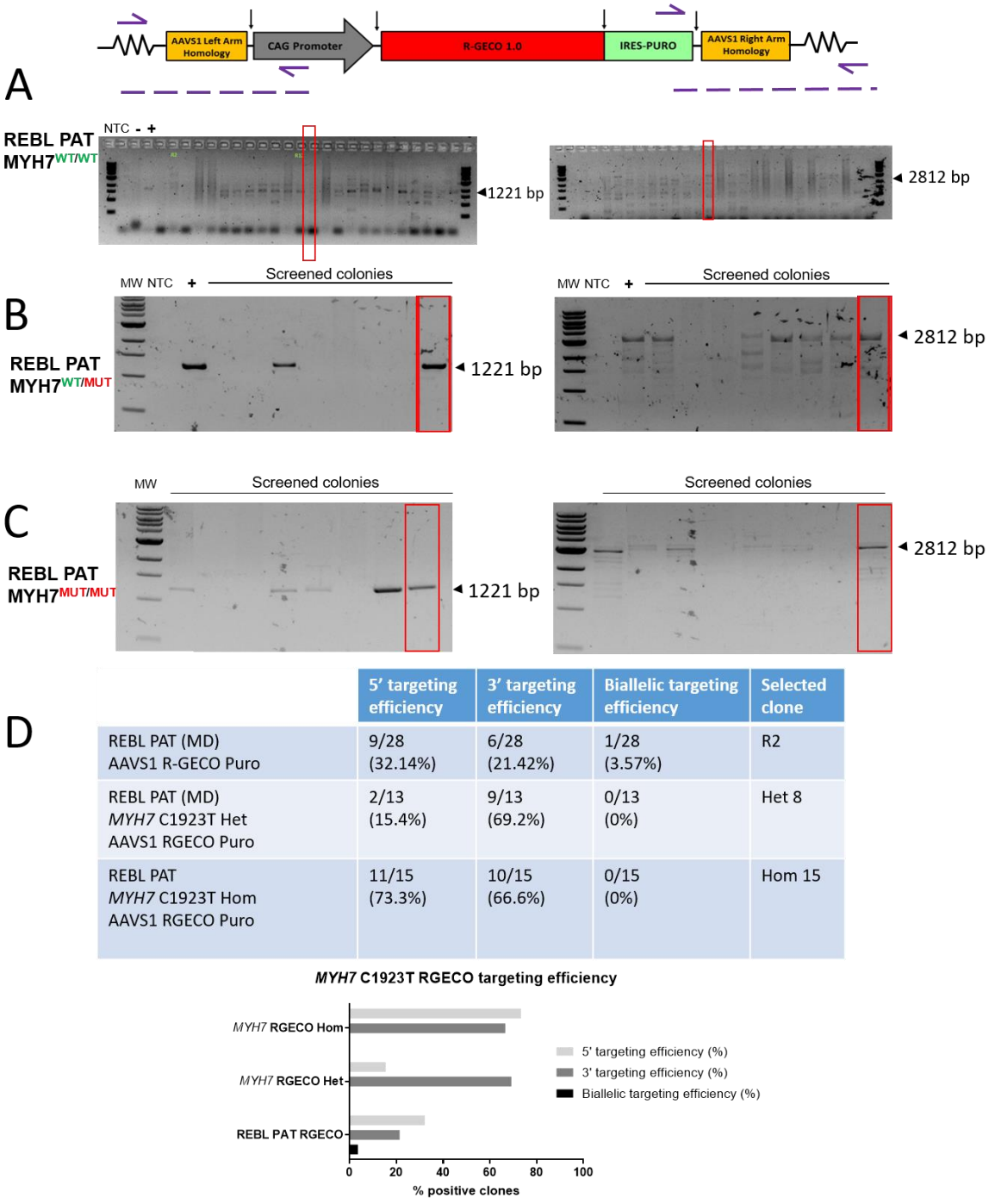




	5' targeting efficiency	3' targeting efficiency	Biallelic targeting efficiency	Selected Het clone	Selected Hom clone
REBL PAT AAVS1 GEM-GECO Puro	7/24 (29.16%)	4/24 (16.66%)	1/24 (4.1%)	GM12	GM23
REBL PAT AAVS1 R-GECO Puro	9/28 (32.14%)	6/28 (21.42%)	1/28 (3.57%)	R2	R12



To screen for *AAVS1* targeting in the *MYH7* C9123T isogenic set, PCR genotyping was again utilised (**Figure 3.21**). The R2 and R12 clones from the previous wild-type REBL PAT R-GECO targeting events were used as the healthy isogenic control for the REBL PAT *MYH7* C9123T isogenic set (**Figure 3.21A**). *MYH7* C9123T heterozygote (**Figure 3.21B**) and homozygote (**Figure 3.21C**) clones were also screened for R-GECO insertion. No biallelic targeting events were found in the targeting of the mutant lines. A high efficiency of, albeit monoallelic, targeting was achieved with the *MYH7* C9123T Homozygous line (66.6%) (**Figure 3.21D**), and positively targeted RGECO clones were frozen. The selected clones, Het 8 and Hom 15 were expanded and banked.

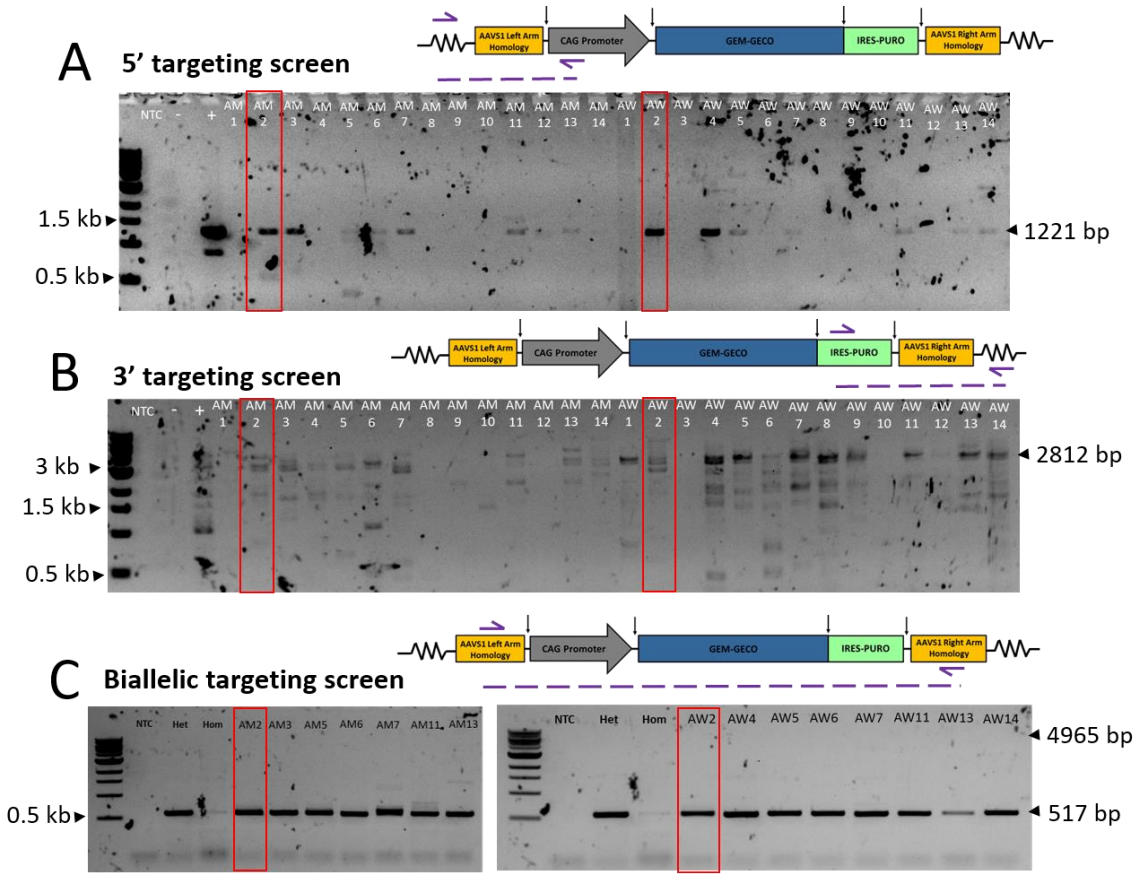


	5' targeting efficiency	3' targeting efficiency	Biallelic targeting efficiency	Selected clone
REBL PAT (MD) AAVS1 R-GECO Puro	9/28 (32.14%)	6/28 (21.42%)	1/28 (3.57%)	R2
REBL PAT (MD) *MYH7* C1923T Het AAVS1 RGECO Puro	2/13 (15.4%)	9/13 (69.2%)	0/13 (0%)	Het 8
REBL PAT *MYH7* C1923T Hom AAVS1 RGECO Puro	11/15 (73.3%)	10/15 (66.6%)	0/15 (0%)	Hom 15

Figure 3.21. PCR genotyping of isogenic *MYH7* C9123T R-GECO clones.

(A-C) 5' targeting PCR screens (left panels), and 3' targeting PCR screens on healthy, *MYH7* C9123T heterozygous and homozygous clones. Positive 5' targeting is indicated with a 1221bp product. Positive 3' targeting is indicated with a 2812bp product. Red boxes indicated selected clones. Note: *MYH7* C9123T mutation was introduced into the REBL PAT background, so existing REBL PAT RGECO clones served as healthy controls for this isogenic set. **(D)** Targeting efficiencies for all three isogenic lines.

The ratiometric GEM-GECO indicator was targeted to the isogenic duo of P2 *ACTC1* G301A hiPSCs and genotyping was performed in the same way as the REBL PAT and *MYH7* C9123T sets (**Figure 3.22A-C**). Again, no biallelic targeting events were discovered, but the targeting efficiency was 50% for the P2 *ACTC1*$^{WT/WT}$ clones and 57.14% for the P2 *ACTC1*$^{WT/MUT}$ clones (**Figure 3.22D**). The P2 *ACTC1*$^{WT/WT}$ clone AW2, and P2 *ACTC1*$^{WT/MUT}$ clone AM2, were expanded and banked for downstream experiments.



D

	5' targeting efficiency	3' targeting efficiency	Biallelic targeting efficiency	Selected clone
P2 *ACTC1*$^{WT/WT}$ AW AAVS1 GEM-GECO	7/14 (50%)	11/14 (78.57%)	0/14 (0%)	AW 2
P2 *ACTC1*$^{WT/MUT}$ AM AAVS1 GEM-GECO	8/14 (57.14%)	9/14 (64.28%)	0/14 (0%)	AM 2

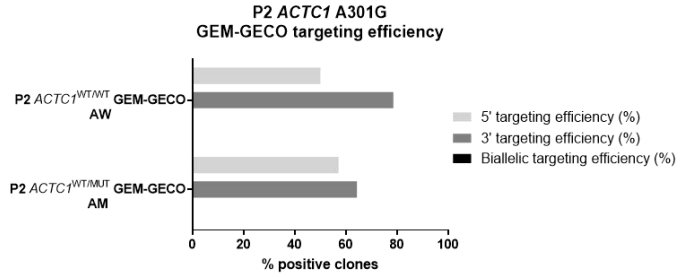


Figure 3.22. PCR genotyping of isogenic P2 *ACTC1* G301A GEM-GECO clones.

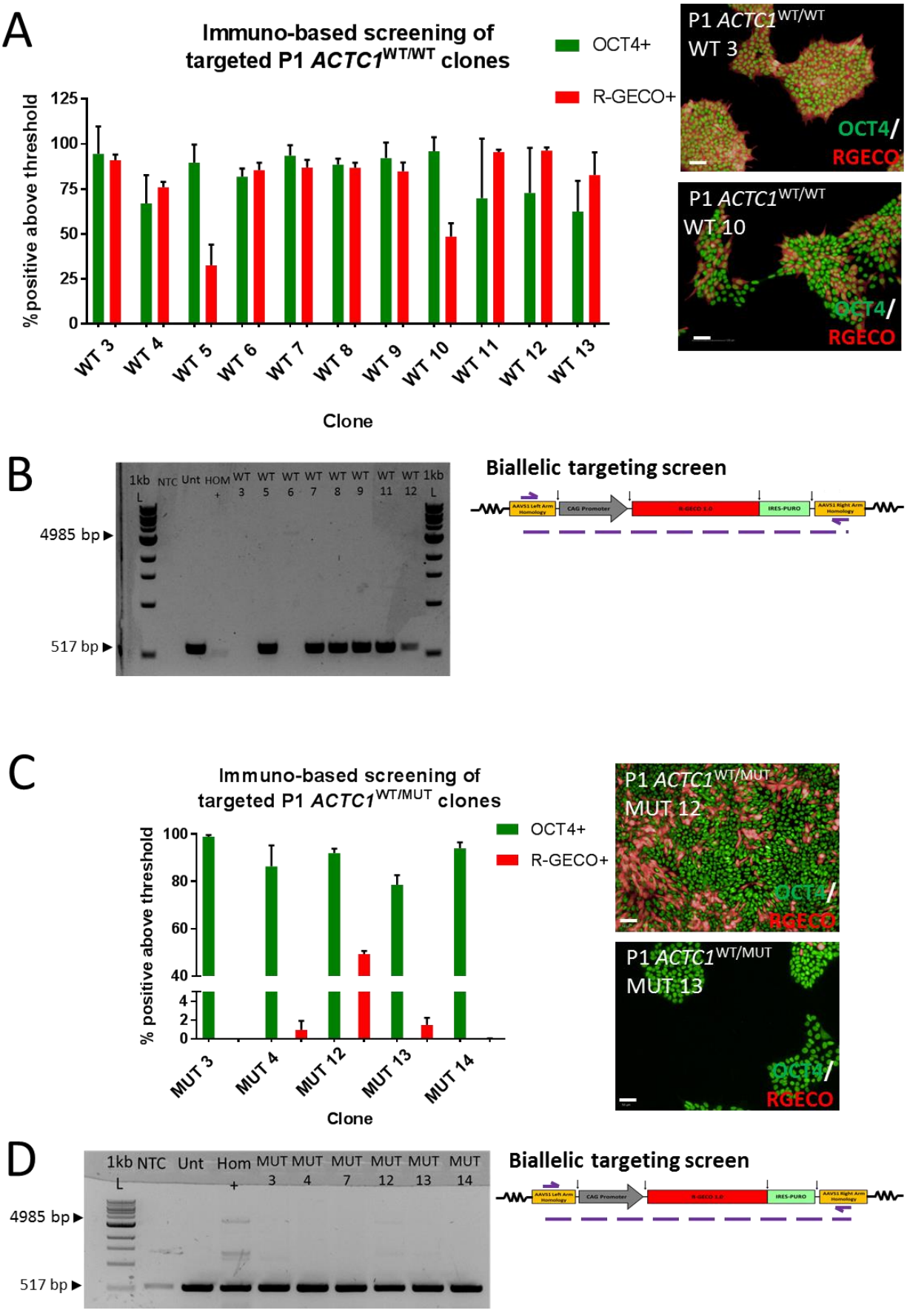
(A) 5' targeting screen on colony lysates with primers from outside the AAVS1 left arm of homology (endogenous *AAVS1*) to the CAG promoter. Positive targeting is indicated with a 1221bp product. **(B)** 3' targeting screen on colony lysates with primers spanning the IRES-Puro cassette to outside the *AAVS1* right arm of homology (endogenous *AAVS1*). Positive targeting is indicated with a 2812 bp product. **(C)** Biallelic targeting screen on colony lysates using primers spanning the entire cassette. Homozygous clones will give a 4965bp product or PCR failure. Heterozygous or negative clones will give a 517 bp product. Red boxes indicate selected clones for expansion and banking. **(D)** Targeting efficiencies for both lines including incidence of biallelic targeting events.

To complement the existing *MYH7* C9123T RGECO isogenic trio, an isogenic set of P1 *ACTC1* G301A RGECO cell lines was sought so that direct comparisons between these two HCM-causing mutations could be made using the same GECI. Rather than using PCR genotyping to identify positively-expressing clones, an immunocytochemistry-based screening method, using an anti-RFP antibody, was developed in an attempt to select clones with the highest R-GECO expression (**Figure 3.23**). A dual-stain screen for OCT4 positive, R-GECO positive hiPSCs pointed to clones with high pluripotency and high expression of the GECI. We hypothesised that clones that were highly pluripotent would be more amenable to cardiac differentiation, and that clones with high expression of R-GECO would retain that expression level as hiPSC-CMs. Using high content image analysis, P1 *ACTC1*$^{WT/WT}$ clone WT3 was found to be 94.53% OCT4 positive and 91.06% R-GECO positive, in contrast to clone P1 *ACTC1*$^{WT/WT}$ clone WT10 which was 96.04% OCT4 positive and 48.59% R-GECO positive (**Figure 3.23A**).

A biallelic targeting screen using PCR primers spanning the cassette suggested that both P1 *ACTC1*$^{WT/WT}$ clones WT3 and WT10 were homozygous for R-GECO at the *AAVS1* locus (**Figure 3.23B**). The P1 *ACTC1*$^{WT/MUT}$ clones were less successful, with fewer clones surviving until the screen and lower R-GECO expression levels. The strongest clone in terms of R-GECO expression was P1 *ACTC1*$^{WT/MUT}$ clone MUT12 with 49.37% of cells giving a positive signal (**Figure 3.23C**). Pluripotency, however, remained high at 91.93% of hiPSCs being OCT4 positive. Given these results it was unsurprising that no biallelic targeting events were found (**Figure 3.23D**). Nevertheless, both P1 *ACTC1*$^{WT/WT}$ clone WT3 and P1 *ACTC1*$^{WT/MUT}$ clone MUT12 were selected for further expansion, banking and downstream applications.

Figure 3.23. Immunocytochemistry-based screening for targeted isogenic P1 *ACTC1* G301A hiPSCs.

(A) P1 *ACTC1*$^{WT/WT}$ hiPSC clones dual-stained for OCT4 (green) and R-GECO (red) to find the highest R-GECO-expressing clone. P1 *ACTC1*$^{WT/WT}$ clone WT3 had the highest percentage of pluripotent (94.53% OCT4+) and R-GECO (91.06% ±1.73%) hiPSCs. Mean ±SD, n = 3 wells. Scale bars = 50 µm. **(B)** Biallelic targeting PCR screen on isolated gDNA showing homozygous clones failure to generate the 517bp PCR product. **(C)** P1 *ACTC1*$^{WT/MUT}$ clones dual stained for OCT4 (green) and R-GECO (red) to find the highest R-GECO-expressing clone. P1 *ACTC1*$^{WT/MUT}$ clone MUT 12 clone had the highest expression of R-GECO (49.37% ±1.33%). Mean ±SD, n = 3 wells. Scale bars = 50 µm. **(D)** Biallelic targeting PCR screen showing that all P1 *ACTC1*$^{WT/MUT}$ clones tested gave a 517bp product and were therefore heterozygous for *AAVS1* targeting.


A
Immuno-based screening of targeted P1 ACTC1WT/WT clones
OCT4+
R-GECO+
% positive above threshold
125
100
75
50
25
0
WT 3
WT 4
WT 5
WT 6
WT 7
WT 8
WT 9
WT 10
WT 11
WT 12
WT 13
Clone
P1 ACTC1WT/WT
WT 3
OCT4/
RGECO
P1 ACTC1WT/WT
WT 10
OCT4/
RGECO
B
1kb L
NTC
Unt
HOM +
WT 3
WT 5
WT 6
WT 7
WT 8
WT 9
WT 11
WT 12
1kb L
4985 bp
517 bp
Biallelic targeting screen
AAVS1 Left Arm Homology
CAG Promoter
R-GECO 1.0
IRES-PURO
AAVS1 Right Arm Homology
C
Immuno-based screening of targeted P1 ACTC1WT/MUT clones
OCT4+
R-GECO+
% positive above threshold
100
80
60
40
4
2
0
MUT 3
MUT 4
MUT 12
MUT 13
MUT 14
Clone
P1 ACTC1WT/MUT
MUT 12
OCT4/
RGECO
P1 ACTC1WT/MUT
MUT 13
OCT4/
RGECO
D
1kb L
NTC
Unt
Hom +
MUT 3
MUT 4
MUT 7
MUT 12
MUT 13
MUT 14
4985 bp
517 bp
Biallelic targeting screen
AAVS1 Left Arm Homology
CAG Promoter
R-GECO 1.0
IRES-PURO
AAVS1 Right Arm Homology

3.3.7 Refinement of clone selection for robust GECI expression

Upon differentiation of the REBL PAT *MYH7* C9123T RGECO isogenic set, it was discovered that the healthy control, *MYH7*$^{WT/WT}$ R2, which was heterozygous for RGECO at the *AAVS1* locus, was challenging to differentiate. In differentiation conditions that were ideal for the vast majority of cell lines, the *MYH7*$^{WT/WT}$ R2 clone often failed to differentiate or gave a poor cardiomyocyte yield. This was investigated by staining for the cardiac marker α-actinin (**Figure 3.24**). In a parallel differentiation of multiple lines, the *MYH7*$^{WT/WT}$ R2 clone produced significantly fewer cardiomyocytes than the *MYH7* C9123T heterozygous and homozygous clones (* p = 0.0304; *** p = 0.0004). Crucially, the *MYH7*$^{WT/WT}$ R2 clone was significantly less efficient at cardiac differentiation compared to the *MYH7*$^{WT/WT}$ R12 clone (** p = 0.0051) (**Figure 3.24**). Although the *MYH7*$^{WT/WT}$ R12 clone was homozygous for R-GECO at the *AAVS1* locus, it was still used as a healthy control to the *MYH7* heterozygous and homozygous clones, which were themselves heterozygous for the GECI.

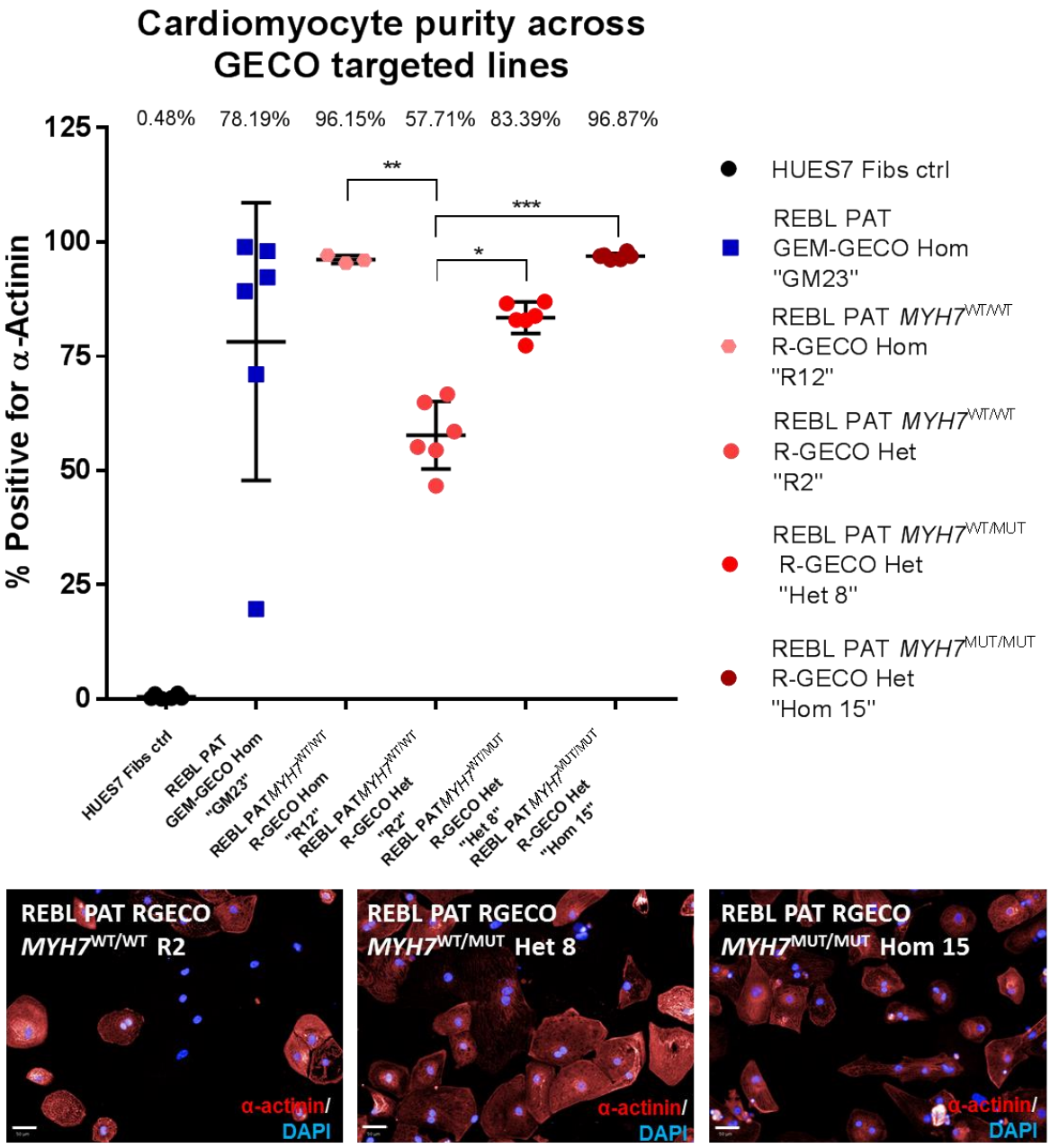


Figure 3.24. Assessing cardiac differentiation efficiency in targeted clones.

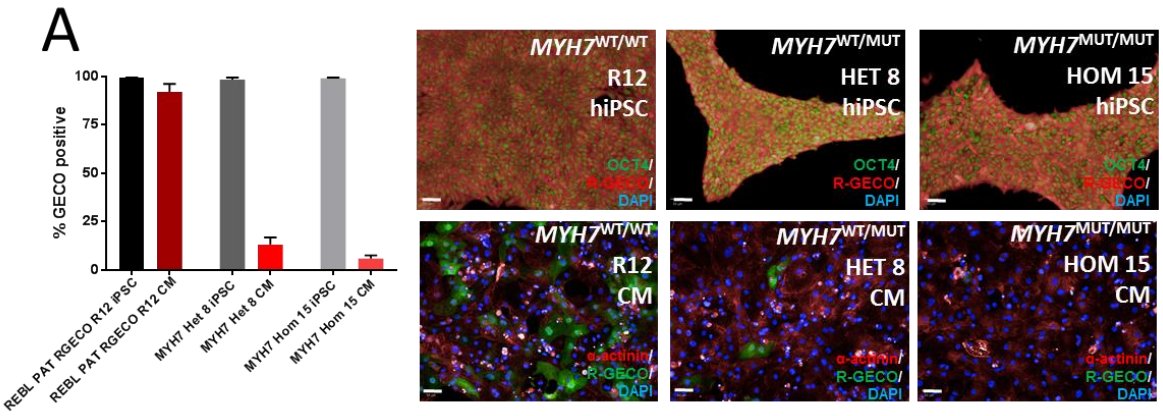
Differentiation efficiencies of targeted clones were assessed by staining for the cardiac marker α-actinin (red). The biallelically targeted REBL PAT *MYH7*$^{WT/WT}$ RGECO R12 clone differentiated to a cardiomyocyte fate at a higher percentage than the monoallelically targeted REBL PAT *MYH7*$^{WT/WT}$ RGECO R2 clone. Mean ±SD, n = 3 wells. One-way ANOVA with Tukey's multiple comparison test, * p = 0.0304; ** p = 0.0051; *** p = 0.0004. Scale bars = 50 μm.

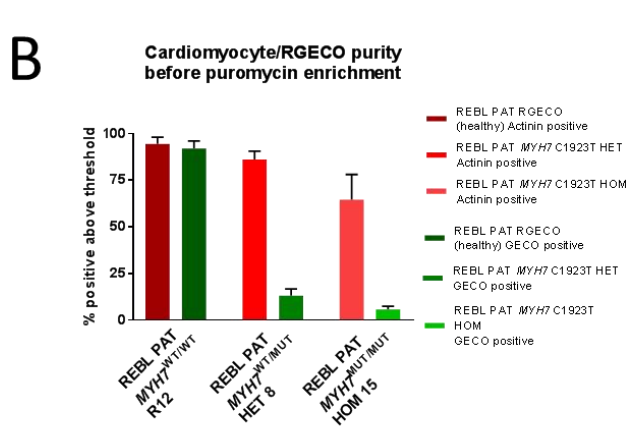
In terms of R-GECO expression, the *MYH7* C9123T trio all displayed above 98% expression as hiPSCs when immunostained for the R-GECO protein (**Figure 3.25A**). However, upon differentiation to cardiomyocytes this dropped to 13.03% in the *MYH7*$^{WT/MUT}$ Het 8 line, and 5.77% in the *MYH7*$^{MUT/MUT}$ Hom 15 line (**Figure 3.25A**). Whilst still useful for downstream assays, this silencing upon differentiation made it tedious to find individual hiPSC-CMs to assay, especially with the *MYH7*$^{MUT/MUT}$ Hom 15 line.

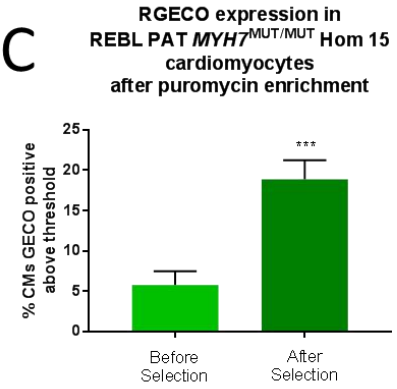
In order to enrich the R-GECO positive hiPSC-CMs, hiPSC culture and differentiation was carried out in 0.3 µg/ml puromycin. It was postulated that *MYH7*$^{MUT/MUT}$ Hom 15 could be a mixed clone and serial passage in antibiotic selection could remedy this. Indeed, before enrichment, *MYH7*$^{MUT/MUT}$ Hom 15 CMs were only 5.77% R-GECO positive (**Figure 3.25B**). This significantly increased to 18.86% GECO positive upon extended puromycin treatment (*** $p = 0.0003$) (**Figure 3.25C**). However, due to the previous high efficiency of *AAVS1* targeting in the *MYH7* C9123T clones, many clones had not yet been differentiated or tested for R-GECO expression. Five clones were expanded and differentiated, of which *MYH7*$^{MUT/MUT}$ Hom 1 (34.78%) and *MYH7*$^{MUT/MUT}$ Hom 2 (93.07%) had significantly higher R-GECO expression than their counterparts (** $p < 0.006$; **** $p < 0.0001$) (**Figure 3.25D**). As such, *MYH7*$^{MUT/MUT}$ Hom 2 replaced *MYH7*$^{MUT/MUT}$ Hom 15 for all subsequent experiments.

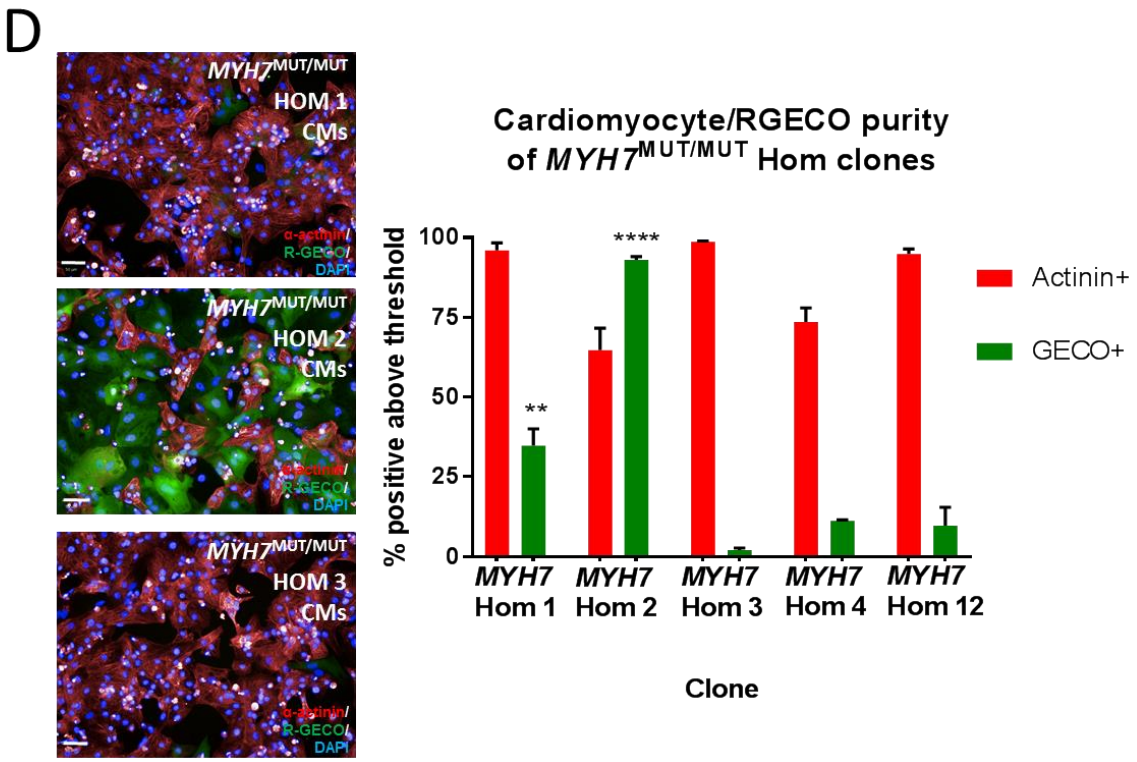
Figure 3.25. Puromycin enrichment of poorly expressing *MYH7* C1923T clones and immunocytochemistry-based selection of robustly expressing clones.

(A) Immunocytochemistry using an antibody to detect R-GECO expression shows a reduction in signal in *MYH7*$^{WT/MUT}$ Het 8 and *MYH7*$^{MUT/MUT}$ Hom 15 clones upon differentiation from hiPSCs to hiPSC-CMs. **(B)** Targeted hiPSC lines show variations in expression of R-GECO protein upon differentiation. Percentage purity data for cardiomyocytes determined by alpha-actinin staining (red), for R-GECO by RFP staining (green). **(C)** R-GECO expression in *MYH7*$^{MUT/MUT}$ Hom 15 cardiomyocytes is significantly improved with three passages of hiPSC cell culture in 0.3 µg/ml puromycin and differentiation carried out in media supplemented with puromycin. Mean ±SD, n = 3 technical replicates. Unpaired t-test, *** p = 0.0003. **(D)** Re-screening *MYH7*$^{MUT/MUT}$ Hom clones using immunocytochemistry on hiPSC-CMs reveals a significant increase in R-GECO expression in the *MYH7*$^{MUT/MUT}$ Hom 2 clone. Mean ±SD, n = 3 technical replicates. One-way ANOVA with Tukey's multiple comparison test, ** p ≤ 0.006; **** p < 0.0001.


A
% GECO positive
100
75
50
25
0
REBL PAT RGECO R12 iPSC
REBL PAT RGECO R12 CM
MYH7 Het 8 iPSC
MYH7 Het 8 CM
MYH7 Hom 15 iPSC
MYH7 Hom 15 CM
MYH7WT/WT R12 hiPSC
MYH7WT/MUT HET 8 hiPSC
MYH7MUT/MUT HOM 15 hiPSC
OCT4/ R-GECO/ DAPI
MYH7WT/WT R12 CM
MYH7WT/MUT HET 8 CM
MYH7MUT/MUT HOM 15 CM
α-actinin/ R-GECO/ DAPI


B
Cardiomyocyte/RGECO purity before puromycin enrichment
% positive above threshold
100
75
50
25
0
REBL PAT MYH7WT/WT R12
REBL PAT MYH7WT/MUT HET 8
REBL PAT MYH7MUT/MUT HOM 15
REBL PAT RGECO (healthy) Actinin positive
REBL PAT MYH7 C1923T HET Actinin positive
REBL PAT MYH7 C1923T HOM Actinin positive
REBL PAT RGECO (healthy) GECO positive
REBL PAT MYH7 C1923T HET GECO positive
REBL PAT MYH7 C1923T HOM GECO positive


C
RGECO expression in REBL PAT MYH7MUT/MUT Hom 15 cardiomyocytes after puromycin enrichment
% CMs GECO positive above threshold
25
20
15
10
5
0
***
Before Selection
After Selection


D
MYH7MUT/MUT HOM 1 CMs
MYH7MUT/MUT HOM 2 CMs
MYH7MUT/MUT HOM 3 CMs
α-actinin/ R-GECO/ DAPI
Cardiomyocyte/RGECO purity of MYH7MUT/MUT Hom clones
% positive above threshold
100
75
50
25
0
**
****
Actinin+
GECO+
MYH7 Hom 1
MYH7 Hom 2
MYH7 Hom 3
MYH7 Hom 4
MYH7 Hom 12
Clone

As a final confirmation of the five selected *AAVS1*-targeted R-GECO HCM lines, a final PCR genotyping screen on extracted hiPSC gDNA was carried out. The 5' screen showed the expected PCR product at 1221bp, which was sequenced and revealed the correct sequence in the junction between the *AAVS1* left arm and the start of the CAG promoter (**Figure 3.26A**). Similarly, all five lines generated the 1186bp product in the 3' targeting screen, with Sanger sequencing chromatograms confirming a clean puromycin-*AAVS1* right arm junction (**Figure 3.26B**). The PCR screens for P1 *ACTC1*$^{WT/WT}$ clone WT3 and P1 *ACTC1*$^{WT/MUT}$ clone MUT12 support the immunocytochemistry-based screening in **Figure 3.23**, by confirming the presence of the cassette within the *AAVS1* locus. All five lines retained R-GECO expression as hiPSC-CMs (**Figure 3.26C**), and could be carried forward to assess calcium flux in healthy and diseased HCM cardiomyocytes *in vitro*.

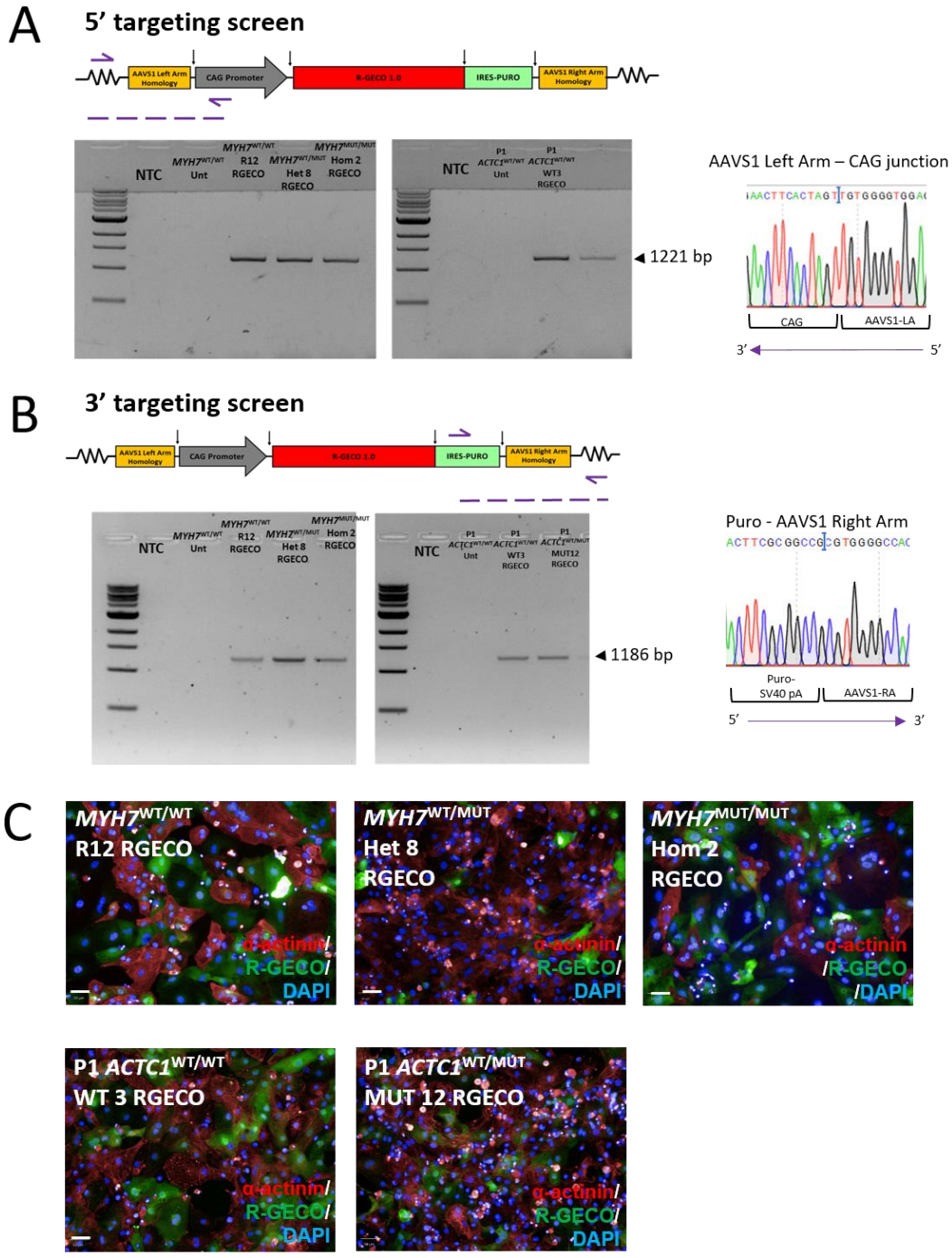


Figure 3.26. Selected R-GECO clones and their expression status.

(A) Confirmatory 5' targeting PCR screen on gDNA isolated from the *MYH7* C1923T RGECO isogenic trio (left) and the *ACTC1* E99K RGECO duo (right). Positive 5' targeting is indicated with a 1221bp product. These products were sequenced to show the junction between the *AAVS1* left arm homology and the start of the CAG promoter. **(B)** Confirmatory 3' targeting PCR screen on gDNA isolated from the *MYH7* C1923T RGECO isogenic trio (left) and the *ACTC1* E99K RGECO duo (right). Positive 3' targeting is indicated with an 1186bp product. Sequencing of PCR products show the junction between the puromycin-SV40 pA sequence and the *AAVS1* right arm homology. **(C)** The five selected R-GECO expressing clones differentiated to hiPSC-CMs and stained for the cardiac marker α-actinin (red) and R-GECO (green). Scale bars = 50 μm.

3.4 Discussion

In this chapter, isogenic sets of hiPSCs have been targeted at the *AAVS1* locus using CRISPR/Cas9. Targeting conditions were optimised to maximise targeting events, and the targeting vectors used to deliver the GECI underwent iterative improvements. These included swapping the promoter from EF1α to CAG and removing the inefficient P2A self-cleaving peptide sequence. Targeted clones were initially found by PCR on genomic DNA, but a direct PCR cell lysis buffer was preferred in later experiments to improve throughput. Taking advantage of the fluorescent protein epitopes of R-GECO, immunocytochemistry was used to screen for hiPSC clones with robust expression. Clone selection was then refined based on R-GECO expression as differentiated hiPSC-CMs. These lines were taken forward to analyse calcium transients in hiPSC-CMs in chapters 4 and 5.

3.4.1 Modular cloning

A variety of modular targeting constructs for introducing GECIs to the *AAVS1* safe harbour locus have been cloned. These plasmids, and the nature of their construction, have allowed for relatively straightforward interchange of different reporter genes within the cassette. PCR amplification with primers containing unique, complementary restriction sites were often employed to achieve this. An alternative cloning method is Gibson assembly, where fragments to be annealed are extended by PCR so that they overlap. An exonuclease then removes 5' ends, allowing sticky ends to be ligated together (Gibson et al., 2009). Gibson assembly offers some advantages to conventional cut-and-paste cloning such as the ability to simultaneously combine up to 5 DNA fragments in a single reaction step, and the ability to perform site-directed mutagenesis (Yonemoto and Weyman, 2017). However, the difficulties encountered trying to PCR amplify the GC-rich CAG promoter, demonstrates that PCR-based methods of cloning are not always ideal.

The CAG promoter proved extremely refractory to PCR, even with the use of specialised GC buffers, or additives known to aid in GC-rich PCRs such as DMSO and betaine (Pratyush et al., 2012). The routine loss of large segments of the CAG promoter during attempts at amplification were likely due to the formation of secondary structures within the >85% GC-rich regions of the promoter (**Figure 3.15**), causing the polymerase to either fall off of the extending strand, or simply skip the sequence. Attempts to circumvent this region entirely led to the generation of a truncated CAG promoter, containing the CMV enhancer and chicken ß–actin promoter without the ß–globin intron sequence – referred to in this chapter as 'short CAG' (**Figure 3.16**).

Ultimately, the use of phosphorylated linker oligonucleotides enabled the ligation of non-compatible ends, and the entire CAG promoter was cloned into the targeting vector (**Figure 3.15**). This was important, as inclusion of the ß-globin intron in CAG is thought to improve mammalian expression (Niwa et al., 1991).

3.4.2 Functional failure of *AAVS1*-EF1α-Myc constructs upon targeting

Perhaps the greatest challenge faced was the failure of the original *AAVS1*-EF1α-Myc-GECO constructs to result in fluorescent signal detection from fully *AAVS1*-targeted hiPSC-CMs that expressed GECO at the RNA level (**Figure 3.14**). After a number of modifications to the targeting strategy, the culprits for this lack of expression were identified as the promoter, the targeting locus and an inefficient P2A peptide cleavage sequence, with the latter being the most likely contributor to lack of protein expression. These factors are discussed below.

Initially, the hypothesis was that this was due to context-dependent promoter weakness. It has previously been shown that the use of the EF1α promoter to drive expression of copepod green fluorescent protein (copGFP) in hiPSCs targeted at the *AAVS1* locus with TALENS also failed to show fluorescence (Luo et al., 2014). This paper verified full biallelic integration into the *AAVS1* locus and detected copGFP protein expression by Western blot. However, the amount of fluorescent protein accumulated was not sufficient to image using microscopy. In addition, amilRFP (red fluorescent protein from *Acropora millepora*) failed to be expressed to a detectable level when targeted to the same locus under the control of the cytomegalovirus 7 (CMV7) promoter (Luo et al., 2014).

This is supported by a study comparing promoter efficiencies using PhiC31 integrase mediated cassette exchange at the Rosa26 locus in mouse embryonic stem cells (mESCs). Interestingly, when comparing 9 different ubiquitous promoters driving luciferase, CAG performed 9 times better than the endogenous *Rosa26* promoter, whilst EF1α performed just 2 times better than the endogenous promoter (Chen et al., 2011a). Some authors even claim that EF1α causes methylation at the targeting site (Macarthur et al., 2012), whereas others show that the open chromatin structure is maintained even if the EF1α promoter is used (Lombardo et al., 2011). Taken together, these studies suggest that attention must be paid to the choice of constitutive promoter in situations where expression level of the transgene is vital.

Promoter comparison was somewhat explored with transient transfection of constructs driven by different promoters into 293T BL15 cells (**Figure 3.16**). These experiments showed a significant increase in R-GECO fluorescence intensity when the CAG promoter, including the ß-globin intron, were used to drive expression. However, robust transient expression does not always result in strong stable expression. Indeed, the differences between CAG and EF1α that were seen at the targeted *Rosa26* locus by Chen *et al.*, were not subsequently seen in transiently transfected mESCs (Chen et al., 2011a). Nevertheless, given the number of successful studies involving genome targeting of fluorescent proteins or reporter constructs to the *AAVS1* locus with CAG-driven cassettes (Luo et al., 2014, Maddah et al., 2015, Pei et al., 2015, Shiba et al., 2012), as well as the transient transfection data generated in this chapter, there was some confidence in switching the promoter from EF1α to CAG.

The main culprit for lack of targeted expression was likely the failure of the P2A peptide cleavage sequence to adequately cleave between the MYC and GECO proteins being translated (**Figure 3.17**). This was surprising given that "2A" cleavage sites are preferred to IRES sequences when expressing bicistronic genes due to their short length and equal expression of proteins flanking the 2A sequence (Donnelly et al., 2001). It has even been claimed that the P2A cleavage sequence is the most efficient self-cleaving peptide, followed by T2A and E2A, when used to cleave a bicistronic vector in three different human cell lines, including HeLa (Kim et al., 2011). We cannot reconcile this with our data, as targeting multicistronic cassettes to the *AAVS1* locus in hiPSCs has resulted in efficient cleavage by the IRES sequence and the T2A sequence, but not the P2A sequence.

The poor cleavage efficiency of P2A explains why RNA expression was detected by RT-PCR (**Figure 3.14**), but functional protein was not. It may also explain why transient transfection of the Myc-P2A-GECO constructs gave detectable fluorescent protein, as accumulation of multiple copies of GECO overcame the inefficiency of cleavage. Given the success of Kim *et al.*, and others when using the P2A cleavage sequence, the lack of cleavage efficiency may be a context-dependent effect. However, our data support the finding that the expression of a fluorescent protein can be as much as 70% reduced if it follows a P2A site (Liu et al., 2017b).

Fortunately, the P2A-Myc section of the targeting cassette could be dispensed with in this chapter. Initially, Myc was included as a method of detecting GECO protein in targeted cells (Chang et al., 2017). However, once it was discovered that GEM-GECO

could be detected with an anti-GFP antibody, and R-GECO could be detected with an anti-RFP antibody, Myc was no longer required.

3.4.3 Characterisation of clones

PCR was heavily relied upon for identifying positively targeted clones, and detecting biallelic *AAVS1* targeting in this chapter. Initially, column purification of genomic DNA was used to screen clones (**Figure 3.14**). This was time-consuming and unwieldy when dealing with, at times, up to 60 clones. The use of DirectPCR™ lysis kit to lyse cells in situ (See Materials and Methods for details), provided genomic material in a single step and vastly improved throughput. Hence with the use of direct PCR cell lysis reagent, time was saved on expanding clones and processing cell pellets. This had the unwanted side effect of producing smeared electrophoresis gels due to contaminating proteins.

A curious phenomenon that was observed throughout the PCR screens in this chapter was that some clones displayed 5' integration but not 3' integration, or vice versa (**Figure 3.14**). This may have been due to partial transgene integration, although this has not been reported in the literature. A possibility is that the DNA repair complex failed during HDR (Maher et al., 2011), or reverted to using the endogenous DNA as a template, rather than the exogenous targeting cassette.

A number of factors can affect CRISPR Cas9 targeting efficiency including target locus, insert size, Cas9 activity, sgRNA design, delivery method and cell type (Chu et al., 2015, Peng et al., 2016). Targeting experiments carried out in our own lab have found efficiencies ranging from 8% to 67% depending on the gene targeted (Kondrashov et al., 2018).

Nonetheless, these observations highlight the need to perform comprehensive screens across the entire target site.

3.4.4 Refinement of clone selection

High content image analysis allowed the detection of RGECO expression in hiPSC clones, and thus, the identification of clones with robust expression (**Figure 3.23**). However, *AAVS1*-targeted clones displayed varying levels of R-GECO expression upon differentiation to hiPSC-CMs, despite robust expression as hiPSCs (**Figure 3.25**). This supports the study by Ordovas *et al.*, in which bisulphite sequencing was used to discover DNA methylation in regions upstream of the *AAVS1* locus targeting site (Ordovas et al., 2015). It is thought that de-novo methylation can occur upon differentiation, leading to transgene silencing. This seems to suggest that the *AAVS1* insulator regions described previously (Ogata et al., 2003), do not ensure transgene expression.

It has been claimed that the *CLYBL* safe harbour locus can deliver 5-10 fold greater fluorescent transgene expression than *AAVS1*, when targeted with copGFP (Cerbini et al., 2015). We were keen to test this, and developed targeting vectors by swapping the *AAVS1* arms of homology for *CLYBL* arms of homology, as well as designing sgRNAs for the locus. Although antibiotic-resistant colonies were made, no targeting events were observed. This may have been due to the use of Cas9 nuclease rather than D10A nickase, or poor selection of screening primers. Nevertheless, some *AAVS1*-targeted clones expressed the transgene at high levels, most notably the REBL PAT *MYH7*$^{WT/WT}$ R-GECO clone R12, which was 92% positive for R-GECO upon differentiation to cardiomyocytes (**Figure 3.24**). This clone was targeted on both alleles, and was homozygous for the R-GECO transgene, which goes some way to explaining the high expression.

The incidence of biallelic targeting is correlated to the efficiency of CRISPR/Cas9, and it is no surprise that these events were seen in later targeting experiments when nucleofection was used to deliver the plasmids at efficiencies of up to 90.38% (**Figure 3.11).** Targeting efficiency can also be enhanced with the addition of small molecules that modulate DNA repair pathways (Yu et al., 2015). A small molecule inhibitor of DNA ligase IV, SCR7, which causes HDR to be favoured over NHEJ, has been shown to achieve 100% targeting efficiency when used in conjunction with antibiotic selection. Furthermore, the net yield of biallelically targeted clones was doubled (Chu et al., 2015).

The retention of the antibiotic selection cassette upon targeting allowed for enrichment of R-GECO expressing hiPSC-CMs with as few as three passages of cell

culture in the presence of puromycin (**Figure 3.25**). Despite this, the *MYH7*$^{MUT/MUT}$ Hom 2 clone was preferred to the originally chosen *MYH7*$^{MUT/MUT}$ Hom 15 clone due to its inherent high expression of R-GECO (93.07%). Given that the *MYH7*$^{MUT/MUT}$ Hom 2 clone is not homozygous for R-GECO, the cassette may have been introduced to an off-target location. This could be assessed with a Southern blot using probes specific to the R-GECO, or expensive whole genome sequencing (Zischewski et al., 2017). This was beyond the scope of this thesis, and with no obvious adverse effects, these potential off-target clones are still useful as hiPSC-CMs that can be used to model HCM *in vitro* in chapters 4 and 5.

Table 3.4. Summary of cell lines engineered to express genetically encoded calcium indicators

Parent cell line	Genotype	GECI	Selected clone
REBL-PAT	*MYH7*$^{WT/WT}$	R-GECO1.0	R12
REBL-PAT	*MYH7*$^{WT/MUT}$	R-GECO1.0	Het 8
REBL-PAT	*MYH7*$^{MUT/MUT}$	R-GECO1.0	Hom 2
P1	*ACTC1*$^{WT/WT}$	R-GECO1.0	WT3
P1	*ACTC1*$^{WT/MUT}$	R-GECO1.0	MUT12
P2	*ACTC1*$^{WT/WT}$	GEM-GECO	AW2
P2	*ACTC1*$^{WT/MUT}$	GEM-GECO	AM2
REBL-PAT	*MYH7*$^{WT/WT}$ *ACTC1*$^{WT/WT}$	GEM-GECO	GM23

4 Engineered reporter lines and their application to assess calcium transients in human induced pluripotent stem cell derived cardiomyocytes

4.1 Introduction

A series of hiPSC lines that express a genetically encoded calcium indicator were generated in the previous chapter. This chapter explores how these lines, differentiated into cardiomyocytes, can be used to study calcium flux *in vitro*. Healthy hiPSC-CMs expressing RGECO or GEM-GECO are compared to existing chemical calcium indicator dyes to prove their utility in studying calcium transients. A suitable microscopy platform for imaging and quantifying calcium transients in targeted hiPSC-CMs is also investigated. Finally, hiPSC-CMs expressing RGECO or GEM-GECO are used to establish hiPSC-CMs as a valid model system, by interrogating the calcium handling machinery with drugs of known response.

4.1.1 Calcium handling in human induced pluripotent stem cell derived cardiomyocytes

Calcium handling is essential in excitation-contraction (E-C) coupling in cardiomyocytes. This has been reviewed in **Section 3.1.3**. Within this chapter, the specific channels and receptors involved in regulating calcium transients were interrogated.

4.1.1.1 L-type calcium channel inhibitors

L-type Ca^{2+} channels mediate the influx of Ca^{2+} ions into the cardiomyocyte. These voltage-sensitive, Ca^{2+}-selective channels consist of four different subtypes, grouped according to their α1 subunit ($Ca_V1.1$, $Ca_V1.2$, $Ca_V1.3$, and $Ca_V1.4$). Within the heart, the $Ca_V1.2$ subtype, encoded by the gene *CACNA1C*, is predominant (Zamponi et al., 2015). Sinoatrial node and atrioventricular node cardiomyocytes tend to have a greater expression of $Ca_V1.3$, encoded by *CACNA1D* (Zamponi et al., 2015).

The importance of L-type Ca^{2+} channels in maintaining healthy CM activity is underlined by the fact that mutations in the genes encoding these channels lead to cardiac complications. Loss-of-function mutations in *CACNA1D* lead to SAN dysfunction and bradyarrhythmia (Baig et al., 2011). Missense mutations in *CACNA1C* can result in Timothy syndrome and Brugada syndrome, typified by long QT interval and ventricular arrhythmia, respectively (Napolitano and Antzelevitch, 2011).

L-type Ca^{2+} channels are sensitive to three main classes of Ca^{2+}-blockers: dihydropyridines, phenylalkylamines and benzothiazepines. Dihydropyridines include; isradipine, nimodipine, nitrendipine and nifedipine. Phenylalkylamines include fendiline and verapamil. Benzothiazepines include diltiazem. Despite differences in structure, all three classes of drug bind within overlapping regions on the α1 subunit and function by stabilising the inactivated channel state (**Figure 4.1**) (Striessnig et al., 2015). These drugs are not only useful for isolating L-type currents *in vitro*, they often have therapeutic benefit to treat cardiovascular diseases by reducing intracellular Ca^{2+}.

However, these drugs can have different selectivity for L-type Ca^{2+} channel subunits, as well as other cardiac channels. For example, isradipine preferentially binds to CaV1.2 (Kang et al., 2012b). Verapamil and diltiazem can also block inward potassium channels (Zhang et al., 1999, Grissmer et al., 1994).

Given its relative selectivity, nifedipine is utilised in this chapter to assess the presence of functional L-type Ca^{2+} channels.

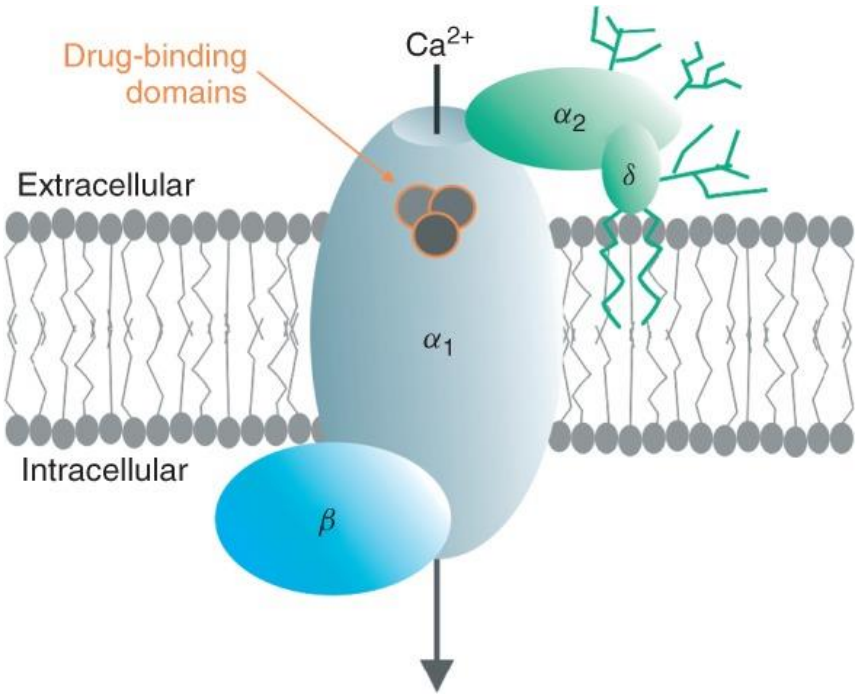


Figure 4.1. The L-type Ca^{2+} channel.

Schematic illustrating the subunit complexes that comprise the voltage-gated L-type Ca^{2+} channel. The drug binding domains for all three classes of calcium channel blocker are located on the α1 subunit (Striessnig et al., 2014).

4.1.1.2 The sarcoplasmic reticulum and ryanodine receptor interaction

The sarcoplasmic reticulum is the intracellular store of Ca^{2+} within cardiomyocytes and plays a central role in calcium handling and E-C coupling. The major Ca^{2+} release channel on the SR is the cardiac ryanodine receptor (RyR2). The main cause of Ca^{2+} release from the SR in healthy cardiomyocytes is calcium induced calcium release (CICR), explored in **Chapter 1.3**.

However, Ca^{2+} release from the SR is not only dependent on an increased cytosolic Ca^{2+} concentration during CICR. The discovery of luminal Ca^{2+} sensing sites suggested that release of Ca^{2+} through the RyRs could also occur as a result of high Ca^{2+} within the SR (Gyorke and Gyorke, 1998). This mechanism of calcium store release is exploited by caffeine.

Millimolar concentrations of caffeine have long been known to induce discharge of the SR store (Rousseau and Meissner, 1989). Its mechanism of action is by reducing the luminal threshold for calcium release through the RyRs (Chen et al., 2014). Other

methylxanthines such as theophylline and aminophylline can also sensitise the RyRs to Ca^{2+} activation (Kong et al., 2008). The emptying of SR stores at millimolar concentrations is temporary, and multiple 'puffs' of caffeine can induce the same spike in intracellular Ca^{2+} in cardiomyocytes, provided the SR has had time to refill its stores (Satin et al., 2008). In this way caffeine serves as a useful tool for assessing SR function within cardiomyocytes *in vitro*.

As well as activation by Ca^{2+}, the cardiac ryanodine receptor (RYR2) can be modulated by its namesake ligand, ryanodine. Ryanodine is a plant alkaloid derived from the South American plant *Ryania speciosa* (Rogers et al., 1948). It has an extremely high affinity for RYR2 (K_d = 0.7 nM). In addition, there is a second binding site with a lower affinity for ryanodine (K_d = 23 nM) (Buck et al., 1992). As a result, ryanodine is thought to stabilise RYR2 in an open conformation at nanomolar concentrations. However, at micromolar concentrations it causes complete closure of the channel (Du et al., 2001). Ryanodine is therefore convenient in assessing the activity of this crucial ion channel in hiPSC-CMs.

4.1.1.3 SERCA inhibition

The sarco/endoplasmic reticulum Ca^{2+}-ATPase (SERCA) is a transmembrane ion transporter involved in the sequestration of cytoplasmic Ca^{2+} to the SR. Consequently, it is responsible for terminating the contraction phase in cardiomyocytes.

The SERCA pump is encoded by a family of three genes, *SERCA1*, *2* and *3*, which are located on different chromosomes. There are several isoforms, but in the context of cardiomyocytes, SERCA2a is the predominant isoform (Periasamy and Kalyanasundaram, 2007). SERCA2a, in contrast to other isoforms such as SERCA1a, is regulated by a protein inhibitor, phospholamban (PLN).

The importance of SERCA2a and its role in healthy cardiac function is highlighted by the fact that inhibition of SERCA by mutant PLN causes dilated cardiomyopathy (Zhai et al., 2000). Furthermore, SERCA2a expression is diminished in heart failure (Lipskaia et al., 2010).

Thapsigargin, a sesquiterpene lactone from the plant *Thapsia garganica*, is a potent inhibitor of all SERCA isoforms (Xu et al., 2004). The binding of thapsigargin within a domain on the cytoplasmic side of the transmembrane protein causes a conformational change which prevents the transport of Ca^{2+} (**Figure 4.2**). As such, it represents a suitable compound to test the function of SERCA2a in this chapter.

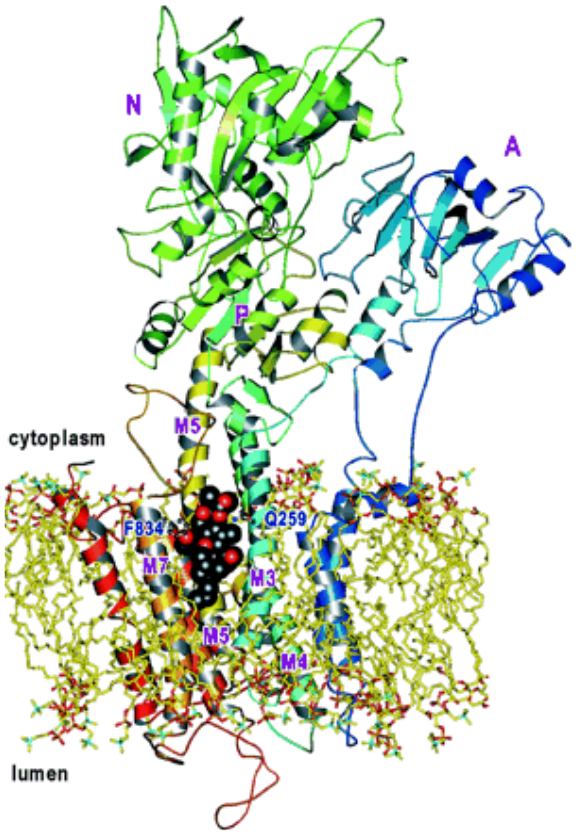


Figure 4.2. Crystal structure of SERCA inhibition by thapsigargin.

Crystal structure of thapsigargin (black/red) bound to sarco/endoplasmic reticulum Ca^{2+}-ATPase embedded in the lipid bilayer based on crystal structure. Thapsigargin binds to a cavity near the cytosolic side of the membrane. Taken from (Xu et al., 2004).

4.1.1.4 NCX interaction

The Na^+/Ca^{2+} exchanger (NCX) is an antiporter membrane protein that extrudes 1 Ca^{2+} ion in exchange for 3 Na^+ ions. NCX is a secondary mechanism for removing intracellular Ca^{2+} during diastole in cardiomyocytes, removing around 28% of intracellular Ca^{2+} in the human cardiomyocyte (Bers, 2002).

NCX is electrogenic, meaning that ions travel along their electrochemical gradient. As such, it can be reversed in situations where intracellular Na^+ is higher than usual, or when Ca^{2+} influx through other channels is inhibited (Bers, 2002).

There are few selective NCX antagonists, and nickel ions are often used to simply displace calcium (Barman et al., 2013).

4.1.1.5 ß-adrenergic stimulation

ß-adrenergic receptors and their associated G protein/adenylyl cyclase signal transduction pathways are crucial to cardiac function. Stimulation of this pathway has positive inotropic and chronotropic effects, which should be reflected by an increased frequency of calcium transient events in cardiomyocytes. The mechanism of action for increased calcium transients in response to ß–adrenergic stimulation is an increased level of cyclic AMP (cAMP) leading to protein kinase A (PKA) phosphorylation of RyRs on the SR (**Figure 4.3**).

There are broadly three ß–adrenoreceptor subtypes; $ß_1$, $ß_2$ and $ß_3$. In the heart, approximately 80% of ß–adrenoreceptors are the $ß_1$ subtype, and 20% the $ß_2$ subtype (Madamanchi, 2007). However, $ß_1$ downregulation can occur as a result of heart failure (Bristow et al., 1986). Furthermore, in the context of hiPSC-CMs, $ß_1$ adrenoreceptor contribution to ß–adrenergic response is not seen until day 60 of maturation (Wu et al., 2015).

Many ß-adrenergic agonists are selective for one of the ß-adrenoreceptor subtypes. For example, the selective $ß_1$ agonist dobutamine or the selective $ß_2$ agonist salbutamol (Ho et al., 2010, Fowler et al., 1982). Given the varying levels of ß–adrenoreceptor subtype expression within hiPSC-CMs, non-selective ß-agonists are preferred to assess ß-adrenergic regulation of calcium transients. One such non-selective ß-adrenoreceptor agonist, isoprenaline, is analogous to the endogenous hormone adrenaline, with the addition of an isopropylamine functional group (Gunn and Gurd, 1940). This structural similarity to endogenous positive chronotropes as well as its proven modulation of excitation-contraction coupling in cardiomyocytes, makes it a worthy candidate for assessing calcium handling in hiPSC-CMs (Ginsburg and Bers, 2004).

Other positive chronotropic drugs such as forskolin, an adenylyl cyclase stimulator, could be used to interrogate the ß-adrenergic system (Lu et al., 2015). However, the more direct activator of the ß-adrenergic system, isoprenaline, was used in this chapter.

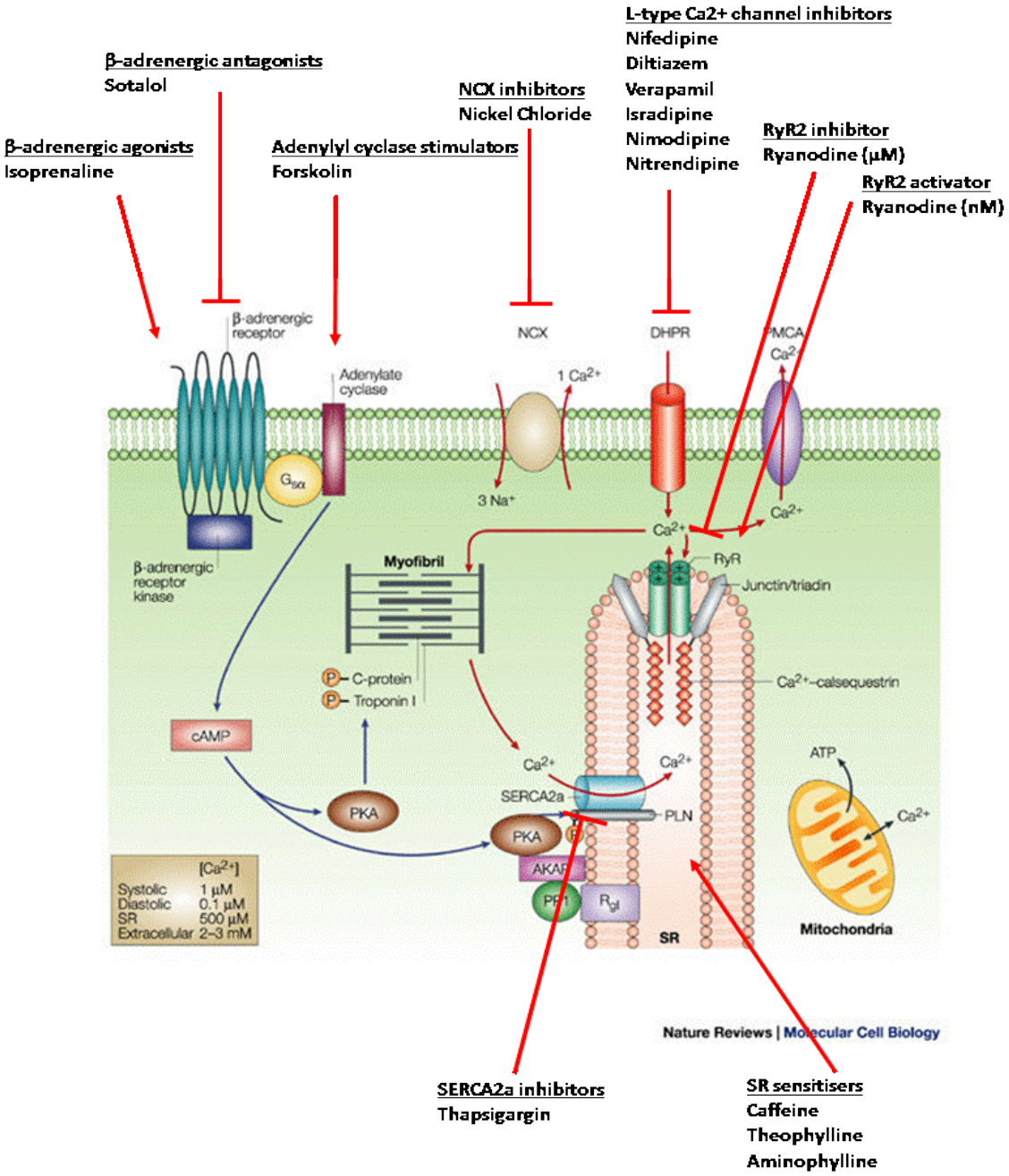


Figure 4.3. Calcium handling in cardiomyocytes and interacting compounds.

Schematic illustrating the calcium handling machinery of cardiomyocytes, their interactions, and how compounds can act upon them. DHPR - dihydropyridine receptors (L-type Ca^{2+} channels), NCX – Na^{+}/Ca^{2+}-exchanger, RyR – ryanodine receptors, PKA – protein kinase A, PLN – phospholamban, SERCA2a – sarco/endoplasmic reticulum Ca^{2+}-ATPase 2a, SR – sarcoplasmic reticulum. Adapted from (MacLennan and Kranias, 2003).

4.1.1.6 Other reference compounds

A small number of other reference compounds with known action on calcium handling in cardiomyocytes could have been utilised in this chapter. For example, the ß-adrenergic and I_{Kr} blocker sotalol, at 50 µM, extends the calcium transient duration (**Figure 4.4A**). Verapamil, an L-type Ca^{2+} channel and I_{Kr} blocker, reduces the calcium transient amplitude (**Figure 4.4B**). BayK 8644, an L-type Ca^{2+} channel agonist, increases the calcium transient amplitude (**Figure 4.4C**) (Lu et al., 2015). Within this chapter, nifedipine, a specific L-type Ca^{2+} channel antagonist was preferred to verapamil. Although not utilised in this chapter to interrogate calcium handling, ß-adrenergic blockers are considered in Chapter 5.

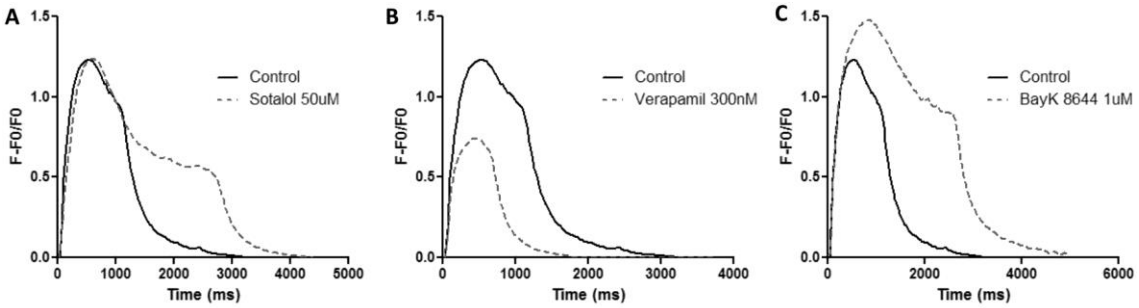


Figure 4.4. hiPSC-CM calcium transient response to reference compounds.

hiPSC-CMs display a reproducible calcium transient response to; **(A)** Sotalol, a ß-adrenergic blocker, **(B)** Verapamil, an L-type Ca^{2+}-channel blocker and **(C)** BayK 8644, a Ca^{2+}-channel agonist. Adapted from (Lu et al., 2015).

4.1.1.7 Calcium handling maturity in hiPSC-CMs

However, concerns about functional immaturity have led to doubts about the calcium handling properties of hiPSC-CMs. Ultrastructural analyses of hESC-CMs have shown a distinct lack of T-tubules, which help to conduct impulses from the sarcolemma to the interior of the cell (Snir et al., 2003, Lieu et al., 2009). Without these invaginations, the efficiency of CICR and Ca^{2+} release from the SR could be reduced. In addition, Western blot analysis of HES2 and H1 hESC-CMs has revealed the absence of the RyR regulatory proteins calsequestrin, triadin and junctin (Liu et al., 2007).

Furthermore, studies with hESC-CMs have shown limited response to caffeine, ryanodine or thapsigargin and a reliance on trans-sarcolemmal Ca^{2+} influx rather than release from the SR (Dolnikov et al., 2006). Other studies have shown that caffeine-sensitive SR Ca^{2+} stores are in fact present in hESC-CMs (Satin et al., 2008), albeit at around half the level found in foetal left ventricular CMs (Liu et al., 2007).

It is therefore important that, in this chapter, the calcium handling machinery of hiPSC-CMs is interrogated with compounds that interact with the receptors, channels and pumps involved in calcium cycling.

4.2 Chapter Aims and Objectives

This aim of this chapter was to look at how hiPSC lines engineered in chapter 3 could be utilised as hiPSC-CMs to study calcium transients *in vitro*, and validate hiPSC-CMs as a useful model for studying calcium handling in cardiomyocytes. The following objectives had to be met to fulfil this aim:

1. Compare the engineered lines to commercially-available chemical calcium indicator dyes.
2. Develop a microscopy system to capture rapid fluorescent changes in targeted hiPSC-CMs caused by genetically encoded calcium indicators.
3. Develop a method to process and analyse calcium transients.
4. Use a variety of drugs with known response, to interrogate the calcium handling machinery of hiPSC-CMs.

4.3 Results

4.3.1 A comparison between genetically encoded calcium indicators and chemical calcium dyes

In order to justify the use of the generated GECI cell lines instead of widely available chemical calcium indicators, a time-course experiment was set up to assess the utility of GECIs over a time period of 12 hours (**Figure 4.5**). The Fluo-4 AM indicator was loaded for 1 hour prior to the experiment to allow for adequate penetration of the dye before the time-course. At the start of the time-course, robust expression from the calcium indicator dye was seen in almost all hiPSC-CMs, which was maintained until at least 2 hours into the time-course (**Figure 4.5A**). However, this fluorescent signal could no longer be detected at 6, 9 or 12 hours into the time-course experiment. In contrast, the REBL PAT RGECO cell line retained a stable fluorescent expression throughout the time-course (**Figure 4.5B**).

Operetta™ high content image analysis was used to detect the number of fluorescent cells at each time point, and this was normalised for variance in cell number between wells (**Figure 4.5C**). Fewer fluorescent cells were detected over time when the dye was used, compared to a relatively stable expression of RGECO over time. There was a significant difference between fluorescent populations detected at the 5 hour time point (* $p < 0.05$). This continued throughout the time-course with maximum divergence in fluorescent signal at 11.5 hours (** $p = 0.0067$). These results highlight the disadvantage of using chemical calcium indicator dyes, which are prone to dye leakage over time. The engineered RGECO cell lines, however, retain robust expression and provide a much wider window for experiments to be completed.

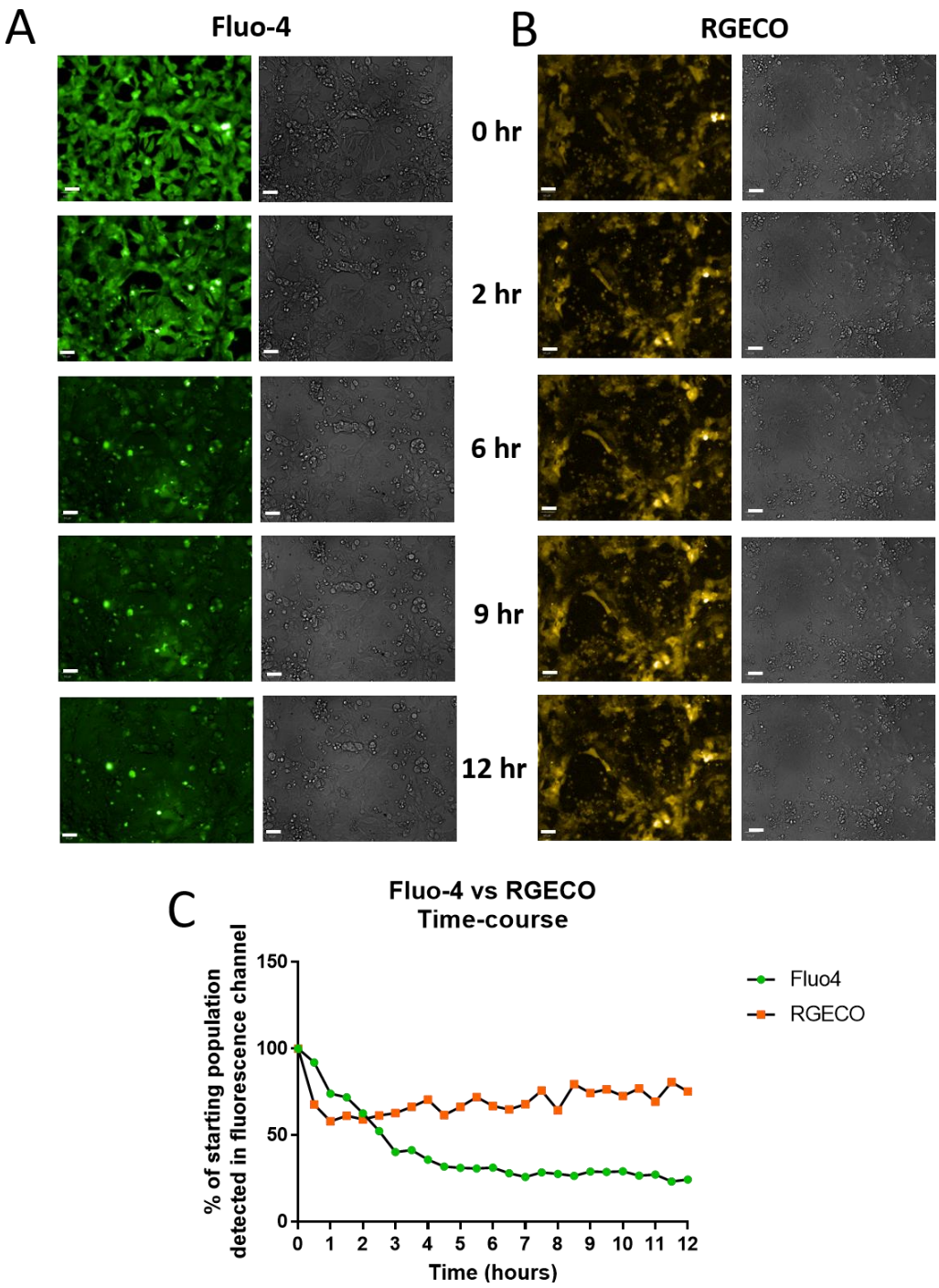


Figure 4.5. A comparison between GECIs and existing chemical calcium indicator dyes - evidence of dye leakage using time-course live imaging.

(A) Time-course live imaging of d28 REBL PAT hiPSC-CMs loaded with 10 µM Fluo-4 1 hour prior to experiment. Fluorescent signal is lost over time. **(B)** Time-course live imaging of REBL PAT RGECO clone R12 hiPSC-CMs. Fluorescent signal is maintained even after 12 hours. Scale bars = 50 µm. **(C)** Proportion of fluorescent cells detected by Operetta™ high content image analysis in a time-course lasting 12 hours, with images taken every 30 minutes. To account for different cell numbers in each well, data were normalised to a percentage of the starting fluorescent population in each well. Therefore each data set began at 100% fluorescent cells detected at 0 hours. Data presented as mean (n = 4 wells).

Cell toxicity associated with acetoxymethyl ester (AM) calcium indicator dyes was assessed by using a commercially available viability kit based on luminescence (**Figure 4.6**). In this assay, viable cells produce ATP which acts as a cofactor for luciferase to catalyse the conversion of the luciferin substrate to the luminescent oxyluciferin product. In this way, the number of viable cells is directly proportional to the amount of luminescence produced. To illustrate the positive relationship between cell number and luminescence, a standard curve was generated by seeding REBL PAT hiPSC-CMs at varying densities and reading their luminescence on a plate reader (**Figure 4.6A**).

As 50,000 cells per well is the seeding density required for hiPSC-CMs to form a beating monolayer, this density was used to assess the effect of increasing calcium indicator dye concentrations on hiPSC-CM viability (**Figure 4.6B, C**). The manufacturer's instruction is to use these AM calcium indicator dyes in a concentration range between 1 µM and 10 µM. However, even at the lowest experimental concentration of 100 nM, Fluo-4 AM reduced the amount of viable cells detected by luminescence from 3.77 x 10^6 RLU to 1.55 x 10^6 RLU (**Figure 4.6B**). Similarly, Calcium Crimson AM reduced the amount of viable cells detected at the lowest concentration of 100 nM. A significant loss of viable cells was seen at 100 µM Calcium Crimson, as luminescence detected dropped from 4.13 x 10^6 RLU to 1.08 x 10^6 RLU (* p = 0.0295) (**Figure 4.6C**).

In contrast, the genetically encoded calcium indicator line, REBL PAT RGECO, had no significant loss of viability compared to the REBL PAT control (**Figure 4.6D**). By adding 20 µM Fluo-4 AM calcium dye, however, viability significantly reduced 3.44 x 10^6 RLU to 2.31 x 10^6 RLU (** p = 0.0016).

Overall, these data illustrate the cytotoxicity associated with the commonly used AM class of calcium indicator dye. This reinforces the requirement for hiPSC-CMs that express GECIs in experiments looking at calcium flux.

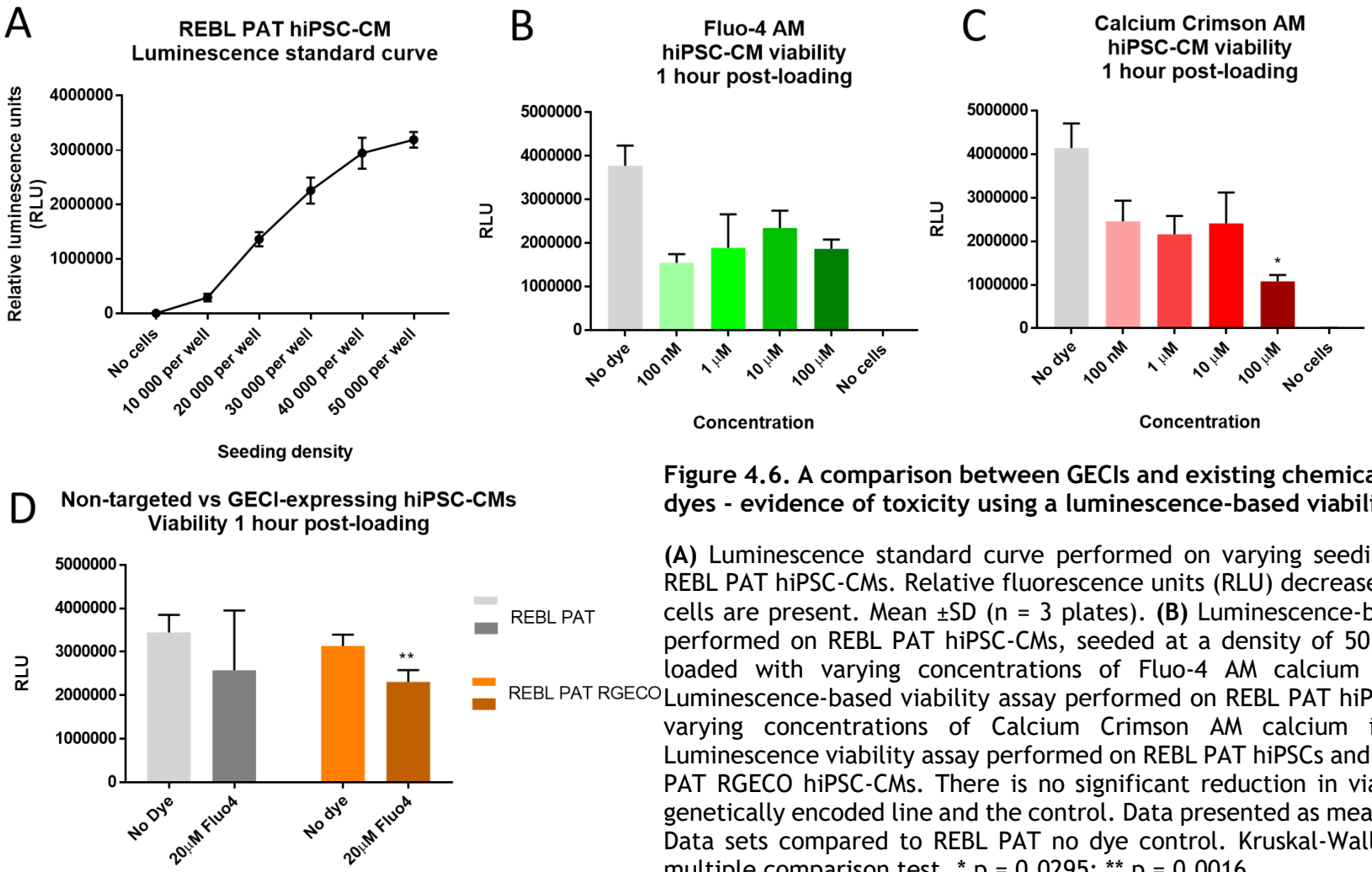


Figure 4.6. A comparison between GECIs and existing chemical calcium indicator dyes - evidence of toxicity using a luminescence-based viability assay.

(A) Luminescence standard curve performed on varying seeding densities of d28 REBL PAT hiPSC-CMs. Relative fluorescence units (RLU) decrease when fewer viable cells are present. Mean ±SD (n = 3 plates). **(B)** Luminescence-based viability assay performed on REBL PAT hiPSC-CMs, seeded at a density of 50,000 cells per well, loaded with varying concentrations of Fluo-4 AM calcium indicator dye. **(C)** Luminescence-based viability assay performed on REBL PAT hiPSC-CMs loaded with varying concentrations of Calcium Crimson AM calcium indicator dye. **(D)** Luminescence viability assay performed on REBL PAT hiPSCs and GECI targeted REBL PAT RGECO hiPSC-CMs. There is no significant reduction in viability between the genetically encoded line and the control. Data presented as mean ±SD (n = 3 plates). Data sets compared to REBL PAT no dye control. Kruskal-Wallis test with Dunn's multiple comparison test, * p = 0.0295; ** p = 0.0016.

4.3.2 Developing a microscopy technique to capture and analyse calcium transients in targeted GECI hiPSC-CMs

In order to successfully use the targeted lines to study calcium transients in hiPSC-CMs, a microscopy platform had to be chosen. The microscope had to be capable of imaging fast changes in fluorescence from beating CMs, as well as being able to image the ratiometric blue-green emission GEM-GECO and the intensiometric red emission RGECO. As an output, numerical data on the parameters of calcium transients was preferred.

Initial live imaging experiments on REBL PAT GEM-GECO hiPSC-CMs used the DeltaVision widefield epifluorescence microscope to generate images using a fast CCD or EM-CCD camera (**Figure 4.7**). The rapid camera acquisition meant that images could be stitched together to form a video, and fluorescent changes in hiPSC-CMs could be captured. However, when imaging the ratiometric REBL PAT GEM-GECO hiPSC-CMs, the emission filter had to switch between each image to capture both wavelengths (**Supplementary Video 1**) (**Figure 4.7A**). As a result, when analysing these videos and plotting region of interest (ROI) fluorescence, readings from both wavelengths could not be made simultaneously, and a ratio between the wavelengths could not be calculated. Instead, each wavelength had to be presented alone, and the switching between filters meant that gaps in data occurred (**Figure 4.7B**). The maximum speed the DeltaVision was capable of was 6.6 frames/second, which increased to 3.3 frames/second if both wavelengths were being measured.

Nevertheless, when used to measure single wavelengths, such as the emission from REBL PAT RGECO hiPSC-CMs, the DeltaVision produced useful videos (**Supplementary Video 2**). Frame by frame analysis of a video taken on the DeltaVision shows a change in fluorescence roughly once every 500 ms (**Figure 4.7C**), emphasising the need for fast acquisition of fluorescence changes in targeted hiPSC-CMs.

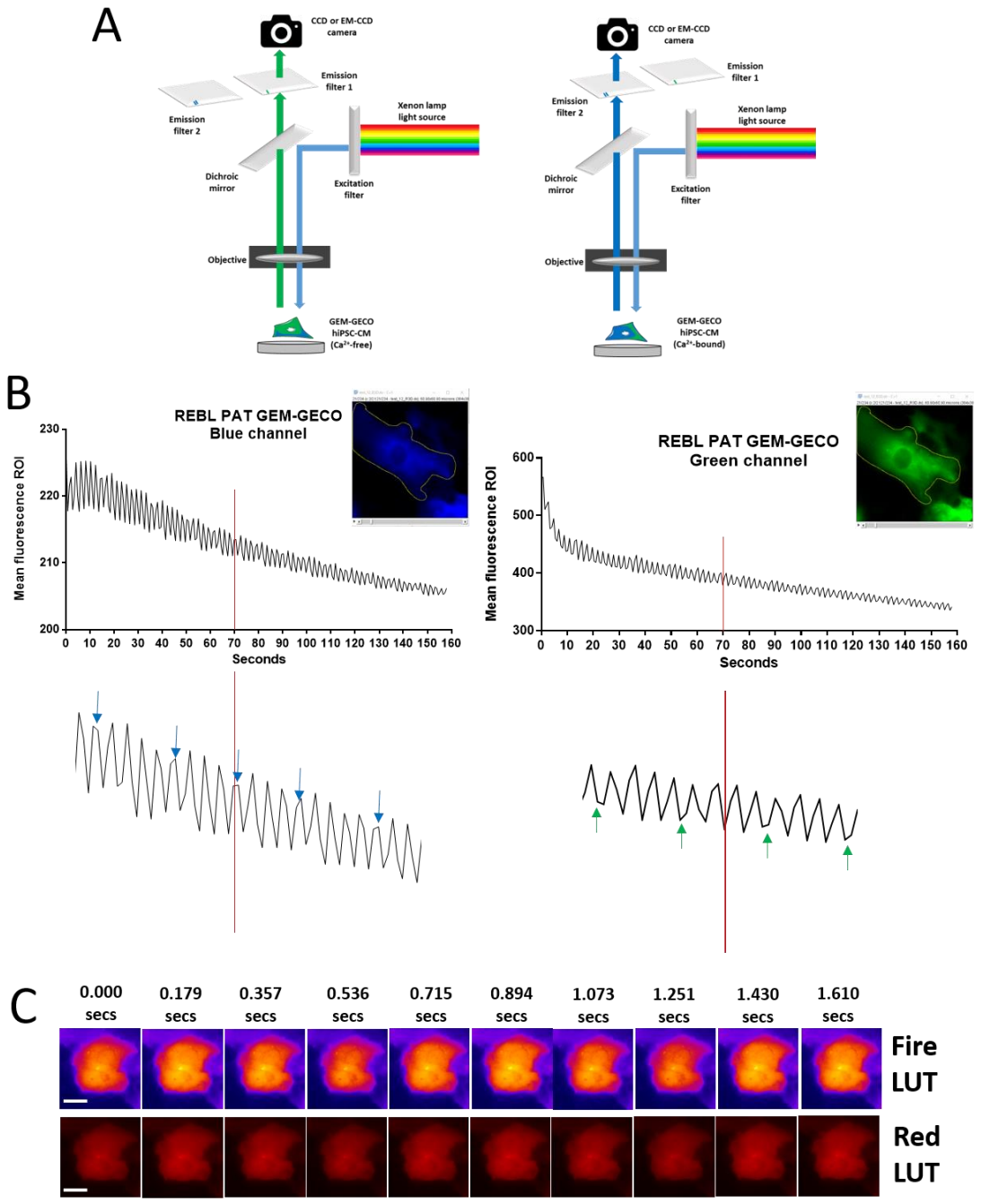


Figure 4.7. Application of DeltaVision widefield epifluorescence microscopy to detect fluorescent changes in targeted hiPSC-CMs.

(A) Schematic of how the DeltaVision widefield epifluorescence microscope functions when imaging hiPSC-CMs that express GEM-GECO. To image fluorescence from two different emission spectra, the emission filter must switch between each image. **(B)** Region of interest (ROI) drawn on video of REBL PAT GEM GECO hiPSC-CMs (inset) taken using DeltaVision microscope. The resulting traces of fluorescence from the blue and green wavelengths are not taken simultaneously (red line), and therefore true ratiometric calculations cannot be made. The time taken to switch between emission filters results in gaps in data (flat peaks/troughs - arrows). **(C)** Live imaging of REBL PAT RGECO hiPSC-CM with DeltaVision widefield microscopy. A frame by frame image of a video captured with the CCD camera shows fluorescence changes as the CM spontaneously beats. Look-up tables (LUT) are used to pseudocolour the image. 50 ms exposure, scale bars = 20 µm.

To address the limitations of widefield microscopy, confocal laser line scan microscopy was used as a platform for measuring calcium transients in targeted GECI hiPSC-CMs. The use of laser excitation and a photomultiplier detector permitted the simultaneous detection of both green (Ca^{2+}-free) and blue (Ca^{2+}-bound) emission wavelengths when imaging hiPSC-CMs that expressed GEM-GECO (**Figure 4.8A**). By drawing a laser line longitudinally across a hiPSC-CM (**Figure 4.8B**), fluorescence signals across the line were measured from both wavelengths every 75 ms (**Figure 4.8C**). In this way, true ratiometric calculations could be made to graphically represent the calcium transient events (**Figure 4.8D**). Each calcium transient event displays a rapid upstroke due to the mechanism of CICR. This is followed by a slower downstroke, as Ca^{2+} is pumped back into SR stores, or pumped out of the cell by the NCX (**Figure 4.8C, D**).

By displaying the fluorescence signal from the line over time as a kymograph, calcium transients can be visualised across the cell. By merging the fluorescent signals from a REBL PAT GEM GECO, the calcium transient appears to be "U-shaped", with calcium influx occurring at the periphery of the cell first, before diffusing to the centre (**Figure 4.8E**).

Given the superior detection speed and ability to measure ratiometric emission, rapid laser line scan confocal microscopy was chosen over widefield microscopy to measure calcium transients in hiPSCM-CMs targeted with RGECO and GEM-GECO.

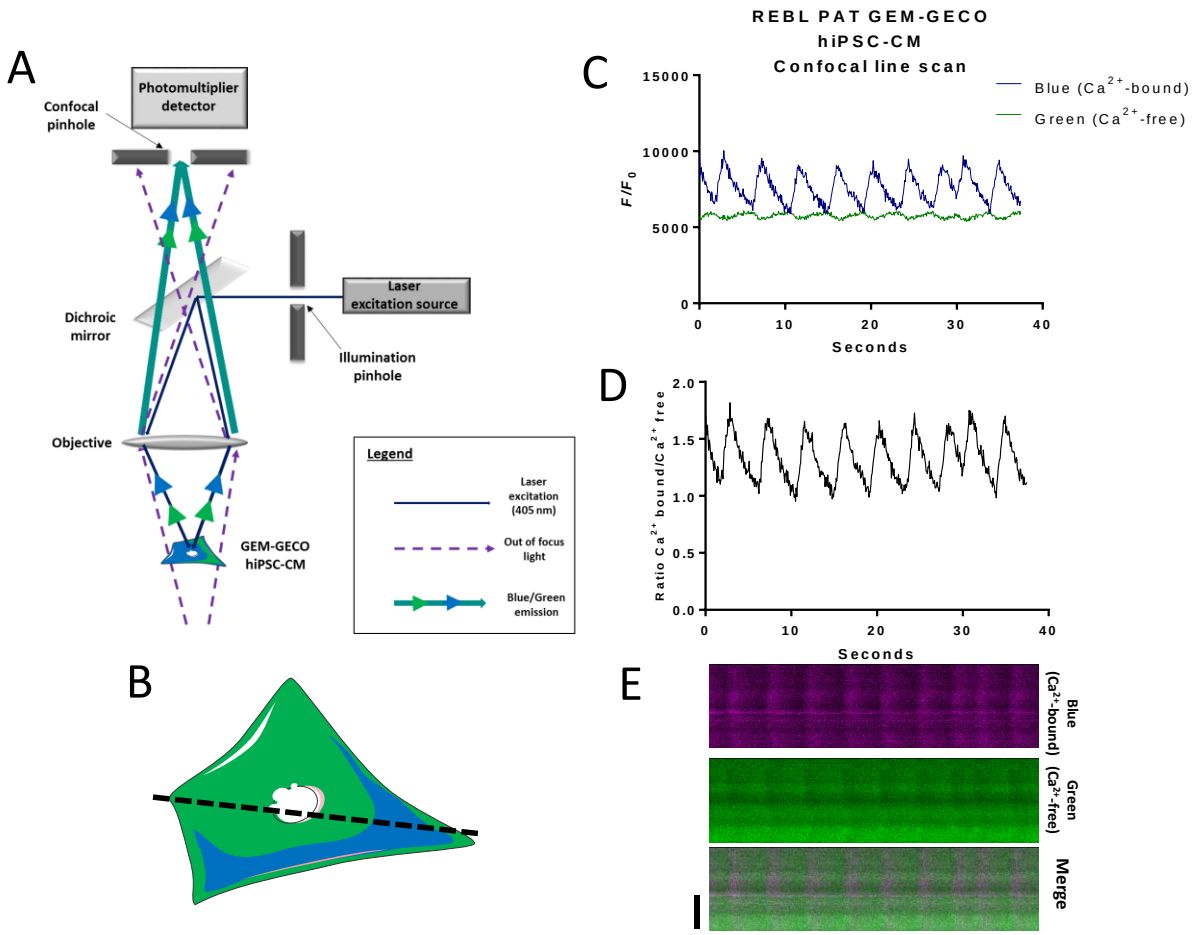


Figure 4.8. Use of confocal laser line scan microscopy to simultaneously detect fluorescence from two separate wavelengths.

(A) Schematic of how confocal microscopy functions when imaging hiPSC-CMs that express GEM-GECO. A laser excites the fluorophore, and both blue (Ca^{2+}-bound) and green (Ca^{2+}-free) emission spectra can be detected by the photomultiplier. Out of focus light fails to pass through the pinhole. **(B)** Schematic of how a confocal laser line is drawn longitudinally across a hiPSC-CM. **(C)** Resulting confocal line scan trace of d32 REBL PAT GEM-GECO hiPSC-CM showing both wavelengths measured every 75 ms. **(D)** Ratiometric calculation of both wavelengths made by dividing calcium-bound signal by calcium-free signal at each timepoint. **(E)** Corresponding line scan kymograph showing fluorescent signal along the laser line over time. Blue emission (magenta), green emission (green), scale bar = 20 µm.

Confocal line scans, once processed into a trace, often produced hundreds of calcium transient events. In order to efficiently count these events and measure their parameters, a patch-clamp electrophysiology analysis software, ClampFit, was repurposed (**Figure 4.9**). Data from confocal line scans, with a fluorescent signal associated to each 75 ms timepoint, were imported into the software. ClampFit then allowed for manual baseline correction of line scans that had undergone photobleaching (**Figure 4.9A**). By setting a baseline, return line and trigger line, calcium transient events could be counted even if they were much smaller than the average event (**Figure 4.9B**). As a rule, the trigger line tended to be drawn at or around 20% of the average peak height, in order to detect smaller events (**Figure 4.9C**).

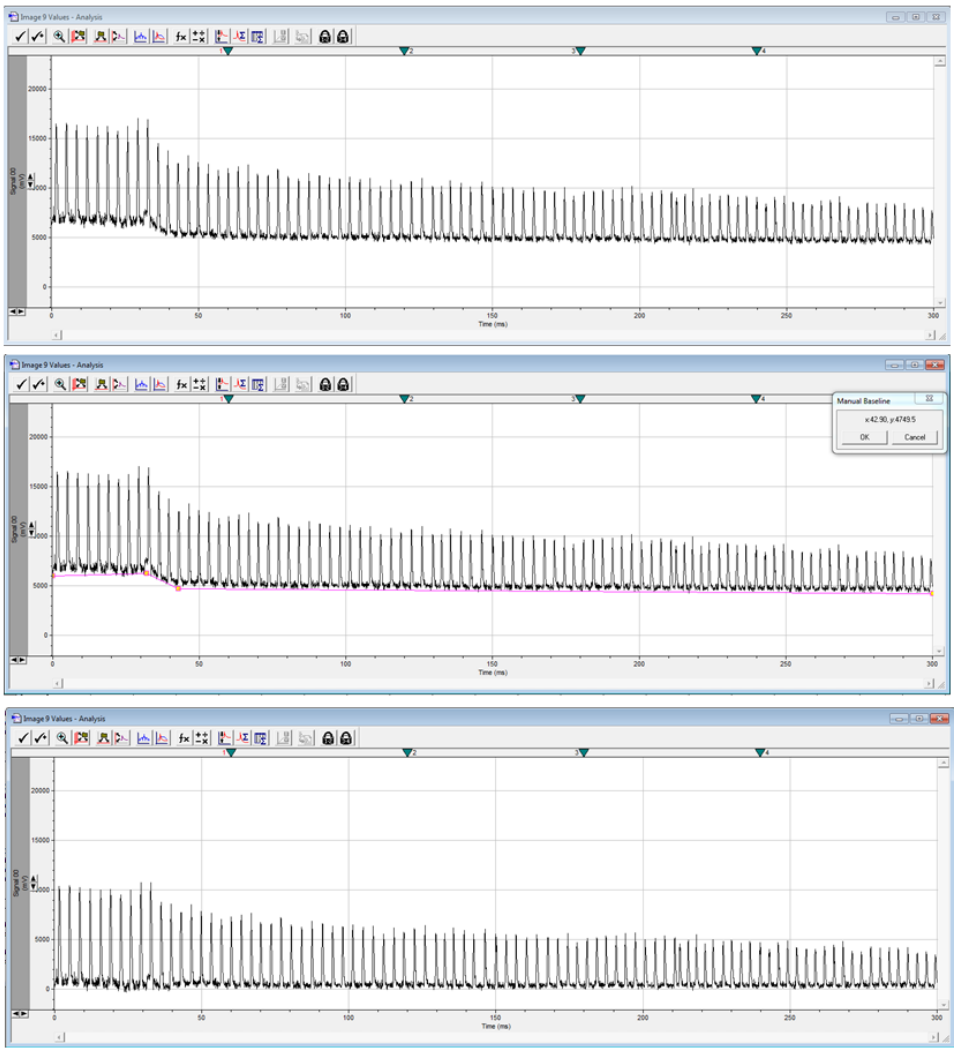
In order to induce these smaller, arrhythmic events, 1 μM ryanodine was added to REBL PAT RGECO hiPSC-CMs for 40 minutes. These smaller events in the line scan were easily identified after event detection, especially when viewed in the event viewer mode which superimposes each event on top of one another (**Figure 4.9C**). In this way, arrhythmic events could be quantified in a swift and unbiased manner.

As well as flexibility of detection on the Y-axis, flexibility of detection on the X-axis could be achieved by counting events between two cursors (**Figure 4.9D**). This allowed for segmental analysis of line scans, particularly useful for when drugs were added during a line scan experiment.

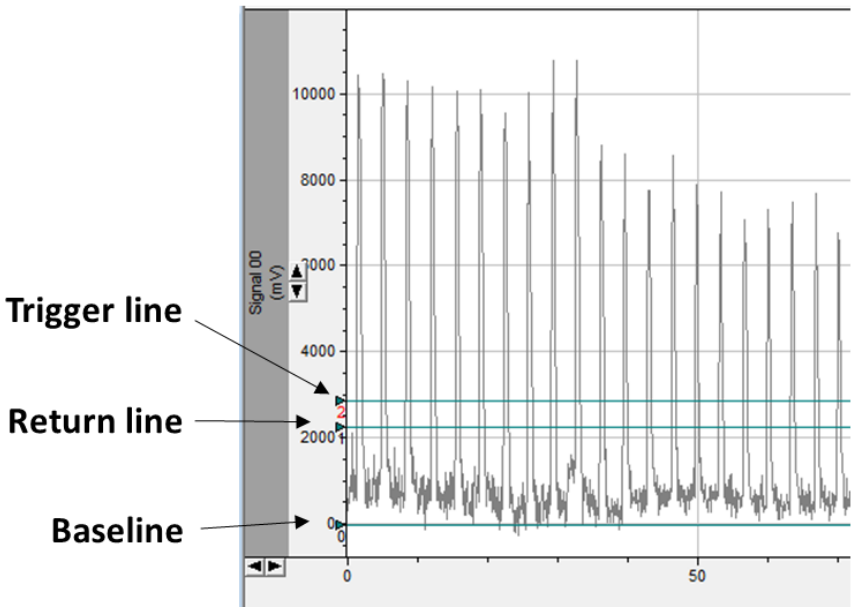
Numerical data outlining the parameters of each individual event were stored and this data could be easily exported to graphical software packages (**Figure 4.9E**). It is important to note, however, that as ClampFit is an electrophysiology program designed for voltage-clamp and current-clamp experiments, fluorescence intensity ratio signal (F/F_0) is displayed as mV and time (seconds) is displayed as ms within the software.

In this way, data from confocal line scans could be quickly analysed to generate data on; number of events, number of abnormal events, peak amplitude, and time to peak. This provided a platform for studying changes in calcium transients of hiPSC-CMs induced by drugs or genetic mutations.

A Baseline correction



B Event detection



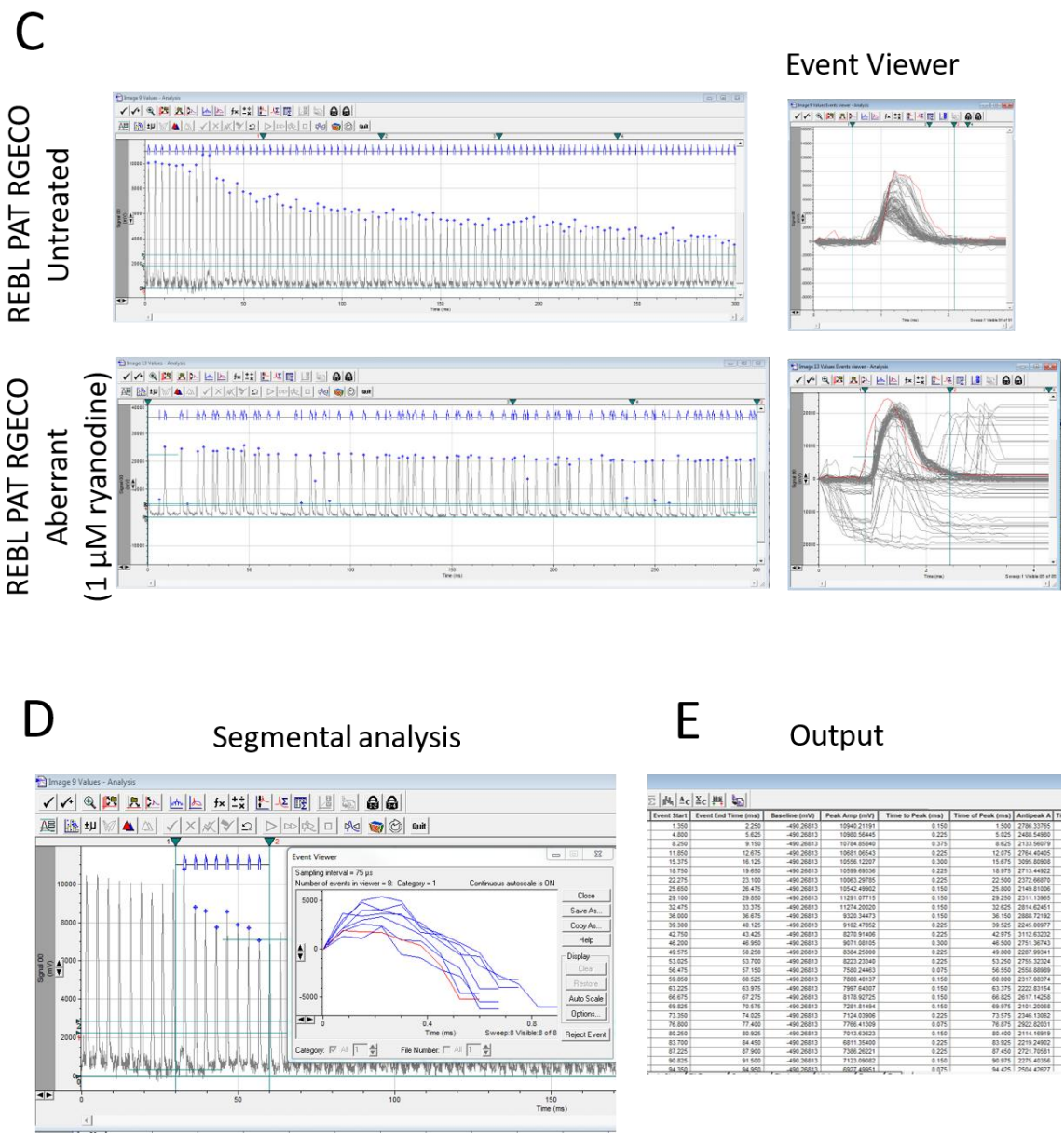


Figure 4.9. ClampFit event detection of calcium transients recorded using confocal laser line scan microscopy.

(A) An example of baseline correction performed on confocal line scan data input into ClampFit. Purple line indicates adjusted baseline. **(B)** Level markers for baseline, return line and trigger line for event detection. The trace must pass through the trigger line on the upstroke, and the previous trace through the return line on the downstroke, for an event to be recorded. **(C)** ClampFit event detection and associated event viewer mode for a regular (top) and arrhythmic (bottom) confocal line scan. Aberrant events were induced by treatment with 1 µM ryanodine. Aberrant events can be easily identified in the event viewer window as events which do not conform to the regular pattern. **(D)** Segments of a confocal line scan can be analysed separately by detecting events between two cursors. **(E)** ClampFit event detection outputs parameters including peak amplitude and time to peak of each individual event. Note that ms in ClampFit is equal to seconds; mV is equal to F/F_0.

4.3.3 Interrogating the calcium handling machinery of hiPSC-CMs with a panel of drugs of known response

Having established confocal line scan microscopy as a method to assess calcium transient events in targeted GECI hiPSC-CMs, calcium handling could be assessed with the addition of drugs that are known to alter calcium handling.

Caffeine is known to induce Ca^{2+} release from the sarcoplasmic reticulum. Initially, this was tested in REBL PAT hiPSC CMs transiently transfected with the ratiometric GEM-GECO targeting construct, as a way to functionally assess the GEM-GECO indicator before a fully targeted cell line was generated. With the addition of 10 mM caffeine during the line scan, a noticeable calcium transient spike occurred almost instantly (**Figure 4.10A**). The increase in signal from the Ca^{2+}-bound blue emission of GEM-GECO coincided with the decrease in signal from the Ca^{2+}-free green emission, which was visible on the corresponding line scan kymograph (**Figure 4.10B**). This experiment was repeated using the P2 *ACTC1*$^{WT/WT}$ GEM-GECO targeted hiPSC-CMs (**Figure 4.10C**). 30 seconds into the line scan, the addition of 10 mM caffeine caused a sharp increase in cytosolic Ca^{2+}, causing a spike in the ratiometric line scan trace (**Figure 4.10C**). The line scan kymograph also illustrates the simultaneous increase in blue emission and decrease in green emission associated with high intracellular calcium concentration (**Figure 4.10D**). The second addition of 10 mM caffeine at 90 seconds failed to cause a spike in the calcium transient, and no further response was seen in the line scan. This showed that the targeted hiPSC-CMs gave the expected response to caffeine by causing Ca^{2+} release from the SR.

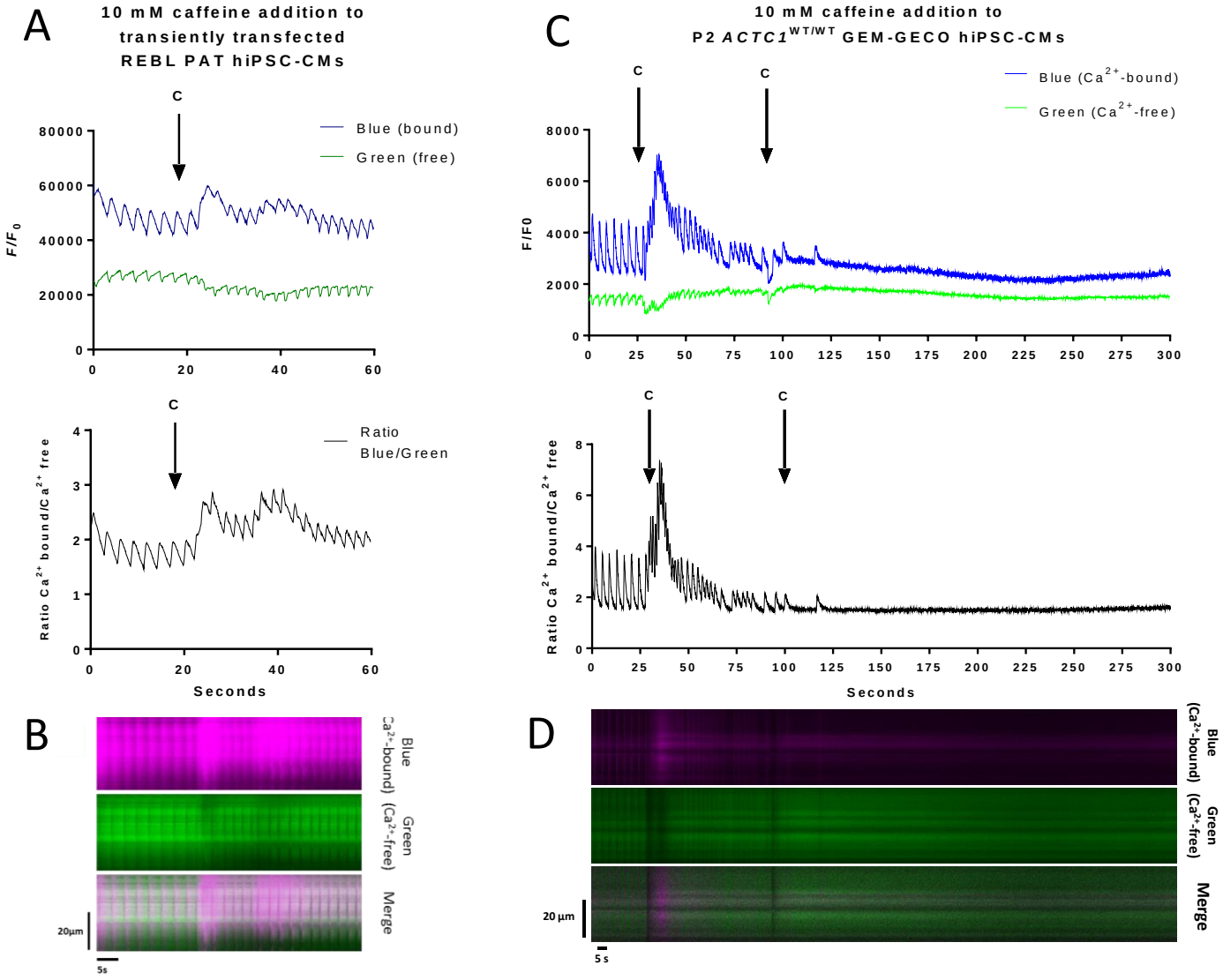
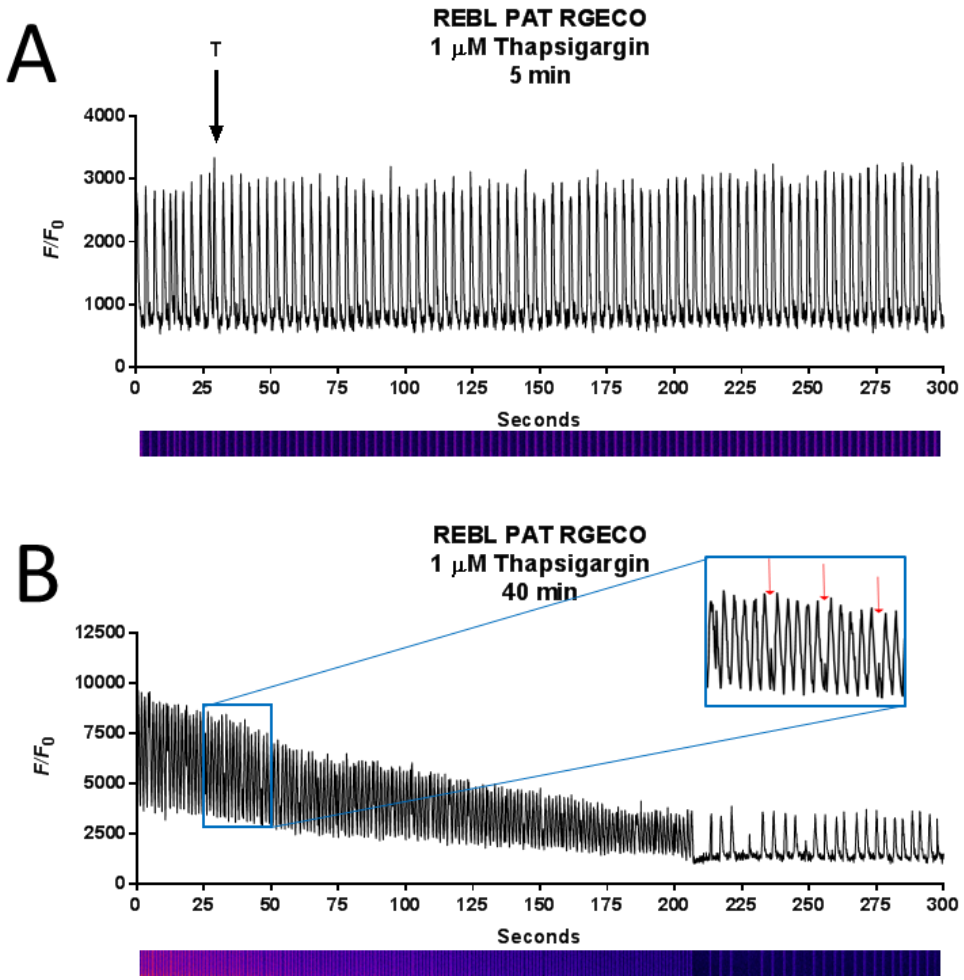


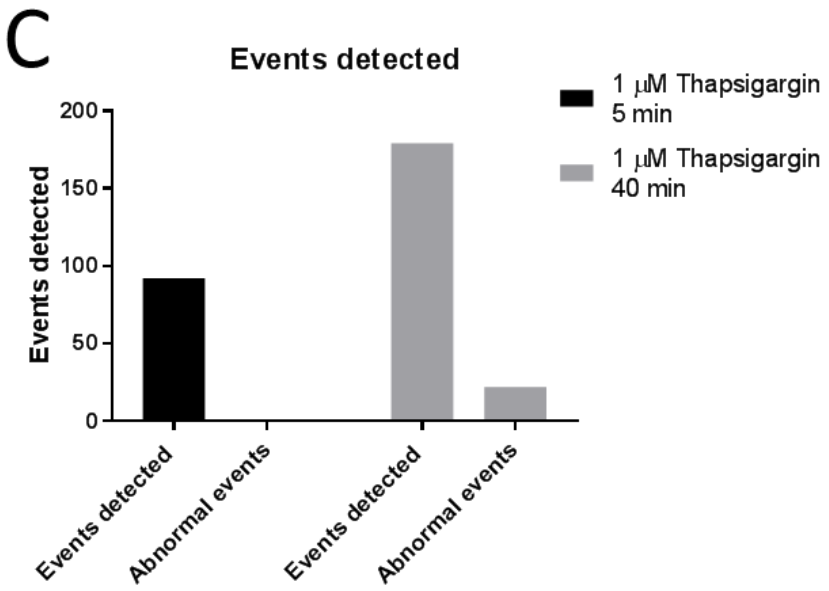
Figure 4.10. Caffeine induces Ca^{2+} release from sarcoplasmic reticulum of hiPSC-CMs.

(A) 60-second confocal laser line scan trace of REBL PAT hiPSC-CM transiently transfected with GEM-GECO targeting construct, showing a response to 10 mM caffeine addition (indicated with arrow) at 20 seconds. The ratio of Ca^{2+}-bound (blue)/Ca^{2+}-free (green) wavelengths demonstrate the release of calcium from SR stores upon addition of 10 mM caffeine. **(B)** Corresponding line scan kymographs showing blue wavelength (magenta), green wavelength (green) and merged emission profile over time. Y-axis scale bar = 20 µm, X-axis scale bar = 5 seconds. **(C)** 300-second confocal laser line scan trace of 10 mM caffeine addition to a P2 *ACTC1*$^{WT/WT}$ GEM-GECO hiPSC-CM at 30 seconds and 90 seconds (indicated with arrows). Calcium transient amplitude increases immediately after first caffeine addition, due to Ca^{2+} release from SR stores. **(D)** Corresponding line scan kymographs showing blue wavelength (magenta), green wavelength (green) and merged emission profile over time. Y-axis scale bar = 20 µm, X-axis scale bar = 5 seconds.

With the knowledge that Ca^{2+} release from the SR could be induced with 10 mM caffeine and detected using confocal line scans on targeted GECI hiPSC-CMs, re-uptake of Ca^{2+} into the SR was blocked with thapsigargin. Thapsigargin is known to inhibit the SERCA family of Ca^{2+} pumps. The addition of 1 μM thapsigargin onto REBL PAT RGECO hiPSC-CMs had no immediate effect, and confocal line scans showed no change in the calcium transient frequency or shape in the immediate aftermath of addition (**Figure 4.11A**). However, after 40 minutes incubation, calcium transients with small amplitudes seemed to follow the regular transients (**Figure 4.11B**). These were deemed abnormal events, and ClampFit event detection quantified them (**Figure 4.11C**). As a percentage of total events, more abnormal events were observed after 40 minute incubation with 1 μM thapsigargin (**Figure 4.11C**). This potentially points to a reduced capacity for calcium re-uptake by SERCA causing high intracellular calcium during diastole which in turn can result in DADs.

In order to assess the ability of thapsigargin to inhibit SERCA, REBL PAT RGECO hiPSC-CMs were incubated for 30 minutes with vehicle only, 100 nM and 1 μM thapsigargin. 10 mM caffeine was then added to the hiPSC-CMs to induce Ca^{2+} release. At 1 μM thapsigargin, no calcium transient spike was observed, suggesting a lack of Ca^{2+} within SR stores (**Figure 4.11D, E**). The calcium transient amplitude was also noticeably reduced with increasing thapsigargin concentration (**Figure 4.11D, E**). This suggests that SERCA blockade impedes the ability to refill the SR store.


A
REBL PAT RGECO
1 μM Thapsigargin
5 min
T
F/F0
Seconds
B
REBL PAT RGECO
1 μM Thapsigargin
40 min
F/F0
Seconds


C
Events detected
Events detected
1 μM Thapsigargin
5 min
1 μM Thapsigargin
40 min
Events detected
Abnormal events
Events detected
Abnormal events

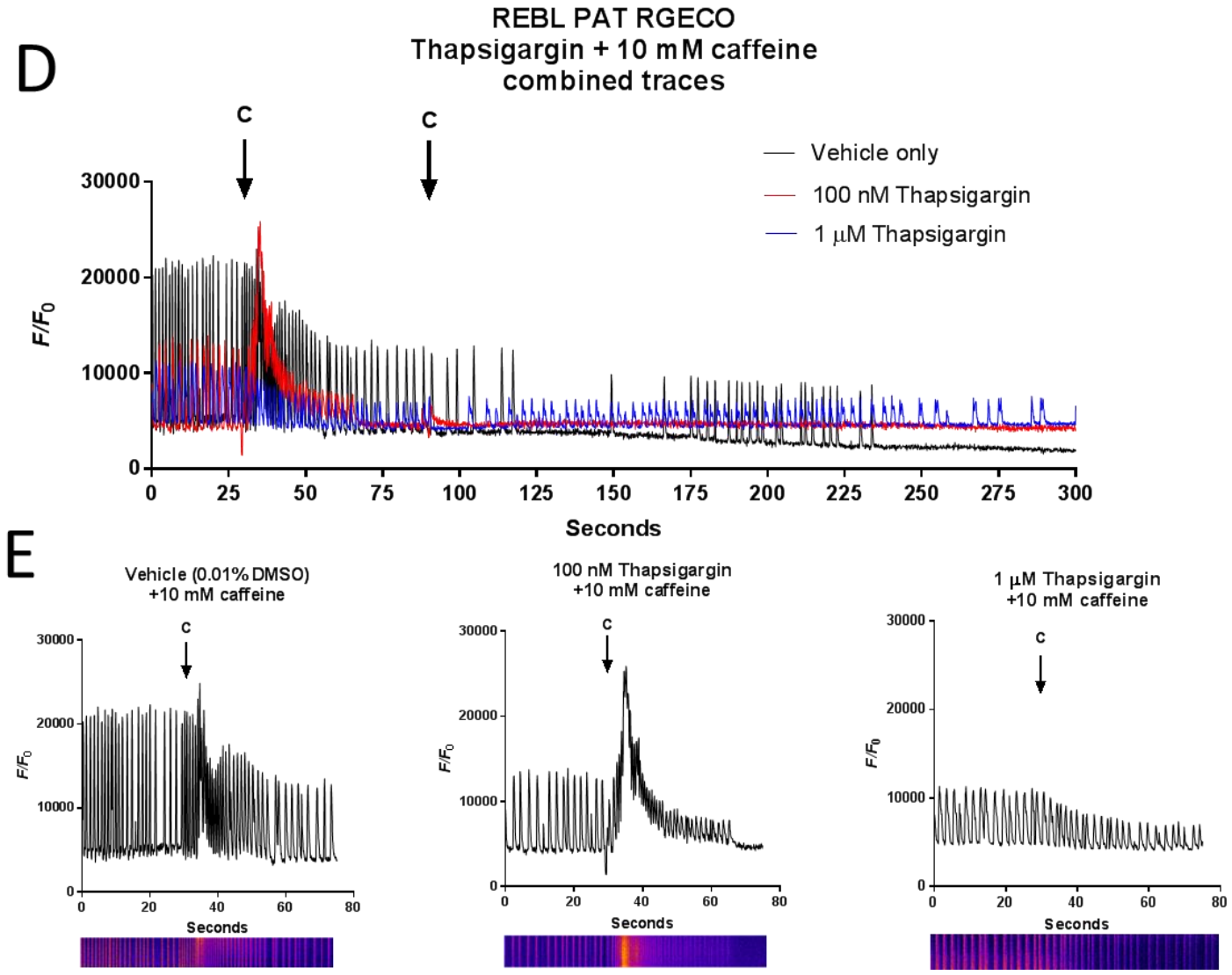


Figure 4.11. Thapsigargin, a non-competitive inhibitor of the sarco/endoplasmic reticulum ATPase, prevents Ca^{2+} re-uptake into the sarcoplasmic reticulum of hiPSC-CMs.

(A) 5-minute confocal line scan of d27 REBL PAT RGECO hiPSC-CM with addition of 1 μM thapsigargin (arrow) at 30 seconds. **(B)** Confocal line scan of REBL PAT RGECO hiPSC-CM after 40 minutes incubation with 1 μM thapsigargin. Several abnormal calcium transients (inset – red arrows) can be observed. **(C)** ClampFit event detection of **A** & **C**, showing more abnormal events after incubation with 1 μM Thapsigargin (n = 1). **(D)** Combined confocal line scans of hiPSC-CMs incubated for 30 minutes with vehicle only, 100 nM or 1 μM thapsigargin. 10 mM caffeine was added at 30 seconds and 90 seconds (arrows) to induce Ca^{2+} release from the SR. **(E)** Confocal line scans from **D**, enlarged for the first 75 seconds of scan. After incubation with 1 μM thapsigargin, no calcium transient spike is seen upon 10 mM caffeine addition (arrows) due to potent inhibition of Ca^{2+} re-uptake into the SR.

To further study the function of the SR in hiPSC-CMs, ryanodine, a ligand for ryanodine receptors (RyRs) was applied to REBL PAT RGECO hiPSC-CMs (**Figure 4.12**). The effect of incubation with 1 μM ryanodine was tested by comparing line scans taken at 5 minutes and 40 minutes after addition. ClampFit event detection of line scans calculated the inter-event interval of each calcium transient event, and a significant variation in this parameter occurred after incubation with ryanodine (**** $p < 0.0001$) (**Figure 4.12A**). This indicated that calcium transients became less regular and more aberrant after a short period of incubation with the drug.

With this in mind, a range of ryanodine concentrations from 100 nM to 3 μM, were applied to REBL PAT RGECO hiPSC-CMs and incubated for 40 minutes before a 300-second line scan was performed. These line scans and their associated kymographs showed a highly irregular calcium transient pattern at 1 μM and 3 μM ryanodine (**Figure 4.12B**). Box plots of the inter-event intervals from these line scans showed a significant difference from vehicle only control at all concentrations of ryanodine, but a particularly large variance at micromolar concentrations (**Figure 4.12C**). This suggests that the aberrant response of hiPSC-CMs to ryanodine begins to occur at micromolar concentrations of the RyR ligand.

Finally, the number of events detected during a 300-second line scan nearly doubled from 240 events in vehicle control, to 443 events in the presence of 300 nM ryanodine. This is in contrast with only 77 events detected at 1 μM ryanodine, likely due to the aberrant pattern of calcium transients (**Figure 4.12D**). This supports the observation that hiPSC-CMs show differential responses to ryanodine depending on whether the drug is applied at nanomolar or micromolar concentrations.

Taken together with previous results from caffeine and thapsigargin, these results point towards a somewhat functional SR within hiPSC-CMs, capable of releasing Ca^{2+} into the cytosol through RyRs, and subsequently replenishing Ca^{2+} stores using SERCA as a pump. However, a substantial reliance on sarcolemmal flux for calcium transient persistence cannot be excluded.

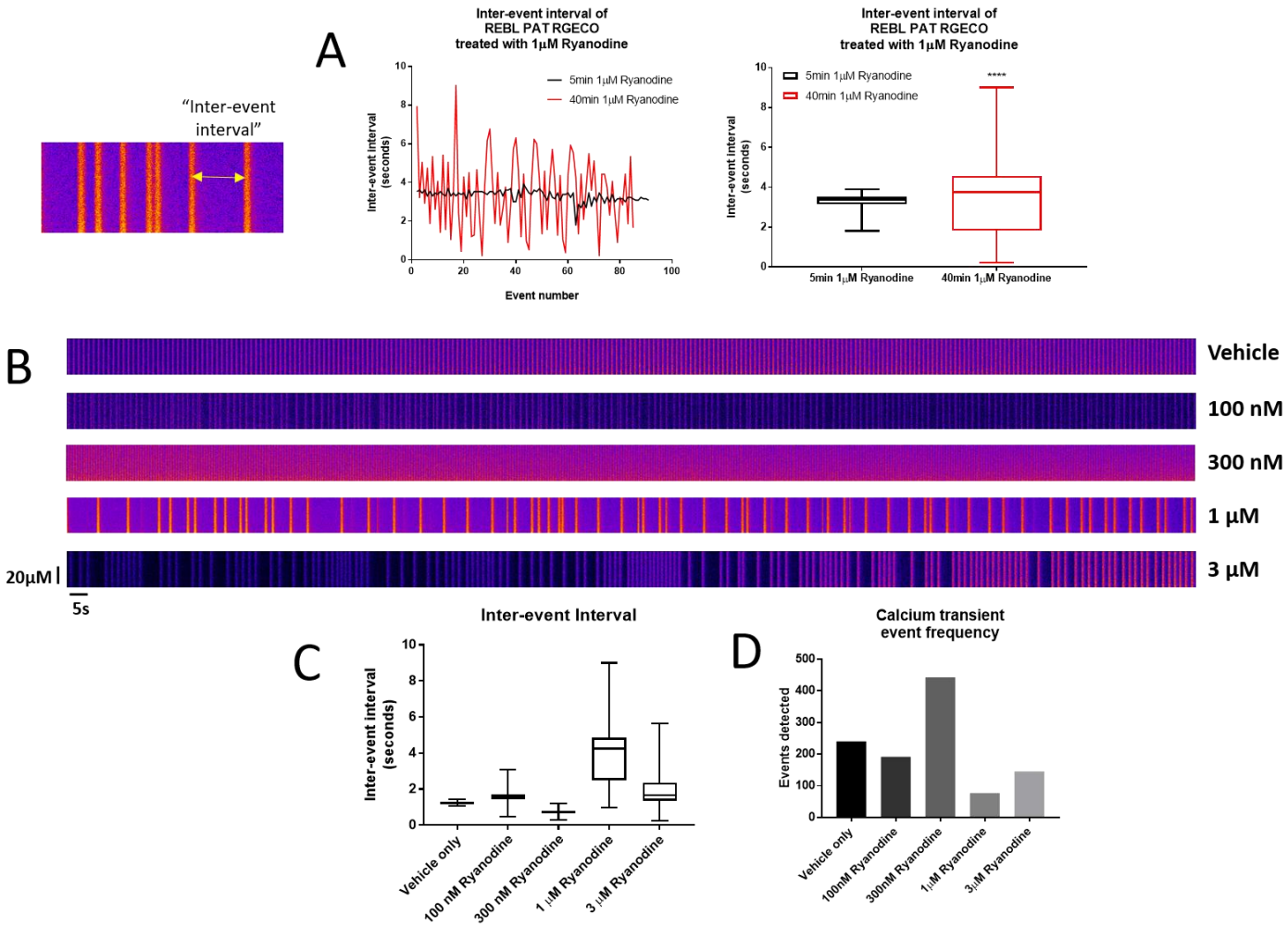


Figure 4.12. Micromolar concentration of ryanodine cause decreased beat rate and an increased frequency of arrhythmic events in targeted hiPSC-CMs.

(A) Addition of 1 μM ryanodine causes greater variation in inter-event interval, and thus, more arrhythmic events, after incubation for 40 minutes (red line). Box plots show significantly greater variance in inter-event interval after 40 minute incubation with 1 μM ryanodine. n = 96 events, F-test for variance, **** $p < 0.0001$. **(B)** 5-minute confocal line scan kymographs of increasing concentrations of ryanodine applied to d23 RGECO hiPSC-CMs and incubated for 40 minutes before analysis. Irregular occurrence of calcium transient events can be seen at 1 μM and 3 μM. **(C)** Min to Max box plots show an increased variance of inter-event interval at micromolar concentrations of ryanodine, compared to nanomolar concentrations. Data sets compared to vehicle only control. n > 83 events. **(D)** Number of calcium transient events detected over a 5 minute confocal line scan at different ryanodine concentrations. Events detected reduce at micromolar concentrations of ryanodine (n = 2 plates).

To test the ß-adrenergic system of hiPSC-CMs, the non-selective ß–adrenoreceptor agonist isoprenaline was added to cells. Confocal line scans of REBL PAT RGECO hiPSC-CMs revealed an immediate response to the addition of as little as 100 nM isoprenaline. After addition, the beat rate increased, as illustrated by the increased frequency of calcium transient events (**Figure 4.13A**).

In REBL PAT RGECO hiPSC-CMs, the number of events detected by ClampFit software during a 300-second line scan increased significantly after just 5 minutes exposure to 3 µM of the ß–adrenoreceptor agonist (* p = 0.0341) (**Figure 4.13B**).

Ratiometric REBL PAT GEM-GECO hiPSC-CMs were then used to further illustrate the effect of isoprenaline. The calcium transient frequency of a hiPSC-CM increased noticeably after 5 minutes incubation with 1 µM isoprenaline (**Figure 4.13C**).

These results confirm that stimulation of the ß–adrenergic system in the hiPSC-CMs generated causes an increase in spontaneous beat rate. Thus, the positive chronotropic effect of isoprenaline within this context is confirmed.

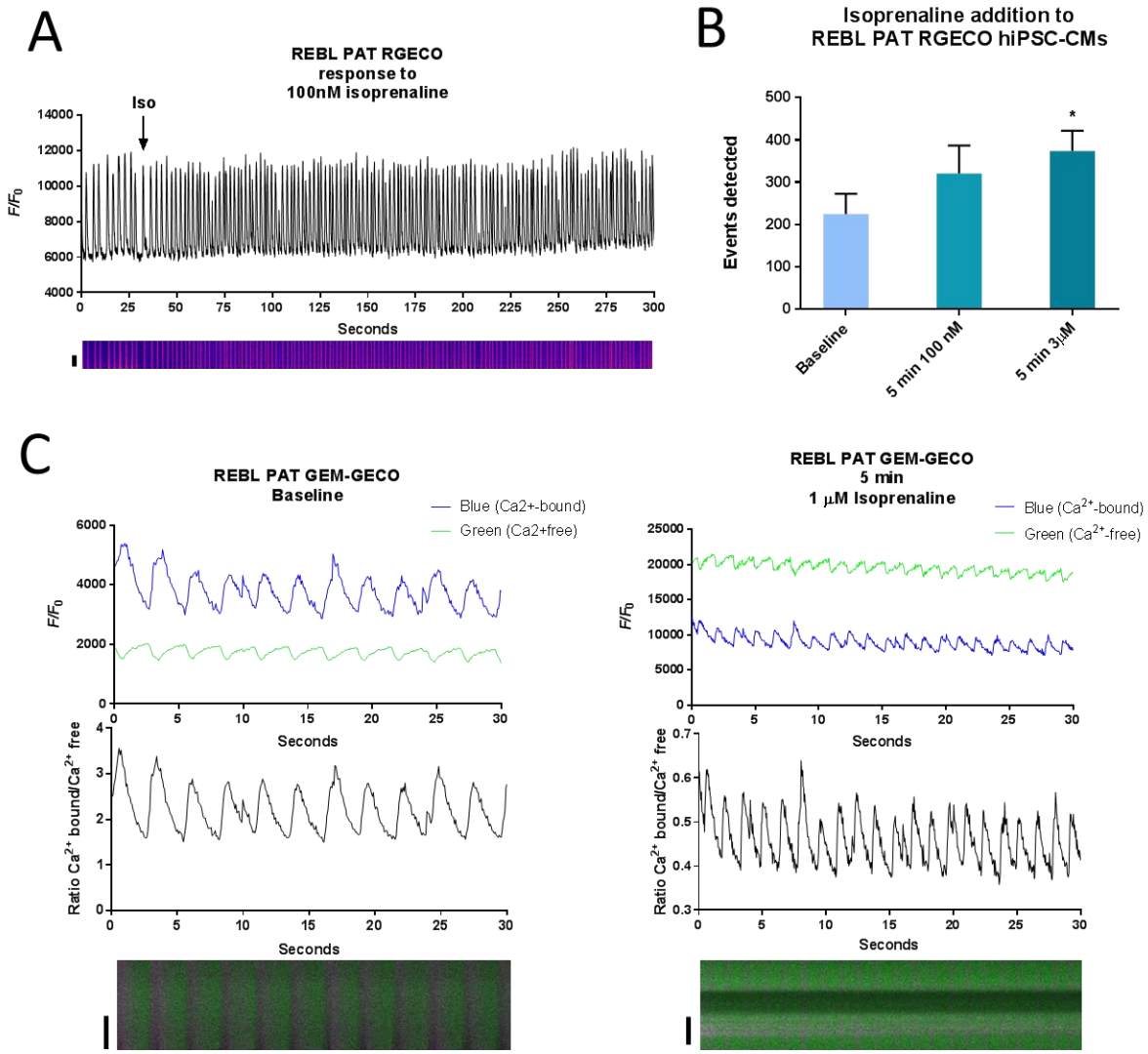


Figure 4.13. Isoprenaline, a non-selective ß-adrenoreceptor agonist, increases calcium transient frequency and beating rate of hiPSC-CMs.

(A) Confocal line scan showing addition of 100 nM isoprenaline to d25 REBL PAT RGECO hiPSC-CM causing an immediate increase in the frequency of calcium transient events. **(B)** ClampFit event detection of 300-second line scans of REBL PAT RGECO hiPSC-CMs exposed to isoprenaline for 5 minutes. Increasing concentration of isoprenaline increases the number of events detected compared to baseline control. Mean ±SD, n = 3 line scans across 2 experiments. Kruskal-Wallis test with Dunn's multiple comparison test, * p = 0.0341. **(C)** Ratiometric confocal line scan of d28 REBL PAT GEM-GECO hiPSC-CM at baseline (left) and after 5 minutes incubation with isoprenaline (right). Increased calcium transient event frequency is seen after isoprenaline treatment. Scale bars = 20 μm.

Nifedipine, an L-type Ca^{2+} channel blocker, is known as a negative chronotrope. A range of concentrations of nifedipine were added to REBL PAT RGECO hiPSC-CMs to establish the level at which an effect could be seen within the standard 300-second confocal line scan (**Figure 4.14**). At 100 nM and 300 nM nifedipine there was a subtle decrease in calcium transient peak amplitude but no immediate reduction in beat rate. However, at 1 µM nifedipine, calcium transient event frequency gradually slowed to a stop within 1 minute of addition. At 3 µM nifedipine, the hiPSC-CM immediately stopped spontaneously beating (**Figure 4.14A**). By calculating the number of calcium transient events occurring in each 30-second segment of the line scan, and normalising for differences in intrinsic beat rate, it is clear that micromolar concentrations of nifedipine are required to block the L-type Ca^{2+} channels of hiPSC-CMs and elicit a negative chronotropic response (**Figure 4.14B**).

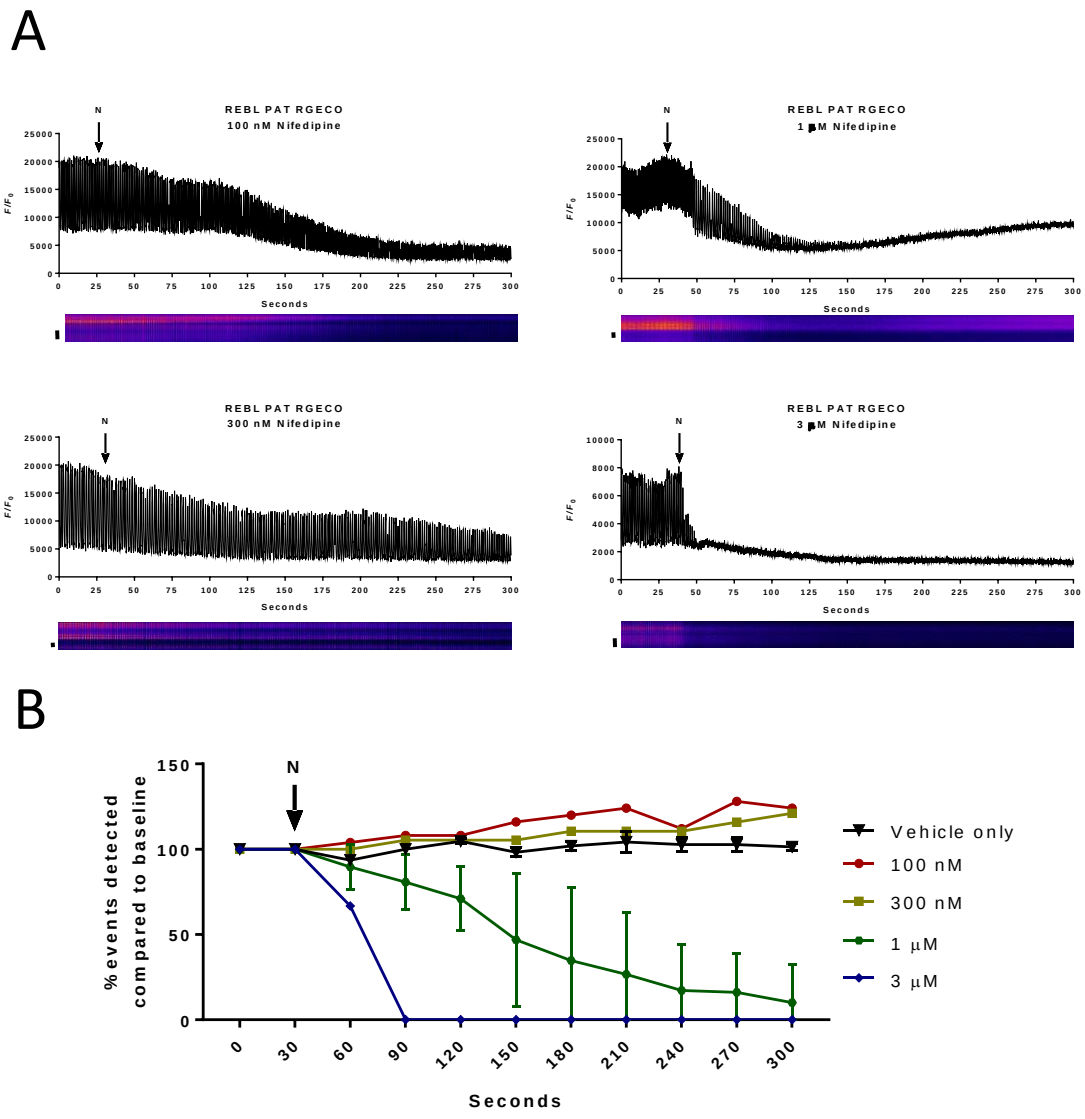


Figure 4.14. Nifedipine, an L-type Ca^{2+} channel blocker, reduces calcium transient frequency and beating rate of healthy hiPSC-CMs.

(A) Confocal laser line scans of d25, d26 or d28 REBL PAT RGECO hiPSC-CMs with addition of varying concentrations of nifedipine at 30 seconds (arrows). At micromolar concentrations of nifedipine, calcium transient events slow down to an eventual stop. Scale bars = 20 µm. **(B)** ClampFit event detection of confocal line scans with events binned into 30-second segments. Number of events were converted into a percentage to normalise for varying beat rate. Event detection failure is seen at micromolar concentrations of nifedipine. Arrows indicate nifedipine addition to the well. Mean ±SD, n = 3 vehicle only; n = 5 1 µM nifedipine; n = 1 all other concentrations.

Finally, the Na^+/Ca^{2+} exchanger (NCX) was blocked with the competitive antagonist nickel chloride (NiCl). The addition of 5 mM (**Figure 4.15A**), and 1 mM (**Figure 4.15B**) NiCl led to the abolition of calcium transient events in hiPSC-CMs within 45 seconds. At a concentration of 500 µM NiCl, inactivity of calcium flux was only temporary, and returned to baseline levels (**Figure 4.15C**). This highlights the competitive antagonist mechanism of NiCl inhibition of NCX. At lower concentrations of 100 µM NiCl, no apparent change occurred to the calcium transients detected during the line scan (**Figure 4.15D**). This shows that competitive inhibition of NCX, or other calcium channels such as L-type calcium channels, by nickel ions occurs in concentration-dependent manner.

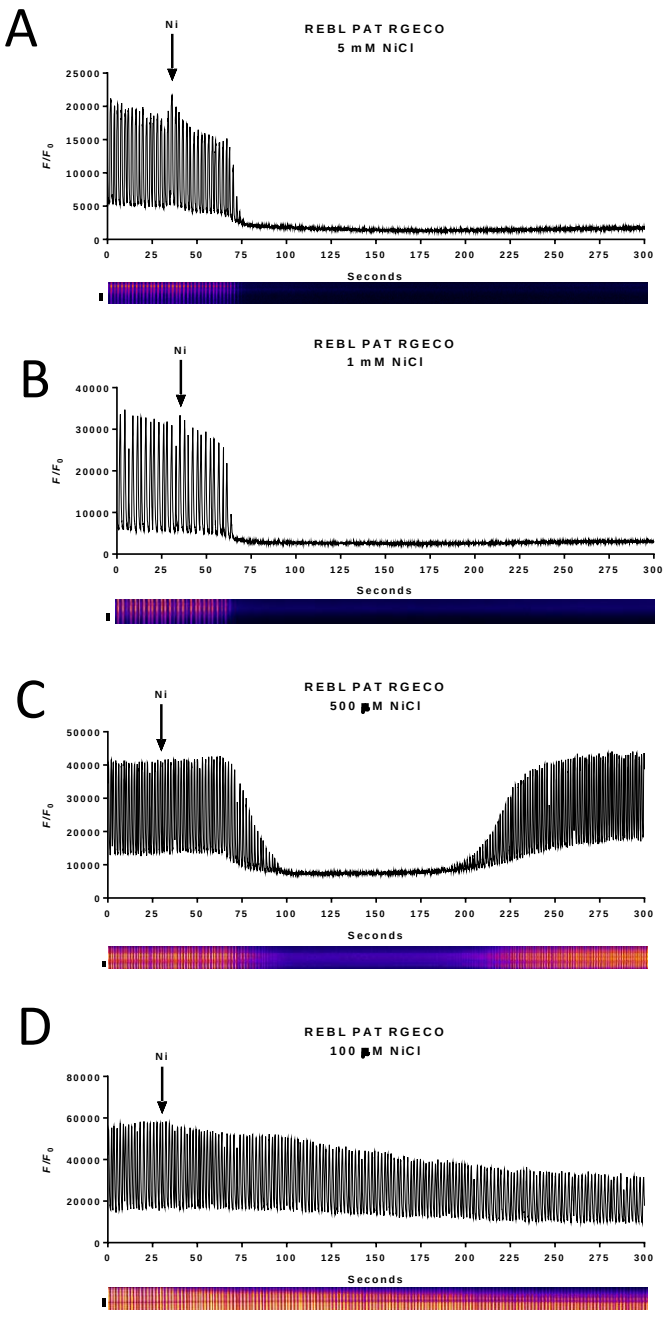


Figure 4.15. Inhibition of the Na^+/Ca^{2+} exchanger by nickel chloride.

Confocal line scans of d24 REBL PAT RGECO hiPSC-CMs with the addition of **(A)** 5 mM, **(B)** 1 mM, **(C)** 500 µM or **(D)** 100 µM nickel chloride at 30 seconds (indicated with arrow). Scale bars = 20 µm.

4.4 Discussion

In this chapter, wild-type hiPSC-CMs that expressed genetically encoded calcium indicators were applied as tools to study calcium transients *in vitro*. In direct comparisons with chemical calcium indicator dyes, targeted hiPSC-CMs displayed their superiority in terms of cell viability and long-term usage. An appropriate microscopy platform for detecting calcium transients was chosen, and ClampFit electrophysiology software was repurposed in order to efficiently quantify calcium transient events. Wild-type GEM-GECO and R-GECO hiPSC-CMs were then challenged with a range of compounds of known action to interrogate their calcium handling ability. Our hiPSC-CMs display functional L-type Ca^{2+} channels, a sarcoplasmic reticulum Ca^{2+} store that is released through ryanodine receptors, and can remove intracellular calcium via SERCA2a or NCX. In addition, our hiPSC-CMs have a functioning β–adrenergic system, capable of inducing a positive chronotropic response. These hiPSC-CMs are therefore adequate *in vitro* surrogates for cardiomyocytes, and can be used in the next chapter to model calcium dysfunction as a result of genetic mutations.

4.4.1 GECIs offer increased experimental flexibility compared to chemical calcium indicator dyes

Chemical calcium indicators were compared to GECIs by observing dye extrusion over time (**Figure 4.5**) and cell viability in response to dye (**Figure 4.6**).

The extrusion of the chemical calcium indicator Fluo-4 AM illustrates the limitations of using this method during experiments that are performed over the space of a few hours. Given that this extrusion is a gradual process, data from the start of experiments may not necessarily be comparable to data generated at the end of experiments when dyes are used to measure calcium transients. Indeed, studies conducted in other laboratories using Fluo-4 AM on hiPSC-CMs have shown a 10x decrease in fluorescence amplitude after just 3 hours (Cerignoli et al., 2012). This severely limits the application of calcium dyes for high-throughput drug screening applications.

The percentage of RGECO fluorescent cells detected also reduced slightly during the first hour of the time-course (**Figure 4.5C**). This is likely due to permanent photobleaching, caused by photolysis of covalent bonds surrounding the fluorophore (Greenbaum et al., 2000). These issues have recently been addressed with iterative rounds of molecular evolution using fungi to develop a new green GECI, FGCaMP

(Barykina et al., 2017). FGCaMP can return to 100% fluorescence recovery after photobleaching, compared to only 50% for G-GECO1.2.

Both Fluo-4 AM and Calcium Crimson AM calcium indicator dyes caused a significant loss of hiPSC-CM viability (**Figure 4.6**). Although required to cross the lipid membrane, cleavage of the acetoxymethyl ester bond is known to release the cytotoxic by-products formaldehyde and acetic acid (Schultz et al., 1993). Calcium Crimson AM also suffers from poor loading efficiency (Zhao et al., 1997), and this was experienced when attempting to image hiPSC-CMs loaded with Calcium Crimson AM on the Operetta™ high content platform (data not shown). A recent review claimed that Calcium Crimson AM has only featured in ten publications (Oheim et al., 2014), underlining its ineffectiveness.

Despite the increased workload associated with generating GECI lines, these experiments justify the use of genetically encoded calcium indicators to study calcium transients *in vitro* in an efficient and reproducible manner.

4.4.2 Confocal line scans are more suited to data acquisition from ratiometric calcium indicators

On the DeltaVision widefield microscope, slow acquisition of fluorescence signal from GEM-GECO was caused by the need to switch emission filters between each image. Simultaneous emission detection and thus ratiometric measurements, could not be made as a result. This eventually led to migration to the confocal microscope for data acquisition.

Confocal laser line scan microscopy provided data on whole-cell Ca^{2+} transients over time. Notably, the line scan kymographs revealed a "U-shaped" calcium transient, indicating a propagation of Ca^{2+} starting at the periphery of the cell and moving towards the centre (**Figure 4.8E**). This is commonly seen in confocal line scan images of neonatal cardiomyocytes and is caused by loose coupling between sarcolemmal Ca^{2+} channels and the SR (Louch et al., 2015). This provides some evidence that our hiPSC-CMs are not entirely mature, and lack certain ultrastructural components such as t-tubules, that are instrumental in efficient Ca^{2+} wave propagation. Indeed, mature ventricular cardiomyocytes display a uniform calcium transient on confocal line scans due to a near synchronous SR calcium release facilitated by an extensive t-tubule system (**Figure 4.16**) (Satin et al., 2008).

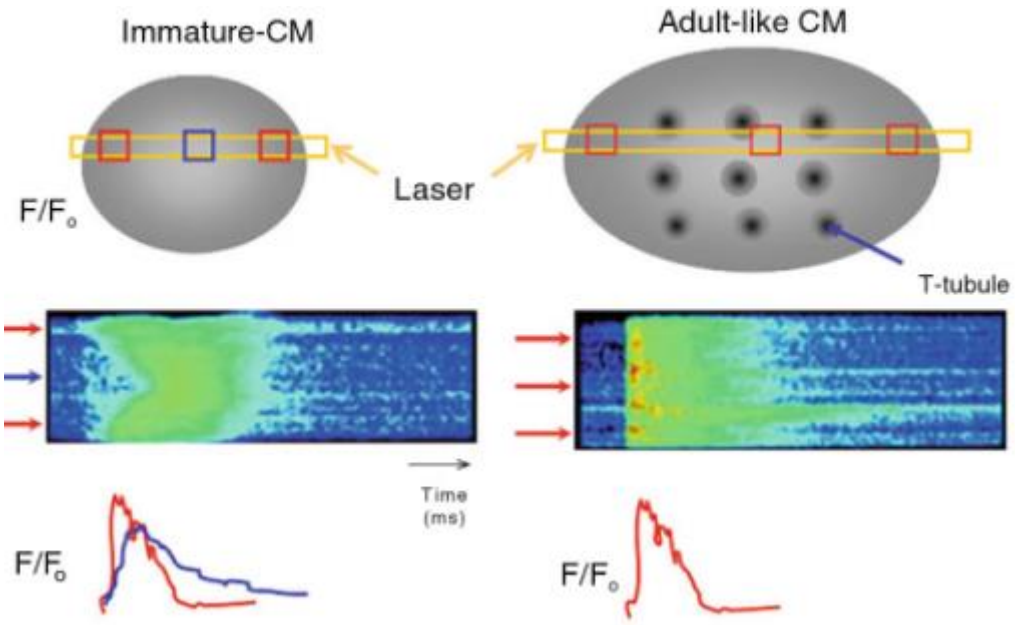


Figure 4.16. Principle of confocal line scan kymographs to assess cardiomyocyte maturity.

Confocal laser line scan microscopy is performed by drawing a laser line across a cardiomyocyte. Temporal fluorescence changes across the whole cell are measured. A U-shaped wavefront is seen in immature cardiomyocytes, as Ca^{2+} wave propagation from the periphery to the centre is slow (left). In mature CMs, the presence of T-tubules allows for fast Ca^{2+} wave propagation and calcium transients appear to be aligned as straight bands. Adapted from (Lee et al., 2011)

Recent advances in maturation of hiPSC-CMs have shown an improvement in Ca^{2+} wave propagation. Treatment of hiPSC-CMs with T3 and dexamethasone, followed by 5 days culture on a matrigel mattress supposedly produces hiPSC-CMs with increased t-tubule density and a uniform calcium transient (Parikh et al., 2017). This demonstrates the potential utility of our targeted hiPSC lines for assessing the effectiveness of new CM maturation protocols.

ClampFit event detection was adapted for use in quantification and measurement of calcium transient frequency and shape. Although useful, this software was not originally intended for calcium transient analysis. Bespoke imaging systems with a focus on optical calcium and voltage measurements from CMs are beginning to be developed. By using a beamsplitter to separate emission wavelengths, a high speed EMCCD camera and custom software to analyse fluorescence changes, optical mapping

of calcium transients in hiPSC-CMs is possible (Lee et al., 2012). Optical mapping can produce even more in-depth data on hiPSC-CMs, such as conduction velocity.

Within our laboratory, a custom-built platform for voltage, contraction and calcium measurements is now available (CellOPTIQ™ – Clyde Biosciences). This platform allows for measurement of fluorescence changes on hiPSC-CMs seeded in multiwell plates, and proprietary software generates data on a wealth of kinetic measurements such as action potential duration, calcium transient duration and contraction force (Duncan et al., 2017). Unfortunately, detection of wavelengths occupied by GEM-GECO and RGECO is not yet possible.

The aforementioned studies rely on calcium dyes, which as discussed, are suboptimal. It will be interesting to apply our targeted hiPSC-CMs to these advanced systems, and future work will aim to achieve this on the CellOPTIQ™ platform.

4.4.3 The calcium handling machinery of hiPSC-CMs is functional yet immature

The individual components of calcium handling in hiPSC-CMs were tested with a variety of inhibitors and activators. These experiments verified a functional, yet somewhat immature calcium handling system in our hiPSC-CMs.

The ratiometric GEM-GECO hiPSC-CMs were ideal for assessing Ca^{2+} release from the SR, as intracellular Ca^{2+} concentration could be more accurately estimated. A single application of 10 mM caffeine successfully released calcium from the SR store, although continued calcium transients suggest some continued reliance on sarcolemmal flux (**Figure 4.10**). Partial or quantal release of Ca^{2+} has been shown with 200 μM caffeine (Kong et al., 2008), and this may have been useful in determining the sensitivity of the SR in our hiPSC-CMs. A further advantage of using genetically encoded calcium indicators in this instance is that caffeine has been shown to interact with commonly used chemical calcium indicator dyes such as fura-2 and fluo-3 (Muschol et al., 1999).

Thapsigargin was applied to RGECO hiPSC-CMs and, after sufficient incubation, began to elicit abnormal calcium transient events (**Figure 4.11A**). This may be caused by the inability of SERCA2a to remove intracellular Ca^{2+} efficiently enough. In adult human cardiomyocytes, SERCA2a is responsible for the re-uptake of around 70% of the

intracellular Ca^{2+} (Bers, 2002). As intracellular Ca^{2+} is then too high during diastole, delayed afterdepolarisations may occur (MacLennan and Kranias, 2003).

On the other hand, the observation that thapsigargin reduced the calcium transient amplitude, suggests a reduced SR Ca^{2+} content leading to a reduced intracellular Ca^{2+} concentration. This has been previously reported in hESC-CMs treated with thapsigargin (Zhu et al., 2009).

The fact that thapsigargin-treated hiPSC-CMs were still able to spontaneously beat, albeit at a lower amplitude, suggests a possible compensatory mechanism. Sarcolemmal Ca^{2+} flux may instead take a leading role in generating calcium transients, and this limited reliance on the SR may point to a more immature phenotype (Liu et al., 2007).

The addition of ryanodine to RGECO hiPSC-CMs resulted in concentration-dependent differences in the calcium transients observed. Calcium transients occurred at a regular rate in the nanomolar range, but became highly irregular at concentrations of 1 μM and above. (**Figure 4.12**). These arrhythmic patterns may be as a result of SOICR, as luminal Ca^{2+} levels increase and sporadic Ca^{2+} leak occurs through the closed RyRs (**Figure 4.17**). This is similar to the mechanism of arrhythmic episodes in catecholaminergic polymorphic ventricular tachycardia (CPVT), a condition caused by mutation to *RYR2* (MacLennan and Chen, 2009).

Nickel ions were used in an attempt to block NCX. However, this approach is very non-selective, and the transient abolition of calcium transients may have been due to competitive antagonism of other Ca^{2+} channels. Recently discovered selective inhibitors of NCX such as ORM-10962 will facilitate more in-depth studies on NCX function in hiPSC-CMs in future (Kohajda et al., 2016).

The interpretation of these experiments would have been vastly enhanced with the addition of qRT-PCR to compare expression levels of each of the calcium handling components to adult CM controls. As previously mentioned, the expression levels of the SR auxiliary proteins calsequestrin, triadin and junctin are thought to be lower in hiPSC-CMs (Liu et al., 2007). Nevertheless, the functional data presented show that

our hiPSC-CMs, although not fully mature, serve as a valid model for disease modelling in chapter 5.

4.4.4 Limitations of using GECIs in hiPSC-CMs for *in vitro* drug screening

The approaches described within this chapter are not without their limitations. Primarily, the immaturity of the hiPSC-CMs that are generated affects the functionality

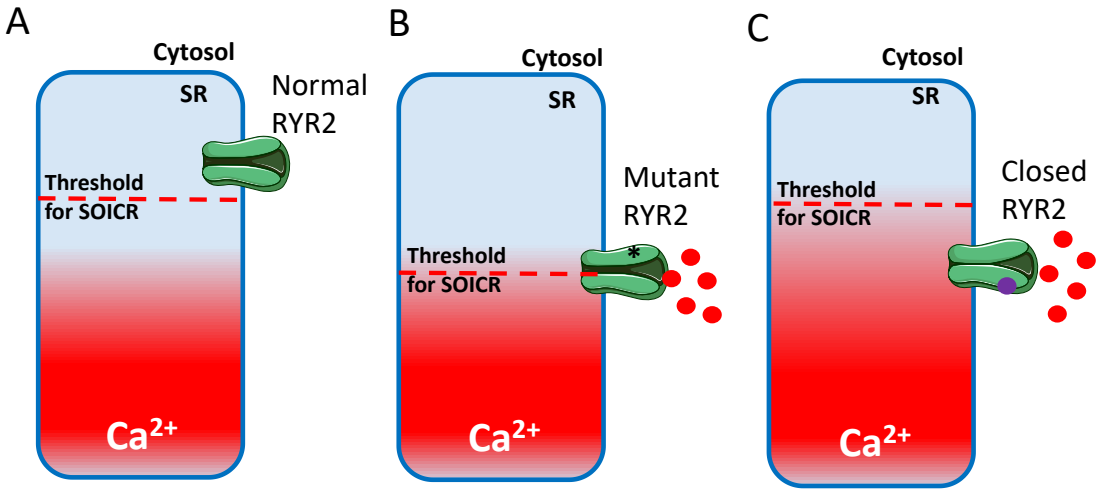


Figure 4.17. The cardiac ryanodine receptor and store overload-induced Ca^{2+} release.

(A) During normal function of RYR2, the threshold for SOICR is not reached and Ca^{2+} is only released during systole. **(B)** Dysfunction of RYR2 caused by mutations, such as in CPVT, lowers the luminal threshold for Ca^{2+} release. Diastolic Ca^{2+} leak through RYR2 results in arrhythmias. **(C)** Micromolar concentrations of ryanodine prevent release of Ca^{2+}, until calcium overload causes diastolic leak of Ca^{2+}. This results in arrhythmias. Adapted from (Jones et al., 2008).

of the cardiomyocytes, and thus alters the interpretation of any drug response (**Section 1.5.7**) (Yang et al., 2014). Some of the drugs of known action tested in this chapter gave unexpected or non-standard responses.

For example, administration of caffeine to adult cardiomyocytes should result in a calcium transient spike followed by a cessation of further calcium transients if the sarcoplasmic reticulum has been fully emptied (Zhu et al., 2009). In the experiments presented in this chapter, calcium transients persisted (**Figure 4.10**). These non-standard responses point to sarcolemmal flux continuing to play a role as a key regulator of calcium transients in hiPSC-CMs due to the immaturity of the calcium handling machinery.

Furthermore, the immediate cessation of beating upon 1 μM nifedipine treatment of hiPSC-CMs correlates with other reports which show that calcium transients in hiPSC-

CMs rely heavily on sarcolemmal flux (**Figure 4.14**) (Itzhaki et al., 2011, Kane et al., 2015). It has also been reported that hiPSC-CMs display non-standard responses to calcium channel agonists such as Bay K8644, showing no significant increase in calcium current amplitude (Kang et al., 2012a).

Other studies have shown that, in hiPSC-CMs, isoprenaline can increase the beating rate, but will not show the same level of positive increase in contraction force that adult cardiomyocytes exhibit (Germanguz et al., 2011). These non-standard drug responses highlight the need to carefully interpret data generated using immature hiPSC-CMs for drug screening.

Another limitation of the approaches used within this chapter is the use of R-GECO1.0 or GEM-GECO as the chosen GECIs for assessing whole cell calcium transients. R-GECO1.0 has a K_d for calcium of 480 nM, whereas GEM-GECO has a K_d for calcium of 340 nM (**Table 3.2**). Given that the intracellular calcium concentration of a cardiomyocyte at rest is approximately 100 nM (Pinnell et al., 2007), a GECI with a K_d of 100 nM would be capable of accurately detecting subtle changes in cytoplasmic calcium. More recently developed GECIs such as GCaMP6f have a K_d for calcium of approximately 90 nM at 37ºC, and may be more suited for use in cardiomyocytes (Helassa et al., 2016).

Despite these limitations, GECIs in hiPSC-CMs provide a valuable tool for assessing the response to different drugs or phenotypic changes that may arise due to mutations.

5 The application of engineered calcium reporter lines for modelling hypertrophic cardiomyopathy and screening potential pharmacological interventions *in vitro*

5.1 Introduction

Having established confocal line scan microscopy as a useful tool for assessing calcium transients in healthy hiPSC-CMs expressing RGECO or GEM-GECO, this chapter utilises the isogenic sets of hiPSC-CMs harbouring mutations to the sarcomeric proteins β-myosin heavy chain (*MYH7* C9123T) or α-cardiac actin (*ACTC1* G301A). These two mutations are known to cause hypertrophic cardiomyopathy (HCM), and this chapter explores how hiPSC-CMs with these mutations, and their wild-type isogenic counterparts, can be used to phenotype HCM *in vitro*. Efforts are then made to rescue the phenotype using pharmacological interventions. Finally, optogenetic pacing of hiPSC-CMs is explored, demonstrating the potential for combination with GECIs and an improved *in vitro* phenotyping and drug screening approach.

5.1.1 Current approaches for treatment of hypertrophic cardiomyopathy

Hypertrophic cardiomyopathy (HCM) is a prevalent disease, with ~1300 causative mutations, characterised by excessive thickening of the left ventricle. Severe complications include arrhythmias, outflow obstruction, and sudden cardiac death (Houston and Stevens, 2014, Marian and Braunwald, 2017) (**Section 1.2**).

Current pharmacological interventions are aimed at preventing the frequency and severity of arrhythmic episodes and preventing obstruction with anticoagulant and antiplatelet drugs. In severe cases, drastic surgery (septal myectomy) may be performed (Maron et al., 2011a), or an artificial cardiac pacemaker installed.

As the model developed within this thesis is a 2D, *in vitro* model, it is most suited to assessing the effectiveness of antiarrhythmic drugs. However, current antiarrhythmics may not be effective for all cases of HCM, or may cause adverse side-effects (Spoladore et al., 2012). Here, we explore current and future pharmacological interventions for HCM.

In terms of tackling arrhythmia in HCM, the primary treatment would be the use of ß-blockers such as propranolol (Frank et al., 1983, Östman-Smith, 2014). Propranolol is a non-selective ß-adrenergic receptor blocker (**Figure 5.1**), and has been a mainstay in HCM treatment for decades (Spoladore et al., 2012). Its ability to slow the heart rate has beneficial effects on ventricular relaxation time and excitability. However, adverse side-effects such as breathing problems and dizziness can occur. In some patients, propranolol is not effective and arrhythmic episodes persist. In these cases, other ß-blockers such as bisoprolol are an option, although its specificity for the ß1-adrenoreceptor subtype renders is less useful for studies involving hiPSC-CMs, which lack robust ß1-adrenoreceptor expression (Wu et al., 2015).

The Ca^{2+} channel blocker verapamil is often the next standard drug of choice for the treatment of non-obstructive HCM (Spoladore et al., 2012). Ca^{2+} channel blockers in general are favoured for their negative chronotropic and inotropic properties. By reducing the influx of Ca^{2+}, the risk of diastolic release of Ca^{2+} from the SR is reduced. For these reasons, diltiazem is undergoing phase III clinical trials for the treatment of preclinical HCM (Ho et al., 2015) (**Table 5.1**).

Other approved antiarrhythmic drugs include amiodarone, sotalol, disopyramide and cibenzoline (Houston and Stevens, 2014) (**Table 5.1**) (**Figure 5.1**). However, a retrospective study based on a patient cohort of 173 found that sudden cardiac death could still occur in patients on continual pharmaceutical therapy. Sudden death occurred in 20% of patients administered amiodarone (6/30), 9% each of patients taking verapamil (4/46) or beta blockers (7/76), and 0% of those taking sotalol (0/21) (Melacini et al., 2007). This highlights the need to develop better antiarrhythmics for HCM, to protect against the risk of sudden cardiac death in patients.

Table 5.1. Approved drugs for the treatment of symptoms associated with hypertrophic cardiomyopathy.

Drug	Antiarrhythmic classification	Mechanism	IC_{50}	References
Propranolol	Class II	Non-selective ß-adrenergic receptor blocker	12 nM	(Frank et al., 1983)
Amiodarone	Class III	Ca^{2+}, Na^{+}, K^{+} blocker	2.8 µM (I_{Kr}) 3.84 µM (I_{Ks}) 4.84 µM (I_{Na}) 5.8 µM (I_{CaL}) 15.6 µM (I_{NaK})	(Elliott et al., 2014, Loewe, 2016)
Sotalol	Class III	Non-selective ß-adrenergic receptor blocker, K^{+} blocker	12 nM (ß-AR) 1.2 mM (I_{Kr})	(Tendera et al., 1993, Vormberge et al., 2006)
Verapamil	Class IV	L-type Ca^{2+} channel blocker, inward potassium (K_{ir}) blocker	150 nM (I_{CaL}) 9 µM (K_{ir}) 37.6 µM (I_{Na})	(Houston and Stevens, 2014, Gregor and Čurila, 2015)
Diltiazem	Class IV	L-type Ca^{2+} channel blocker, inward potassium (K_{ir}) blocker	150 nM (I_{CaL}) 53.2 µM (I_{Na}) 6.57 µM (I_{Kr})	(Houston and Stevens, 2014, Ho et al., 2015, Gregor and Čurila, 2015)

Disopyramide	Class IA	K+ blocker, fast sodium channel ($Na_V1.5$) inhibitor	302.3 µM ($Na_V1.5$) 4 µM (I_{Kr})	(Verlinden and Coons, 2015, Harmer et al., 2011)
Cibenzoline	Class IA	K^+ blocker	2 µM (I_{Kr}) 46.5 µM ($Na_V1.5_L$)	(Hamada et al., 1997, Crumb et al., 2016)

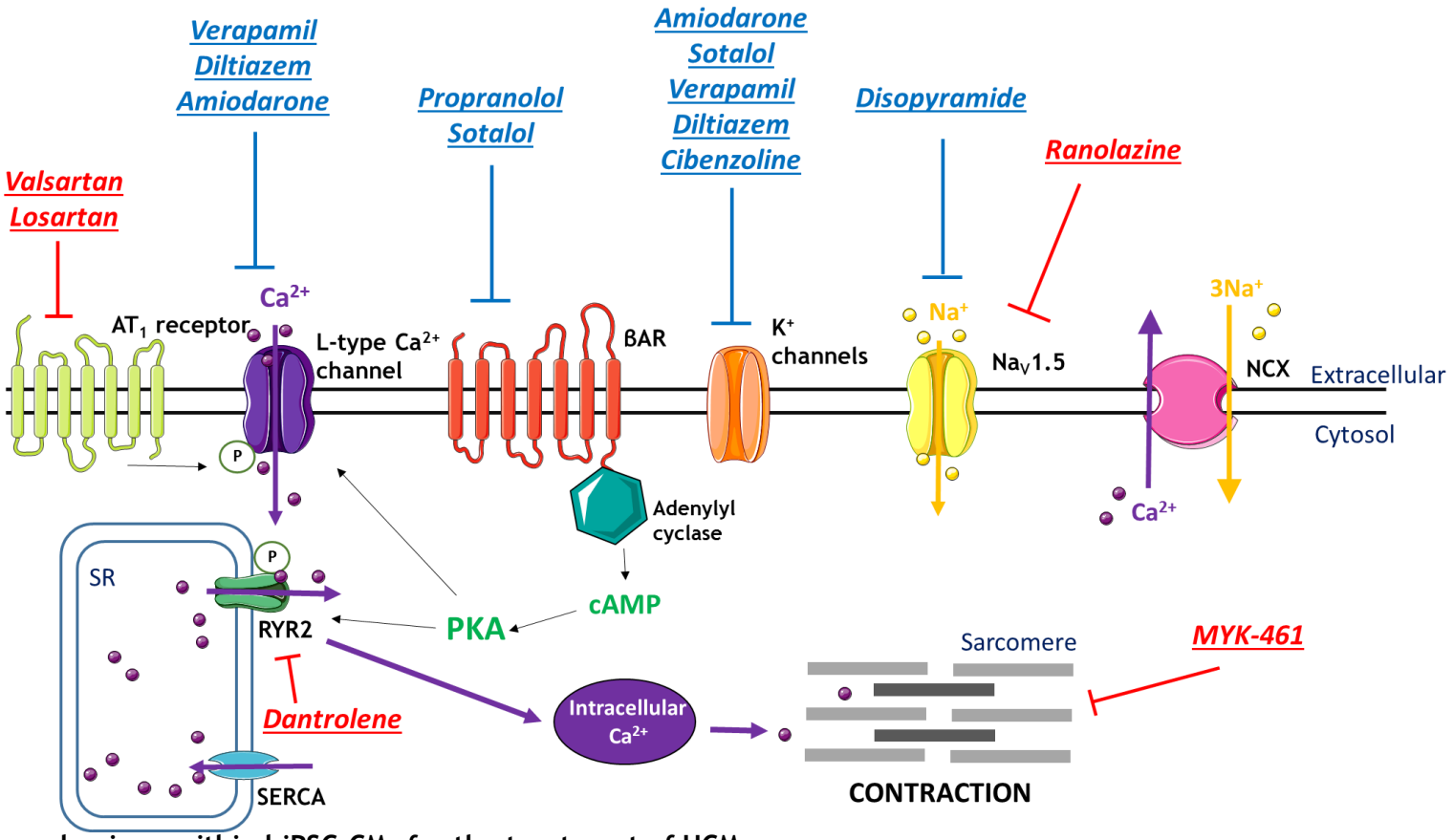


Figure 5.1. Drug mechanisms within hiPSC-CMs for the treatment of HCM.

Schematic of approved and potential drugs for HCM and their mechanism of action. Almost all compounds directly or indirectly reduce intracellular Ca^{2+}. Approved drugs in blue, experimental compounds in red. AT_1 receptor – angiotensin II receptor; βAR - β-adrenergic receptor; NaV1.5 – sodium channel; NCX – Na^+/Ca^{2+} exchanger; SR – sarcoplasmic reticulum; SERCA – sarcoplasmic reticulum Ca^{2+}/ATPase; RYR2 – ryanodine receptor; P – phosphorylation.

Angiotensin II converting enzyme (ACE) inhibitors may also be beneficial for patients with non-obstructive HCM. Though most studies to date have focused on the ability of ACE inhibitors to prevent myocyte disarray and fibrosis in mouse models of HCM by downregulating the angiotensin-renin system (Lim et al., 2001a).

Angiotensin II receptor blockers (ARBs) such as losartan and valsartan, on the other hand, have a more relevant mechanism as angiotensin II receptors are known to phosphorylate and activate L-type calcium channels (Ho et al., 2017) (**Figure 5.1**). In this way, they may have utility in regulating heart rate and arrhythmic episodes in a similar way to approved Ca^{2+} channel blockers like verapamil. However, losartan has recently shown no clinical benefit compared to placebo in a large, randomised trial (Axelsson et al., 2016), and thus valsartan will be assessed in this chapter.

Ranolazine, a late sodium channel (I_{NaL}) blocker, has been tested on cardiomyocytes isolated from patients with severe HCM undergoing septal myectomy (Coppini et al., 2013). It is thought that ranolazine shortens the action potential duration in diseased cardiomyocytes, reducing the occurrence of arrhythmias by improving the kinetics of calcium transients. Furthermore, the reduction in intracellular Na^+ theoretically enhances the rate at which NCX removes intracellular Ca^{2+}, thereby preventing arrhythmias associated with intracellular calcium overload (Rayner-Hartley and Sedlak, 2016) (**Figure 5.1**).

Dantrolene is an antiarrhythmic drug that has found utility in treating catecholaminergic polymorphic ventricular tachycardia (CPVT) *in vitro*, through its mechanism of stabilising the ryanodine receptor and preventing diastolic Ca^{2+} leak (Jung et al., 2012) (**Figure 5.1**). However, few studies have tried to apply this drug to a human model of HCM, with only mouse models of a troponin T mutation having been evaluated (Okuda et al., 2018).

Hypercontractility is a hallmark of some forms of hypertrophic cardiomyopathy, including the *ACTC1* G301A mutation (Song et al., 2011). Efforts to reduce contractility are now finding traction, and an experimental ß-MHC ATPase, MYK-461 has recently gained orphan drug designation by the FDA for the treatment of HCM (Green et al., 2016).

Contractile force is mediated by the relationship between β-myosin heads and actin filaments. Upon binding, these two sarcomeric proteins slide past each other and this causes contraction (**Figure 5.2**). The hydrolysis of ATP is essential for the uncoupling of this partnership, and for the cycle to start again (**Figure 5.2**). The β-MHC spends around 10% of its ATPase chemomechanical time strongly bound to actin (**Figure 5.2**, lower illustrations) (Kawas et al., 2017, Green et al., 2016). MYK-461 inhibits this ATPase, preventing more myosin heads from releasing the actin filament and producing contractile force. In this way, an overall reduction in force is achieved, and hypercontractility can be relieved. Given the specificity of MYK-461 for β-MHC, and the hypercontractile phenotype seen in mouse models of *ACTC1* G301A, we sought to test this novel compound in our *in vitro* HCM models.

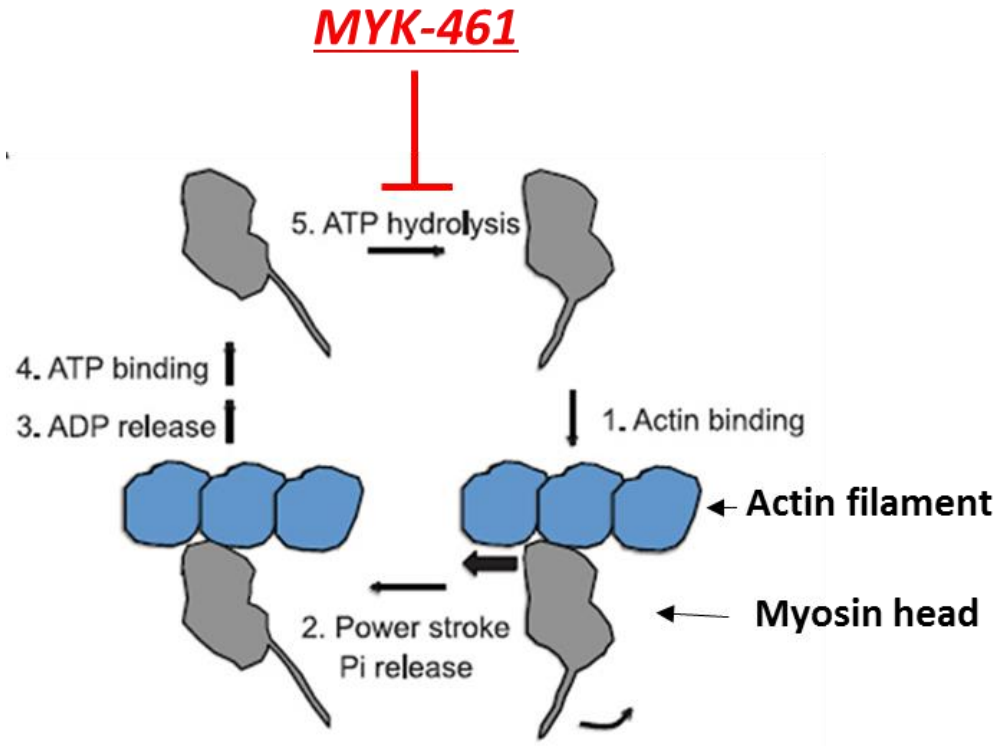


Figure 5.2. MYK-461 inhibition of myosin ATPase reduces contractile force by slowing actin binding.

Contractile force is mediated by the interaction between myosin (grey) and actin (blue). When bound, force is generated. The hydrolysis of ATP by myosin ATPase permits binding of myosin to actin. MYK-461 inhibition of this process results in more myosin heads being unable to bind actin, and therefore reduces contractility. Adapted from (Green et al., 2016).

Drug	Mechanism	IC_{50}	References
MYK-461	β-MHC ATPase inhibitor	710 nM	(Green et al., 2016, Kawas et al., 2017)
Losartan	Angiotensin II receptor I (AT_1) antagonist	20 nM (AT_1 receptor)	(Shimada et al., 2013, Axelsson et al., 2016, Kurtz and Kajiya, 2012)
Valsartan	Angiotensin II receptor I (AT_1) antagonist	44.9 nM (AT_1 receptor)	(Ho et al., 2017, Kurtz and Kajiya, 2012)
Ranolazine	Late sodium current (I_{NaL}) inhibitor	6.4 μM (I_{Kr}) 7.8 μM (I_{NaL})	(Coppini et al., 2013, Crumb et al., 2016)
Dantrolene	RYR2 antagonist	160 nM (RYR2)	(Jung et al., 2012, Okuda et al., 2018, Oo et al., 2015)

Table 5.2. Experimental drugs for the treatment of symptoms associated with hypertrophic cardiomyopathy.

Due to the heterogeneity of causative gene mutations and clinical outcome, there is a need to test antiarrhythmic drugs *in vitro* within different genetic backgrounds. The *MYH7* C9123T isogenic trio, and *ACTC1* G301A isogenic pair of hiPSC-CMs generated in **Chapter 3**, allow us to investigate both current and future drug therapies on two different human models of HCM. The detection and analysis of GECI response to calcium transients developed in **Chapter 4** will help to evaluate phenotype and drug response.

5.1.2 Optogenetics and the advent of optical pacing in hiPSC-CMs

In the realm of *in vitro* drug screening, the pacing of hiPSC-CMs is desired, as it enables the assessment of drugs throughout the physiological range of heart rate (Huang et al., 2017). Furthermore, as protocols to enhance the maturity of hiPSC-CMs progress, spontaneous beating activity will be lost, and pacing will be essential (Satin et al., 2004).

Optogenetics has been defined as the ability to control the function of genetically engineered cells with light (Nagel et al., 2003, Deisseroth et al., 2006). The capacity to initiate action potentials with light has been utilised extensively in the field of neuroscience (Ng et al., 2002, Boyden et al., 2005), and has recently expanded into the field of cardiac optogenetics (Koopman et al., 2017).

Optical control of cells with light is achieved with the use of light-gated ion channels, which permit the flow of ions in or out of cells upon stimulation with specific wavelengths. A gene derived from the algae *Chlamydomonas reinhardtii* that encodes a light-gated cation channel, channelrhodopsin-2 (ChR2), was one of the first optogenetic actuators to be exploited for optical control (Nagel et al., 2003, Hegemann et al., 2005).

ChR2 is a transmembrane protein of the light-sensitive rhodopsin family of opsins, and relies on all-trans-retinal to absorb photons (Muller et al., 2011, G et al., 2013) (**Figure 5.3A**). Upon photostimulation with blue (470 – 480 nm) light, rapid depolarisation occurs within 50 milliseconds of illumination (G et al) (**Figure 5.3B**). In this way, ChR2 can mediate precise control of action potentials.

However, ChR2 can suffer from desensitisation, whereby repeated illumination can lead to an 80% reduction in peak response to a steady state level (Nagel 2002). As a result, this desensitisation means that a fivefold higher expression of ChR2 is required to achieve depolarisation above threshold after desensitisation. Poor membrane trafficking can also negatively affect the use of ChR2 (Lin et al., 2009).

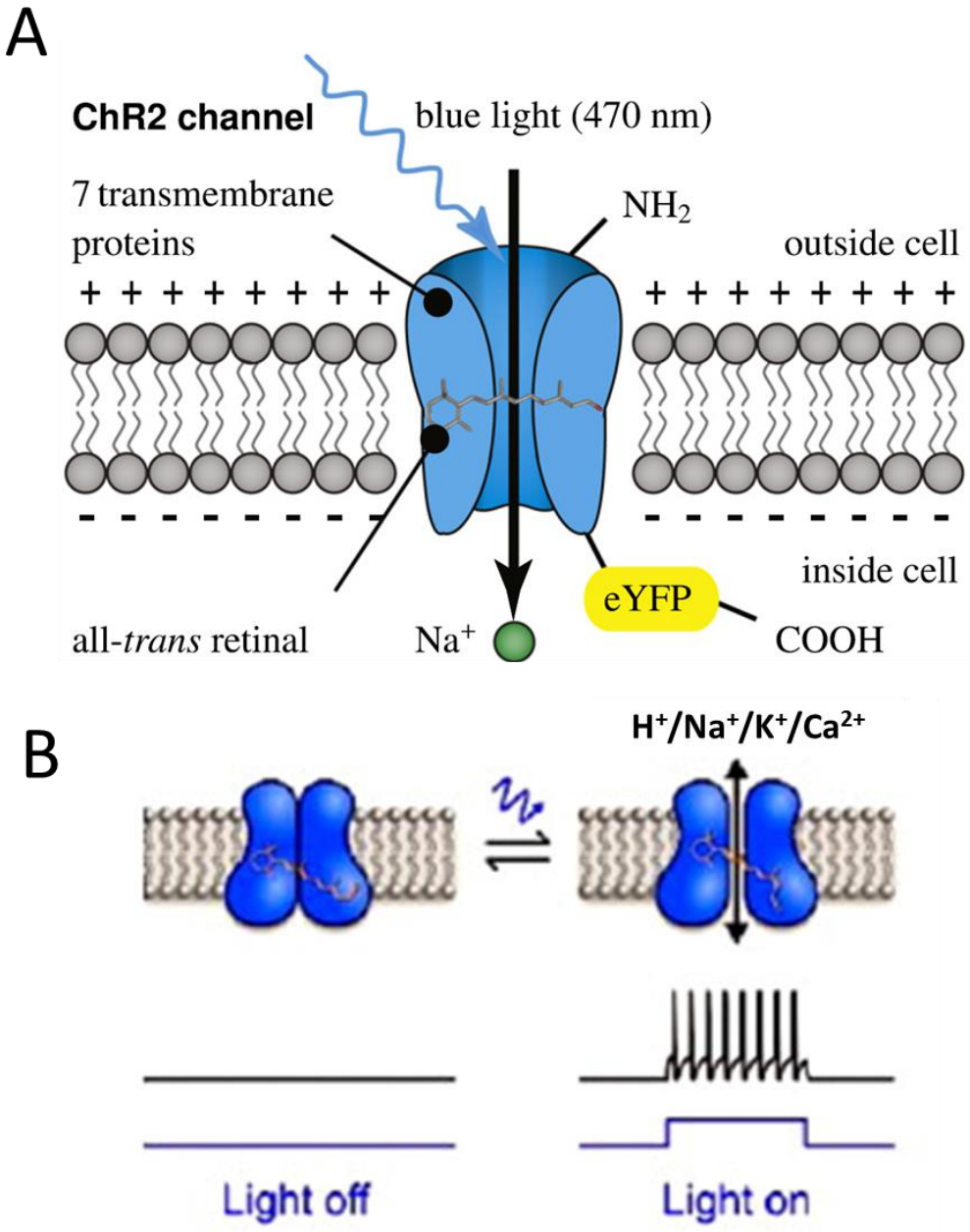


Figure 5.3. An illustration of the light-gated cation channel channelrhodopsin-2 (ChR2).

(A) Illustration of ChR2-EYFP fusion protein localised to the membrane of a cardiomyocyte. **(B)** Maximal activation of the cation channel occurs with blue light at 470 nm, allowing the influx of Na^+ and the initiation of depolarisation. Adapted from (G et al., 2013).

To address some of the limitations, new variants of ChR2 are continually being developed. For example, improvements have been made to alter ion selectivity (CatCh) (Kleinlogel et al., 2011), peak spectral excitation wavelength (ReaChR) (Lin et al., 2013) and kinetics (ChETA) (Gunaydin et al., 2010).

Towards the end of this chapter, the ChR2-H134R variant is utilised, which exhibits 3 times higher conductance than wild-type ChR2 (Lin, 2012). This is tethered to EYFP as a fusion protein to aid visualisation of membrane localisation.

Overall, optogenetic pacing of hiPSC-CMs is more attractive than field stimulation with electrodes because it is non-invasive, repeatable and allows for spatiotemporally precise control of depolarisation. In addition, the use of a blue light-activated ChR2-H134R variant facilitates simultaneous calcium imaging with the spectrally distant red GECI, RGECO1.0.

5.2 Chapter Aims and Objectives

The aim of this chapter was to compare and contrast two different HCM-causing mutations, using GECIs as a tool to phenotype the disease *in vitro*. Once a phenotype could be identified, various drug treatments could be explored. The following objectives had to be achieved:

1. Utilise confocal line scans and ClampFit event detection to quantify and assess calcium transient changes in *ACTC1* G301A or *MYH7* C9123T hiPSC-CMs.
2. Establish what phenotype, if any, *ACTC1* G301A hiPSC-CMs and *MYH7* C9123T hiPSC-CMs express compared to healthy isogenic controls.
3. Cross-compare *ACTC1* G301A to *MYH7* C9123T hiPSC-CMs.
4. Use rational choices of drug treatment to rescue the phenotype.
5. Seek improvements to the in vitro phenotyping and drug screening approach.

5.3 Results

5.3.1 Isogenic sets of hiPSC-CMs that express GECIs reveal an arrhythmic phenotype in mutated HCM cell lines

Patients with HCM occasionally exhibit abnormalities in calcium handling and, consequently, are at a higher risk of ventricular arrhythmias (Kumar et al., 2015). Therefore, confocal line scan microscopy was used to compare calcium handling in healthy and diseased hiPSC-CMs.

5.3.1.1 Confocal line scan analysis of calcium transients from isogenic P2 *ACTC1* G301A GEM-GECO hiPSC-CMs

Confocal line scan traces were performed to compare P2 *ACTC1*$^{WT/WT}$ GEM-GECO hiPSC-CMs to its isogenic mutant counterpart P2 *ACTC1*$^{WT/MUT}$. These traces showed few obvious differences between the patient-derived P2 *ACTC1*$^{WT/WT}$ line and the mutant P2 *ACTC1*$^{WT/MUT}$ apart from an increase in calcium transient event frequency (**Figure 5.4A, B**).

Upon ClampFit event detection analysis an apparent increase in arrhythmic DAD-like events in the P2 *ACTC1*$^{WT/MUT}$ line was observed, however this was not significant. In addition, there was a significant decrease in systolic calcium (* p = 0.0268), as measured by calcium transient peak amplitude (**Figure 5.4D**). Moreover, there was a significant increase in spontaneous beat rate from 52.8 ± 1.225 bpm to 78.45 ± 6.659 bpm (** p = 0.0091) (**Figure 5.4E**), as well as a significant decrease in calcium transient time to peak (T_{peak}) from 180.4 ± 14.01 ms to 118.2 ± 18.27 ms (* p = 0.0356) in the mutant line (**Figure 5.4F**).

Despite these differences, P2 *ACTC1*$^{WT/MUT}$ GEM-GECO hiPSC-CMs do not recapitulate the calcium handling abnormalities seen in HCM.

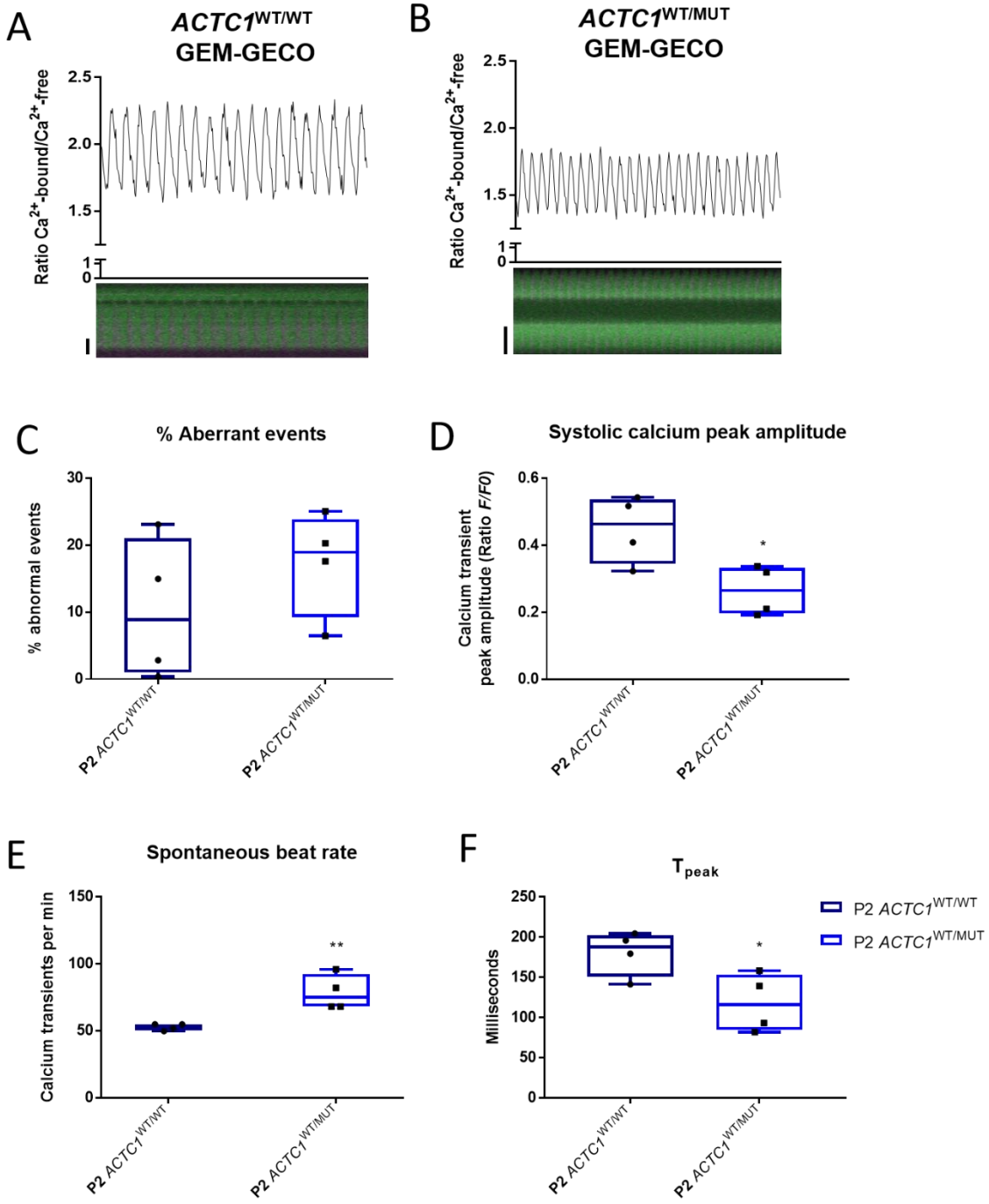


Figure 5.4. Targeted GEM-GECO hiPSC-CMs harbouring *ACTC1* G301A mutation display decreased systolic calcium and increased beat rate.

(A-B) Representative 25-second segment of confocal line scan traces and corresponding kymographs for **(A)** P2 *ACTC1*$^{WT/WT}$ and **(B)** P2 *ACTC1*$^{WT/MUT}$ GEM-GECO hiPSC-CMs at d25 or d27. Presented as ratio between calcium-bound wavelength (magenta) and calcium-free wavelength (green). Scale bars = 20 µm. **(C)** Box-plot showing % of total calcium transient events detected deemed abnormal by ClampFit detection. **(D)** Mean calcium transient peak amplitude. **(E)** Number of calcium transient events detected per minute. **(F)** Calcium transient time to peak. Data presented as mean ±SD, n = 4 hiPSC-CMs from 3 differentiations. Unpaired t-test; * $p < 0.0356$, ** $p = 0.0091$.

5.3.1.2 Confocal line scan analysis of calcium transients from isogenic P1 *ACTC1* G301A RGECO hiPSC-CMs

Next, we compared RGECO hiPSC-CMs from the patient-derived P1 *ACTC1*$^{WT/MUT}$ line, and the corrected isogenic line P1 *ACTC1*$^{WT/WT}$. Confocal line scan traces revealed an increased occurrence of abnormal calcium transient events in the mutant hiPSC-CMs (**Figure 5.5B**). These events appeared to be smaller in amplitude than usual, and resembled delayed afterdepolarisations (DADs). This was quantified using ClampFit event detection and showed a significant increase in DAD-like events from 6.697% ± 0.574% to 15.65% ± 1.857% (* p = 0.0118) (**Figure 5.5C**).

The increased frequency of DAD-like events is thought to occur as a result of high intracellular calcium. Although calcium transient peak amplitude, an indicator of intracellular calcium level, increased with heterozygous mutation of *ACTC1*, this was not statistically significant (**Figure 5.5D**).

Likewise, the change in spontaneous beat rate from a mean of 40.9 bpm to 38.9 bpm was not statistically significant (**Figure 5.5E**). However, the F-test for variance showed a significant increase in beat rate variance (*** p = 0.0002) in the P1 *ACTC1*$^{WT/MUT}$ line.

P1 *ACTC1*$^{WT/MUT}$ hiPSC-CMs also exhibited a slower calcium transient T_{peak} of 74.33 ms compared to 141.5 ms in P2 *ACTC1*$^{WT/WT}$ hiPSC-CMs (**** p < 0.0001) (**Figure 5.5F**).

By comparing the results from **Figure 5.4** and **Figure 5.5**, it is interesting to see that the same *ACTC1* G301A mutation in different genetic backgrounds results in different phenotypes. The frequency of DAD-like calcium transient events increases in both lines, but this is only significant in P1 *ACTC1*$^{WT/MUT}$ RGECO hiPSC-CMs (**Figure 5.4C**, **Figure 5.5C**). Calcium transient peak amplitude decreases in P2 *ACTC1*$^{WT/MUT}$ GEM-GECO hiPSC-CMs, but there is a non-significant increase in P1 *ACTC1*$^{WT/MUT}$ RGECO hiPSC-CMs (**Figure 5.4D**, **Figure 5.5D**). The increase in spontaneous beat rate observed in P2 *ACTC1*$^{WT/MUT}$ hiPSC-CMs is not reflected in P1 *ACTC1*$^{WT/MUT}$ hiPSC-CMs (**Figure 5.4E**, **Figure 5.5E**). In both lines, the *ACTC1* G301A mutation leads to a significantly slower T_{peak} (**Figure 5.4F**, **Figure 5.5F**).

In summary, it can be seen that the *ACTC1* G301A mutation may not be sufficient on its own to cause a severe phenotype, and that the patient's genetic background may influence the manifestation of HCM symptoms.

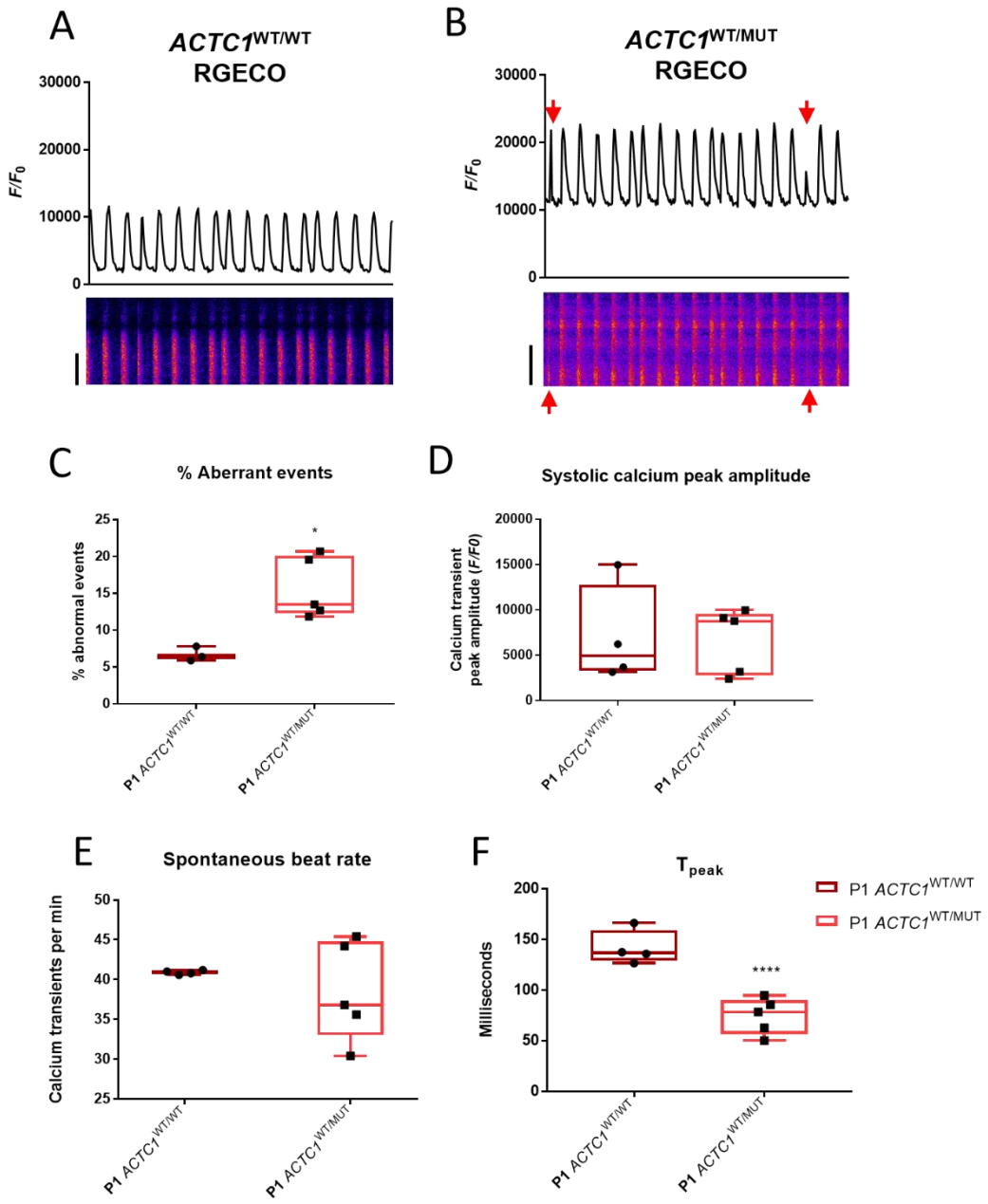


Figure 5.5. Targeted RGECO hiPSC-CMs harbouring *ACTC1* G301A mutation display arrhythmic events.

(A-B) Representative 25-second segment of confocal line scan traces and corresponding kymographs for **(A)** P1 *ACTC1*$^{WT/WT}$ and **(B)** P1 *ACTC1*$^{WT/MUT}$ RGECO hiPSC-CMs at d24 or d30. DAD-like arrhythmic events are indicated (arrows). Scale bars = 20 µm. **(C)** Box-plot showing % of total calcium transient events detected deemed abnormal by ClampFit detection. **(D)** Mean calcium transient peak amplitude. **(E)** Number of calcium transient events detected per minute. **(F)** Calcium transient time to peak. Data presented as mean ±SD, n = 5 cells from 3 differentiations. Unpaired t-test; * p = 0.0118, **** p < 0.0001.

5.3.1.3 Confocal line scan analysis of calcium transients from isogenic *MYH7* C9123T RGECO hiPSC-CMs

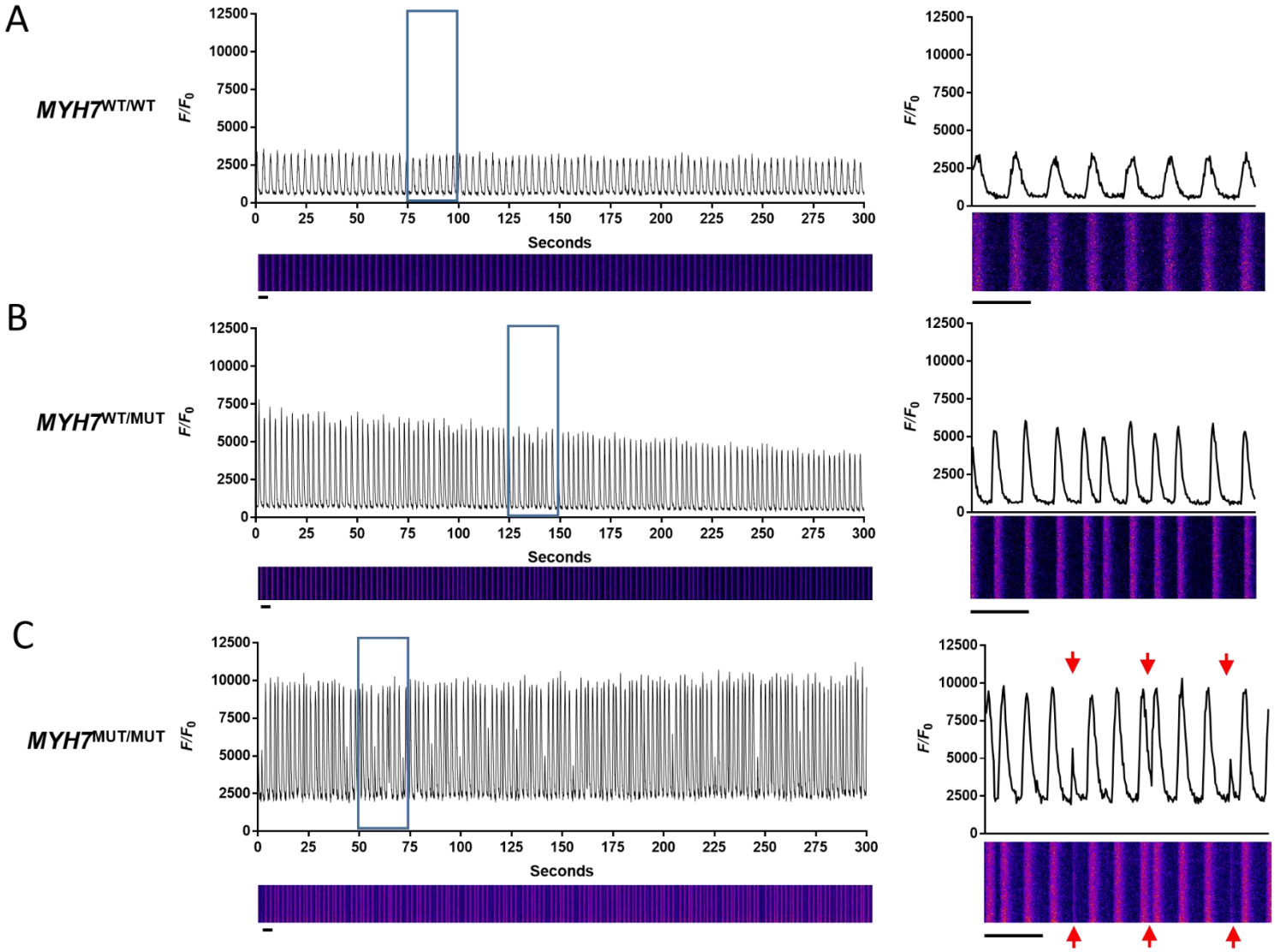
HCM is a complex disease, and has many causative mutations (Cahill et al., 2013). Therefore, we sought to assess calcium handling in an isogenic trio of *MYH7* C9123T RGECO hiPSC-CMs. In this way, some more direct comparisons could be made to the *ACTC1* G301A RGECO isogenic pair.

Confocal line scan traces of *MYH7*$^{MUT/MUT}$ C9123T RGECO hiPSC-CMs revealed an increased frequency of DAD-like calcium transients, with triggered aftercontractions as well as smaller calcium transient events (**Figure 5.6A-C**). This was quantified by ClampFit and showed that *MYH7*$^{WT/WT}$ only presented 1.13% DAD-like calcium transients, increasing to 4.329% in *MYH7*$^{WT/MUT}$ hiPSC-CMs, and significantly increasing to 11.2% in *MYH7*$^{MUT/MUT}$ hiPSC-CMs (** $p = 0.0018$) (**Figure 5.6D**). This represented a ten-fold increase in the occurrence of arrhythmias in the homozygote mutant compared to healthy control. In addition, the increased severity of abnormal calcium transient waveforms with mutation load in an isogenic background shows that the *MYH7* C9123T mutation is sufficient to cause arrhythmias in cardiomyocytes.

Systolic calcium peak amplitude, a surrogate for intracellular calcium content, also significantly increased in both *MYH7*$^{WT/MUT}$ and *MYH7*$^{MUT/MUT}$ hiPSC-CM lines compared to healthy control (**Figure 5.6E**). Calcium transient amplitude, as measured by fluorescence intensity ratio signal-to-noise (*F/F0*), more than doubled from 3041.94 to 6233.91 in *MYH7*$^{WT/MUT}$ hiPSC-CMs (**** $p < 0.0001$). This indicates a higher intracellular calcium content, which likely contributed to the DAD-like waveforms seen in *MYH7* mutant hiPSC-CMs.

Spontaneous beat rate, calculated by calcium transient event frequency, visibly increased in *MYH7* mutant hiPSC-CMs (**Figure 5.6A-C**). However, these changes were not statistically significant (**Figure 5.6F**). Calcium transient T_{peak} also significantly increased in *MYH7* mutant hiPSC-CMs (*** $p < 0.0008$), although this may simply be as a result of higher calcium transient amplitudes causing an increased T_{peak} (**Figure 5.6G**).

For the *MYH7* C9123T mutation, a clear increase in arrhythmic events, intracellular calcium and calcium transient T_{peak} occurs with increasing mutation load. *MYH7* mutant hiPSC-CMs can therefore recapitulate HCM-associated calcium handling abnormalities *in vitro*.


A
MYH7WT/WT
B
MYH7WT/MUT
C
MYH7MUT/MUT
F/F0
Seconds
12500
10000
7500
5000
2500
0
0
25
50
75
100
125
150
175
200
225
250
275
300

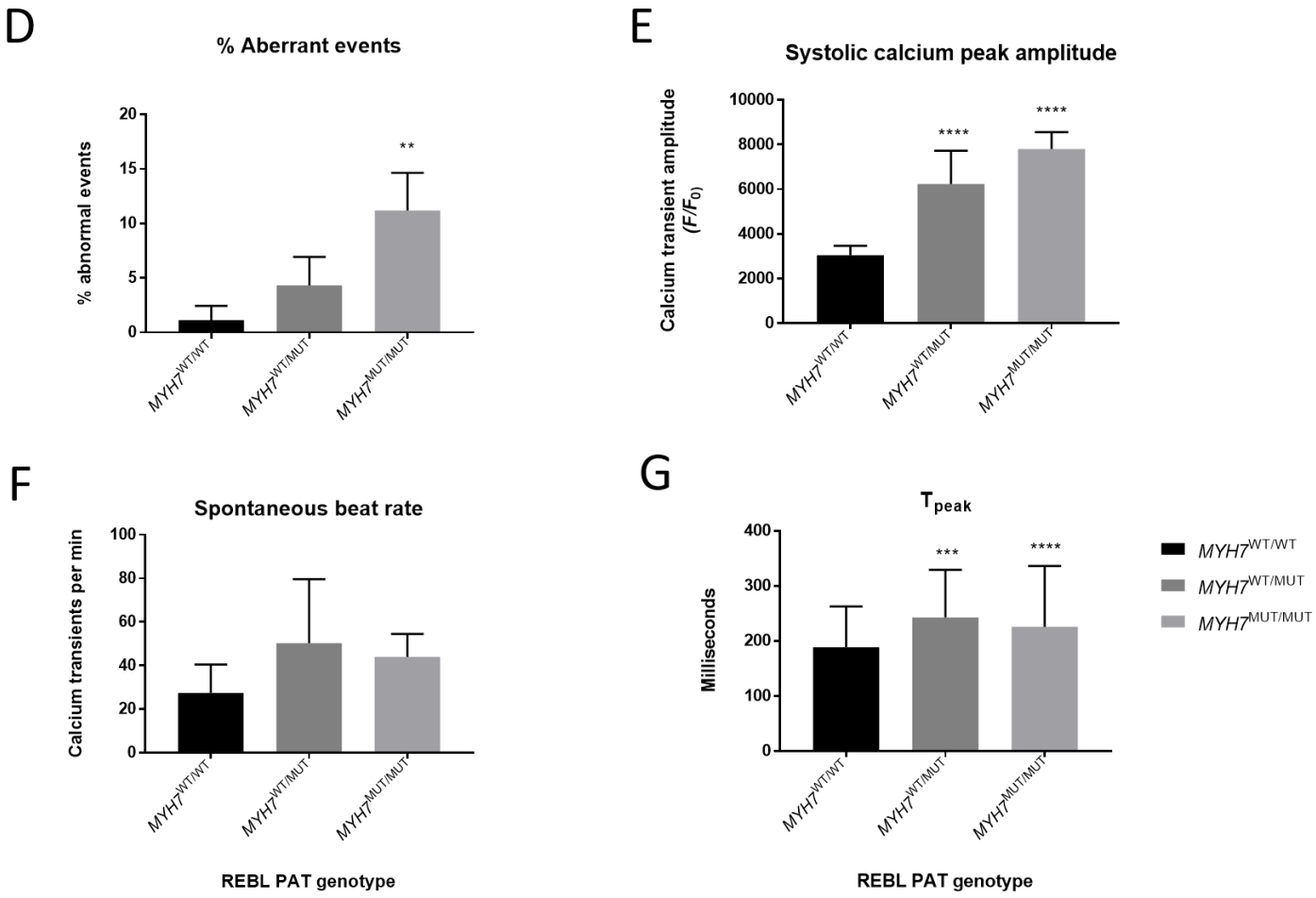


Figure 5.6. Targeted RGECO hiPSC-CMs harbouring *MYH7* C9123T mutation display arrhythmic events, increased systolic calcium and increased beat rate.

(A-C) Representative confocal line scan traces and corresponding kymographs for REBL PAT **(A)** *MYH7*$^{WT/WT}$, **(B)** *MYH7*$^{WT/MUT}$ and **(C)** *MYH7*$^{MUT/MUT}$ RGECO hiPSC-CMs at d24, d26 or d29. Insets (blue boxes) showing enlarged 25 second segment of each line scan to illustrate DAD-like events (arrows). Scale bars = 5 seconds. **(D)** Bar graph showing % of total calcium transient events detected deemed abnormal by ClampFit detection. **(E)** Mean calcium transient peak amplitude showing increased systolic calcium with mutation load. **(F)** Number of calcium transient events detected per minute. **(G)** Calcium transient time to peak. Data presented as mean ±SD, n = 6 wells across 3 experiments. Kruskal-Wallis test with Dunn's multiple comparison test; ** p = 0.0018, *** p = 0.0008, **** p < 0.0001.

5.3.1.4 Cross-comparing the *ACTC1* G301A mutation with the *MYH7* C9123T mutation

When compared to P1 *ACTC1*$^{WT/MUT}$ RGECO hiPSC-CMs, *MYH7* mutants show some similar calcium transient changes, particularly the increase in arrhythmic events (**Figure 5.5D, Figure 5.6D**). However, there are opposing effects on T_{peak}, with *MYH7* mutants showing a slower in T_{peak}, and *ACTC1* mutants experiencing a faster T_{peak} (**Figure 5.5G, Figure 5.6G**). Changes to spontaneous beat rate and systolic peak amplitude are also much more pronounced in the *MYH7* mutants (**Figure 5.5E&F, Figure 5.6E&F**).

This shows that mutations to two different sarcomeric proteins are capable of causing similar calcium handling abnormalities, whilst also resulting in subtle differences in phenotype.

Overall, the increasing severity of phenotypic abnormalities seen in the *MYH7* isogenic trio illustrate the advantage of having a full set of wild-type, heterozygote and homozygote clones to study the mutation phenotype.

5.3.1.5 Investigating the role of calcium in mutant hiPSC-CMs

Having observed increased systolic calcium transient amplitudes and an increased occurrence of DAD-like calcium transient events in *MYH7* mutants, we hypothesised that mutant hiPSC-CMs existed in a high intracellular calcium state. In order to prevent the influx of Ca^{2+}, the L-type calcium channel blocker nifedipine was added to the isogenic trio (**Figure 5.7**).

Interestingly, both *MYH7*$^{WT/MUT}$ and *MYH7*$^{MUT/MUT}$ lines exhibited a resistance to nifedipine, with calcium transients being maintained after drug addition (**Figure 5.7A-C**). After just 120 seconds exposure to 1 μM nifedipine, the beating rate of *MYH7*$^{WT/WT}$ hiPSC-CMs had reduced to 46.82% of the baseline beating rate. In contrast, *MYH7*$^{WT/MUT}$ hiPSC-CMs continued to beat at a rate that was 98.14% of the baseline beat rate before drug addition (* p = 0.0155) (**Figure 5.7D**). By the end of a 300-second confocal line scan, healthy *MYH7*$^{WT/WT}$ hiPSC-CMs had slowed considerably to 10% of the original calcium transient event frequency. *MYH7*$^{WT/MUT}$ and *MYH7*$^{MUT/MUT}$ hiPSC-CMs continued to elicit calcium transients, albeit at a slower rate of 83.77% (*** p = 0.0003) and 71.84% (** p = 0.0026) of baseline, respectively (**Figure 5.7D**).

Contrary to patterns seen in **Figure 5.6**, the resistance to nifedipine did not seem to increase with mutation load, as *MYH7*$^{WT/MUT}$ hiPSC-CMs were able to maintain a regular beat rate for longer than *MYH7*$^{MUT/MUT}$ hiPSC-CMs. It is important to note, however, that no statistically significant differences in beat rate were observed between *MYH7*$^{WT/MUT}$ and *MYH7*$^{MUT/MUT}$ hiPSC-CMs at any point after nifedipine addition.

Nevertheless, the resistance to nifedipine suggested that the mutant hiPSC-CMs may be capable of coping without Ca^{2+} influx due to an already high level of intracellular calcium.

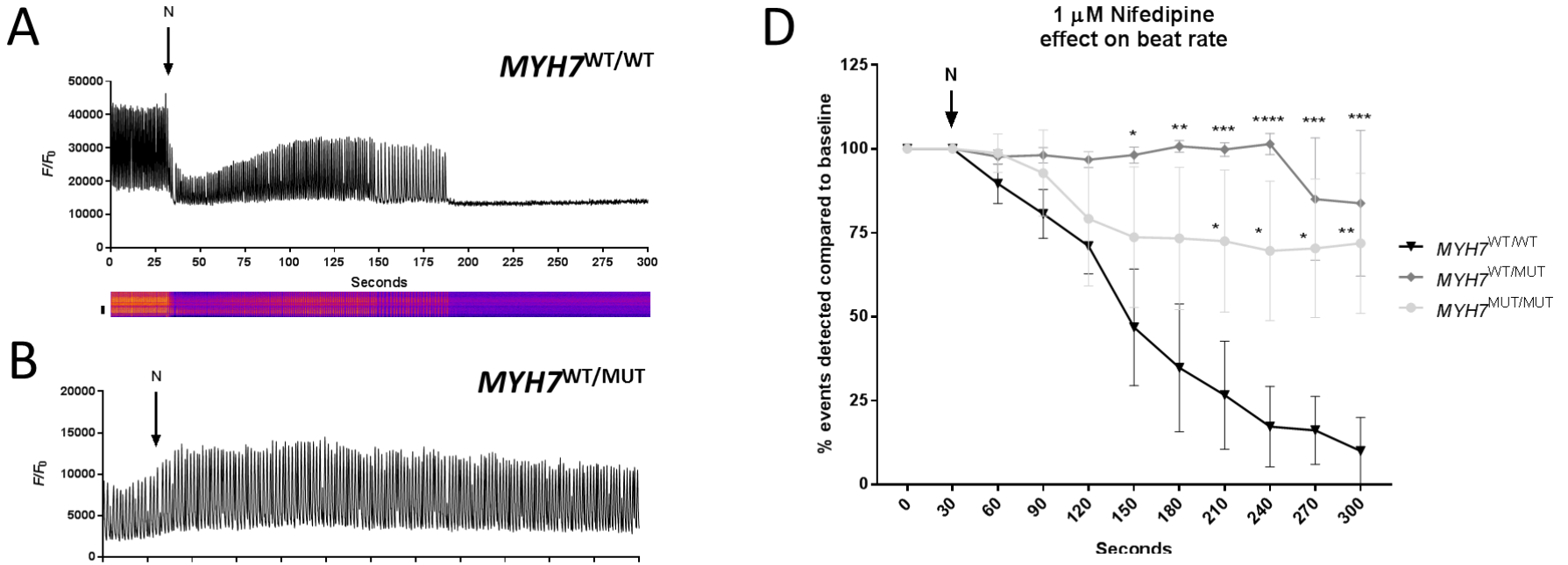


Figure 5.7. Targeted hiPSC-CMs harbouring an *MYH7* C9123T mutation display a delayed response to the L-type calcium channel blocker nifedipine.

(A-C) Confocal line scan traces and corresponding kymographs of d25, d26 or d28 REBL PAT RGECO hiPSC CMs with addition of 1 µM nifedipine (N) at 30 seconds (arrows). **(A)** Calcium transients from *MYH7*$^{WT/WT}$ hiPSC-CMs slow down and eventually stop altogether. **(B)** *MYH7*$^{WT/MUT}$ and **(C)** *MYH7*$^{MUT/MUT}$ hiPSC-CMs continue to beat and elicit calcium transients after nifedipine addition. **(D)** ClampFit event detection of confocal line scans with events binned into 30-second segments. Number of events were converted to a percentage of baseline to normalise for varying beat rate. Data presented as mean ±SD, n = 5 wells across 2 experiments. Two-way ANOVA with Tukey's multiple comparison test; * $p < 0.0347$, ** $p < 0.0098$, *** $p < 0.0007$, **** $p < 0.0001$.

These results pointed towards a potential phenotype of calcium sensitivity in *MYH7* mutants, whereby mutant hiPSC-CMs were capable of functioning in low calcium conditions. To test this, we exposed the isogenic trio of *MYH7* mutants to varying levels of extracellular calcium, to assess their ability to generate calcium transients (**Figure 5.8**).

In *MYH7*$^{WT/WT}$ hiPSC-CMs, both low (0.1 mM) and high (3 mM) extracellular Ca^{2+} induced more arrhythmic calcium transient events than physiological (1.8 mM) extracellular Ca^{2+} conditions (* p = 0.0239) (**Figure 5.8A-C**). Likewise, in *MYH7*$^{WT/MUT}$ hiPSC-CMs, low and high extracellular Ca^{2+} resulted in more arrhythmic events than physiological conditions (* p = 0.0366) (**Figure 5.8D-F**). However, low extracellular Ca^{2+} conditions significantly reduced the occurrence of arrhythmic calcium transients in *MYH7*$^{MUT/MUT}$ hiPSC-CMs compared to both physiological and high Ca^{2+} conditions (* $p \leq 0.0194$) (**Figure 5.8G-H**).

By comparing the frequency of arrhythmic event frequency across the isogenic trio of hiPSC-CM lines, it can be seen that the established pattern of increasing severity of phenotype with mutation load at 1.8 mM Ca^{2+} is enhanced at 3 mM Ca^{2+}, and diminished at 0.1 mM Ca^{2+} (**Figure 5.8**). Although arrhythmic event frequency is reduced at 0.1 mM Ca^{2+} in *MYH7*$^{MUT/MUT}$ hiPSC-CMs, low extracellular Ca^{2+} does not relieve the phenotype in *MYH7*$^{WT/MUT}$ hiPSC-CMs.

Systolic calcium peak amplitude was again used as a surrogate for intracellular calcium concentration. In *MYH7*$^{MUT/MUT}$ hiPSC-CMs, calcium transient peak amplitude significantly increased in a linear fashion with increasing extracellular Ca^{2+} concentration (**** $p < 0.0001$) (**Figure 5.8**). This suggests that the reduction of extracellular Ca^{2+} leads to a reduction in intracellular Ca^{2+} which, in turn, reduces the incidence of arrhythmias in *MYH7*$^{MUT/MUT}$ hiPSC-CMs.

These results show that there may be a link between the amount of calcium available to *MYH7* mutant hiPSC-CMs and the prevalence of DAD-like arrhythmic events. Indeed, the significant reduction in arrhythmic event frequency in *MYH7*$^{MUT/MUT}$ hiPSC-CMs, combined with the lower systolic calcium transient peak amplitude in low calcium conditions, suggests that strategies aimed at reducing intracellular Ca^{2+} may be beneficial in tackling calcium handling abnormalities associated with the *MYH7* C9123T mutation.

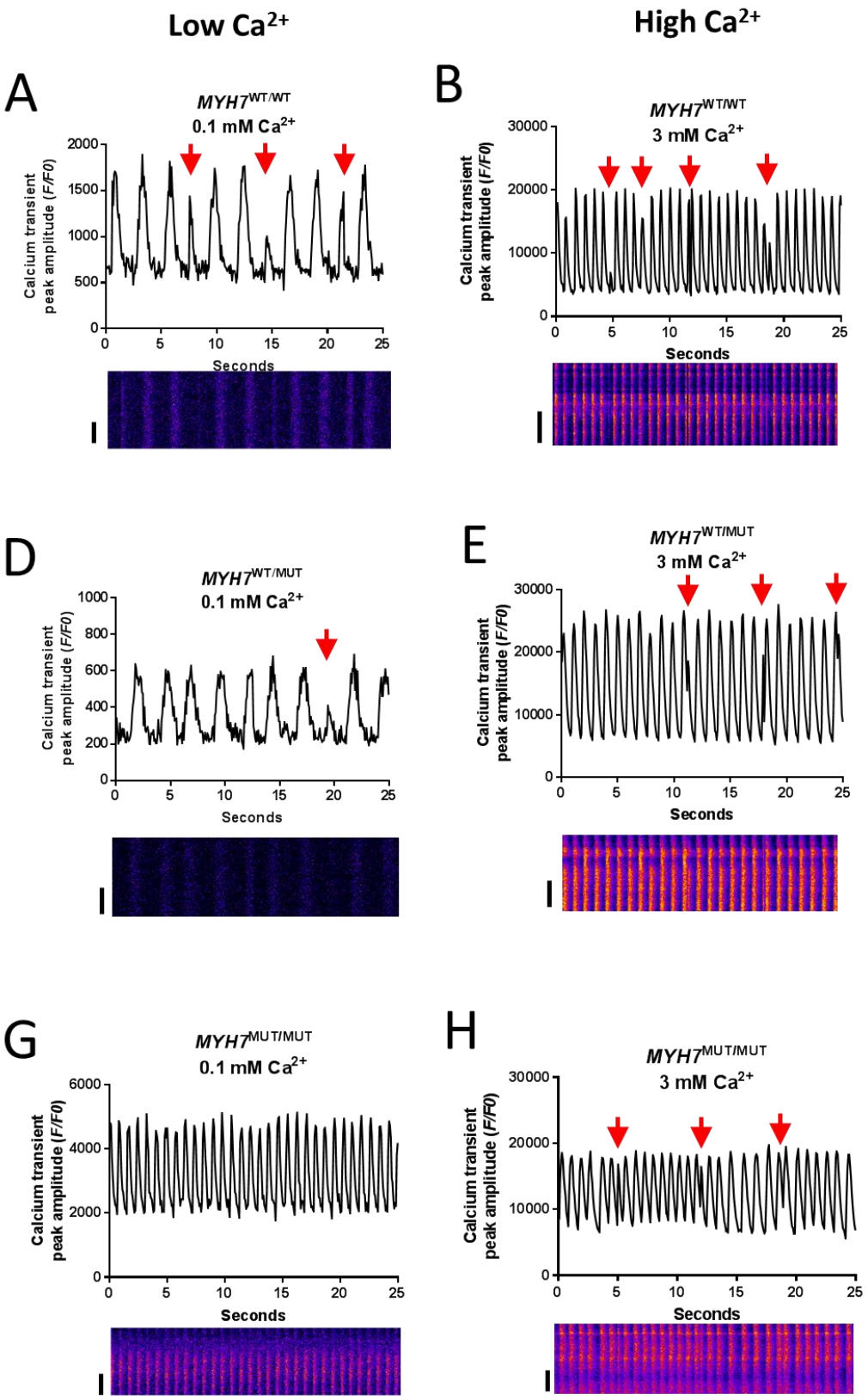
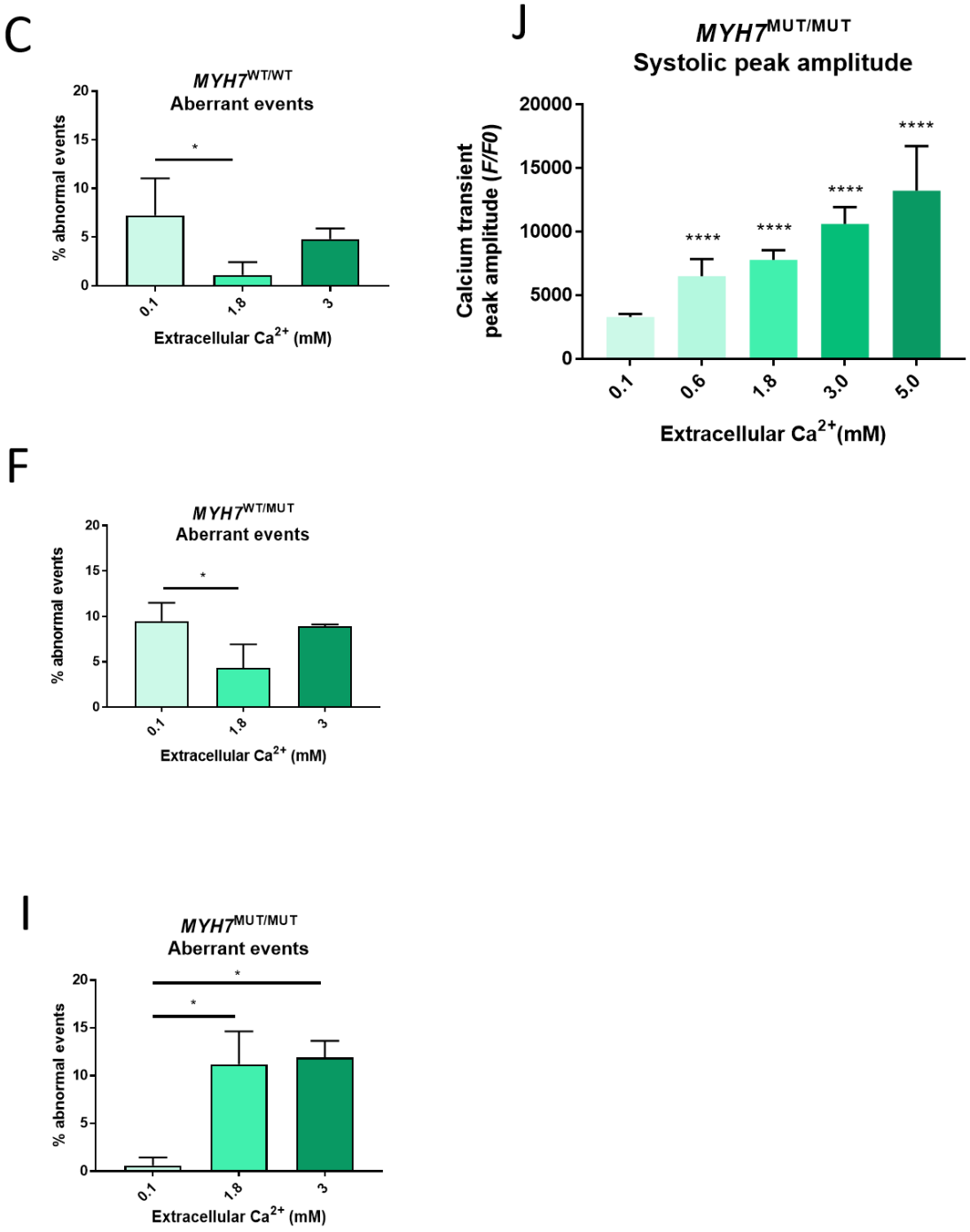


Figure 5.8. The response of targeted hiPSC-CMs harbouring an *MYH7* C1923T mutation to varying extracellular calcium concentrations.

(A-B) Confocal line scan traces and kymographs of d23 or d25 *MYH7*$^{WT/WT}$ RGECO hiPSC-CMs exposed to **(A)** 0.1 mM or **(B)** 3 mM extracellular Ca^{2+} showing increased frequency of arrhythmic events (red arrows). **(C)** ClampFit event detection of arrhythmic events in *MYH7*$^{WT/WT}$ hiPSC-CMs at low (0.1 mM), physiological (1.8 mM) and high (3 mM) extracellular Ca^{2+}. **(D-F)** Confocal line scan traces and arrhythmic event calculation



for *MYH7*$^{WT/MUT}$ RGECO hiPSC-CMs. **(G-I)** Confocal line scan traces and arrhythmic event calculation for *MYH7*$^{MUT/MUT}$ RGECO hiPSC-CMs showing reduced occurrence of arrhythmic events in low Ca^{2+} conditions. Scale bars = 20 µm. $^{+}$ Data presented as mean ±SD, n ≥ 3 wells across 2 experiments. Kruskal-Wallis test with Dunn's multiple comparison test; * p ≤ 0.0366. **(J)** Increasing mean systolic calcium peak amplitude in *MYH7*$^{MUT/MUT}$ RGECO hiPSC-CMs with increasing extracellular Ca^{2+} concentration. Mean ±SD, n ≥ 3 wells across 2 experiments. One-way ANOVA with Tukey's multiple comparison test using 0.1 mM Ca^{2+} as control; **** p < 0.0001. Post test for linear trend; **** p < 0.0001.

5.3.2 The application of drugs to targeted hiPSC-CMs in an attempt to alleviate aberrant calcium transient events associated with HCM

Having established an aberrant calcium transient phenotype in *MYH7* mutant hiPSC-CMs caused in the presence of high extracellular calcium, we sought to attenuate these characteristics using a suite of pharmacological interventions. Each of these drugs was chosen for their antiarrhythmic properties or ability to reduce intracellular calcium.

5.3.2.1 Non-selective ß-adrenergic receptor antagonist propranolol shows no effect on aberrant calcium transients

Propranolol is a non-selective ß–adrenergic receptor antagonist and is clinically approved for relieving obstructive HCM and ventricular tachycardia (Spoladore et al., 2012, Houston and Stevens, 2014). The *MYH7* C9123T isogenic trio of hiPSC-CMs were incubated with 200 nM of propranolol for 24 hours and then assessed for calcium transient changes by confocal line scan and ClampFit analysis. In all three lines there was no significant reduction in arrhythmic event frequency (**Figure 5.9A**), systolic calcium (**Figure 5.9B**), calcium transient time to peak (**Figure 5.9C**) or spontaneous beat rate (**Figure 5.9D**).

Having found that a clinically established antiarrhythmic agent was not sufficient to reduce arrhythmias and systolic calcium peak amplitude in *MYH7* mutant hiPSC-CMs, some more experimental drugs were tested.

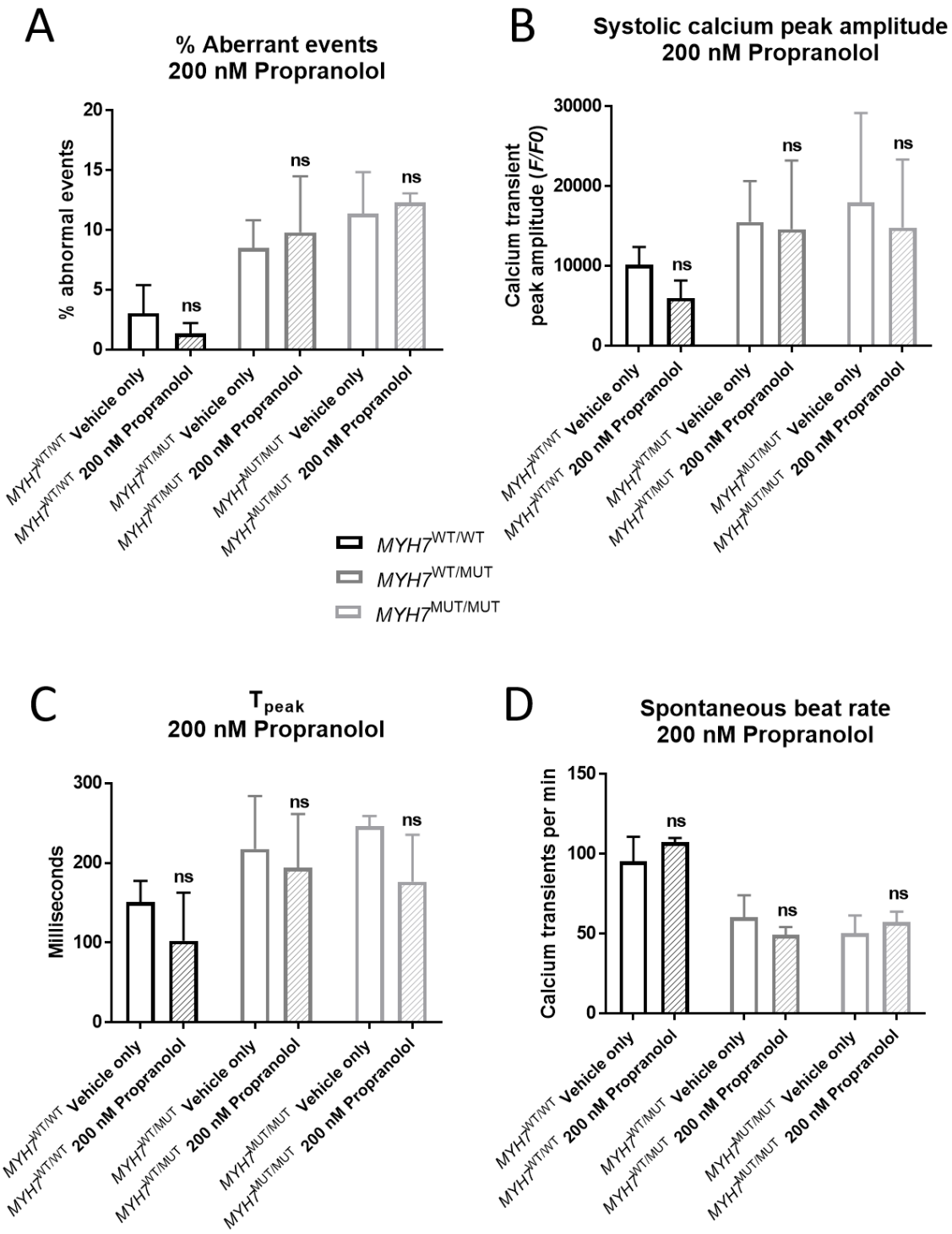


Figure 5.9. Calcium transient changes in *MYH7* C1923T RGECO hiPSC-CMs treated with the ß-adrenergic antagonist propranolol.

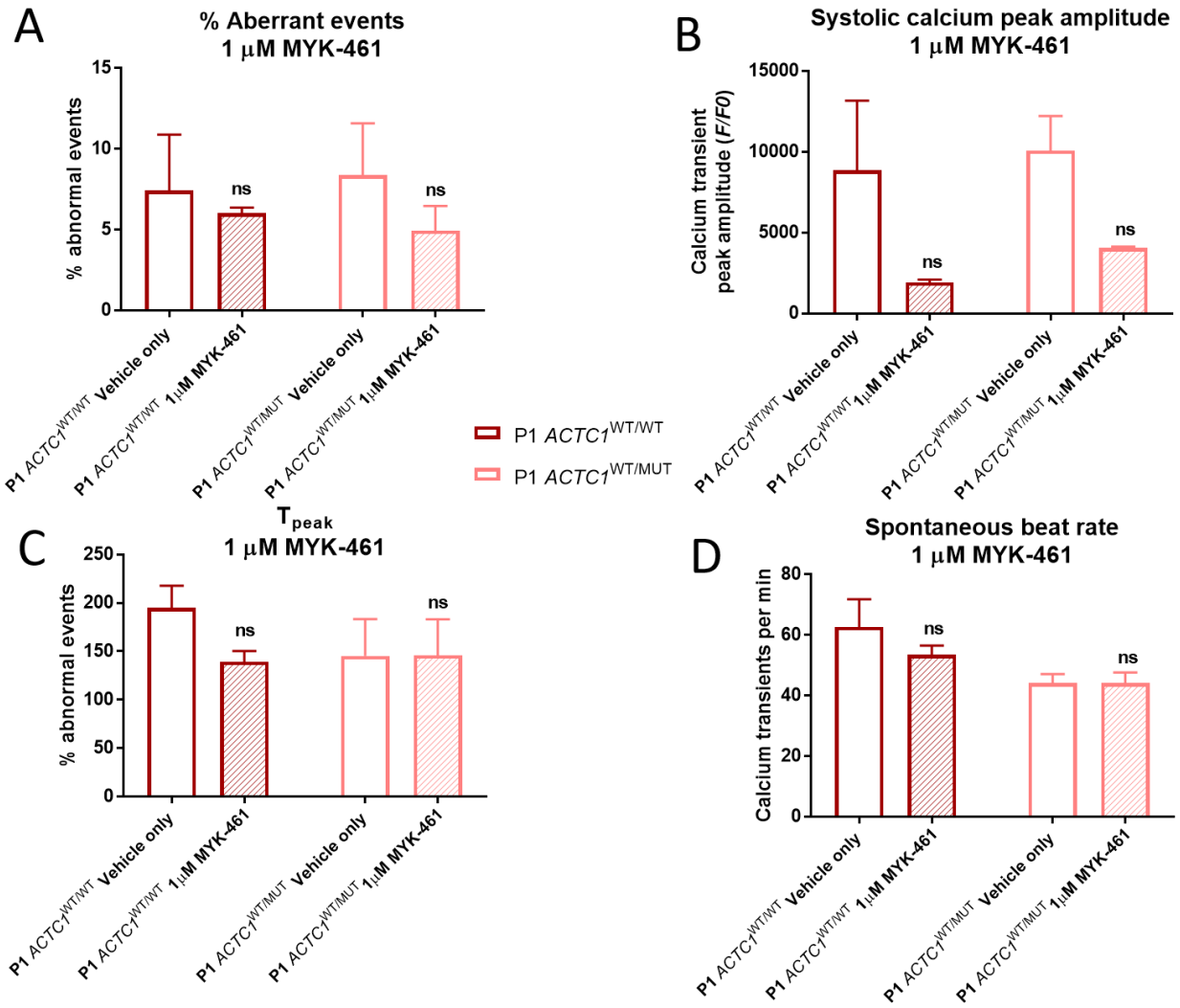
ClampFit event detection analysis of confocal line scans of d24 or d29 *MYH7*$^{WT/WT}$, *MYH7*$^{WT/MUT}$ and *MYH7*$^{MUT/MUT}$ RGECO hiPSC-CMs incubated with 200 nM propranolol or DMSO vehicle only for 24 hours. **(A)** Percentage of arrhythmic DAD-like events calcium transient events detected. **(B)** Mean calcium transient peak amplitude. **(C)** Calcium transient time to peak. **(D)** Number of calcium transient events detected per minute. Data presented as mean ±SD, n = 4 wells across 2 experiments. Kruskal-Wallis test with Dunn's multiple comparison test; ns – not significant.

5.3.2.2 Myosin ATPase inhibitor MYK-461 does not rescue calcium handling abnormalities in mutant hiPSC-CMs

The small molecule MYK-461 is an inhibitor of ATPase activity in the beta myosin heavy chain (β-MHC), and has shown promise in reducing contractility in mouse models of HCM (Green et al., 2016). Given the hyper-contractile phenotype in *ACTC1* G301A mutants (Song et al., 2011) (Smith et al., 2018) and the hypo-contractile phenotype in *MYH7* C9123T mutants (Witjas-Paalberends et al., 2013, Mosqueira et al., 2018) , we tested MYK-461 on both of these available HCM models to see if an altered dynamic relationship between α–cardiac actin and β-MHC had any downstream effect on calcium transients.

Incubation with 1 μM MYK-461 for 1 hour prior to confocal line scan analysis had no significant effect on any of the calcium transient parameters assessed in *ACTC1* G301A mutant hiPSC-CMs (**Figure 5.10A-D**). Similarly, there was no significant reduction in arrhythmic event frequency (**Figure 5.10E**), systolic calcium transient peak amplitude (**Figure 5.10F**) or calcium transient T_{peak} (**Figure 5.10G**) in *MYH7* C9123T mutant hiPSC-CMs. However, there was a significant increase in spontaneous beat rate in $MYH7^{MUT/MUT}$ hiPSC-CMs, exacerbating the established phenotype of high beat rate in *MYH7* mutants (**Figure 5.10H**).

The fact that MYK-461 caused a significant change in $MYH7^{MUT/MUT}$ hiPSC-CMs beat rate, and not $ACTC1^{WT/MUT}$ hiPSC-CMs is likely due to its mechanism of binding to the β–MHC and not the α–cardiac actin filament. Nevertheless, no change was seen in the vast majority of calcium transient parameters measured across both models of HCM. Further efforts to induce a measurable change in phenotype focused on compounds with more direct mechanisms of reducing intracellular calcium content.


A
% Aberrant events
1 μM MYK-461
% abnormal events
15
10
5
0
ns
ns
P1 ACTC1WT/WT Vehicle only
P1 ACTC1WT/WT 1μM MYK-461
P1 ACTC1WT/MUT Vehicle only
P1 ACTC1WT/MUT 1μM MYK-461
B
Systolic calcium peak amplitude
1 μM MYK-461
Calcium transient peak amplitude (F/F0)
15000
10000
5000
0
ns
ns
P1 ACTC1WT/WT Vehicle only
P1 ACTC1WT/WT 1μM MYK-461
P1 ACTC1WT/MUT Vehicle only
P1 ACTC1WT/MUT 1μM MYK-461
P1 ACTC1WT/WT
P1 ACTC1WT/MUT
C
Tpeak
1 μM MYK-461
% abnormal events
250
200
150
100
50
0
ns
ns
P1 ACTC1WT/WT Vehicle only
P1 ACTC1WT/WT 1μM MYK-461
P1 ACTC1WT/MUT Vehicle only
P1 ACTC1WT/MUT 1μM MYK-461
D
Spontaneous beat rate
1 μM MYK-461
Calcium transients per min
80
60
40
20
0
ns
ns
P1 ACTC1WT/WT Vehicle only
P1 ACTC1WT/WT 1μM MYK-461
P1 ACTC1WT/MUT Vehicle only
P1 ACTC1WT/MUT 1μM MYK-461

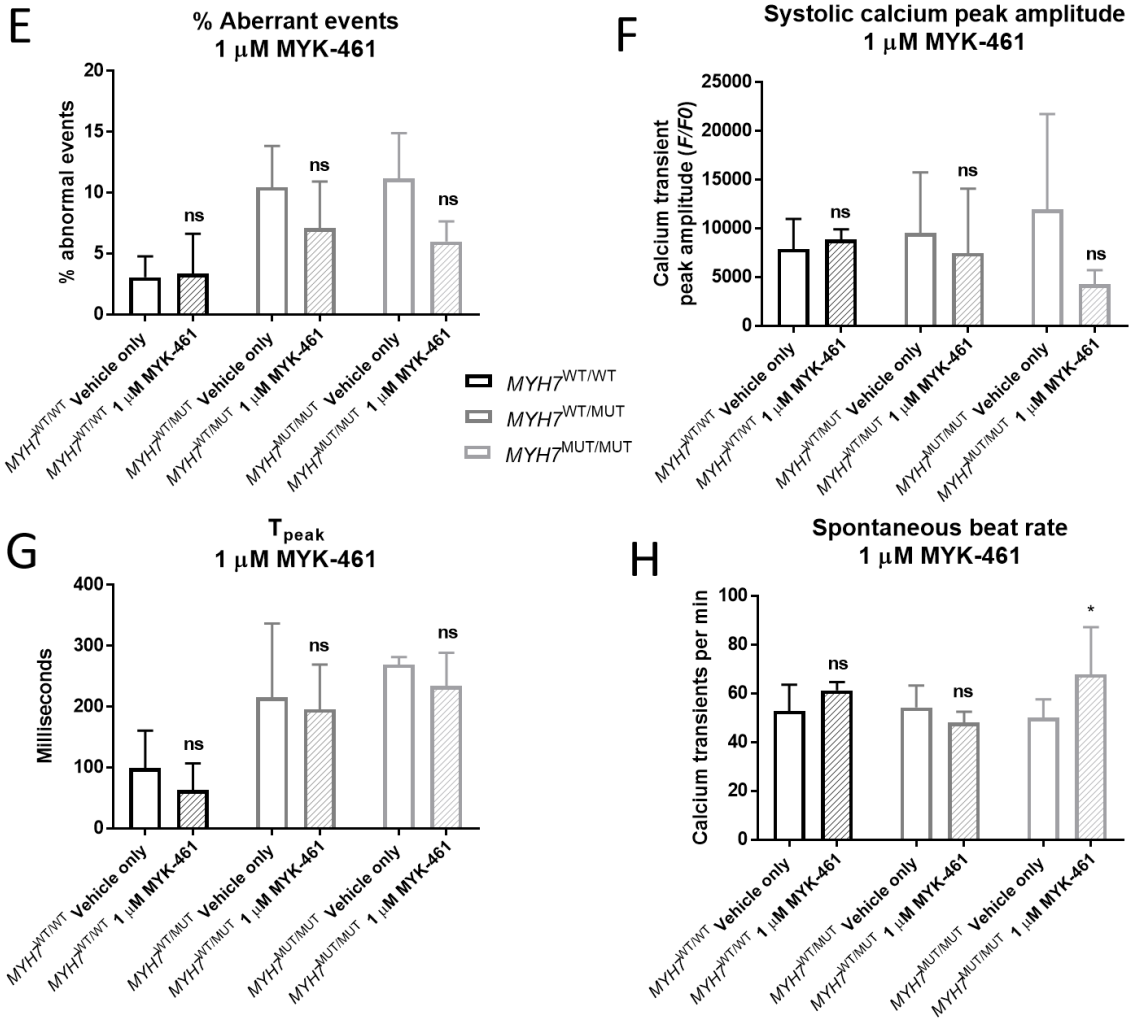


Figure 5.10. Calcium transient changes in *ACTC1* G301A and *MYH7* C1923T RGECO hiPSC-CMs treated with the ß-MHC ATPase MYK-461.

(A-D) ClampFit event detection analysis of confocal line scans of d28 P1 *ACTC1*$^{WT/WT}$ and P1 *ACTC1*$^{WT/MUT}$ RGECO hiPSC-CMs incubated with 1 μM MYK-461 or DMSO vehicle only for 1 hour. **(A)** Percentage of arrhythmic DAD-like calcium transient events detected. **(B)** Mean calcium transient amplitude. **(C)** Calcium transient time to peak. **(D)** Number of calcium transient events detected per minute. **(E-H)** ClampFit event detection analysis of confocal line scans of d28 *MYH7*$^{WT/WT}$, *MYH7*$^{WT/MUT}$ and *MYH7*$^{MUT/MUT}$ RGECO hiPSC-CMs incubated with 1 μM MYK-461 or DMSO vehicle only for 1 hour. **(E)** Percentage of arrhythmic DAD-like events calcium transient events detected. **(F)** Mean calcium transient peak amplitude. **(G)** Number of calcium transient events detected per minute. **(H)** Number of calcium transient events detected per minute. Data presented as mean ±SD, n = 3 wells. Kruskal-Wallis test with Dunn's multiple comparison test; * p = 0.0437, ns – not significant.

5.3.2.3 Valsartan, an angiotensin II receptor antagonist, does not rescue calcium handling abnormalities in mutant hiPSC-CMs

Valsartan, an angiotensin II receptor antagonist, is undergoing clinical trials for the relief of HCM (Ho et al., 2017). By blocking the angiotensin II receptor, valsartan prevents the phosphorylation of L-type Ca^{2+} channels, thereby reducing Ca^{2+} influx.

The addition of 1 μM valsartan to *MYH7* mutant hiPSC-CMs for 24 hours led to a non-significant reduction in the frequency of arrhythmic DAD-like events (**Figure 5.11A**), as well as a non-significant reduction in systolic calcium transient amplitude (**Figure 5.11B**). Valsartan also reduced the calcium transient time to peak in *MYH7* mutants (**Figure 5.11C**), but resulted in a faster spontaneous beat rate (**Figure 5.11D**).

Overall, valsartan was unsuccessful in rescuing any of the *MYH7* mutant phenotypes. With limited success being achieved by restricting Ca^{2+} influx, efforts were focused on enhancing Ca^{2+} efflux to reduce intracellular Ca^{2+}.

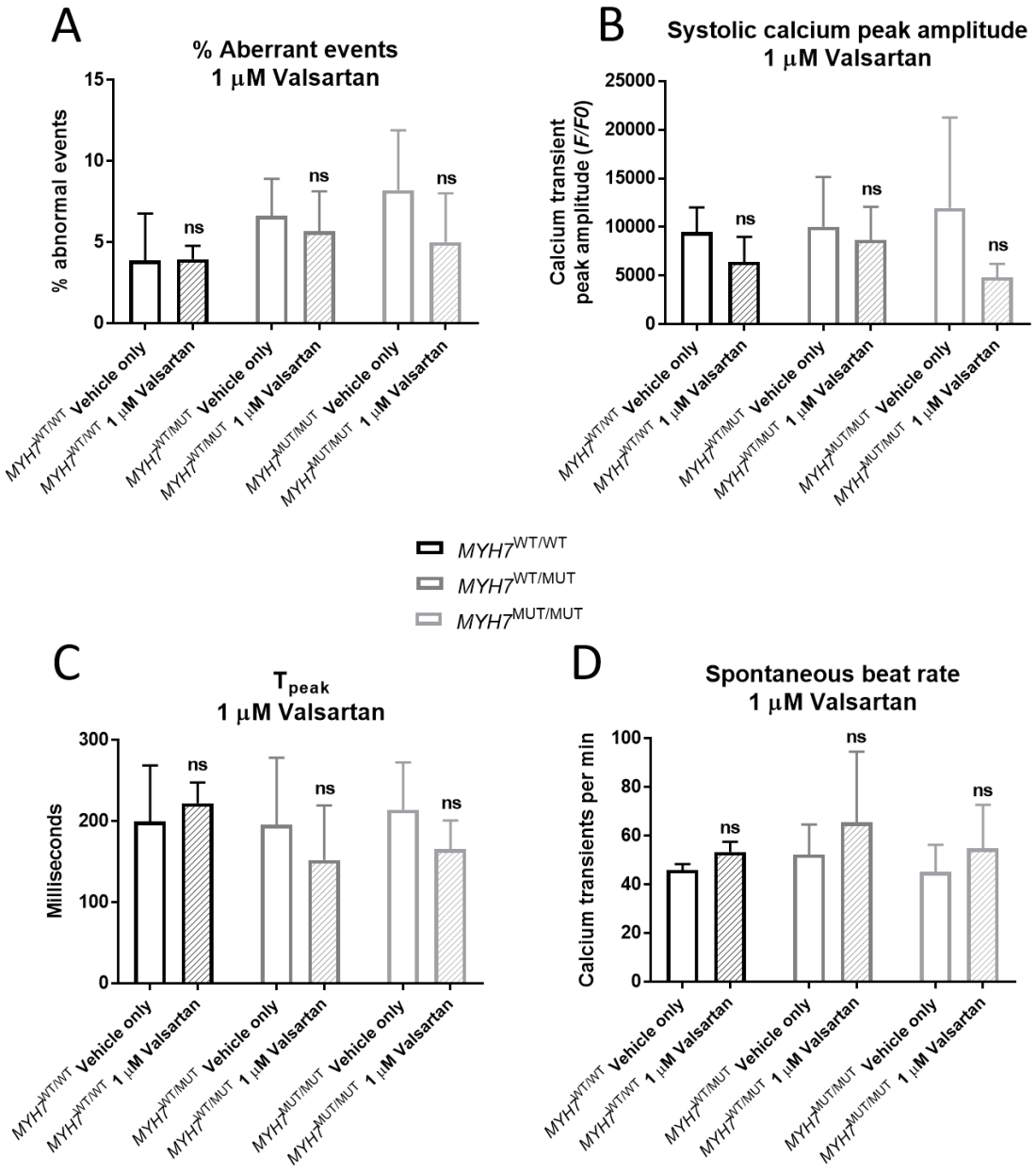


Figure 5.11. Calcium transient changes in *MYH7* C1923T RGECO hiPSC-CMs treated with the angiotensin II receptor antagonist valsartan.

ClampFit event detection analysis of confocal line scans of d24 *MYH7*$^{WT/WT}$, *MYH7*$^{WT/MUT}$ and *MYH7*$^{MUT/MUT}$ RGECO hiPSC-CMs incubated with 1 μM valsartan or DMSO vehicle only for 24 hours. **(A)** Percentage of arrhythmic DAD-like events calcium transient events detected. **(B)** Mean calcium transient peak amplitude. **(C)** Calcium transient time to peak. **(D)** Number of calcium transient events detected per minute. Data presented as mean ±SD, n = 3 wells. Kruskal-Wallis test with Dunn's multiple comparison test; ns – not significant.

5.3.2.4 The late sodium channel antagonist ranolazine rescues the arrhythmic phenotype of *MYH7* mutant hiPSC-CMs

Ranolazine is a late sodium channel (I_{Na}) antagonist that enhances Ca^{2+} efflux through NCX by reducing intracellular Na^{+} (Coppini et al., 2013). This mechanism was exploited in an effort to reduce intracellular calcium during diastole and alleviate arrhythmias in *MYH7* C9123T hiPSC-CMs.

Treatment with either 1 µM or 10 µM ranolazine for 24 hours prior to testing failed to significantly change systolic peak amplitude (**Figure 5.12B**), T_{peak} (**Figure 5.12C**) or spontaneous beat rate (**Figure 5.12D**) in *MYH7* mutant hiPSC-CMs. At the higher dose of 10 µM, a very significant improvement in arrhythmic event frequency was seen in $MYH7^{MUT/MUT}$ hiPSC-CMs (** p = 0.0213) (**Figure 5.12A**). Despite no significant alleviation of arrhythmias in $MYH7^{WT/MUT}$ hiPSCs treated with 10 µM ranolazine, these results indicate that blockade of the late sodium current in *MYH7* mutant hiPSC-CMs is a viable pharmaceutical option for reducing arrhythmias.

Furthermore, these results illustrate the utility of using pharmacological approaches based on reducing intracellular calcium to treat symptoms associated with HCM.

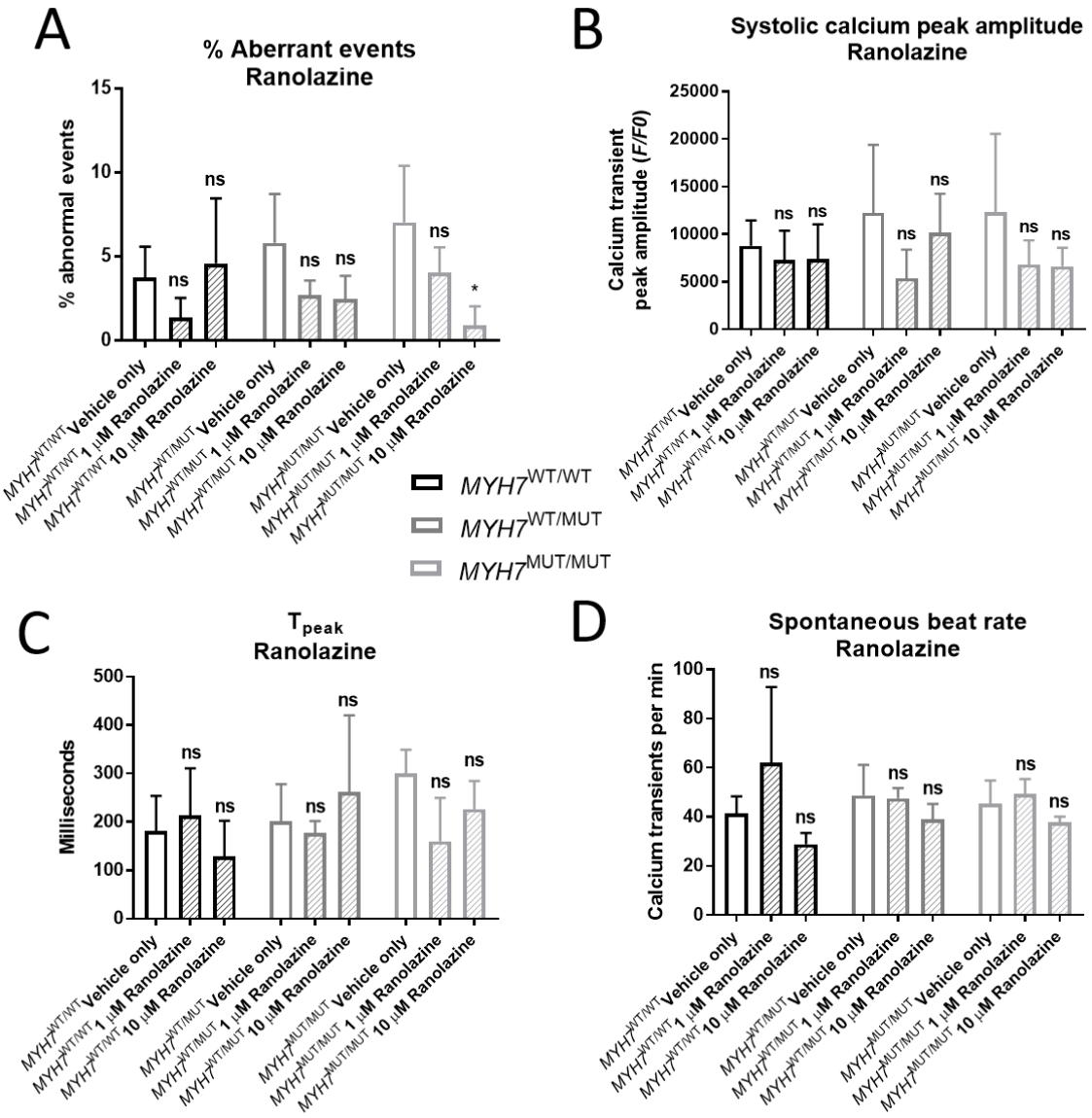


Figure 5.12. Reduced arrhythmic calcium transient event frequency in *MYH7* C1923T RGECO hiPSC-CMs treated with the late sodium current inhibitor ranolazine.

ClampFit event detection analysis of confocal line scans of d25, d26 or d28 *MYH7*$^{WT/WT}$, *MYH7*$^{WT/MUT}$ and *MYH7*$^{MUT/MUT}$ RGECO hiPSC-CMs incubated with 1 μM ranolazine, 10 μM ranolazine or DMSO vehicle only for 24 hours. **(A)** Percentage of arrhythmic DAD-like calcium events. **(B)** Mean calcium transient peak amplitude. **(C)** Calcium transient time to peak. **(D)** Number of calcium transient events per minute. Data presented as mean ±SD, n = 16 vehicle, 4 drug. Kruskal-Wallis test with Dunn's multiple comparison test, using vehicle only as the control; * p = 0.0213.

5.3.2.5 The ryanodine receptor antagonist dantrolene rescues high systolic calcium in *MYH7* homozygous mutant hiPSC-CMs

Whilst ranolazine was successful in reducing the occurrence of arrhythmic events in *MYH7* mutant hiPSC-CMs, it functions by indirectly reducing intracellular calcium during diastole. We therefore sought to directly limit Ca^{2+} release from the SR during systole with the ryanodine receptor antagonist dantrolene. Although commonly used to treat arrhythmogenesis in CPVT, dantrolene has only recently been applied as an antiarrhythmic agent in mouse models of HCM (Jung et al., 2012, Okuda et al., 2018).

Both the P1 *ACTC1* G301A isogenic pair and the REBL PAT *MYH7* C9123T isogenic trio of RGECO hiPSC-CMs were treated with 10 μM dantrolene for 24 hours before confocal line scan analysis (**Figure 5.13**). In this way, the application of dantrolene as an antiarrhythmic in two different human *in vitro* models of HCM could be assessed.

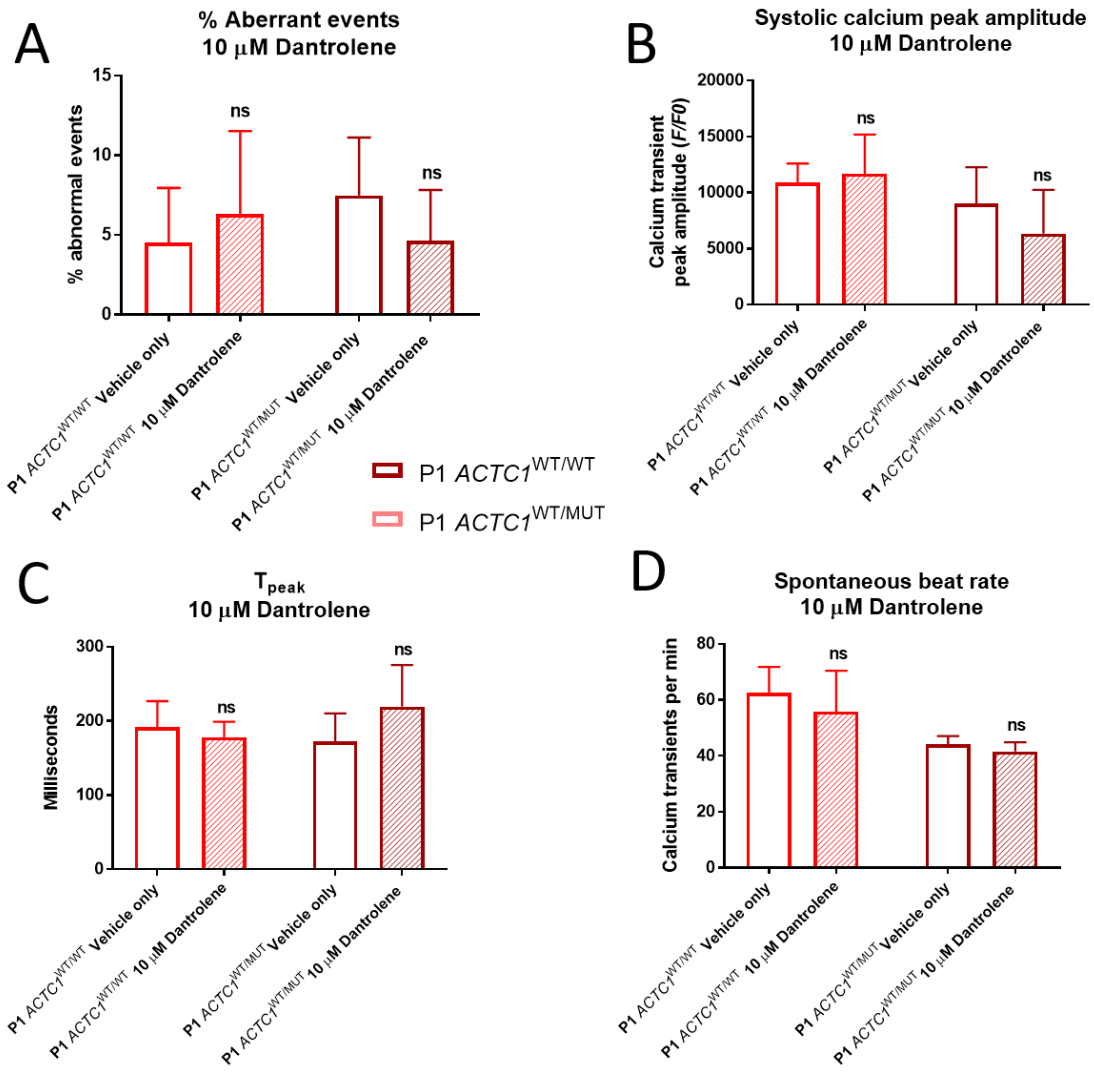
In P1 *ACTC1*$^{WT/MUT}$ RGECO hiPSC-CMs, there was a non-significant reduction in arrhythmic event frequency from 7.48% in vehicle control to 4.65% in dantrolene treated ($p = 0.45$). (**Figure 5.13A**). There were also no significant changes to systolic calcium (**Figure 5.13B**), T_{peak} (**Figure 5.13C**) or spontaneous beat rate (**Figure 5.13D**) in P1 *ACTC1*$^{WT/WT}$ or P1 *ACTC1*$^{WT/MUT}$ RGECO hiPSC-CMs.

Dantrolene also failed to significantly reduce aberrant events in *MYH7* C9123T RGECO hiPSC-CMs, reducing aberrant event frequency in *MYH7*$^{MUT/MUT}$ hiPSC-CMs from 7.37% to 3.99% (**Figure 5.13E**).

Dantrolene treatment did, however, significantly reduce systolic calcium peak amplitude from 12105 fluorescence a.u. (*F/F0)* to 3590 fluorescence a.u. (*F/F0)* in *MYH7*$^{MUT/MUT}$ hiPSC-CMs (* $p = 0.0205$) (**Figure 5.13F**). In this instance, the reduction of Ca^{2+} release from the SR by dantrolene can be seen.

There were no other significant changes in *MYH7* mutant hiPSC-CMs to either T_{peak} (**Figure 5.13G**) or spontaneous beat rate (**Figure 5.13H**) upon dantrolene treatment.

Nevertheless, these results show that ryanodine receptor inhibition may reduce systolic intracellular calcium in some forms of HCM.


A
% Aberrant events
10 μM Dantrolene
% abnormal events
ns
ns
P1 ACTC1WT/WT Vehicle only
P1 ACTC1WT/WT 10 μM Dantrolene
P1 ACTC1WT/MUT Vehicle only
P1 ACTC1WT/MUT 10 μM Dantrolene
P1 ACTC1WT/WT
P1 ACTC1WT/MUT
B
Systolic calcium peak amplitude
10 μM Dantrolene
Calcium transient peak amplitude (F/F0)
C
Tpeak
10 μM Dantrolene
Milliseconds
D
Spontaneous beat rate
10 μM Dantrolene
Calcium transients per min

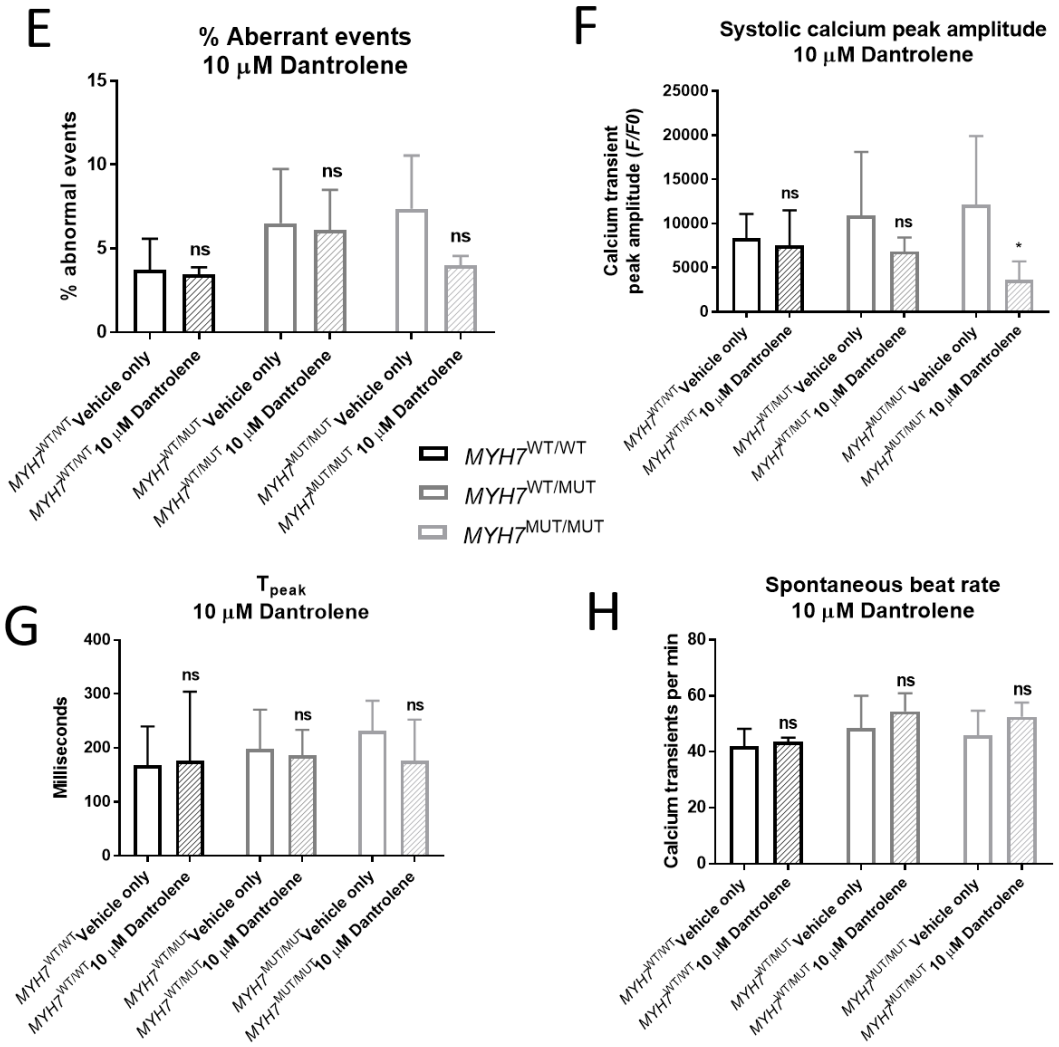


Figure 5.13. Reduced systolic calcium peak amplitude in *MYH7* C9123T RGECO hiPSC-CMs treated with the ryanodine receptor antagonist dantrolene is not reflected in *ACTC1* G301A RGECO hiPSC-CMs.

(A-D) ClampFit event detection analysis of confocal line scans of d24 or d26 P1 *ACTC1*$^{WT/WT}$ and P1 *ACTC1*$^{WT/MUT}$ RGECO hiPSC-CMs incubated with 10 μM dantrolene or DMSO vehicle only for 24 hours. **(A)** Percentage of arrhythmic DAD-like calcium transient events detected. **(B)** Mean calcium transient amplitude. **(C)** Calcium transient time to peak. **(D)** Number of calcium transient events detected per minute. Data presented as mean ±SD, n = 6 vehicle, 4 drug. One-way ANOVA with Sidak's multiple comparison test; ns – not significant. **(E-H)** ClampFit event detection analysis of confocal line scans of d24, d26 or d27 *MYH7*$^{WT/WT}$, *MYH7*$^{WT/MUT}$ and *MYH7*$^{MUT/MUT}$ RGECO hiPSC-CMs incubated with 10 μM dantrolene or DMSO vehicle only for 24 hours. **(E)** Percentage of arrhythmic DAD-like events calcium transient events detected. **(F)** Mean calcium transient peak amplitude. **(G)** Number of calcium transient events detected per minute. **(H)** Number of calcium transient events detected per minute. Data presented as mean SD, n = 16 vehicle, 4 drug. Kruskal-Wallis test with Dunn's multiple comparison test; * p = 0.0205, ns – not significant.

5.3.2.6 Combination treatment of ranolazine and dantrolene rescues the arrhythmic phenotype in *MYH7* mutant hiPSC-CMs, but not *ACTC1* mutant hiPSC-CMs

Having demonstrated the ability of ranolazine to reduce arrhythmias, and the ability of dantrolene to reduce systolic calcium in *MYH7* C9123T hiPSC-CMs, a combination of the both drugs was tested (**Figure 5.14**). A key question was whether or not co-treatment could enhance the effects seen in *MYH7* mutants, or elicit any significant response in *ACTC1* mutant hiPSC-CMs.

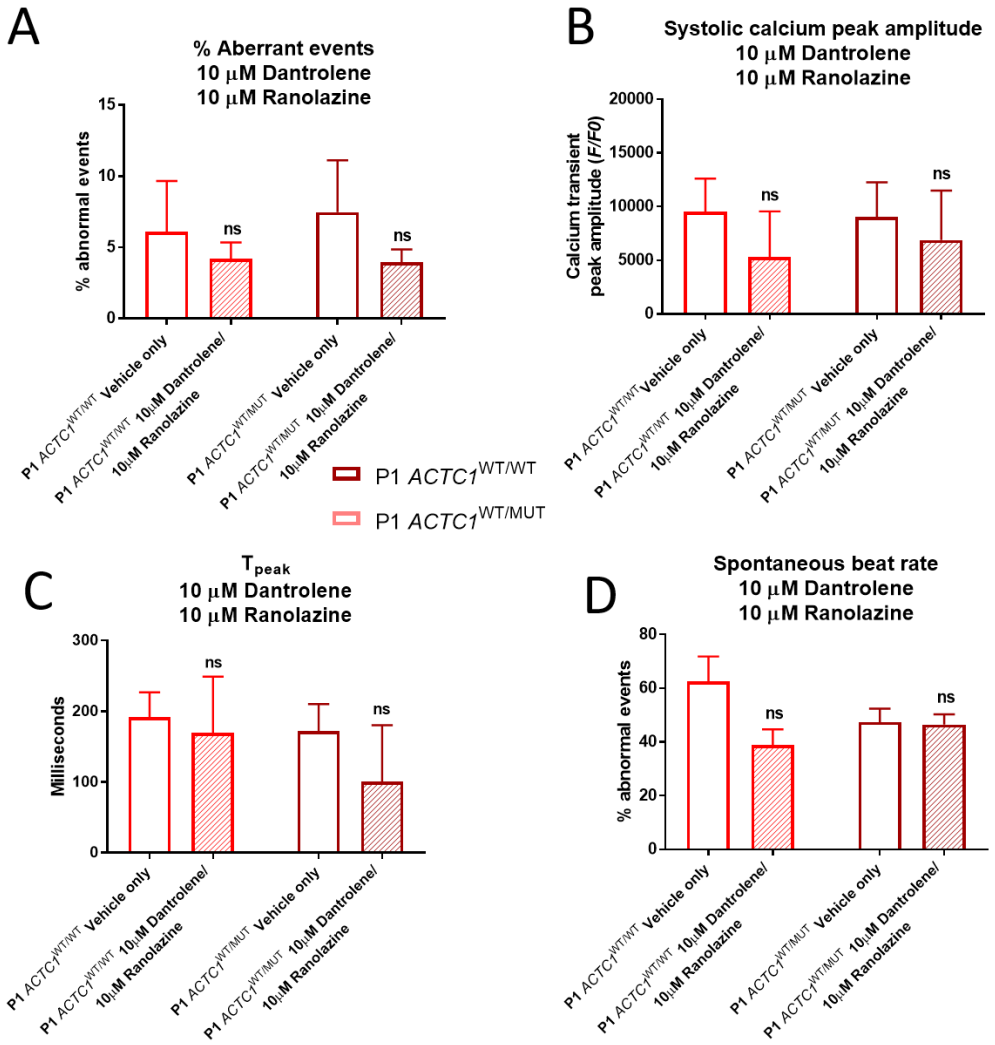
Co-treatment of P1 *ACTC1*$^{WT/MUT}$ hiPSC-CMs with dantrolene and ranolazine led to non-significant reductions in arrhythmic event frequency (**Figure 5.14A**), systolic calcium (**Figure 5.14B**), T_{peak} (**Figure 5.14C**) and spontaneous beat rate (**Figure 5.14D**).

In contrast, co-treatment of *MYH7*$^{WT/MUT}$ and *MYH7*$^{MUT/MUT}$ hiPSC-CMs with dantrolene and ranolazine led to significant amelioration of the arrhythmic phenotype (* p = 0.0207, * p = 0.0154 respectively) (**Figure 5.14E**). This was concomitant with a non-significant reduction in systolic calcium peak amplitude (**Figure 5.14F**).

Calcium transient time to peak was not significantly shortened upon treatment (**Figure 5.14G**), and a no change in spontaneous beat rate was observed (**Figure 5.14H**).

Overall, significant reduction in the arrhythmic phenotype has been discovered in both *MYH7*$^{WT/MUT}$ and *MYH7*$^{MUT/MUT}$ C9123T hiPSC-CMs upon treatment with ranolazine on its own or in conjunction with dantrolene. The reduction in intracellular calcium brought about by these drugs reduces the likelihood of spontaneous Ca^{2+} release from the SR and the appearance of DAD-like arrhythmic events.

On the other hand, P1 *ACTC1*$^{WT/MUT}$ G301A hiPSC-CMs do not display as severe a phenotype, and none of the drug treatments tested were successful in eliciting a significant reduction in arrhythmic event frequency. This indicates a mechanistic difference between the two sarcomeric gene mutations explored in this thesis, and highlights the need for continued drug screening to rescue the phenotype.


A
% Aberrant events
10 μM Dantrolene
10 μM Ranolazine
% abnormal events
15
10
5
0
ns
ns
P1 ACTC1WT/WT Vehicle only
P1 ACTC1WT/WT 10μM Dantrolene/ 10μM Ranolazine
P1 ACTC1WT/MUT Vehicle only
P1 ACTC1WT/MUT 10μM Dantrolene/ 10μM Ranolazine
P1 ACTC1WT/WT
P1 ACTC1WT/MUT
B
Systolic calcium peak amplitude
10 μM Dantrolene
10 μM Ranolazine
Calcium transient peak amplitude (F/F0)
20000
15000
10000
5000
0
ns
ns
C
Tpeak
10 μM Dantrolene
10 μM Ranolazine
Milliseconds
300
200
100
0
ns
ns
D
Spontaneous beat rate
10 μM Dantrolene
10 μM Ranolazine
% abnormal events
80
60
40
20
0
ns
ns

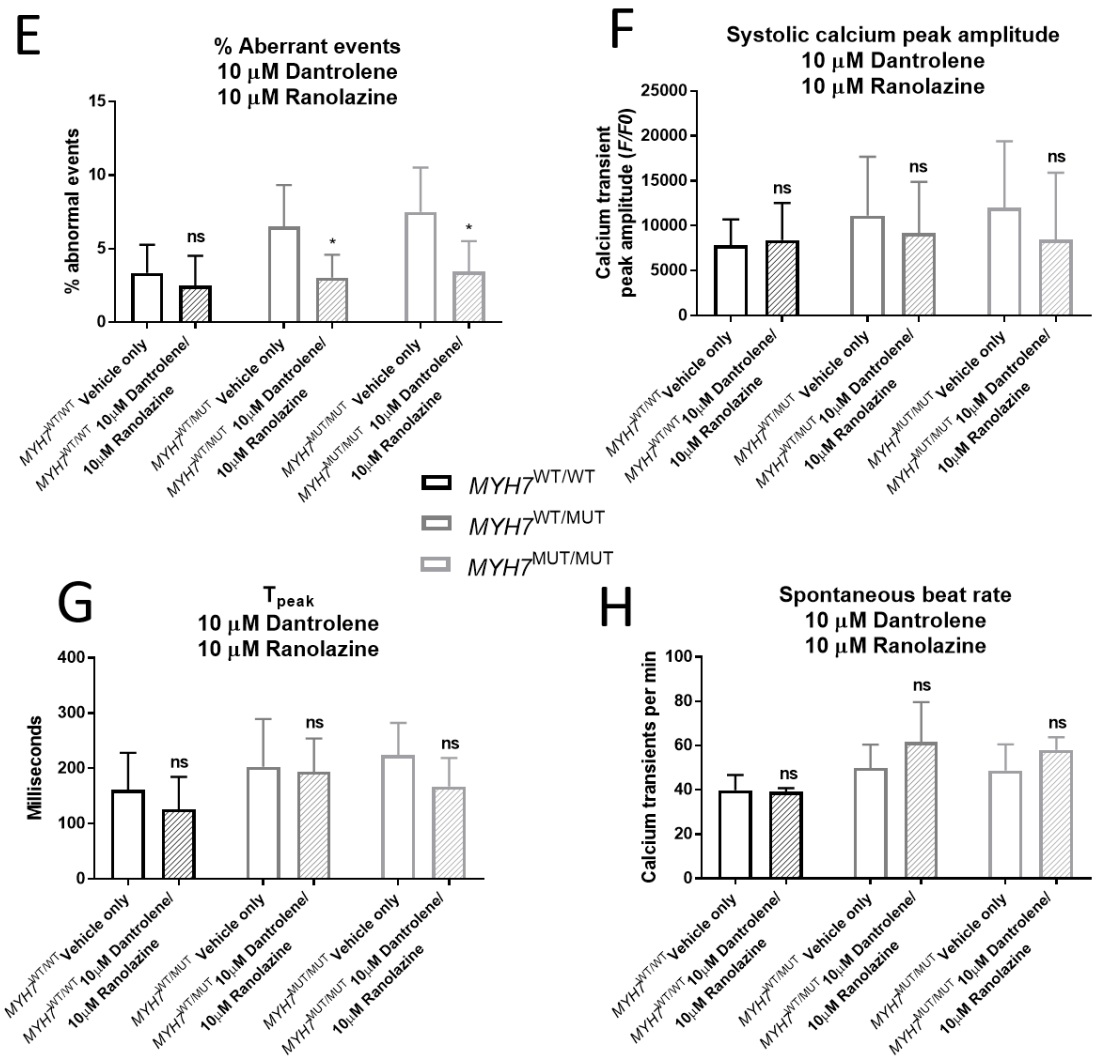


Figure 5.14. Reduced arrhythmic calcium transient event frequency in *MYH7* C1923T RGECO hiPSC-CMs in response to combined dantrolene and ranolazine treatment is not reflected in *ACTC1* G301A RGECO hiPSC-CMs.

(A-D) ClampFit event detection analysis of confocal line scans of d28 or d30 P1 *ACTC1*$^{WT/WT}$ and P1 *ACTC1*$^{WT/MUT}$ RGECO hiPSC-CMs incubated with 10 μM dantrolene and 10 μM ranolazine combined treatment or DMSO vehicle only for 24 hours. **(A)** Percentage of arrhythmic DAD-like calcium transient events detected. **(B)** Mean calcium transient amplitude. **(C)** Calcium transient time to peak. **(D)** Number of calcium transient events detected per minute. Data presented as mean ±SD, n = 6 vehicle, 4 drug. Kruskal-Wallis test with Dunn's multiple comparison test; ns – not significant. **(E-H)** ClampFit event detection analysis of confocal line scans of d26, d28 or d30 *MYH7*$^{WT/WT}$, *MYH7*$^{WT/MUT}$ and *MYH7*$^{MUT/MUT}$ RGECO hiPSC-CMs incubated with 10 μM dantrolene and 10 μM ranolazine combined treatment or DMSO vehicle only for 24 hours. **(E)** Percentage of arrhythmic DAD-like events calcium transient events detected. **(F)** Mean calcium transient peak amplitude. **(G)** Number of calcium transient events detected per minute. **(H)** Number of calcium transient events detected per minute. Data presented as mean ±SD, n = 16 vehicle, 6 drug across 3 experiments. Kruskal-Wallis test with Dunn's multiple comparison test; * $p \leq 0.0207$, ns – not significant.

5.3.3 The use of optogenetics in hiPSC-CMs towards optical pacing

A major shortcoming of the drug screening tests shown is that the hiPSC-CMs are not paced, and are therefore liable to beat at different frequencies. This has a knock-on effect on parameters such as T_{peak}. However, electrical pacing with field stimulation electrodes can be cumbersome, and limits the timeframe of phenotyping experiments (Chang et al., 2017). To overcome these challenges, efforts are now being made towards optogenetic pacing of hiPSC-CMs. Optical pacing of hiPSC-CMs with blue-light stimulation (~480 nm) of the light-gated ion channel, ChR2, lends itself to being multiplexed with the RGECO reporter lines as they are both spectrally distinct.

Within our laboratory, healthy P1 hiPSCs have been randomly targeted with ChR2 by using an excision-incompetent PiggyBac transposase to randomly integrate a ChR2-EYFP-T2A-BSD cassette into the genome (**Figure 5.15A**). Fusion of ChR2 to EYFP allows for detection of the fusion protein in hiPSCs, localised within the cell membrane (**Figure 5.15B**) (Cell line generated by Dr Mine Bakar Dogu).

These ChR2-expressing hiPSCs were then successfully differentiated to cardiomyocytes and used in optical pacing experiments on the CellOPTIQ™ platform (**Figure 5.15C-J**). The proprietary software package provided with the CellOPTIQ™ uses pixel displacement of beating hiPSC-CMs to calculate and plot contraction parameters (**Figure 5.15C-E**).

A region of hiPSC-CMs within a single well of a 96-well plate was shown to spontaneously beat at a very slow rate of ~ 18 bpm. With blue-light pulses of approximately 1 second applied to the same area of hiPSC-CMs at a frequency of 0.5 Hz, the beat rate increased to ~24 bpm (**Figure 5.15C**). However, given the extended blue-light pulse time, there was an extended contraction time during the downstroke. This was reflected as a significantly longer contraction duration at 10% amplitude (CD_{10}) (**Figure 5.15H**) and downstroke time (Dn_{90}) (**Figure 5.15J**) at 0.5 Hz (**** $p < 0.0001$).

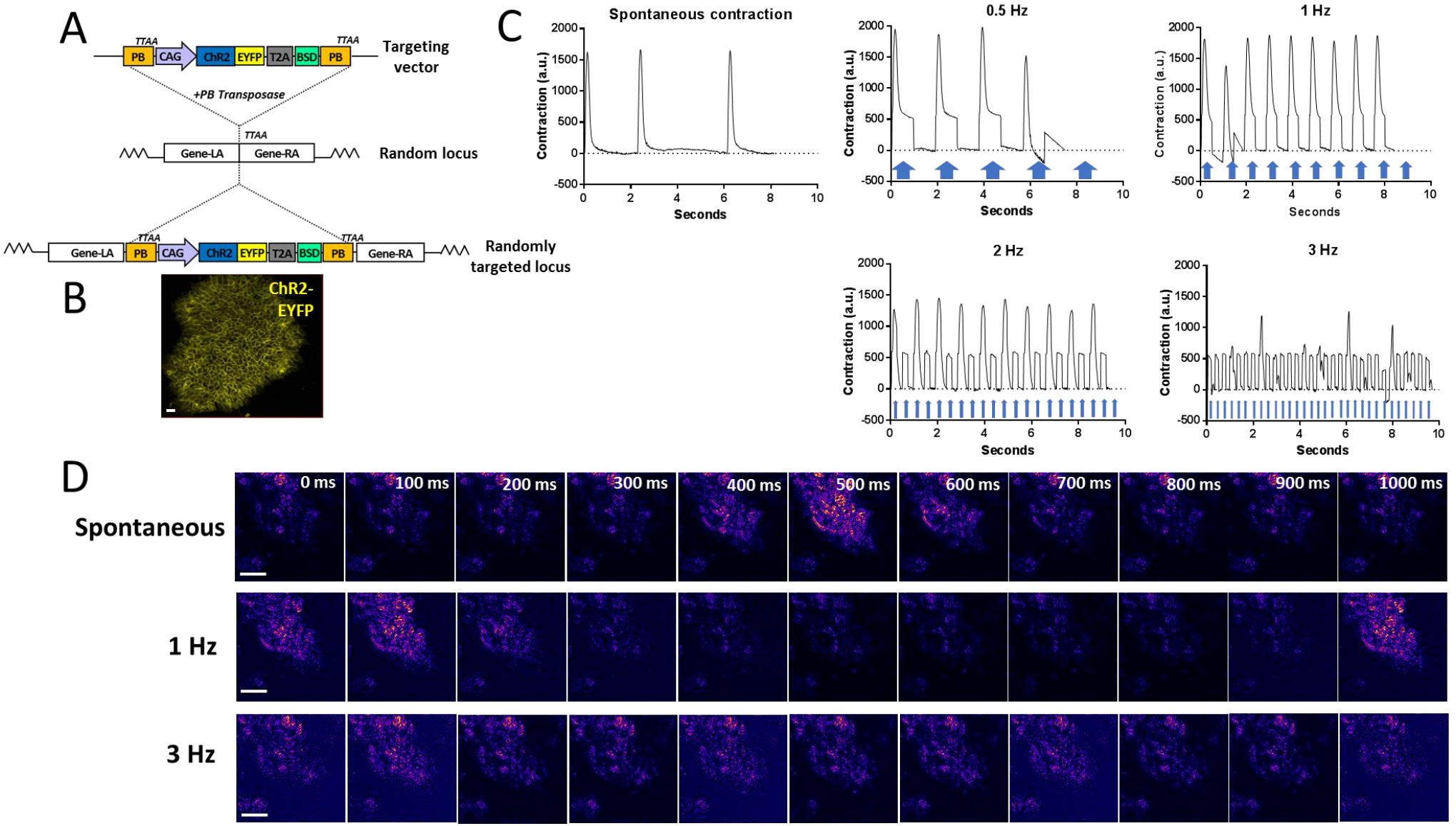
Optical pacing of ChR2 hiPSC-CMs was also successful at 1 Hz (500 ms), 2 Hz (250 ms) and 3 Hz (166 ms) blue-light pulses (**Figure 5.15C**). With increasing frequency of optical pacing, the contraction rate increased simultaneously, illustrated with a significantly shorter inter-event interval at higher pacing frequencies (**** $p < 0.0001$) (**Figure 5.15F**).

Increased frequency of pacing also led to a parallel decrease in contraction amplitude which was significant at 2 Hz (** $p = 0.0026$) and 3 Hz (**** $p < 0.0001$) (**Figure 5.15G**). This illustrates the negative force-frequency relationship that is seen in foetal- and hiPSC-CMs (Germanguz et al., 2011, Feric and Radisic, 2016).

Both the increased rate of contraction, and the decreased force of contraction with optical pacing can be seen visually using a heat-map style video of the hiPSC-CMs, where brighter areas correspond to greater contraction force (**Figure 5.15D, Supplementary videos 3-7**).

These preliminary experiments exploring the use of optogenetic pacing of hiPSC-CMs demonstrate a way in which the disease-phenotyping and drug screening experiments within this chapter can be improved upon and made more comparable. These results are proof-of-principle for simultaneous pacing with blue-light and calcium transient measurements from RGECO, for more accurate analyses of HCM phenotype and potential drug rescue.

The application of engineered calcium reporter lines for modelling hypertrophic cardiomyopathy and screening potential pharmacological interventions in vitro



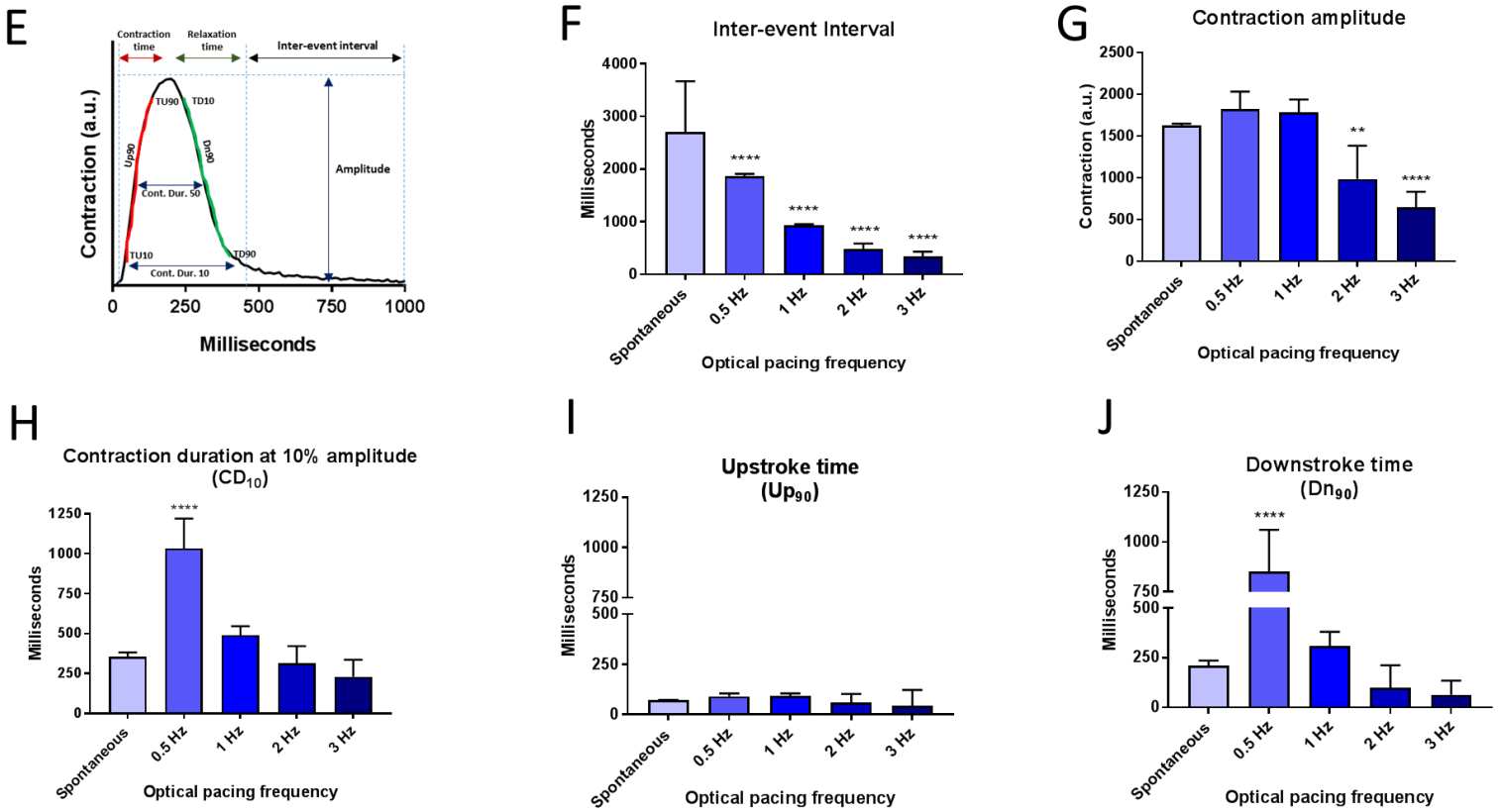


Figure 5.15. Random integration of ChR2, a light-gated ion channel, into P1 hiPSCs allows for optogenetic pacing of hiPSC-CMs on the CellOPTIQ™ platform.

(A) Schematic of ChR2-EYFP hiPSC line generation. The targeting vector consists of a ChR2-EYFP-T2A-BSD cassette flanked with PiggyBac (PB) inverted terminal repeats. This is co-transfected into hiPSCs with an excision-incompetent PB transposase for random integration into regions of the genome containing the TTAA site. **(B)** Confocal frame-scan image of a selected hiPSC clone with even expression of ChR2-EYFP on the cell membrane (yellow). Scale bars = 20 µm. Cell line generated by Dr Mine Bakar Dogu. **(C)** d30 ChR2-EYFP hiPSC-CMs paced with 480 nm blue light (arrows) at different frequencies using the CellOPTIQ™ and software to calculate contraction based on pixel movement. **(D)** Video stills from ChR2-EYFP hiPSC-CMs being optically paced on the CellOPTIQ™ (Supplementary videos 3, 5, 7). Scale bars = 20 µm. **(E)** Contraction parameters that are calculated using CellOPTIQ™ software. CD_{10} – contraction duration at 10% amplitude, Up_{90} – upstroke time, Dn_{90} – downstroke time **(F)** Reduced inter-event interval with increasing frequency of optical pacing. **(G)** Contraction amplitude decreases with increasing pacing frequency demonstrating the negative force-frequency relationship. **(H)** Faster contraction duration with increasing pacing frequency. **(I)** Time to 90% contraction (upstroke time). **(J)** Time to 90% relaxation (downstroke time) is faster with increasing pacing frequency. Data presented as mean ±SD, n = 9 traces. One-way ANOVA with Dunnett's multiple comparison test; ** $p = 0.0026$, **** $p < 0.0001$.

5.4 Discussion

HCM is a highly complex disease with approximately 1300 causative mutations (Marian and Braunwald, 2017). Therefore, this chapter focused on comparing the *ACTC1* G301A mutation to the *MYH7* C9123T mutation using GECIs as a tool to assess calcium transients.

P2 *ACTC1*$^{WT/MUT}$ GEM-GECO hiPSC-CMs had no significant increase in arrhythmic events, lower systolic calcium, faster spontaneous beat rate and a faster calcium transient T_{peak}. In contrast, P1 *ACTC1*$^{WT/MUT}$ RGECO hiPSC-CMs had significant increases in arrhythmic event frequency, no change in systolic calcium or beat rate, and a faster calcium transient T_{peak} when compared to healthy isogenic controls. The differing phenotype severities in two hiPSC lines harbouring the same mutation demonstrates the role that genetic background plays in disease progression, albeit with the use of different GECI in each case. Indeed, these results suggest that *ACTC1* G301A may be necessary yet not sufficient to cause calcium handling abnormalities.

MYH7 C9123T hiPSC-CMs, however, displayed a more severe phenotype of; highly arrhythmic calcium transients, increased spontaneous beat rate, higher systolic calcium illustrated by a higher calcium transient fluorescence amplitude, and a longer T_{peak} suggesting longer calcium transient duration. These hallmarks were more readily identified due to the presence of a homozygous mutant and increased phenotypic severity with mutation load. Resistance to the L-type calcium channel blocker nifedipine, and reduced arrhythmic event frequency in 0.1 mM extracellular Ca^{2+}, suggested that high intracellular Ca^{2+} instigating Ca^{2+} release from the SR may the likely culprit for aberrant calcium transient events in *MYH7* mutant hiPSC-CMs. Based on this hypothesis, a selection of drugs were tested to rescue the phenotype.

Within this chapter, ranolazine was found to reduce the arrhythmic phenotype in *MYH7* C9123T hiPSC-CMs, but not *ACTC1* G301A hiPSC-CMs. This highlights the differences between these two mutations and points towards the requirement for bespoke, genotype-dependent treatments for patients suffering with HCM.

5.4.1 The severity of the *MYH7* C9123T phenotype compared to the *ACTC1* G301A phenotype

Mutations to *MYH7* are found in approximately 41% of familial HCM cases, and is the gene most likely to be mutated in patient cohorts with a malignant prognosis (Woo et al., 2003, Richard et al., 2003) (**Section 1.2.1**). The *MYH7* C9123T mutation is particularly severe, as it affects the actin binding site, and is associated with relatively early-onset hypertrophy and a short life expectancy of ~33 years old (Watkins et al., 1992). This is reflected in the phenotyping results presented in **Figure 5.6** in which a tenfold increase in DAD-like arrhythmic events is seen in *MYH7*$^{MUT/MUT}$ compared to *MYH7*$^{WT/WT}$ hiPSC-CMs.

In contrast, *ACTC1* mutations are found in less than 1% of HCM cases (Olson et al., 2000), and have more variable penetrance. The *ACTC1* G301A mutation occurs in an area of α–cardiac actin that binds myosin, and mutations in this area of *ACTC1* result in varying cardiomyopathies ranging from apical remodelling and non-compaction to septal defects (Arad et al., 2005). Indeed, it has been shown that α-cardiac actin mutations can lead to diverse outcomes even within members of the same family, suggesting that other modifiers may alter expressivity (Augiere et al., 2015).

Our results support these findings, as P1 *ACTC1*$^{WT/MUT}$ hiPSC-CMs seem to show a more severe phenotype than P2 *ACTC1*$^{WT/MUT}$ hiPSC-CMs (**Figure 5.4, Figure 5.5**). P1 hiPSCs were derived from an older patient with the mutation, and P2 hiPSCs were derived from a younger, healthy relative. Our model demonstrates that the genetic background of P1 may play a role in phenotype severity.

The specific genetic modifiers that may be exacerbating the HCM phenotype in P1 are not known, but one can speculate that there may be genetic differences in any one of 36 or more sarcomeric, cytoskeletal, protein synthesis, calcium handling or ion channel genes associated with HCM, as well as those with unknown function (Maron et al., 2012, Lim et al., 2001b). In addition, epigenetic modifiers are now being explored as potential contributors to the HCM phenotype, with the acetylation status of the transcriptional co-activators CBP and p300 being linked to the hypertrophic response of cardiomyocytes (Kalozoumi et al., 2012, Gusterson et al., 2003).

Transcriptomic analysis of the *MYH7* C9123T mutation in two more isogenic sets of hPSC-CMs, additional to the REBL-PAT based lines described in this thesis, have

revealed the upregulation of several as yet unannotated long non-coding RNAs (lncRNAs) (Mosqueira et al., 2018). Previous studies have failed to identify the function of dysregulated lncRNAs in HCM (Yang et al., 2015), and this approach highlights the utility of using RNAseq and 'big data' analysis to elucidate factors involved in disease progression and severity.

The weaker arrhythmic phenotype observed in P2 *ACTC1*$^{WT/MUT}$ G301A hiPSC-CMs may be reflective of genotype-positive, phenotype-negative 'silent' gene carriers (Maron et al., 2011b). These patients are often diagnosed as adults and show no obvious phenotype. However, a follow-up study of a genotype-positive, phenotype negative patient population revealed that 18% then went on to present some form of cardiac complication in later life (Christiaans et al., 2011, Ingles et al., 2015). P2 *ACTC1*$^{WT/MUT}$ hiPSC-CMs therefore offer the opportunity to model this HCM phenotype onset, possibly with mechanical stimulation or further maturation to induce a phenotypic response (Jung et al., 2016, Parikh et al., 2017, Tiburcy et al., 2017). In this way, P2 *ACTC1*$^{WT/MUT}$ hiPSC-CMs may have utility in screening long-term pharmacological treatments to prevent the onset of HCM in asymptomatic patients. The GECIs described herein are suited to long-term, repeated optical measurements in this type of study.

In summary, the results within this chapter demonstrate the complexity of HCM. HCM can be described as an 'umbrella term' encompassing a wide range of mutations, phenotypes and severities. In some cases, such as contractility and calcium sensitivity, these phenotypes can be opposing (van der Velden et al., 2015). It is therefore crucial that clinical treatments for HCM do not use a 'one size fits all' approach if improved clinical outcomes are to be realised.

5.4.2 Mechanistic insights into *MYH7*-associated HCM

The resistance of *MYH7* mutant hiPSC-CMs to the L-type Ca^{2+} channel blocker nifedipine (**Figure 5.7**), together with a reduced frequency of arrhythmic events in low (0.1 mM) extracellular Ca^{2+} (**Figure 5.8**), led to the hypothesis that high intracellular calcium was responsible for the arrhythmic phenotype. This is similar to the studies conducted by Lan et al., in which a hypothesis of "Ca^{2+}-trapping" within the myofilament is posited, with limited supporting evidence (Lan et al., 2013, Fatkin et al., 2000). Nevertheless, significantly higher systolic calcium in *MYH7* mutants (**Figure 5.6**), suggested a potential relationship between intracellular calcium regulation and phenotypic severity.

Our recent study subscribed to the "energy-depletion" model of HCM with respect to *MYH7* C9123T mutation. Increased ATP production in the absence of increased mitochondrial mass suggests that *MYH7* mutant hiPSC-CMs possess a disorganised sarcomere that causes inefficient ATP usage resulting in an energetic deficit. This impairs the ability of the cardiomyocyte to effectively restore calcium to basal levels (Ashrafian et al., 2003, Mosqueira et al., 2018).

Efforts to reduce intracellular calcium with drugs and subsequently alleviate the abnormal calcium transients in mutant hiPSC-CMs in this chapter had mixed success. The I_{Na} blocker ranolazine was capable of reducing aberrant calcium transient events by enhancing Ca^{2+} efflux through NCX during diastole (Coppini et al., 2013). Co-immunoprecipitation studies have shown a potential role for Ca^{2+}/calmodulin-dependent protein kinase II (CaMKII) in modulating both Na^+ and Ca^{2+} influx in HCM CMs through L-type Ca^{2+} channels and I_{Na}, respectively (Coppini et al., 2013). Ranolazine acts to counteract this CaMKII-mediated Na^+ overload.

The ryanodine receptor antagonist dantrolene was also applied to *MYH7* mutant hiPSC-CMs, achieving a reduction in systolic calcium, but no significant effect on abnormal calcium transient event frequency. To date, dantrolene has only been applied in the context of HCM on a mouse model of troponin-T HCM (Okuda et al., 2018). The aforementioned study proposed that CaMKII phosphorylation of ryanodine receptors is higher in mutated CMs, leading to aberrant Ca^{2+} release. Dantrolene is able to negate this effect by stabilising the ryanodine receptor.

Both ranolazine and dantrolene seem to counteract the negative effects of CaMKII in CMs with HCM. Indeed, nuclear CaMKII has been shown to increase hypertrophic gene expression by phosphorylating nuclear histone deacetylases (Zhang et al., 2007). Cytoplasmic CaMKII can phosphorylate L-type Ca^{2+} channels, ryanodine receptors and phospholamban to perpetuate a positive feedback loop that leads to calcineurin activation of hypertrophic gene expression through the transcription factor MEF2 (Passier et al., 2000) (**Figure 5.16**).

In the proposed model, the mutation to β-MHC results in an energetic deficit that hampers the energetically demanding SERCA2a pump (Ashrafian et al., 2003, Lipskaia et al., 2010), leading to increased intracellular Ca^{2+}. Calcium then activates calcineurin-based hypertrophic signals as well as CaMKII phosphorylation of L-type Ca^{2+} channels, ryanodine receptors and the late sodium channel. This leads to both Ca^{2+} and

Na^+ overload, reducing the efficiency of NCX, and potentially even reversing its direction (Terracciano et al., 2001, Coppini et al., 2013). Calcium overload during diastole then leads to delayed afterdepolarisations (Katra and Laurita, 2005).

Calcium dysfunction therefore precedes hypertrophic remodelling, and CaMKII may be a potential upstream target for therapeutic interventions.

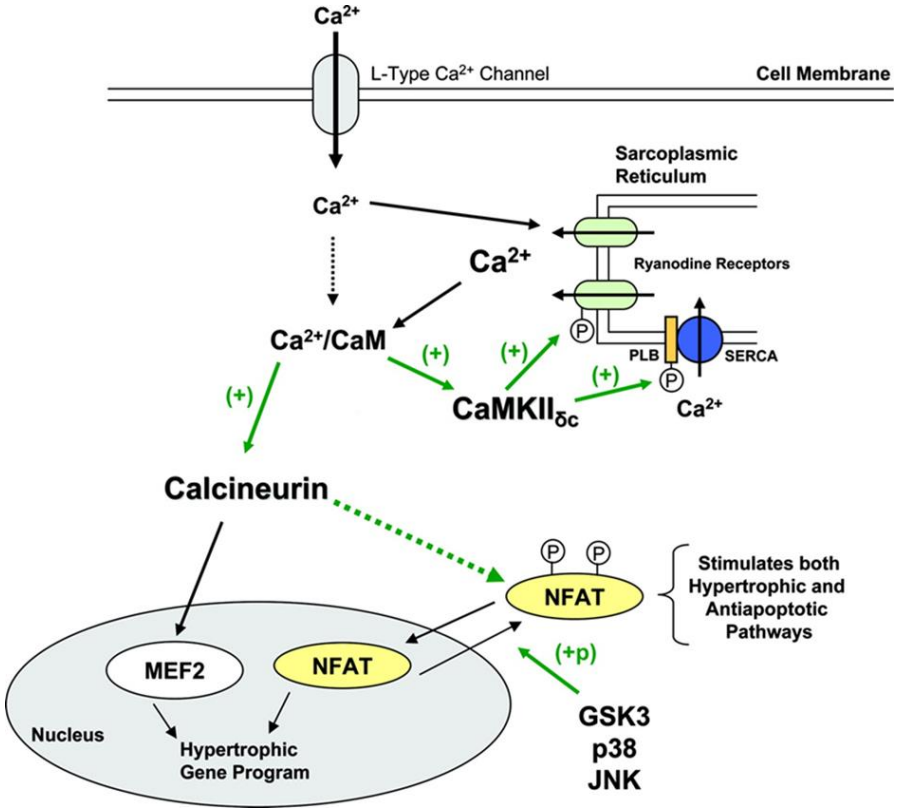


Figure 5.16. Both calcineurin and CaMKII are involved in hypertrophic remodelling and calcium dysfunction in HCM.

Increased cytosolic calcium activates calcineurin which can directly induce MEF2 transcription of hypertrophic genes. Calcineurin can also de-phosphorylate NFAT to induce translocation to the nucleus and the intiation of hypertrophic gene expression. Increased cytosolic calcium also intiates a positive feedback loop with CaMKII which phosphorylates L-type Ca^{2+} channels, ryanodine receptors and the late sodium channel (I_{Na}). Adapted from (MacDonnell et al., 2009)

6 General discussion

The aim of this thesis was to investigate the calcium handling properties of hiPSC-CMs with mutations known to cause hypertrophic cardiomyopathy (HCM) utilising genetically encoded calcium indicators (GECIs). HCM is notoriously variable in causative genes, penetrance and expressivity. Therefore, utilising the contemporary genome editing technique CRISPR Cas9, isogenic sets of hiPSCs harbouring the *ACTC1* G301A or *MYH7* C9123T mutations were targeted with the GECIs GEM-GECO or RGECO.

These lines were used as tools to demonstrate that the calcium handling of healthy hiPSC-CMs, although immature, involve the use of basic organelles, receptors and channels including the sarcoplasmic reticulum, SERCA, ryanodine receptors and L-type Ca^{2+} channels.

Furthermore, these reporter cell lines revealed calcium handling abnormalities in mutated hiPSC-CMs, and recapitulated a dangerous hallmark of HCM – aberrant calcium transient events. Calcium channel antagonists and variation of extracellular calcium concentrations helped to elucidate a potential mechanism of high intracellular calcium as a cause of the aberrant transient phenotype. This information was then used to perform a focussed screen using a panel of potential drugs. Treatment with the late Na^{+} antagonist ranolazine emerged as a beneficial drug for alleviating the established phenotype in *MYH7* mutants, as did combination treatment of ranolazine and the ryanodine receptor antagonist dantrolene. However, the calcium transient abnormality of *ACTC1* mutants varied in severity, and these drugs showed limited benefit.

6.1 Fulfilment of thesis objectives

There were five main thesis objectives outlined in **section 1.7** which have been addressed throughout this thesis:

6.1.1 Objective 1: Utilise CRISPR/Cas9 to generate GECI-expressing hiPSC lines in an HCM background, with healthy isogenic controls

Despite some initial setbacks with incomplete peptide cleavage of the targeting cassette by the P2A sequence (**Figure 3.17**), several isogenic sets of hiPSCs were targeted with GECIs in **section 3.3**.

The *AAVS1* loci of REBL PAT *MYH7*$^{WT/WT}$, *MYH7*$^{WT/MUT}$ and *MYH7*$^{MUT/MUT}$ hiPSCs were successfully targeted with RGECO (**Figure 3.21**). Similarly, P1 *ACTC1*$^{WT/WT}$ and P1 *ACTC1*$^{WT/MUT}$ hiPSCs were targeted with RGECO (**Figure 3.23**). Finally, P2 *ACTC1*$^{WT/MUT}$ and P2 *ACTC1*$^{WT/WT}$ hiPSCs were targeted with GEM-GECO (**Figure 3.22**). This provided a vital resource for studying calcium handling in isogenic healthy and diseased hiPSC-CMs, as well as being able to cross-compare the effects of the *MYH7* C9123T mutation to the *ACTC1* G301A mutation using the same GECI - RGECO.

However, silencing of the RGECO transgene occurred upon differentiation in some clones, and in **Figure 3.25D**, clones were reselected for high expression. In addition, puromycin selection was maintained for extended periods of at least 3 passages to retain high expression of RGECO in **Figure 3.25C**. Therefore, some questions remain with regard to how much of a 'safe harbour' the *AAVS1* locus is. Luo et al claimed weak EF1α-driven transgene expression within *AAVS1* could be remedied by changing to the CAG promoter (Luo et al., 2014). This informed the decision to change to the CAG promoter in this study. However, in some clones, silencing has still occurred upon differentiation to cardiomyocytes.

Silencing may have been caused by epigenetic modifications. The *AAVS1* locus may undergo *de novo* DNA methylation upon differentiation to a cardiomyocyte fate, and this phenomenon has been observed in hESCs differentiated to hepatocyte-like cells (Ordovas et al., 2015).

Further investigations are required to understand why some clones are not silenced, and express RGECO robustly. Despite using a high-fidelity nickase strategy to reduce off-target integrations (Ran et al., 2013a), inaccurate targeting may have occurred and a list of potential integration sites is provided in **Appendix II**.

6.1.2 Objective 2: Develop a method to optically analyse calcium transients and quantify changes in response to drugs or disease-causing mutations

Microscopy methods for calcium transient imaging were explored in **section 4.3.2**.

Unfortunately, the DeltaVision epifluorescence widefield microscopy system could not be used for the detection of the ratiometric blue-green GEM-GECO indicator (**Figure 4.7**). The absence of a beamsplitter meant that the emission filter had to switch between each image. This meant that simultaneous ratiometric imaging of the blue and green emissions was not possible.

In addition, due to the time taken to excite the fluorophore, the maximum imaging speed achieved for imaging RGECO was 10 frames/second. This decreased to 3.3 frames/second when imaging GEM-GECO. However, the manufacturer claims the CCD camera can achieve 11 frames/second using full frame 1392 x 1040 pixels, or 57 frames/second with 512 x 512 pixels and 4x binning (Davies et al., 2013). Therefore the DeltaVision system may still be useful for detection of the RGECO fluorophore; further optimisation may be required to reduce image quality in favour of fast data acquisition.

Confocal line scan microscopy was found to be capable of data acquisition at a speed of 13.3 frames/second. Crucially, the ratiometric GEM-GECO indicator could be simultaneously imaged in both blue and green emission wavelengths (**Figure 4.8**).

This led to the repurposing of a patch-clamp software package, ClampFit, for calcium transient event detection and quantification (**Figure 4.9**). Indeed, **Figure 4.12** illustrates the capability of ClampFit analysis of confocal line scan data to identify and quantify aberrant events in hiPSC-CMs in response to micromolar concentrations of ryanodine.

However, ClampFit software cannot provide accurate measurements of all calcium transient parameters, especially calcium transient duration (CTD) and T_{decay} which are important for disease modelling cardiomyopathies (Jung et al., 2012, Han et al., 2014) and drug screening with hiPSC-CMs (Sirenko et al., 2013, Dempsey et al., 2016).

By moving towards integrated, multiwell plate systems such as the CellOPTIQ™ with dedicated software for calcium and voltage imaging, high throughput fluorescent reporter imaging can be achieved (Lu et al., 2017, Duncan et al., 2017).

6.1.3 Objective 3: Validate the utility of hiPSC-CMs to model disease *in vitro* and demonstrate their ability to recapitulate hallmarks of calcium handling

The utility of hiPSC-CMs for studying calcium handling was tested with a variety of drugs of known action in **section 4.3.3**.

The application of caffeine was used to demonstrate that the hiPSC-CMs used in this thesis were capable of releasing Ca^{2+} from the sarcoplasmic reticulum (SR) (**Figure 4.10**). Thapsigargin, a SERCA2a antagonist, was used to demonstrate an ability for Ca^{2+} re-uptake into the SR (**Figure 4.11**). However, continued calcium transients being evoked after addition of these drugs suggest a reliance on sarcolemmal flux.

It was important to establish that a basic functional calcium handling machinery existed within our hiPSC-CMs, as a number of reports have shown calcium handling immaturity in hESC- and hiPSC-CMs (Dolnikov et al., 2006, Lee et al., 2011, Yang et al., 2014).

The inclusion of qRT-PCR analysis to assess the expression of key genes such as *RYR2*, *SERCA2a*, *CSQ2*, *TRDN* and others would have enhanced this thesis, as these key calcium handling genes are thought to be downregulated in hiPSC-CMs. It would also have been beneficial to look at the expression of these genes in the isogenic HCM lines, particularly as *RYR2* and *SERCA2a* have been shown to be downregulated in an in vitro model of HCM (Han et al., 2014), albeit from unrelated donors.

Nevertheless, confocal line scans showed that calcium transient waveforms of hiPSC-CMs in this thesis were U-shaped, and this was likely due to a lack of T-tubules (Louch et al., 2015) (**Figure 4.8**, **Figure 4.17**). Although immature, these hiPSC-CMs were deemed suitable for disease modelling and drug screening applications.

6.1.4 Objective 4: Use GECI-expressing hiPSC-CMs as a tool to detect HCM phenotypes and compare phenotypes between different gene mutations

Confocal line scan microscopy and ClampFit event detection analysis were used to phenotype isogenic sets of hiPSC-CMs harbouring mutations associated with HCM in **section 5.3.1.**

The *ACTC1* mutant phenotype was variable between P1 and P2, albeit with the use of different GECI (**Figure 5.4, Figure 5.5**). Although more challenging to delineate patterns due to the lack of a homozygous mutant, it could be seen that aberrant transient events were more frequent in P1 than in P2. This supports the notion of variable expressivity in *ACTC1* mutants (Arad et al., 2005).

Further phenotyping experiments found that *MYH7* mutants displayed more aberrant transient events, higher systolic calcium and a longer calcium transient time to peak (**Figure 5.6**). This correlates well with studies which have shown that mutation to *MYH7* can cause abnormal calcium transients, higher diastolic calcium and a longer calcium transient duration (Han et al., 2014)

MYH7 mutants were resistant to the L-type Ca^{2+} channel blocker nifedipine (**Figure 5.7**) and aberrant events were reduced in low extracellular calcium conditions (**Figure 5.8**). This supported the hypothesis that high intracellular calcium results in delayed afterdepolarisation-like events (Katra and Laurita, 2005, Huke and Knollmann, 2010).

However, these studies only look at calcium transient changes, which are only a single aspect of HCM. This does not give an insight into other important phenotypes such as contractility, myofibrillar disarray, mitochondrial demand and hypertrophy which have been explored in other *in vitro* HCM phenotyping publications (Birket et al., 2015a, Tanaka et al., 2014).

6.1.5 Objective 5: Use drugs in an attempt to alleviate the HCM phenotype

The hypothesis that high intracellular calcium caused calcium transient changes in mutant hiPSC-CMs was tested by screening a panel of drugs in **section 5.3.2** to significantly reduce the frequency of aberrant calcium transient events.

Some drugs which are used clinically to treat HCM, such as the ß–blocker propranolol, were not found to be efficacious in *MYH7* or *ACTC1* mutants (**Figure 5.9**) (Östman-Smith, 2014). This emphasises the fact that current treatment options may not be beneficial for all HCM mutations, and further drug development is warranted for this disease (Spoladore et al., 2012).

MYK-461, a ß–myosin ATPase inhibitor undergoing clinical trials for HCM was tested, but found to have no effect on calcium transient parameters (Stern et al., 2016, Kawas et al., 2017) (**Figure 5.10**). However, this drug is likely to have altered contractility and underscores the need to consider multiple phenotypic readouts.

The late sodium current blocker ranolazine was successful in significantly reducing the frequency of aberrant calcium transients in *MYH7* mutant hiPSC-CMs (**Figure 5.12**). In addition, combination treatment with the ryanodine receptor antagonist dantrolene had beneficial effects for *MYH7* mutant hiPSC-CMs. These drug screens helped to provide information as to the potential mechanisms behind HCM in *MYH7* mutants. Specifically, that Na^{+} and Ca^{2+} overload lead to arrhythmias, and may potentially activate downstream hypertrophic signalling pathways.

However, these drug screens were relatively low throughput, with a limited concentration range tested. In addition, these drug screens were not performed under paced conditions, and this will affect calcium transient parameters and consistency between drug treatments (Butler et al., 2015).

6.2 Calcium and its role in HCM progression

6.2.1 Phenotyping HCM *in vitro*

A wide range of papers have investigated changes in calcium handling in order to study and phenotype HCM. Some of these papers, however, rely on animal models (Song et al., 2011, Lim et al., 2001a) or skinned primary samples (Coppini et al., 2013). Animal models may not faithfully recapitulate the disease in vitro due to species differences, and primary samples can be difficult to obtain and maintain in culture. Although somewhat immature, hiPSC-CMs provide an accessible, physiologically relevant model. At the time of writing, there are only three published examples of hiPSC-CMs being used *in vitro* to investigate calcium handling in HCM (**Table 6.1**).

In contrast to other studies which use calcium imaging to inform HCM phenotype, this thesis utilises GECIs instead of calcium indicator dyes (**Table 6.1**). These GECI lines have the capability to be repeatedly assayed, even if this property was not fully exploited herein. Furthermore, GECIs ensure that potential acetoxymethyl-related toxicity does not influence any results. However, it took a significant amount of time and effort to engineer and select GECI clones.

The studies conducted by Ojala et al. were progressive due to the inclusion of two different HCM-causing mutations, rather than focusing on a single SNP (Ojala et al., 2016). Key differences between the *TPM1* Asp175Asn mutation and the *MYBPC3* Gln1061X were seen, including a more severe arrhythmic phenotype in *TPM1* mutants, and a longer action potential duration. This shows the importance of studying multiple mutations to fully understand HCM, as its expressivity is highly variable. This thesis has also found phenotypic differences between mutations, with *MYH7* mutants displayin more aberrant calcium transients than *ACTC1* mutants.

Crucially, this study has used CRISPR Cas9 corrected and mutated isogenic control lines (**Table 6.1**). This has allowed the precise study of the genotype-phenotype relationship and also demonstrated differences between related P1 and P2 *ACTC1* mutants. As such, the elucidation of background genetic modifiers which are responsible for these differences will be crucial for understanding HCM. In the context of phenotyping cardiomyopathy in hiPSC-CMs, isogenics have so far only been used to study an *in vitro* model of dilated cardiomyopathy (DCM), with a phenotypic readout of contractility rather than calcium handling (Stillitano et al., 2016).

Unsurprisingly, the *MYH7* Arg453Cys mutants presented here broadly correlate with the previously published *MYH7* Arg663His and *MYH7* Arg442Gly mutants (Lan et al., 2013, Han et al., 2014). There are similarities in the occurrence of aberrant calcium transient events and high intracellular calcium. However, these studies show an increase in aberrant events upon isoprenaline addition, which is rescued with the ß-blockers propranolol (Lan et al., 2013) or metoprolol (Han et al., 2014) (**Table 6.1**). These findings could not be replicated in this study.

Other key differences include the fact that these studies perform multiple days of drug treatment to rescue the phenotype, whilst this study achieves statistically significant reduction of aberrant events in 24 hours. This suggests that with extended ranolazine and dantrolene treatment, the concentrations used herein could be titrated down. Alternatively, more apparent phenotypic rescue may be achieved with the *ACTC1* mutants.

Han et al. have also performed more comprehensive gene expression and transcriptome analysis, showing that *SERCA* can be downregulated, whilst fibrosis associated genes such as *COL1A1* and *COL9A2* are upregulated (Han et al., 2014). These sorts of analyses are important for discovering underlying genetic causes of HCM, other than the mutation studied. Interestingly, an upregulation in *SCN5A* encoding for the sodium channel NaV1.5 is seen in *MYH7* Arg442Gly mutants, lending credence to the assertion that ranolazine elicits its therapeutic benefit by preventing Na^+ overload (Coppini et al., 2013).

Nevertheless, the calcium imaging phenotyping presented in this thesis has supported and supplemented other phenotypic readouts including 3D force generation analysis, 2D contractility, CM hypertrophy and metabolic demand assays to gain a more in-depth knowledge of the effects of the *ACTC1* G301A and *MYH7* C9123T mutations (Mosqueira et al., 2018).

hiPSC source and mutations studied	Fluorescent Ca^{2+} indicator	Calcium handling phenotypes in hiPSC-CMs with HCM	Drug treatments and key findings
(**Lan et al., 2013**) Family with *MYH7* Arg663His mutation. Five with heterozygous mutation, five healthy family members without mutation.	Chemical calcium indicator: Fluo-4 AM (intensiometric)	• Aberrant calcium transient events. • Increased intracellular $[Ca^{2+}]$. • Smaller SR Ca^{2+} release upon caffeine addition. • Higher resistance to nifedipine.	• Isoprenaline increases aberrant event frequency, this is rescued with isoprenaline + 400 nM propranolol. • 5 day treatment with 100 nM verapamil reduces aberrant event frequency. • Increased intracellular $[Ca^{2+}]$ leads to calcineurin-NFAT signalling, implicated in mechanism of hypertrophy. • Myofilament "Ca^{2+}-trapping" hypothesis proposed.
(**Han et al., 2014**) One patient with heterozygous *MYH7* Arg442Gly mutation and two healthy control hiPSC lines from unrelated donors.	Chemical calcium indicator: Rhod-2 AM (ratiometric)	• Aberrant calcium transient events. • Increased intracellular $[Ca^{2+}]$. • Smaller SR Ca^{2+} release upon caffeine addition. • Delayed Ca^{2+} transient decay time.	• Isoprenaline increases aberrant event frequency, this is rescued with isoprenaline + 10 μM metoprolol. • 4 day treatment with 100 nM verapamil reduces aberrant event frequency. • 3 day treatment with 10 nM trichostatin A reduces cell size, prevents NFAT translocation and reduces aberrant event frequency.
(**Ojala et al., 2016**)	Chemical calcium indicator:	• Aberrant waveforms including frequent EADs and DADs.	Differences between mutations:

Two patients with heterozygous *MYBPC3* Gln1061X, two patients with heterozygous *TPM1* Asp175Asn, two healthy control hiPSC lines from unrelated donors.	Fura-2 AM (ratiometric)		• Ca^{2+} handling abnormalities significantly higher in *TPM1* Asp175Asn mutation compared to *MYBPC3* Gln1061X. • Prolonged APD in *TPM1* Asp175Asn mutation.
This thesis Seven lines: One patient with heterozygous *ACTC1* Glu99Lys mutation and CRISPR Cas9 corrected isogenic control. One healthy patient-related donor and CRISPR Cas9 mutated heterozygous *ACTC1* Glu99Lys isogenic mutant. One healthy hiPSC line CRISPR Cas9 mutated to produce heterozygous and homozygous *MYH7* Arg453Cys isogenic mutants.	Genetically encoded calcium indicators: R-GECO1.0 (intensiometric) GEM-GECO (ratiometric)	• Aberrant Ca^{2+} transient events in MYH7 mutants, and one *ACTC1* mutant line • T_{peak} increases in *MYH7* mutants, decreases in *ACTC1* mutants • Systolic Ca^{2+} peak amplitude increases in *MYH7* mutants • Increased spontaneous beat rate in *MYH7* mutants • Higher resistance to nifedipine in *MYH7* mutants • Aberrant events in *MYH7* mutants reduced in low extracellular [Ca^{2+}] conditions	Differences between mutations: • Aberrant events seen in diseased patient-derived *ACTC1*$^{WT/MUT}$ hiPSC-CMs not seen in gene edited healthy patient-derived *ACTC1*$^{WT/MUT}$ hiPSC-CMs. Severity of phenotype influenced by genetic background not just *ACTC1* mutation. • Aberrant calcium transient events in *MYH7* mutants reduced with 24 hour treatment with 10 μM ranolazine or 24 hour co-treatment with 10 μM ranolazine and 10 μM dantrolene. • Phenotypic rescue of *MYH7* mutants not replicated in *ACTC1* mutants. • *MYH7* mutants hypocontractile, *ACTC1* mutants hypercontractile (data not shown).

Table 6.1. Studies where hiPSC-CMs have been used to investigate HCM and changes to calcium handling properties.

6.2.2 Hypertrophic pathway and potential drug targets

The phenotyping experiments performed within this thesis, particularly those focused on *MYH7* mutant hiPSC-CMs, gave clues as to the mechanisms behind HCM. High systolic calcium, frequent occurrence of aberrant events, resistance to the Ca^{2+} blocker nifedipine and the abolition of these aberrant events in low extracellular calcium suggested that high intracellular Ca^{2+} played a central role in HCM.

This was supplemented with the finding that the late sodium current inhibitor ranolazine, and the ryanodine receptor antagonist dantrolene, were capable of reducing abnormal calcium transients in *MYH7* mutants.

Data generated within this group has shown increased ATP generation in *MYH7* mutants without increased mitochondrial content, and this suggests an "energy-depletion" model of HCM (Mosqueira et al., 2018). In this model, mutant sarcomeric proteins lead to inefficient ATP usage during contraction, and an energetic deficit (**Figure 6.1**). This impedes the ability of the SERCA pump to re-sequester Ca^{2+} during diastole, as this requires ATP (Ashrafian et al., 2003, Lipskaia et al., 2010). This contributes to intracellular Ca^{2+} overload.

High intracellular Ca^{2+} can activate Ca^{2+}/CaM which in turn activates $CaMKII_{\delta c}$ (**Figure 6.1**). $CaMKII_{\delta c}$ has a number of potential targets including: phosphorylation of ryanodine receptors, causing Ca^{2+} release from the SR (Fischer et al., 2013); phosphorylation of L-type Ca^{2+} channels, causing Ca^{2+} influx (Koval et al., 2010); and phosphorylation of I_{NaL}, causing Na^{+} influx (Ashpole et al., 2012) (**Figure 6.1**).

Together, this exacerbates Ca^{2+} overload and also leads to Na^{+} overload. Na^{+} overload can in turn reverse the electrogenic Na^{+}/Ca^{2+} exchanger, leading to further Ca^{2+} influx (**Figure 6.1**).

In this study, it is thought that ranolazine blocks the I_{NaL} current, facilitating NCX extrusion of Ca^{2+} (**Figure 6.1**). This is an agreement with two other *in vitro* models of HCM which have used ranolazine successfully the rescue the HCM phenotype (Lan et al., 2013, Coppini et al., 2013). In combination, it is proposed that dantrolene blocks the ryanodine receptors, stemming excessive Ca^{2+} release from the SR (**Figure 6.1**). This drug has been exploited to rescue the CPVT phenotype in hiPSC-CMs (Jung et al., 2012), as well as in a mouse model of HCM (Okuda et al., 2018).

However, there was a limited effect on *ACTC1* mutants using the ranolazine and dantrolene combination. As well as highlighting the inherent variability between HCM-causing mutations, this shows a need to understand the hypertrophic pathway in more detail.

In vitro focused drug screens such as the one presented in this thesis have started to unravel the complex pathways involved in HCM progression. It has been suggested that in pathological HCM, elevated Ca^{2+} leads to calcineurin-dependent hypertrophy (Molkentin, 2004). In this pathway, calcineurin dephosphorylates NFAT and facilitates NFAT translocation to the nucleus (**Figure 6.1**). Here, the formation of a MEF2/NFATc2 transcriptional complex can initiate hypertrophic gene expression (Dewenter et al., 2017) (**Figure 6.1**).

This pathway has been successfully interrupted with three day treatment of trichostatin A to prevent NFAT translocation, reducing arrhythmias and CM size (Han et al., 2014) (**Figure 6.1**). In addition cyclosporine A and FK506 have been shown to inhibit calcineurin, reducing hypertrophy in hiPSC-CM models of HCM (**Figure 6.1**). However, these drugs are highly cardiotoxic due to the central role calcineurin plays within cardiomyocytes (Rao et al., 1997). Therefore work must continue to elucidate pathways involved in HCM progression, and to find more specific signalling pathway targets.

A potential drug target may be TAK1 which has been shown to be an upstream regulator of the calcineurin-NFAT pathway (Liu et al., 2009a, Dewenter et al., 2017). Alternatively, the metabolic modulator perhexiline may be able to correct the energy deficit caused by sarcomeric mutations, halting the hypertrophic signalling pathway at source (Abozguia et al., 2010). By interrogating the complex signalling pathways that lead to hypertrophy, a universal drug target may be found such that *MYH7* and *ACTC1* mutants, together with countless other HCM-causing mutations can be treated.

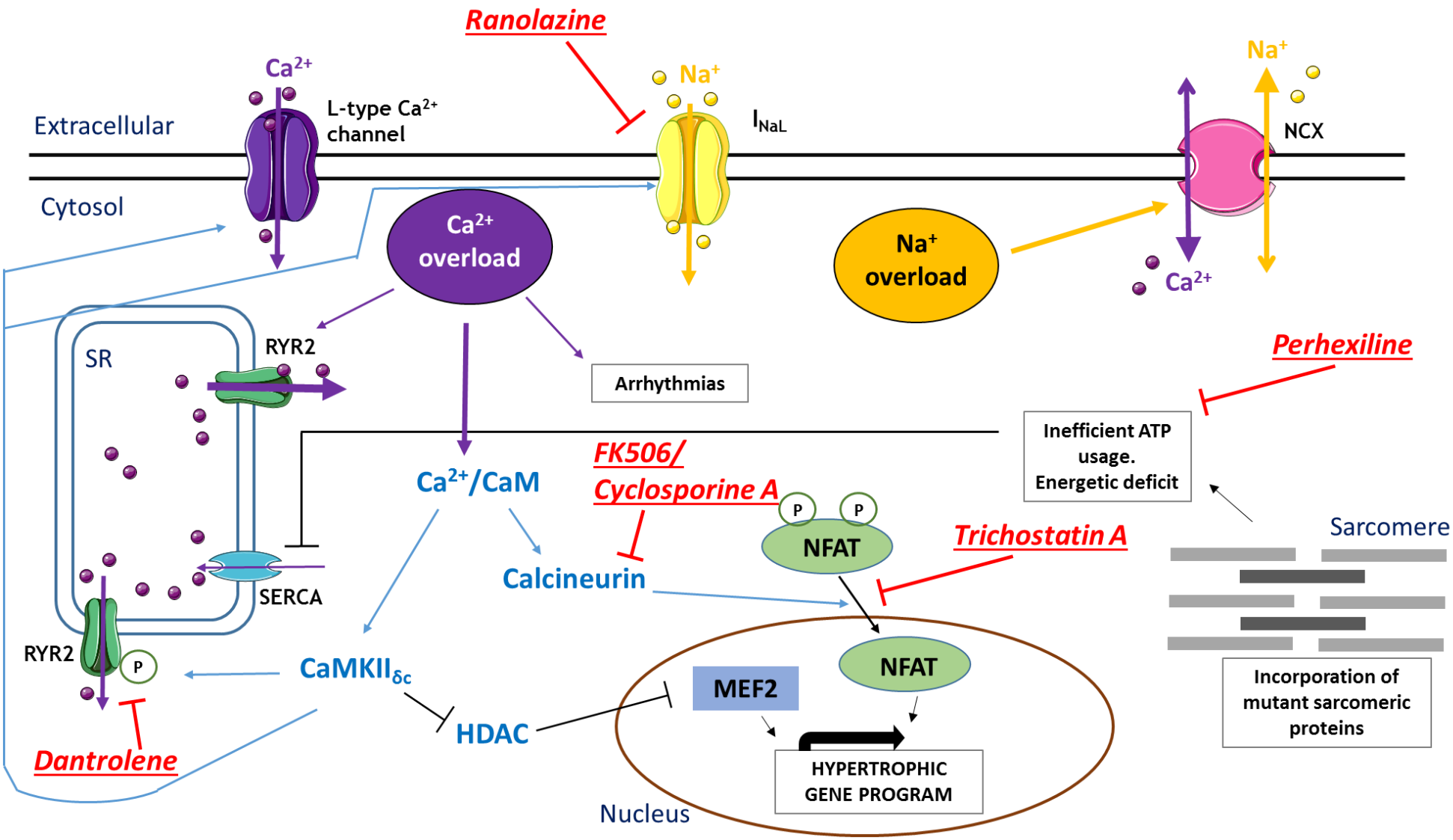

Ranolazine
Ca2+
L-type Ca2+ channel
Na+
INaL
Na+
NCX
Extracellular
Cytosol
Ca2+ overload
Na+ overload
Ca2+
SR
RYR2
Arrhythmias
Perhexiline
Inefficient ATP usage. Energetic deficit
Ca2+/CaM
FK506/ Cyclosporine A
P
P
NFAT
Trichostatin A
Sarcomere
SERCA
Calcineurin
RYR2
P
CaMKIIδc
NFAT
MEF2
HDAC
HYPERTROPHIC GENE PROGRAM
Incorporation of mutant sarcomeric proteins
Dantrolene
Nucleus

Figure 6.1. Ca^{2+} related signalling pathways associated with HCM progression and potential pharmacological interventions.

Schematic outlining the basic mechanism of HCM, signalling pathways involved and drugs which have been shown to successfully alleviate phenotypes. Sarcomeric mutations cause inefficient energy usage, which negatively impacts the ability of the CM to sequester Ca^{2+} via SERCA. This contributes to Ca^{2+} overload, which can result in arrhythmias. This leads to CaMKII-mediated exacerbation of Ca^{2+} overload through activation of ryanodine receptors, L-type Ca^{2+} channels and INaL. This also leads to Na^{+} overload, resulting in reversal of NCX. The hypertrophic gene program can be initiated through a calcineurin-NFAT pathway. Ranolazine acts to counteract increased Na^{+} influx through INaL, thus enabling Ca^{2+} efflux through NCX. Dantrolene acts to counteract excessive Ca^{2+} release from ryanodine receptors. Cyclosporine A and Trichostatin A all interfere with the calcineurin-NFAT pathway. I_{NaL} – late sodium current; NCX – Na^{+}/Ca^{2+} exchanger; RYR2 – ryanodine receptor; SERCA – sarcoplasmic reticulum Ca^{2+}-ATPase; Ca^{2+}/CaM – calmodulin; $CaMKII_{\delta c}$ – Ca^{2+}/calmodulin-dependent protein kinase II delta-C isoform; HDAC – histone deacetylases; NFAT – nuclear factor of activated T-cells family of transcription factors; MEF2 - myocyte enhancer factor-2 transcription factor; P - phosphorylation.

6.3 Limitations and Improvements

6.3.1 *ACTC1* mutant phenotype

A key finding was that the *ACTC1* G301A phenotype was not as obvious as the *MYH7* C9123T phenotype. However, more biological replicates of confocal line scans are required for both P1 and P2 *ACTC1* mutant isogenic pairs, to reinforce the data presented. In addition, some of the functional characterisation that was performed in the *MYH7* isogenic trio, such as nifedipine treatment and changes to extracellular Ca^{2+} concentration, should also be applied to the *ACTC1* isogenic pairs. In this way, a more extensive comparison may be made between *MYH7* C9123T and *ACTC1* G301A.

The lack of a homozygote *ACTC1* G301A mutant also limited the ability to observe phenotypic patterns. Although both *MYH7* and *ACTC1* homozygous mutants are rare, likely due to embryonic or early-onset lethality (Marsiglia and Pereira, 2014), this study showcases their potential for mechanistic insights in vitro. The absence of any biallelic targeting events when generating the *ACTC1* mutants may have been due to the distance between the PAM site and the mutation in the footprint-free *ACTC1* targeting strategy. There was a distance of approximately 300 nucleotides between the PAM site and the mutation in this strategy, compared to just 17 nucleotides in the plasmid-based *MYH7* targeting strategy (Kondrashov et al., 2018). These factors will be considered for future targeting experiments, especially if biallelic targeting is a necessity.

6.3.2 Genetically encoded calcium indicators

The field of genetically encoded calcium indicators moves at a rapid pace, and since embarking on this project, several improved variants have been developed which outperform R-GECO1.0 and GEM-GECO. For example, the recently engineered K-GECO1, which exhibits higher sensitivity, faster kinetics and over 2-fold more brightness than R-GECO1.0 (Shen et al., 2018). Similarly, there are now more advanced variants of G-GECO1.0, such as FGCaMP which is excitation-ratiometric and exhibits 7-fold higher brightness as well as 1.3-fold faster calcium ion dissociation kinetics (Barykina et al., 2017).

A green emission GECI, such as FGCaMP or even G-GECO would be ideal for use on the CellOPTIQ™ system, which is capable of exciting fluorophores at a wavelength of 380 nm and detecting emission at 500 nm. Unfortunately, the CellOPTIQ™ platform is not currently set up to excite fluorophores in the 560 nm range required for red GECIs.

Data presented within this thesis has shown that GECI hiPSC-CMs can be used over long periods of time, without loss of fluorescence. This unique property could have been exploited more by performing repeated measurements of the same hiPSC-CMs at different time points. This would have enhanced the drug screening data presented. However, the low throughput method of confocal line scan microscopy, coupled with its location in a non-sterile area, precluded repeated measurements.

6.3.3 Drug screening improvements

The drug screening experiments presented could have been improved in a number of ways. Primarily, more replicates should be performed to further enhance statistical power. However, this was challenging when using a low throughput confocal line scan method. As such, higher throughput, multiwell plate format assays should be explored, such as the CellOPTIQ™. Higher throughput assays would also enable the testing of drugs at multiple concentrations. No significant phenotypic rescue was observed with valsartan treatment at 1 μM, but higher concentrations may elicit a response.

Finally, the ability to pace hiPSC-CMs would be ideal in order to maintain consistency between hiPSC-CMs and have greater confidence in drug effects.

6.4 Future perspectives

P2 *ACTC1*$^{WT/MUT}$ hiPSC-CMs had a less apparent abnormality in calcium transient shape than both P1 *ACTC1*$^{WT/MUT}$ hiPSC-CMs and *MYH7* mutants. As such, the P2 *ACTC1* mutant may be a useful model of asymptomatic patients. Indeed, it has been reported that disease onset in some HCM patients can take as long as 50 years to emerge (Michels et al., 2017). Endothelin-1 has been implicated in HCM progression (Tanaka et al., 2014), and the endothelin-1 pathway is also thought to become more active with age (Stauffer et al., 2008). This may provide a route to inducing a more severe phenotype in P2 *ACTC1* mutants *in vitro*, so that further drug screens can continue.

Although a therapeutic benefit was seen with ranolazine and dantrolene treatment, future drug screens can build on the knowledge gained. Upstream regulators of the calcineurin-NFAT pathway of hypertrophy such as TAK1 may be potential therapeutic targets (Liu et al., 2009a).

However, the drug screening method and phenotypic readout could be vastly improved. Optical pacing and contractility analysis of these isogenic sets of hiPSC-CMs is a near-term goal. The data presented in **Figure 5.15** provides a preview as to what can be achieved using optogenetics on the CellOPTIQ™ platform.

The ultimate goal would be to combine GECIs, GEVIs and optogenetics in isogenic hiPSC lines of health and disease so that high-throughput drug screens could be performed in a multiwell plate format. This would provide the ability to study large numbers of drugs, at various concentrations, with simultaneous non-invasive pacing and accurate measurements of calcium transient and action potential parameters.

6.5 Final remarks

HCM is a devastating cardiac disease that is a major cause of sudden cardiac death in young adults and seemingly fit athletes (Maron and Maron, 2013). Causative mutations, disease progression and severity are all highly variable in HCM.

As a result, it is important that clinical management of HCM moves towards being tailored to the individual and their genetics. In this study the commonly used ß-blocker propranolol was unable to alleviate abnormal activity in *MYH7* mutants, despite being used clinically (Östman-Smith, 2014, Gregor and Čurila, 2015), and showing some benefit in other *in vitro* models of HCM (Lan et al., 2013). Furthermore, the *ACTC1* mutants were not responsive to ranolazine, whilst *MYH7* mutants were.

Phenotypic variability was also observed between P1 and P2 *ACTC1*$^{WT/MUT}$ lines, suggesting that the *ACTC1* G301A mutation may be necessary yet not sufficient to cause a severe phenotype. Genetic or epigenetic modifiers are presumably responsible for this variability, and this highlights the utility of using isogenic lines to study complex cardiomyopathies. Indeed, isogenic hiPSC-CMs have previously only been used to study dilated cardiomyopathy *in vitro* (Stillitano et al., 2016). The recent emergence of CRISPR Cas9 as an accessible genome engineering tool has made this possible.

Although readily accessible, the use of CRISPR Cas9 involves many considerations including; target locus, guide RNA design, choice of nuclease and targeting vector design. Within this thesis, a P2A peptide cleavage sequence was employed in the original targeting vectors for bicistronic transgene expression. This failed, contrary to reports of P2A being the most efficient of the "2A" peptide cleavage sequences in HeLa cells (Kim et al., 2011). In addition, potential *AAVS1* transgene silencing may have occurred in some clones, as reported elsewhere in the literature (Ordovas et al., 2015), despite *AAVS1* being a 'safe harbour' locus (Oceguera-Yanez et al., 2016). Setbacks such as these, and the time taken to generate, screen and expand successfully targeted clones are important factors to consider when genome engineering hiPSC lines.

Nevertheless, having generated a palette of genetically encoded calcium indicator reporter hiPSC lines, a valuable, self-renewing supply of hiPSC-CMs for studying calcium handling over long periods now exists.

Crucially, these reporter hiPSC-CMs were able to recapitulate the abnormal calcium transient phenotype of HCM *in vitro*. Mutant hiPSC-CMs exhibited calcium transient

and drug responses potentially indicating a high intracellular calcium state. Using this information, ranolazine and dantrolene were successfully applied to alleviate the abnormal calcium transient phenotype in *MYH7* mutants. This has provided insights into disease mechanisms and pathways, and intracellular hypertrophy pathways can now be explored as further potential drug targets.

Overall, the work described herein demonstrates the utility of patient-derived hiPSCs as a self-renewing resource of hiPSC-CMs which can be used to model diseases *in vitro* and observe clinically relevant phenotypes. Combining this with the genome engineering power of CRISPR Cas9 allows the generation of isogenic sets of hiPSCs for in-depth analysis of SNPs, their resulting phenotypes and the role of genetic background. CRISPR Cas9 also enables the generation of calcium reporter lines for non-invasive study of calcium transients in hiPSC-CMs, removing the requirement for toxic, leaky calcium dyes. Finally, phenotypic readouts can inform candidate drug selection for *in vitro* screens and reveal potentially therapeutic compounds.

References

ABI-GERGES, N., POINTON, A., OLDMAN, K. L., BROWN, M. R., PILLING, M. A., SEFTON, C. E., GARSIDE, H. & POLLARD, C. E. 2017. Assessment of extracellular field potential and Ca(2+) transient signals for early QT/pro-arrhythmia detection using human induced pluripotent stem cell-derived cardiomyocytes. *J Pharmacol Toxicol Methods,* 83**,** 1-15.

ABOZGUIA, K., ELLIOTT, P., MCKENNA, W., PHAN, T. T., NALLUR-SHIVU, G., AHMED, I., MAHER, A. R., KAUR, K., TAYLOR, J., HENNING, A., ASHRAFIAN, H., WATKINS, H. & FRENNEAUX, M. 2010. Metabolic modulator perhexiline corrects energy deficiency and improves exercise capacity in symptomatic hypertrophic cardiomyopathy. *Circulation,* 122**,** 1562-9.

ACKERMAN, M. J., VANDRIEST, S. L., OMMEN, S. R., WILL, M. L., NISHIMURA, R. A., TAJIK, A. J. & GERSH, B. J. 2002. Prevalence and age-dependence of malignant mutations in the beta-myosin heavy chain and troponin T genes in hypertrophic cardiomyopathy: a comprehensive outpatient perspective. *J Am Coll Cardiol,* 39**,** 2042-8.

AHRENS-NICKLAS, R. C. & CHRISTINI, D. J. 2009. Anthropomorphizing the mouse cardiac action potential via a novel dynamic clamp method. *Biophys J,* 97**,** 2684-92.

ANDERSON, D., SELF, T., MELLOR, I. R., GOH, G., HILL, S. J. & DENNING, C. 2007. Transgenic enrichment of cardiomyocytes from human embryonic stem cells. *Mol Ther,* 15**,** 2027-36.

ARAD, M., PENAS-LADO, M., MONSERRAT, L., MARON, B. J., SHERRID, M., HO, C. Y., BARR, S., KARIM, A., OLSON, T. M., KAMISAGO, M., SEIDMAN, J. G. & SEIDMAN, C. E. 2005. Gene mutations in apical hypertrophic cardiomyopathy. *Circulation,* 112**,** 2805-11.

ASHPOLE, N. M., HERREN, A. W., GINSBURG, K. S., BROGAN, J. D., JOHNSON, D. E., CUMMINS, T. R., BERS, D. M. & HUDMON, A. 2012. Ca2+/calmodulin-dependent protein kinase II (CaMKII) regulates cardiac sodium channel NaV1.5 gating by multiple phosphorylation sites. *J Biol Chem,* 287**,** 19856-69.

ASHRAFIAN, H., REDWOOD, C., BLAIR, E. & WATKINS, H. 2003. Hypertrophic cardiomyopathy:a paradigm for myocardial energy depletion. *Trends Genet,* 19**,** 263-8.

AUGIERE, C., MEGY, S., EL MALTI, R., BOLAND, A., EL ZEIN, L., VERRIER, B., MEGARBANE, A., DELEUZE, J. F. & BOUVAGNET, P. 2015. A Novel Alpha Cardiac Actin (ACTC1) Mutation Mapping to a Domain in Close Contact with Myosin Heavy Chain Leads to a Variety of Congenital Heart Defects, Arrhythmia and Possibly Midline Defects. *PLoS One,* 10**,** e0127903.

AXELSSON, A., IVERSEN, K., VEJLSTRUP, N., HO, C. Y., HAVNDRUP, O., KOFOED, K. F., NORSK, J., JENSEN, M. & BUNDGAARD, H. 2016. Functional effects of losartan in hypertrophic cardiomyopathy-a randomised clinical trial. *Heart,* 102**,** 285-91.

BAE, K. H., KWON, Y. D., SHIN, H. C., HWANG, M. S., RYU, E. H., PARK, K. S., YANG, H. Y., LEE, D. K., LEE, Y., PARK, J., KWON, H. S., KIM, H. W., YEH, B. I., LEE, H. W., SOHN, S. H., YOON, J., SEOL, W. & KIM, J. S. 2003. Human zinc fingers as building blocks in the construction of artificial transcription factors. *Nat Biotechnol,* 21**,** 275-80.

BAI, F., CASTER, H. M., DAWSON, J. F. & KAWAI, M. 2015. The immediate effect of HCM causing actin mutants E99K and A230V on actin-Tm-myosin interaction in thin-filament reconstituted myocardium. *J Mol Cell Cardiol,* 79**,** 123-32.

BAIG, S. M., KOSCHAK, A., LIEB, A., GEBHART, M., DAFINGER, C., NURNBERG, G., ALI, A., AHMAD, I., SINNEGGER-BRAUNS, M. J., BRANDT, N., ENGEL, J., MANGONI, M. E., FAROOQ, M., KHAN, H. U., NURNBERG, P., STRIESSNIG, J. & BOLZ, H. J. 2011. Loss of Ca(v)1.3 (CACNA1D) function in a human channelopathy with bradycardia and congenital deafness. *Nat Neurosci,* 14**,** 77-84.

BARMAN, P. P., CHENG, H., HANCOX, J. C. & JAMES, A. F. 2013. Nickel inhibits ß-1 adrenoceptor mediated activation of cardiac CFTR chloride channels. *Biochem Biophys Res Commun,* 432**,** 46-51.

BARYKINA, N. V., SUBACH, O. M., PIATKEVICH, K. D., JUNG, E. E., MALYSHEV, A. Y., SMIRNOV, I. V., BOGORODSKIY, A. O., BORSHCHEVSKIY, V. I., VARIZHUK, A. M., POZMOGOVA, G. E., BOYDEN, E. S., ANOKHIN, K. V., ENIKOLOPOV, G. N. & SUBACH, F. V. 2017. Green fluorescent genetically encoded calcium indicator based on calmodulin/M13-peptide from fungi. *PLoS One,* 12**,** e0183757.

BERS, D. M. 2002. Cardiac excitation-contraction coupling. *Nature,* 415**,** 198-205.

BEUMER, K., BHATTACHARYYA, G., BIBIKOVA, M., TRAUTMAN, J. K. & CARROLL, D. 2006. Efficient gene targeting in Drosophila with zinc-finger nucleases. *Genetics,* 172**,** 2391-2403.

BHAYA, D., DAVISON, M. & BARRANGOU, R. 2011. CRISPR-Cas systems in bacteria and archaea: versatile small RNAs for adaptive defense and regulation. *Annu Rev Genet,* 45**,** 273-97.

BIRKET, M. J., RIBEIRO, M. C., KOSMIDIS, G., WARD, D., LEITOGUINHO, A. R., VAN DE POL, V., DAMBROT, C., DEVALLA, H. D., DAVIS, R. P., MASTROBERARDINO, P. G., ATSMA, D. E., PASSIER, R. & MUMMERY, C. L. 2015a. Contractile Defect Caused by Mutation in MYBPC3 Revealed under Conditions Optimized for Human PSC-Cardiomyocyte Function. *Cell Rep,* 13**,** 733-745.

BIRKET, M. J., RIBEIRO, M. C., VERKERK, A. O., WARD, D., LEITOGUINHO, A. R., DEN HARTOGH, S. C., ORLOVA, V. V., DEVALLA, H. D., SCHWACH, V., BELLIN, M., PASSIER, R. & MUMMERY, C. L. 2015b. Expansion and patterning of cardiovascular progenitors derived from human pluripotent stem cells. *Nat Biotechnol,* 33**,** 970-9.

BOCH, J., SCHOLZE, H., SCHORNACK, S., LANDGRAF, A., HAHN, S., KAY, S., LAHAYE, T., NICKSTADT, A. & BONAS, U. 2009. Breaking the code of DNA binding specificity of TAL-type III effectors. *Science,* 326**,** 1509-12.

BOYDEN, E. S., ZHANG, F., BAMBERG, E., NAGEL, G. & DEISSEROTH, K. 2005. Millisecond-timescale, genetically targeted optical control of neural activity. *Nat Neurosci,* 8**,** 1263-8.

BRECKWOLDT, K., LETUFFE-BRENIERE, D., MANNHARDT, I., SCHULZE, T., ULMER, B., WERNER, T., BENZIN, A., KLAMPE, B., REINSCH, M. C., LAUFER, S., SHIBAMIYA, A., PRONDZYNSKI, M., MEARINI, G., SCHADE, D., FUCHS, S., NEUBER, C., KRAMER, E., SALEEM, U., SCHULZE, M. L., RODRIGUEZ, M. L., ESCHENHAGEN, T. & HANSEN, A. 2017. Differentiation of cardiomyocytes and generation of human engineered heart tissue. *Nat Protoc,* 12**,** 1177-1197.

BRISTOW, M. R., GINSBURG, R., UMANS, V., FOWLER, M., MINOBE, W., RASMUSSEN, R., ZERA, P., MENLOVE, R., SHAH, P., JAMIESON, S. & ET AL. 1986. Beta 1- and beta 2-adrenergic-receptor subpopulations in nonfailing and failing human ventricular myocardium: coupling of both receptor subtypes to muscle

contraction and selective beta 1-receptor down-regulation in heart failure. *Circ Res,* 59, 297-309.

BUCK, E., ZIMANYI, I., ABRAMSON, J. J. & PESSAH, I. N. 1992. Ryanodine stabilizes multiple conformational states of the skeletal muscle calcium release channel. *J Biol Chem,* 267, 23560-7.

BURRIDGE, P. W., KELLER, G., GOLD, J. D. & WU, J. C. 2012. Production of de novo cardiomyocytes: human pluripotent stem cell differentiation and direct reprogramming. *Cell Stem Cell,* 10, 16-28.

BURRIDGE, P. W., MATSA, E., SHUKLA, P., LIN, Z. C., CHURKO, J. M., EBERT, A. D., LAN, F., DIECKE, S., HUBER, B., MORDWINKIN, N. M., PLEWS, J. R., ABILEZ, O. J., CUI, B., GOLD, J. D. & WU, J. C. 2014. Chemically defined generation of human cardiomyocytes. *Nat Methods,* 11, 855-60.

BUTLER, L., CROS, C., OLDMAN, K. L., HARMER, A. R., POINTON, A., POLLARD, C. E. & ABI-GERGES, N. 2015. Enhanced characterization of contractility in cardiomyocytes during early drug safety assessment. *Toxicol Sci,* 145, 396-406.

BYRNE, S. M. & CHURCH, G. M. 2015. Crispr-mediated Gene Targeting of Human Induced Pluripotent Stem Cells. *Curr Protoc Stem Cell Biol,* 35, 5a.8.1-22.

CAHILL, T. J., ASHRAFIAN, H. & WATKINS, H. 2013. Genetic cardiomyopathies causing heart failure. *Circ Res,* 113, 660-75.

CARVAJAL-VERGARA, X., SEVILLA, A., D'SOUZA, S. L., ANG, Y.-S., SCHANIEL, C., LEE, D.-F., YANG, L., KAPLAN, A. D., ADLER, E. D. & ROZOV, R. 2010. Patient-specific induced pluripotent stem-cell-derived models of LEOPARD syndrome. *Nature,* 465, 808.

CELIZ, A. D., SMITH, J. G., PATEL, A. K., HOOK, A. L., RAJAMOHAN, D., GEORGE, V. T., FLATT, L., PATEL, M. J., EPA, V. C., SINGH, T., LANGER, R., ANDERSON, D. G., ALLEN, N. D., HAY, D. C., WINKLER, D. A., BARRETT, D. A., DAVIES, M. C., YOUNG, L. E., DENNING, C. & ALEXANDER, M. R. 2015. Discovery of a Novel Polymer for Human Pluripotent Stem Cell Expansion and Multilineage Differentiation. *Adv Mater,* 27, 4006-12.

CERBINI, T., FUNAHASHI, R., LUO, Y., LIU, C., PARK, K., RAO, M., MALIK, N. & ZOU, J. 2015. Transcription activator-like effector nuclease (TALEN)-mediated CLYBL targeting enables enhanced transgene expression and one-step generation of dual reporter human induced pluripotent stem cell (iPSC) and neural stem cell (NSC) lines. *PLoS One,* 10, e0116032.

CERIGNOLI, F., CHARLOT, D., WHITTAKER, R., INGERMANSON, R., GEHALOT, P., SAVCHENKO, A., GALLACHER, D. J., TOWART, R., PRICE, J. H., MCDONOUGH, P. M. & MERCOLA, M. 2012. High throughput measurement of Ca(2)(+) dynamics for drug risk assessment in human stem cell-derived cardiomyocytes by kinetic image cytometry. *J Pharmacol Toxicol Methods,* 66, 246-56.

CHANG, Y. F., BROYLES, C. N., BROOK, F. A., DAVIES, M. J., TURTLE, C. W., NAGAI, T. & DANIELS, M. J. 2017. Non-invasive phenotyping and drug testing in single cardiomyocytes or beta-cells by calcium imaging and optogenetics. *PLoS One,* 12, e0174181.

CHEN, C. M., KROHN, J., BHATTACHARYA, S. & DAVIES, B. 2011a. A comparison of exogenous promoter activity at the ROSA26 locus using a PhiiC31 integrase mediated cassette exchange approach in mouse ES cells. *PLoS One,* 6, e23376.

CHEN, F., PRUETT-MILLER, S. M., HUANG, Y., GJOKA, M., DUDA, K., TAUNTON, J., COLLINGWOOD, T. N., FRODIN, M. & DAVIS, G. D. 2011b. High-frequency genome editing using ssDNA oligonucleotides with zinc-finger nucleases. *Nat Methods,* 8, 753-5.

CHEN, G., GULBRANSON, D. R., HOU, Z., BOLIN, J. M., RUOTTI, V., PROBASCO, M. D., SMUGA-OTTO, K., HOWDEN, S. E., DIOL, N. R., PROPSON, N. E., WAGNER, R., LEE, G. O., ANTOSIEWICZ-BOURGET, J., TENG, J. M. & THOMSON, J. A. 2011c. Chemically defined conditions for human iPSC derivation and culture. *Nat Methods,* 8**,** 424-9.

CHEN, T.-W., WARDILL, T. J., SUN, Y., PULVER, S. R., RENNINGER, S. L., BAOHAN, A., SCHREITER, E. R., KERR, R. A., ORGER, M. B., JAYARAMAN, V., LOOGER, L. L., SVOBODA, K. & KIM, D. S. 2013. Ultra-sensitive fluorescent proteins for imaging neuronal activity. *Nature,* 499**,** 295-300.

CHEN, W., WANG, R., CHEN, B., ZHONG, X., KONG, H., BAI, Y., ZHOU, Q., XIE, C., ZHANG, J., GUO, A., TIAN, X., JONES, P. P., O'MARA, M. L., LIU, Y., MI, T., ZHANG, L., BOLSTAD, J., SEMENIUK, L., CHENG, H., ZHANG, J., CHEN, J., TIELEMAN, D. P., GILLIS, A. M., DUFF, H. J., FILL, M., SONG, L. S. & CHEN, S. R. 2014. The ryanodine receptor store-sensing gate controls Ca2+ waves and Ca2+-triggered arrhythmias. *Nat Med,* 20**,** 184-92.

CHO, S. W., KIM, S., KIM, J. M. & KIM, J. S. 2013. Targeted genome engineering in human cells with the Cas9 RNA-guided endonuclease. *Nat Biotechnol,* 31**,** 230-2.

CHRISTIAANS, I., BIRNIE, E., BONSEL, G. J., MANNENS, M. M., MICHELS, M., MAJOOR-KRAKAUER, D., DOOIJES, D., VAN TINTELEN, J. P., VAN DEN BERG, M. P., VOLDERS, P. G., ARENS, Y. H., VAN DEN WIJNGAARD, A., ATSMA, D. E., HELDERMAN-VAN DEN ENDEN, A. T., HOUWELING, A. C., DE BOER, K., VAN DER SMAGT, J. J., HAUER, R. N., MARCELIS, C. L., TIMMERMANS, J., VAN LANGEN, I. M. & WILDE, A. A. 2011. Manifest disease, risk factors for sudden cardiac death, and cardiac events in a large nationwide cohort of predictively tested hypertrophic cardiomyopathy mutation carriers: determining the best cardiological screening strategy. *Eur Heart J,* 32**,** 1161-70.

CHU, V. T., WEBER, T., WEFERS, B., WURST, W., SANDER, S., RAJEWSKY, K. & KUHN, R. 2015. Increasing the efficiency of homology-directed repair for CRISPR-Cas9-induced precise gene editing in mammalian cells. *Nat Biotechnol,* 33**,** 543-8.

CLAY, S. A., DOMEIER, T. L., HANFT, L. M., MCDONALD, K. S. & KRENZ, M. 2015. Elevated Ca2+ transients and increased myofibrillar power generation cause cardiac hypercontractility in a model of Noonan syndrome with multiple lentigines. *Am J Physiol Heart Circ Physiol,* 308**,** H1086-95.

COLATSKY, T., FERMINI, B., GINTANT, G., PIERSON, J. B., SAGER, P., SEKINO, Y., STRAUSS, D. G. & STOCKBRIDGE, N. 2016. The Comprehensive in Vitro Proarrhythmia Assay (CiPA) initiative — Update on progress. *Journal of Pharmacological and Toxicological Methods,* 81**,** 15-20.

COLEGRAVE, M. & PECKHAM, M. 2014. Structural implications of beta-cardiac myosin heavy chain mutations in human disease. *Anat Rec (Hoboken),* 297**,** 1670-80.

CONG, L., RAN, F. A., COX, D., LIN, S., BARRETTO, R., HABIB, N., HSU, P. D., WU, X., JIANG, W., MARRAFFINI, L. A. & ZHANG, F. 2013. Multiplex genome engineering using CRISPR/Cas systems. *Science,* 339**,** 819-23.

COPPINI, R., FERRANTINI, C., YAO, L., FAN, P., DEL LUNGO, M., STILLITANO, F., SARTIANI, L., TOSI, B., SUFFREDINI, S., TESI, C., YACOUB, M., OLIVOTTO, I., BELARDINELLI, L., POGGESI, C., CERBAI, E. & MUGELLI, A. 2013. Late sodium current inhibition reverses electromechanical dysfunction in human hypertrophic cardiomyopathy. *Circulation,* 127**,** 575-84.

CORNU, T. I. & CATHOMEN, T. 2010. Quantification of zinc finger nuclease-associated toxicity. *Methods Mol Biol,* 649**,** 237-45.

CRUMB, W. J., VICENTE, J., JOHANNESEN, L. & STRAUSS, D. G. 2016. An evaluation of 30 clinical drugs against the comprehensive in vitro proarrhythmia assay (CiPA) proposed ion channel panel. *Journal of Pharmacological and Toxicological Methods,* 81, 251-262.

DAVIES, R., GRAHAM, J. & CANEPARI, M. 2013. Light sources and cameras for standard in vitro membrane potential and high-speed ion imaging. *J Microsc,* 251, 5-13.

DEDERER, H.-G. 2006. Regulation of Human Embryonic Stem Cell Research in Germany. *Journal of International Biotechnology Law*.

DEISSEROTH, K., FENG, G., MAJEWSKA, A. K., MIESENBOCK, G., TING, A. & SCHNITZER, M. J. 2006. Next-generation optical technologies for illuminating genetically targeted brain circuits. *J Neurosci,* 26, 10380-6.

DEMPSEY, G. T., CHAUDHARY, K. W., ATWATER, N., NGUYEN, C., BROWN, B. S., MCNEISH, J. D., COHEN, A. E. & KRALJ, J. M. 2016. Cardiotoxicity screening with simultaneous optogenetic pacing, voltage imaging and calcium imaging. *J Pharmacol Toxicol Methods,* 81, 240-50.

DENNING, C., BORGDORFF, V., CRUTCHLEY, J., FIRTH, K. S., GEORGE, V., KALRA, S., KONDRASHOV, A., HOANG, M. D., MOSQUEIRA, D., PATEL, A., PRODANOV, L., RAJAMOHAN, D., SKARNES, W. C., SMITH, J. G. & YOUNG, L. E. 2016. Cardiomyocytes from human pluripotent stem cells: From laboratory curiosity to industrial biomedical platform. *Biochim Biophys Acta,* 1863, 1728-48.

DEVALLA, H. D., SCHWACH, V., FORD, J. W., MILNES, J. T., EL-HAOU, S., JACKSON, C., GKATZIS, K., ELLIOTT, D. A., CHUVA DE SOUSA LOPES, S. M., MUMMERY, C. L., VERKERK, A. O. & PASSIER, R. 2015. Atrial-like cardiomyocytes from human pluripotent stem cells are a robust preclinical model for assessing atrial-selective pharmacology. *EMBO Mol Med,* 7, 394-410.

DEWENTER, M., VON DER LIETH, A., KATUS, H. A. & BACKS, J. 2017. Calcium Signaling and Transcriptional Regulation in Cardiomyocytes. *Circ Res,* 121, 1000-1020.

DICARLO, J. E., NORVILLE, J. E., MALI, P., RIOS, X., AACH, J. & CHURCH, G. M. 2013. Genome engineering in Saccharomyces cerevisiae using CRISPR-Cas systems. *Nucleic Acids Res,* 41, 4336-43.

DIEZ-GARCIA, J., MATSUSHITA, S., MUTOH, H., NAKAI, J., OHKURA, M., YOKOYAMA, J., DIMITROV, D. & KNOPFEL, T. 2005. Activation of cerebellar parallel fibers monitored in transgenic mice expressing a fluorescent Ca2+ indicator protein. *Eur J Neurosci,* 22, 627-35.

DOLNIKOV, K., SHILKRUT, M., ZEEVI-LEVIN, N., GERECHT-NIR, S., AMIT, M., DANON, A., ITSKOVITZ-ELDOR, J. & BINAH, O. 2006. Functional properties of human embryonic stem cell-derived cardiomyocytes: intracellular Ca2+ handling and the role of sarcoplasmic reticulum in the contraction. *Stem Cells,* 24, 236-45.

DONNELLY, M. L., HUGHES, L. E., LUKE, G., MENDOZA, H., TEN DAM, E., GANI, D. & RYAN, M. D. 2001. The 'cleavage' activities of foot-and-mouth disease virus 2A site-directed mutants and naturally occurring '2A-like' sequences. *J Gen Virol,* 82, 1027-41.

DOUDNA, J. A. & CHARPENTIER, E. 2014. Genome editing. The new frontier of genome engineering with CRISPR-Cas9. *Science,* 346, 1258096.

DRAGIC, T., LITWIN, V., ALLAWAY, G. P., MARTIN, S. R., HUANG, Y., NAGASHIMA, K. A., CAYANAN, C., MADDON, P. J., KOUP, R. A., MOORE, J. P. & PAXTON, W. A. 1996. HIV-1 entry into CD4+ cells is mediated by the chemokine receptor CC-CKR-5. *Nature,* 381, 667-73.

DU, G. G., GUO, X., KHANNA, V. K. & MACLENNAN, D. H. 2001. Ryanodine sensitizes the cardiac Ca(2+) release channel (ryanodine receptor isoform 2) to Ca(2+) activation and dissociates as the channel is closed by Ca(2+) depletion. *Proc Natl Acad Sci U S A,* 98**,** 13625-30.

DUNCAN, G., FIRTH, K., GEORGE, V., HOANG, M. D., STANIFORTH, A., SMITH, G. & DENNING, C. 2017. Drug-Mediated Shortening of Action Potentials in LQTS2 Human Induced Pluripotent Stem Cell-Derived Cardiomyocytes. *Stem Cells Dev,* 26**,** 1695-705.

DYKENS, J. A. & WILL, Y. 2007. The significance of mitochondrial toxicity testing in drug development. *Drug Discov Today,* 12**,** 777-85.

EDWARDS, A. G. & LOUCH, W. E. 2017. Species-Dependent Mechanisms of Cardiac Arrhythmia: A Cellular Focus. *Clinical Medicine Insights. Cardiology,* 11**,** 1179546816686061.

EISELLEOVA, L., PETERKOVA, I., NERADIL, J., SLANINOVA, I., HAMPL, A. & DVORAK, P. 2008. Comparative study of mouse and human feeder cells for human embryonic stem cells. *Int J Dev Biol,* 52**,** 353-63.

ELGIN, S. C. R. & REUTER, G. 2013. Position-Effect Variegation, Heterochromatin Formation, and Gene Silencing in Drosophila. *Cold Spring Harbor Perspectives in Biology,* 5**,** a017780.

ELLIOTT, D. A., BRAAM, S. R., KOUTSIS, K., NG, E. S., JENNY, R., LAGERQVIST, E. L., BIBEN, C., HATZISTAVROU, T., HIRST, C. E., YU, Q. C., SKELTON, R. J., WARD-VAN OOSTWAARD, D., LIM, S. M., KHAMMY, O., LI, X., HAWES, S. M., DAVIS, R. P., GOULBURN, A. L., PASSIER, R., PRALL, O. W., HAYNES, J. M., POUTON, C. W., KAYE, D. M., MUMMERY, C. L., ELEFANTY, A. G. & STANLEY, E. G. 2011. NKX2-5(eGFP/w) hESCs for isolation of human cardiac progenitors and cardiomyocytes. *Nat Methods,* 8**,** 1037-40.

ELLIOTT, P. M., ANASTASAKIS, A., BORGER, M. A., BORGGREFE, M., CECCHI, F., CHARRON, P., HAGEGE, A. A., LAFONT, A., LIMONGELLI, G., MAHRHOLDT, H., MCKENNA, W. J., MOGENSEN, J., NIHOYANNOPOULOS, P., NISTRI, S., PIEPER, P. G., PIESKE, B., RAPEZZI, C., RUTTEN, F. H., TILLMANNS, C. & WATKINS, H. 2014. 2014 ESC Guidelines on diagnosis and management of hypertrophic cardiomyopathy: the Task Force for the Diagnosis and Management of Hypertrophic Cardiomyopathy of the European Society of Cardiology (ESC). *Eur Heart J,* 35**,** 2733-79.

ESVELT, K. M., MALI, P., BRAFF, J. L., MOOSBURNER, M., YAUNG, S. J. & CHURCH, G. M. 2013. Orthogonal Cas9 proteins for RNA-guided gene regulation and editing. *Nat Methods,* 10**,** 1116-21.

FAN, Y., WU, J., ASHOK, P., HSIUNG, M. & TZANAKAKIS, E. S. 2015. Production of human pluripotent stem cell therapeutics under defined xeno-free conditions: progress and challenges. *Stem Cell Rev,* 11**,** 96-109.

FATKIN, D., MCCONNELL, B. K., MUDD, J. O., SEMSARIAN, C., MOSKOWITZ, I. G., SCHOEN, F. J., GIEWAT, M., SEIDMAN, C. E. & SEIDMAN, J. G. 2000. An abnormal Ca(2+) response in mutant sarcomere protein-mediated familial hypertrophic cardiomyopathy. *J Clin Invest,* 106**,** 1351-9.

FERIC, N. T. & RADISIC, M. 2016. Towards adult-like human engineered cardiac tissue: Maturing human pluripotent stem cell-derived cardiomyocytes in human engineered cardiac tissues. *Adv Drug Deliv Rev,* 96**,** 110-34.

FISCHER, T. H., HERTING, J., TIRILOMIS, T., RENNER, A., NEEF, S., TOISCHER, K., ELLENBERGER, D., FORSTER, A., SCHMITTO, J. D., GUMMERT, J., SCHONDUBE, F. A., HASENFUSS, G., MAIER, L. S. & SOSSALLA, S. 2013. Ca2+/calmodulin-

dependent protein kinase II and protein kinase A differentially regulate sarcoplasmic reticulum Ca2+ leak in human cardiac pathology. *Circulation,* 128**,** 970-81.

FONOUDI, H., ANSARI, H., ABBASALIZADEH, S., LARIJANI, M. R., KIANI, S., HASHEMIZADEH, S., ZARCHI, A. S., BOSMAN, A., BLUE, G. M., PAHLAVAN, S., PERRY, M., ORR, Y., MAYORCHAK, Y., VANDENBERG, J., TALKHABI, M., WINLAW, D. S., HARVEY, R. P., AGHDAMI, N. & BAHARVAND, H. 2015. A Universal and Robust Integrated Platform for the Scalable Production of Human Cardiomyocytes From Pluripotent Stem Cells. *Stem Cells Translational Medicine,* 4**,** 1482-1494.

FOWLER, M. B., TIMMIS, A. D., CRICK, J. P., VINCENT, R. & CHAMBERLAIN, D. A. 1982. Comparison of haemodynamic responses to dobutamine and salbutamol in cardiogenic shock after acute myocardial infarction. *Br Med J (Clin Res Ed),* 284**,** 73-6.

FRANK, M. J., ABDULLA, A. M., WATKINS, L. O., PRISANT, L. & STEFADOUROS, M. A. 1983. Long-term medical management of hypertrophic cardiomyopathy: usefulness of propranolol. *Eur Heart J,* 4 Suppl F**,** 155-64.

FUSAKI, N., BAN, H., NISHIYAMA, A., SAEKI, K. & HASEGAWA, M. 2009. Efficient induction of transgene-free human pluripotent stem cells using a vector based on Sendai virus, an RNA virus that does not integrate into the host genome. *Proceedings of the Japan Academy, Series B,* 85**,** 348-362.

G, N., TAN, A., FARHATNIA, Y., RAJADAS, J., HAMBLIN, M. R., KHAW, P. T. & SEIFALIAN, A. M. 2013. Channelrhodopsins: visual regeneration and neural activation by a light switch. *N Biotechnol,* 30**,** 461-74.

GERMANGUZ, I., SEDAN, O., ZEEVI-LEVIN, N., SHTRICHMAN, R., BARAK, E., ZISKIND, A., ELIYAHU, S., MEIRY, G., AMIT, M., ITSKOVITZ-ELDOR, J. & BINAH, O. 2011. Molecular characterization and functional properties of cardiomyocytes derived from human inducible pluripotent stem cells. *J Cell Mol Med,* 15**,** 38-51.

GHASEMI-DEHKORDI, P., ALLAHBAKHSHIAN-FARSANI, M., ABDIAN, N., MIRZAEIAN, A., SAFFARI-CHALESHTORI, J., HEYBATI, F., MARDANI, G., KARIMI-TAGHANAKI, A., DOOSTI, A., JAMI, M. S., ABOLHASANI, M. & HASHEMZADEH-CHALESHTORI, M. 2015. Comparison between the cultures of human induced pluripotent stem cells (hiPSCs) on feeder-and serum-free system (Matrigel matrix), MEF and HDF feeder cell lines. *J Cell Commun Signal,* 9**,** 233-46.

GIBSON, D. G., YOUNG, L., CHUANG, R. Y., VENTER, J. C., HUTCHISON, C. A., 3RD & SMITH, H. O. 2009. Enzymatic assembly of DNA molecules up to several hundred kilobases. *Nat Methods,* 6**,** 343-5.

GINSBURG, K. S. & BERS, D. M. 2004. Modulation of excitation–contraction coupling by isoproterenol in cardiomyocytes with controlled SR Ca(2+) load and Ca(2+) current trigger. *J Physiol,* 556**,** 463-80.

GREEN, E. M., WAKIMOTO, H., ANDERSON, R. L., EVANCHIK, M. J., GORHAM, J. M., HARRISON, B. C., HENZE, M., KAWAS, R., OSLOB, J. D., RODRIGUEZ, H. M., SONG, Y., WAN, W., LEINWAND, L. A., SPUDICH, J. A., MCDOWELL, R. S., SEIDMAN, J. G. & SEIDMAN, C. E. 2016. A small-molecule inhibitor of sarcomere contractility suppresses hypertrophic cardiomyopathy in mice. *Science,* 351**,** 617-21.

GREENBAUM, L., ROTHMANN, C., LAVIE, R. & MALIK, Z. 2000. Green fluorescent protein photobleaching: a model for protein damage by endogenous and exogenous singlet oxygen. *Biol Chem,* 381**,** 1251-8.

GREGOR, P. & ČURILA, K. 2015. Medical treatment of hypertrophic cardiomyopathy – What do we know about it today? *Cor et Vasa,* 57**,** e219-e224.

GRIESBECK, O., BAIRD, G. S., CAMPBELL, R. E., ZACHARIAS, D. A. & TSIEN, R. Y. 2001. Reducing the Environmental Sensitivity of Yellow Fluorescent Protein: MECHANISM AND APPLICATIONS. *Journal of Biological Chemistry,* 276**,** 29188-29194.

GRIMM, F. A., IWATA, Y., SIRENKO, O., BITTNER, M. & RUSYN, I. 2015. High-Content Assay Multiplexing for Toxicity Screening in Induced Pluripotent Stem Cell-Derived Cardiomyocytes and Hepatocytes. *Assay Drug Dev Technol,* 13**,** 529-46.

GRISSMER, S., NGUYEN, A. N., AIYAR, J., HANSON, D. C., MATHER, R. J., GUTMAN, G. A., KARMILOWICZ, M. J., AUPERIN, D. D. & CHANDY, K. G. 1994. Pharmacological characterization of five cloned voltage-gated K+ channels, types Kv1.1, 1.2, 1.3, 1.5, and 3.1, stably expressed in mammalian cell lines. *Mol Pharmacol,* 45**,** 1227-34.

GUATIMOSIM, S., GUATIMOSIM, C. & SONG, L. S. 2011. Imaging calcium sparks in cardiac myocytes. *Methods Mol Biol,* 689**,** 205-14.

GUNAYDIN, L. A., YIZHAR, O., BERNDT, A., SOHAL, V. S., DEISSEROTH, K. & HEGEMANN, P. 2010. Ultrafast optogenetic control. *Nat Neurosci,* 13**,** 387-92.

GUNN, J. A. & GURD, M. R. 1940. The action of some amines related to adrenaline: phenylallylamine, phenylbutenylamine, diphenylethylamine. *J Physiol,* 98**,** 424-41.

GUPTA, R. M. & MUSUNURU, K. 2014. Expanding the genetic editing tool kit: ZFNs, TALENs, and CRISPR-Cas9. *J Clin Invest,* 124**,** 4154-61.

GUSTERSON, R. J., JAZRAWI, E., ADCOCK, I. M. & LATCHMAN, D. S. 2003. The transcriptional co-activators CREB-binding protein (CBP) and p300 play a critical role in cardiac hypertrophy that is dependent on their histone acetyltransferase activity. *J Biol Chem,* 278**,** 6838-47.

GYORKE, I. & GYORKE, S. 1998. Regulation of the cardiac ryanodine receptor channel by luminal Ca2+ involves luminal Ca2+ sensing sites. *Biophys J,* 75**,** 2801-10.

GYÖRKE, I., HESTER, N., JONES, L. R. & GYÖRKE, S. 2004. The Role of Calsequestrin, Triadin, and Junctin in Conferring Cardiac Ryanodine Receptor Responsiveness to Luminal Calcium. *Biophysical Journal,* 86**,** 2121-2128.

HAMADA, M., SHIGEMATSU, Y., IKEDA, S., HARA, Y., OKAYAMA, H., KODAMA, K., OCHI, T. & HIWADA, K. 1997. Class Ia antiarrhythmic drug cibenzoline: a new approach to the medical treatment of hypertrophic obstructive cardiomyopathy. *Circulation,* 96**,** 1520-4.

HAN, L., LI, Y., TCHAO, J., KAPLAN, A. D., LIN, B., LI, Y., MICH-BASSO, J., LIS, A., HASSAN, N., LONDON, B., BETT, G. C., TOBITA, K., RASMUSSON, R. L. & YANG, L. 2014. Study familial hypertrophic cardiomyopathy using patient-specific induced pluripotent stem cells. *Cardiovasc Res,* 104**,** 258-69.

HARMER, A. R., VALENTIN, J. P. & POLLARD, C. E. 2011. On the relationship between block of the cardiac Na(+) channel and drug-induced prolongation of the QRS complex. *Br J Pharmacol,* 164**,** 260-73.

HARVEY, P. A. & LEINWAND, L. A. 2011. The cell biology of disease: cellular mechanisms of cardiomyopathy. *J Cell Biol,* 194**,** 355-65.

HEGEMANN, P., EHLENBECK, S. & GRADMANN, D. 2005. Multiple photocycles of channelrhodopsin. *Biophys J,* 89**,** 3911-8.

HEIJMAN, J., VOIGT, N., CARLSSON, L. G. & DOBREV, D. 2014. Cardiac safety assays. *Curr Opin Pharmacol,* 15**,** 16-21.

HEISTER, T., HEID, I., ACKERMANN, M. & FRAEFEL, C. 2002. Herpes simplex virus type 1/adeno-associated virus hybrid vectors mediate site-specific integration at the adeno-associated virus preintegration site, AAVS1, on human chromosome 19. *J Virol,* 76**,** 7163-73.

HELASSA, N., PODOR, B., FINE, A. & TOROK, K. 2016. Design and mechanistic insight into ultrafast calcium indicators for monitoring intracellular calcium dynamics. *Sci Rep,* 6**,** 38276.

HERRON, T. J., LEE, P. & JALIFE, J. 2012. Optical imaging of voltage and calcium in cardiac cells & tissues. *Circ Res,* 110**,** 609-23.

HO, C. Y., LAKDAWALA, N. K., CIRINO, A. L., LIPSHULTZ, S. E., SPARKS, E., ABBASI, S. A., KWONG, R. Y., ANTMAN, E. M., SEMSARIAN, C., GONZALEZ, A., LOPEZ, B., DIEZ, J., ORAV, E. J., COLAN, S. D. & SEIDMAN, C. E. 2015. Diltiazem treatment for pre-clinical hypertrophic cardiomyopathy sarcomere mutation carriers: a pilot randomized trial to modify disease expression. *JACC Heart Fail,* 3**,** 180-8.

HO, C. Y., MCMURRAY, J. J. V., CIRINO, A. L., COLAN, S. D., DAY, S. M., DESAI, A. S., LIPSHULTZ, S. E., MACRAE, C. A., SHI, L., SOLOMON, S. D., ORAV, E. J. & BRAUNWALD, E. 2017. The Design of the Valsartan for Attenuating Disease Evolution in Early Sarcomeric Hypertrophic Cardiomyopathy (VANISH) Trial. *Am Heart J,* 187**,** 145-155.

HO, D., YAN, L., IWATSUBO, K., VATNER, D. E. & VATNER, S. F. 2010. Modulation of β-Adrenergic Receptor Signaling in Heart Failure and Longevity: Targeting Adenylyl Cyclase Type 5. *Heart Fail Rev,* 15**,** 495-512.

HOCKEMEYER, D., SOLDNER, F., BEARD, C., GAO, Q., MITALIPOVA, M., DEKELVER, R. C., KATIBAH, G. E., AMORA, R., BOYDSTON, E. A., ZEITLER, B., MENG, X., MILLER, J. C., ZHANG, L., REBAR, E. J., GREGORY, P. D., URNOV, F. D. & JAENISCH, R. 2009. Efficient targeting of expressed and silent genes in human ESCs and iPSCs using zinc-finger nucleases. *Nat Biotechnol,* 27**,** 851-7.

HOCKEMEYER, D., WANG, H., KIANI, S., LAI, C. S., GAO, Q., CASSADY, J. P., COST, G. J., ZHANG, L., SANTIAGO, Y., MILLER, J. C., ZEITLER, B., CHERONE, J. M., MENG, X., HINKLEY, S. J., REBAR, E. J., GREGORY, P. D., URNOV, F. D. & JAENISCH, R. 2011. Genetic engineering of human pluripotent cells using TALE nucleases. *Nat Biotechnol,* 29**,** 731-4.

HOEKSTRA, M., MUMMERY, C., WILDE, A., BEZZINA, C. & VERKERK, A. 2012. Induced pluripotent stem cell derived cardiomyocytes as models for cardiac arrhythmias. *Frontiers in Physiology,* 3.

HOLT, N., WANG, J., KIM, K., FRIEDMAN, G., WANG, X., TAUPIN, V., CROOKS, G. M., KOHN, D. B., GREGORY, P. D., HOLMES, M. C. & CANNON, P. M. 2010. Human hematopoietic stem/progenitor cells modified by zinc-finger nucleases targeted to CCR5 control HIV-1 in vivo. *Nature Biotechnology,* 28**,** 839.

HOU, Z., ZHANG, Y., PROPSON, N. E., HOWDEN, S. E., CHU, L. F., SONTHEIMER, E. J. & THOMSON, J. A. 2013. Efficient genome engineering in human pluripotent stem cells using Cas9 from Neisseria meningitidis. *Proc Natl Acad Sci U S A,* 110**,** 15644-9.

HOUSTON, B. A. & STEVENS, G. R. 2014. Hypertrophic Cardiomyopathy: A Review. *Clin Med Insights Cardiol,* 8**,** 53-65.

HSU, P. D., LANDER, E. S. & ZHANG, F. 2014. Development and applications of CRISPR-Cas9 for genome engineering. *Cell,* 157**,** 1262-78.

HSU, P. D., SCOTT, D. A., WEINSTEIN, J. A., RAN, F. A., KONERMANN, S., AGARWALA, V., LI, Y., FINE, E. J., WU, X., SHALEM, O., CRADICK, T. J., MARRAFFINI, L. A., BAO, G. & ZHANG, F. 2013. DNA targeting specificity of RNA-guided Cas9 nucleases. *Nat Biotechnol,* 31**,** 827-32.

HU, J. H., MILLER, S. M., GEURTS, M. H., TANG, W., CHEN, L., SUN, N., ZEINA, C. M., GAO, X., REES, H. A., LIN, Z. & LIU, D. R. 2018. Evolved Cas9 variants with broad PAM compatibility and high DNA specificity. *Nature*.

HUANG, H., PUGSLEY, M. K., FERMINI, B., CURTIS, M. J., KOERNER, J., ACCARDI, M. & AUTHIER, S. 2017. Cardiac voltage-gated ion channels in safety pharmacology: Review of the landscape leading to the CiPA initiative. *Journal of Pharmacological and Toxicological Methods,* 87**,** 11-23.

HUKE, S. & KNOLLMANN, B. C. 2010. Increased myofilament Ca2+-sensitivity and arrhythmia susceptibility. *J Mol Cell Cardiol,* 48**,** 824-33.

INGLES, J., BURNS, C., BARRATT, A. & SEMSARIAN, C. 2015. Application of Genetic Testing in Hypertrophic Cardiomyopathy for Preclinical Disease Detection. *Circ Cardiovasc Genet,* 8**,** 852-9.

IRION, S., LUCHE, H., GADUE, P., FEHLING, H. J., KENNEDY, M. & KELLER, G. 2007. Identification and targeting of the ROSA26 locus in human embryonic stem cells. *Nat Biotechnol,* 25**,** 1477-82.

ITSKOVITZ-ELDOR, J., SCHULDINER, M., KARSENTI, D., EDEN, A., YANUKA, O., AMIT, M., SOREQ, H. & BENVENISTY, N. 2000. Differentiation of human embryonic stem cells into embryoid bodies compromising the three embryonic germ layers. *Molecular medicine,* 6**,** 88.

ITZHAKI, I., RAPOPORT, S., HUBER, I., MIZRAHI, I., ZWI-DANTSIS, L., ARBEL, G., SCHILLER, J. & GEPSTEIN, L. 2011. Calcium handling in human induced pluripotent stem cell derived cardiomyocytes. *PLoS One,* 6**,** e18037.

JACOBY, D. L., DEPASQUALE, E. C. & MCKENNA, W. J. 2013. Hypertrophic cardiomyopathy: diagnosis, risk stratification and treatment. *Cmaj,* 185**,** 127-34.

JONES, P. P., JIANG, D., BOLSTAD, J., HUNT, D. J., ZHANG, L., DEMAUREX, N. & CHEN, S. R. 2008. Endoplasmic reticulum Ca2+ measurements reveal that the cardiac ryanodine receptor mutations linked to cardiac arrhythmia and sudden death alter the threshold for store-overload-induced Ca2+ release. *Biochem J,* 412**,** 171-8.

JUNG, C. B., MORETTI, A., MEDEROS Y SCHNITZLER, M., IOP, L., STORCH, U., BELLIN, M., DORN, T., RUPPENTHAL, S., PFEIFFER, S., GOEDEL, A., DIRSCHINGER, R. J., SEYFARTH, M., LAM, J. T., SINNECKER, D., GUDERMANN, T., LIPP, P. & LAUGWITZ, K. L. 2012. Dantrolene rescues arrhythmogenic RYR2 defect in a patient-specific stem cell model of catecholaminergic polymorphic ventricular tachycardia. *EMBO Mol Med,* 4**,** 180-91.

JUNG, G., FAJARDO, G., RIBEIRO, A. J., KOOIKER, K. B., CORONADO, M., ZHAO, M., HU, D. Q., REDDY, S., KODO, K., SRIRAM, K., INSEL, P. A., WU, J. C., PRUITT, B. L. & BERNSTEIN, D. 2016. Time-dependent evolution of functional vs. remodeling signaling in induced pluripotent stem cell-derived cardiomyocytes and induced maturation with biomechanical stimulation. *Faseb j,* 30**,** 1464-79.

KAESTNER, L., SCHOLZ, A., TIAN, Q., RUPPENTHAL, S., TABELLION, W., WIESEN, K., KATUS, H. A., MULLER, O. J., KOTLIKOFF, M. I. & LIPP, P. 2014. Genetically encoded Ca2+ indicators in cardiac myocytes. *Circ Res,* 114**,** 1623-39.

KALOZOUMI, G., TZIMAS, C. & SANOUDOU, D. 2012. The expanding role of epigenetics. *Glob Cardiol Sci Pract,* 2012.

KANE, C., COUCH, L. & TERRACCIANO, C. M. N. 2015. Excitation–contraction coupling of human induced pluripotent stem cell-derived cardiomyocytes. *Frontiers in Cell and Developmental Biology,* 3.

KANG, J., CHEN, X. L., JI, J., LEI, Q. & RAMPE, D. 2012a. Ca(2)(+) channel activators reveal differential L-type Ca(2)(+) channel pharmacology between native and stem cell-derived cardiomyocytes. *J Pharmacol Exp Ther,* 341**,** 510-7.

KANG, S., COOPER, G., DUNNE, S. F., DUSEL, B., LUAN, C. H., SURMEIER, D. J. & SILVERMAN, R. B. 2012b. CaV1.3-selective L-type calcium channel antagonists as potential new therapeutics for Parkinson's disease. *Nat Commun,* 3**,** 1146.

KATRA, R. P. & LAURITA, K. R. 2005. Cellular mechanism of calcium-mediated triggered activity in the heart. *Circ Res,* 96**,** 535-42.

KAWAS, R. F., ANDERSON, R. L., INGLE, S. R. B., SONG, Y., SRAN, A. S. & RODRIGUEZ, H. M. 2017. A small-molecule modulator of cardiac myosin acts on multiple stages of the myosin chemomechanical cycle. *J Biol Chem,* 292**,** 16571-16577.

KILLEEN, M. J. 2009. Drug-induced arrhythmias and sudden cardiac death: implications for the pharmaceutical industry. *Drug Discov Today,* 14**,** 589-97.

KIM, H. & KIM, J. S. 2014. A guide to genome engineering with programmable nucleases. *Nat Rev Genet,* 15**,** 321-34.

KIM, J. H., LEE, S. R., LI, L. H., PARK, H. J., PARK, J. H., LEE, K. Y., KIM, M. K., SHIN, B. A. & CHOI, S. Y. 2011. High cleavage efficiency of a 2A peptide derived from porcine teschovirus-1 in human cell lines, zebrafish and mice. *PLoS One,* 6**,** e18556.

KIM, J. M., KIM, D., KIM, S. & KIM, J. S. 2014a. Genotyping with CRISPR-Cas-derived RNA-guided endonucleases. *Nat Commun,* 5**,** 3157.

KIM, S., KIM, D., CHO, S. W., KIM, J. & KIM, J. S. 2014b. Highly efficient RNA-guided genome editing in human cells via delivery of purified Cas9 ribonucleoproteins. *Genome Res,* 24**,** 1012-9.

KIRSCHNER, S. E., BECKER, E., ANTOGNOZZI, M., KUBIS, H. P., FRANCINO, A., NAVARRO-LOPEZ, F., BIT-AVRAGIM, N., PERROT, A., MIRRAKHIMOV, M. M., OSTERZIEL, K. J., MCKENNA, W. J., BRENNER, B. & KRAFT, T. 2005. Hypertrophic cardiomyopathy-related beta-myosin mutations cause highly variable calcium sensitivity with functional imbalances among individual muscle cells. *Am J Physiol Heart Circ Physiol,* 288**,** H1242-51.

KLEINLOGEL, S., FELDBAUER, K., DEMPSKI, R. E., FOTIS, H., WOOD, P. G., BAMANN, C. & BAMBERG, E. 2011. Ultra light-sensitive and fast neuronal activation with the Ca(2)+-permeable channelrhodopsin CatCh. *Nat Neurosci,* 14**,** 513-8.

KNOPFEL, T. 2012. Genetically encoded optical indicators for the analysis of neuronal circuits. *Nat Rev Neurosci,* 13**,** 687-700.

KOHAJDA, Z., FARKAS-MORVAY, N., JOST, N., NAGY, N., GERAMIPOUR, A., HORVATH, A., VARGA, R. S., HORNYIK, T., CORICI, C., ACSAI, K., HORVATH, B., PROROK, J., ORDOG, B., DERI, S., TOTH, D., LEVIJOKI, J., POLLESELLO, P., KOSKELAINEN, T., OTSOMAA, L., TOTH, A., BACZKO, I., LEPRAN, I., NANASI, P. P., PAPP, J. G., VARRO, A. & VIRAG, L. 2016. The Effect of a Novel Highly Selective Inhibitor of the Sodium/Calcium Exchanger (NCX) on Cardiac Arrhythmias in In Vitro and In Vivo Experiments. *PLoS One,* 11**,** e0166041.

KONDRASHOV, A., DUC HOANG, M., SMITH, J., BHAGWAN, J., DUNCAN, G., MOSQUEIRA, D., MUNOZ, M., VO, N. T. N. & DENNING, C. 2018. Simplified footprint-free Cas9/CRISPR editing of cardiac-associated genes in human pluripotent stem cells. *Stem Cells Dev.*

KONG, H., JONES, P. P., KOOP, A., ZHANG, L., DUFF, H. J. & CHEN, S. R. 2008. Caffeine induces Ca2+ release by reducing the threshold for luminal Ca2+ activation of the ryanodine receptor. *Biochem J,* 414**,** 441-52.

KOOPMAN, C. D., ZIMMERMANN, W. H., KNÖPFEL, T. & DE BOER, T. P. 2017. Cardiac optogenetics: using light to monitor cardiac physiology. *Basic Res Cardiol,* 112.

KOTLIKOFF, M. I. 2007. Genetically encoded Ca2+ indicators: using genetics and molecular design to understand complex physiology. *J Physiol,* 578**,** 55-67.

KOVAL, O. M., GUAN, X., WU, Y., JOINER, M.-L., GAO, Z., CHEN, B., GRUMBACH, I. M., LUCZAK, E. D., COLBRAN, R. J., SONG, L.-S., HUND, T. J., MOHLER, P. J. & ANDERSON, M. E. 2010. Ca_V1.2 ß-subunit coordinates CaMKII-triggered cardiomyocyte death and afterdepolarizations. *Proceedings of the National Academy of Sciences,* 107**,** 4996-5000.

KUMAR, K. R., MANDLEYWALA, S. N. & LINK, M. S. 2015. Atrial and ventricular arrhythmias in hypertrophic cardiomyopathy. *Card Electrophysiol Clin,* 7**,** 173-86.

KURTZ, T. W. & KAJIYA, T. 2012. Differential pharmacology and benefit/risk of azilsartan compared to other sartans. *Vascular Health and Risk Management,* 8**,** 133-143.

LAFLAMME, M. A., CHEN, K. Y., NAUMOVA, A. V., MUSKHELI, V., FUGATE, J. A., DUPRAS, S. K., REINECKE, H., XU, C., HASSANIPOUR, M., POLICE, S., O'SULLIVAN, C., COLLINS, L., CHEN, Y., MINAMI, E., GILL, E. A., UENO, S., YUAN, C., GOLD, J. & MURRY, C. E. 2007. Cardiomyocytes derived from human embryonic stem cells in pro-survival factors enhance function of infarcted rat hearts. *Nat Biotechnol,* 25**,** 1015-24.

LAN, F., LEE, A. S., LIANG, P., SANCHEZ-FREIRE, V., NGUYEN, P. K., WANG, L., HAN, L., YEN, M., WANG, Y., SUN, N., ABILEZ, O. J., HU, S., EBERT, A. D., NAVARRETE, E. G., SIMMONS, C. S., WHEELER, M., PRUITT, B., LEWIS, R., YAMAGUCHI, Y., ASHLEY, E. A., BERS, D. M., ROBBINS, R. C., LONGAKER, M. T. & WU, J. C. 2013. Abnormal calcium handling properties underlie familial hypertrophic cardiomyopathy pathology in patient-specific induced pluripotent stem cells. *Cell Stem Cell,* 12**,** 101-13.

LANDESBERG, A. & SIDEMAN, S. 1994. Coupling calcium binding to troponin C and cross-bridge cycling in skinned cardiac cells. *Am J Physiol,* 266**,** H1260-71.

LANDSTROM, A. P., ADEKOLA, B. A., BOS, J. M., OMMEN, S. R. & ACKERMAN, M. J. 2011. PLN-encoded phospholamban mutation in a large cohort of hypertrophic cardiomyopathy cases: summary of the literature and implications for genetic testing. *Am Heart J,* 161**,** 165-71.

LEE, P., KLOS, M., BOLLENSDORFF, C., HOU, L., EWART, P., KAMP, T. J., ZHANG, J., BIZY, A., GUERRERO-SERNA, G., KOHL, P., JALIFE, J. & HERRON, T. J. 2012. Simultaneous voltage and calcium mapping of genetically purified human induced pluripotent stem cell-derived cardiac myocyte monolayers. *Circ Res,* 110**,** 1556-63.

LEE, Y. K., NG, K. M., LAI, W. H., CHAN, Y. C., LAU, Y. M., LIAN, Q., TSE, H. F. & SIU, C. W. 2011. Calcium homeostasis in human induced pluripotent stem cell-derived cardiomyocytes. *Stem Cell Rev,* 7**,** 976-86.

LI, S., XUE, H., WU, J., RAO, M. S., KIM, D. H., DENG, W. & LIU, Y. 2015. Human Induced Pluripotent Stem Cell NEUROG2 Dual Knockin Reporter Lines Generated by the CRISPR/Cas9 System. *Stem Cells Dev,* 24**,** 2925-42.

LIEU, D. K., LIU, J., SIU, C. W., MCNERNEY, G. P., TSE, H. F., ABU-KHALIL, A., HUSER, T. & LI, R. A. 2009. Absence of transverse tubules contributes to non-uniform

Ca(2+) wavefronts in mouse and human embryonic stem cell-derived cardiomyocytes. *Stem Cells Dev,* 18**,** 1493-500.

LIM, D. S., LUTUCUTA, S., BACHIREDDY, P., YOUKER, K., EVANS, A., ENTMAN, M., ROBERTS, R. & MARIAN, A. J. 2001a. Angiotensin II blockade reverses myocardial fibrosis in a transgenic mouse model of human hypertrophic cardiomyopathy. *Circulation,* 103**,** 789-91.

LIM, D. S., ROBERTS, R. & MARIAN, A. J. 2001b. Expression profiling of cardiac genes in human hypertrophic cardiomyopathy: insight into the pathogenesis of phenotypes. *J Am Coll Cardiol,* 38**,** 1175-80.

LIN, J. Y. 2012. Optogenetic excitation of neurons with channelrhodopsins: light instrumentation, expression systems, and channelrhodopsin variants. *Prog Brain Res,* 196**,** 29-47.

LIN, J. Y., KNUTSEN, P. M., MULLER, A., KLEINFELD, D. & TSIEN, R. Y. 2013. ReaChR: a red-shifted variant of channelrhodopsin enables deep transcranial optogenetic excitation. *Nat Neurosci,* 16**,** 1499-508.

LIN, J. Y., LIN, M. Z., STEINBACH, P. & TSIEN, R. Y. 2009. Characterization of engineered channelrhodopsin variants with improved properties and kinetics. *Biophys J,* 96**,** 1803-14.

LIN, S., STAAHL, B. T., ALLA, R. K. & DOUDNA, J. A. 2014. Enhanced homology-directed human genome engineering by controlled timing of CRISPR/Cas9 delivery. *eLife,* 3**,** e04766.

LIPSKAIA, L., CHEMALY, E. R., HADRI, L., LOMPRE, A. M. & HAJJAR, R. J. 2010. Sarcoplasmic reticulum Ca(2+) ATPase as a therapeutic target for heart failure. *Expert Opin Biol Ther,* 10**,** 29-41.

LIU, J., FU, J. D., SIU, C. W. & LI, R. A. 2007. Functional sarcoplasmic reticulum for calcium handling of human embryonic stem cell-derived cardiomyocytes: insights for driven maturation. *Stem Cells,* 25**,** 3038-44.

LIU, Q., BUSBY, J. C. & MOLKENTIN, J. D. 2009a. Interaction between TAK1-TAB1-TAB2 and RCAN1-calcineurin defines a signalling nodal control point. *Nat Cell Biol,* 11**,** 154-61.

LIU, R., PAXTON, W. A., CHOE, S., CERADINI, D., MARTIN, S. R., HORUK, R., MACDONALD, M. E., STUHLMANN, H., KOUP, R. A. & LANDAU, N. R. 1996. Homozygous defect in HIV-1 coreceptor accounts for resistance of some multiply-exposed individuals to HIV-1 infection. *Cell,* 86**,** 367-77.

LIU, Y., LI, Z., GUO, X., JING, X., ZHANG, X., SHAO, H., GUAN, Y. & ABRAHAM, M. R. 2017a. Recent Advances in Hypertrophic Cardiomyopathy: A System Review. *Genetic Polymorphisms*.

LIU, Y., THYAGARAJAN, B., LAKSHMIPATHY, U., XUE, H., LIEU, P., FONTES, A., MACARTHUR, C. C., SCHEYHING, K., RAO, M. S. & CHESNUT, J. D. 2009b. Generation of platform human embryonic stem cell lines that allow efficient targeting at a predetermined genomic location. *Stem Cells Dev,* 18**,** 1459-72.

LIU, Z., CHEN, O., WALL, J. B. J., ZHENG, M., ZHOU, Y., WANG, L., RUTH VASEGHI, H., QIAN, L. & LIU, J. 2017b. Systematic comparison of 2A peptides for cloning multi-genes in a polycistronic vector. *Sci Rep,* 7**,** 2193.

LOEWE, A. 2016. *Modeling Human Atrial Patho-Electrophysiology from Ion Channels to ECG - Substrates, Pharmacology, Vulnerability, and P-Waves*, KIT Scientific Publishing.

LOMBARDO, A., CESANA, D., GENOVESE, P., DI STEFANO, B., PROVASI, E., COLOMBO, D. F., NERI, M., MAGNANI, Z., CANTORE, A., LO RISO, P., DAMO, M., PELLO, O.

M., HOLMES, M. C., GREGORY, P. D., GRITTI, A., BROCCOLI, V., BONINI, C. & NALDINI, L. 2011. Site-specific integration and tailoring of cassette design for sustainable gene transfer. *Nat Methods,* 8**,** 861-9.

LOMBARDO, A., GENOVESE, P., BEAUSEJOUR, C. M., COLLEONI, S., LEE, Y. L., KIM, K. A., ANDO, D., URNOV, F. D., GALLI, C., GREGORY, P. D., HOLMES, M. C. & NALDINI, L. 2007. Gene editing in human stem cells using zinc finger nucleases and integrase-defective lentiviral vector delivery. *Nat Biotechnol,* 25**,** 1298-306.

LOUCH, W. E., KOIVUMAKI, J. T. & TAVI, P. 2015. Calcium signalling in developing cardiomyocytes: implications for model systems and disease. *J Physiol,* 593**,** 1047-63.

LOWEY, S. 2002. Functional Consequences of Mutations in the Myosin Heavy Chain at Sites Implicated in Familial Hypertrophic Cardiomyopathy. *Trends in Cardiovascular Medicine,* 12**,** 348-354.

LU, H. R., HORTIGON-VINAGRE, M. P., ZAMORA, V., KOPLJAR, I., DE BONDT, A., GALLACHER, D. J. & SMITH, G. 2017. Application of optical action potentials in human induced pluripotent stem cells-derived cardiomyocytes to predict drug-induced cardiac arrhythmias. *J Pharmacol Toxicol Methods,* 87**,** 53-67.

LU, H. R., WHITTAKER, R., PRICE, J. H., VEGA, R., PFEIFFER, E. R., CERIGNOLI, F., TOWART, R. & GALLACHER, D. J. 2015. High Throughput Measurement of Ca++ Dynamics in Human Stem Cell-Derived Cardiomyocytes by Kinetic Image Cytometery: A Cardiac Risk Assessment Characterization Using a Large Panel of Cardioactive and Inactive Compounds. *Toxicol Sci,* 148**,** 503-16.

LUO, Y., LIU, C., CERBINI, T., SAN, H., LIN, Y., CHEN, G., RAO, M. S. & ZOU, J. 2014. Stable enhanced green fluorescent protein expression after differentiation and transplantation of reporter human induced pluripotent stem cells generated by AAVS1 transcription activator-like effector nucleases. *Stem Cells Transl Med,* 3**,** 821-35.

LYONS, G. E., SCHIAFFINO, S., SASSOON, D., BARTON, P. & BUCKINGHAM, M. 1990. Developmental regulation of myosin gene expression in mouse cardiac muscle. *J Cell Biol,* 111**,** 2427-36.

MACARTHUR, C. C., XUE, H., VAN HOOF, D., LIEU, P. T., DUDAS, M., FONTES, A., SWISTOWSKI, A., TOUBOUL, T., SEERKE, R., LAURENT, L. C., LORING, J. F., GERMAN, M. S., ZENG, X., RAO, M. S., LAKSHMIPATHY, U., CHESNUT, J. D. & LIU, Y. 2012. Chromatin insulator elements block transgene silencing in engineered human embryonic stem cell lines at a defined chromosome 13 locus. *Stem Cells Dev,* 21**,** 191-205.

MACDONNELL, S. M., WEISSER-THOMAS, J., KUBO, H., HANSCOME, M., LIU, Q., JALEEL, N., BERRETTA, R., CHEN, X., BROWN, J. H., SABRI, A. K., MOLKENTIN, J. D. & HOUSER, S. R. 2009. CaMKII negatively regulates calcineurin-NFAT signaling in cardiac myocytes. *Circ Res,* 105**,** 316-25.

MACLENNAN, D. H. & CHEN, S. R. W. 2009. Store overload-induced Ca(2+) release as a triggering mechanism for CPVT and MH episodes caused by mutations in RYR and CASQ genes. *J Physiol,* 587**,** 3113-5.

MACLENNAN, D. H. & KRANIAS, E. G. 2003. Phospholamban: a crucial regulator of cardiac contractility. *Nat Rev Mol Cell Biol,* 4**,** 566-77.

MADAMANCHI, A. 2007. Beta-adrenergic receptor signaling in cardiac function and heart failure. *Mcgill J Med,* 10**,** 99-104.

MADDAH, M., HEIDMANN, J. D., MANDEGAR, M. A., WALKER, C. D., BOLOUKI, S., CONKLIN, B. R. & LOEWKE, K. E. 2015. A non-invasive platform for functional

characterization of stem-cell-derived cardiomyocytes with applications in cardiotoxicity testing. *Stem Cell Reports,* 4**,** 621-31.

MAEDER, M. L., THIBODEAU-BEGANNY, S., OSIAK, A., WRIGHT, D. A., ANTHONY, R. M., EICHTINGER, M., JIANG, T., FOLEY, J. E., WINFREY, R. J., TOWNSEND, J. A., UNGER-WALLACE, E., SANDER, J. D., MULLER-LERCH, F., FU, F., PEARLBERG, J., GOBEL, C., DASSIE, J. P., PRUETT-MILLER, S. M., PORTEUS, M. H., SGROI, D. C., IAFRATE, A. J., DOBBS, D., MCCRAY, P. B., JR., CATHOMEN, T., VOYTAS, D. F. & JOUNG, J. K. 2008. Rapid "open-source" engineering of customized zinc-finger nucleases for highly efficient gene modification. *Mol Cell,* 31**,** 294-301.

MAHER, R. L., BRANAGAN, A. M. & MORRICAL, S. W. 2011. Coordination of DNA Replication and Recombination Activities in the Maintenance of Genome Stability. *Journal of cellular biochemistry,* 112**,** 2672-2682.

MALI, P., YANG, L., ESVELT, K. M., AACH, J., GUELL, M., DICARLO, J. E., NORVILLE, J. E. & CHURCH, G. M. 2013. RNA-guided human genome engineering via Cas9. *Science,* 339**,** 823-6.

MANK, M. & GRIESBECK, O. 2008. Genetically Encoded Calcium Indicators. *Chemical Reviews,* 108**,** 1550-1564.

MANK, M., REIFF, D. F., HEIM, N., FRIEDRICH, M. W., BORST, A. & GRIESBECK, O. 2006. A FRET-based calcium biosensor with fast signal kinetics and high fluorescence change. *Biophys J,* 90**,** 1790-6.

MAO, Z., BOZZELLA, M., SELUANOV, A. & GORBUNOVA, V. 2008. Comparison of nonhomologous end joining and homologous recombination in human cells. *DNA Repair (Amst),* 7**,** 1765-71.

MARIAN, A. J. & BRAUNWALD, E. 2017. Hypertrophic Cardiomyopathy: Genetics, Pathogenesis, Clinical Manifestations, Diagnosis, and Therapy. *Circ Res,* 121**,** 749-770.

MARON, B. J. & MARON, M. S. 2013. Hypertrophic cardiomyopathy. *Lancet,* 381**,** 242-55.

MARON, B. J., MARON, M. S. & SEMSARIAN, C. 2012. Genetics of Hypertrophic Cardiomyopathy After 20 Years: Clinical Perspectives. *Journal of the American College of Cardiology,* 60**,** 705-715.

MARON, B. J., YACOUB, M. & DEARANI, J. A. 2011a. Controversies in cardiovascular medicine. Benefits of surgery in obstructive hypertrophic cardiomyopathy: bring septal myectomy back for European patients. *Eur Heart J,* 32**,** 1055-8.

MARON, B. J., YEATES, L. & SEMSARIAN, C. 2011b. Clinical challenges of genotype positive (+)-phenotype negative (-) family members in hypertrophic cardiomyopathy. *Am J Cardiol,* 107**,** 604-8.

MARSIGLIA, J. D. C. & PEREIRA, A. C. 2014. Hypertrophic Cardiomyopathy: How do Mutations Lead to Disease? *Arquivos brasileiros de cardiologia,* 102**,** 295-304.

MARTIN, M. J., MUOTRI, A., GAGE, F. & VARKI, A. 2005. Human embryonic stem cells express an immunogenic nonhuman sialic acid. *Nat Med,* 11**,** 228-32.

MATSA, E., RAJAMOHAN, D., DICK, E., YOUNG, L., MELLOR, I., STANIFORTH, A. & DENNING, C. 2011. Drug evaluation in cardiomyocytes derived from human induced pluripotent stem cells carrying a long QT syndrome type 2 mutation. *European heart journal,* 32**,** 952-962.

MCCONNELL, T. H. & HULL, K. L. 2010. *Human Form, Human Function: Essentials of Anatomy & Physiology,* Lippincott Williams & Wilkins.

MELACINI, P., MARON, B. J., BOBBO, F., BASSO, C., TOKAJUK, B., ZUCCHETTO, M., THIENE, G. & ILICETO, S. 2007. Evidence that pharmacological strategies lack efficacy for the prevention of sudden death in hypertrophic cardiomyopathy. *Heart,* 93, 708-10.

MICHELS, M., OLIVOTTO, I., ASSELBERGS, F. W. & VAN DER VELDEN, J. 2017. Life-long tailoring of management for patients with hypertrophic cardiomyopathy: Awareness and decision-making in changing scenarios. *Netherlands Heart Journal,* 25, 186-199.

MILLER, J. C., HOLMES, M. C., WANG, J., GUSCHIN, D. Y., LEE, Y. L., RUPNIEWSKI, I., BEAUSEJOUR, C. M., WAITE, A. J., WANG, N. S., KIM, K. A., GREGORY, P. D., PABO, C. O. & REBAR, E. J. 2007. An improved zinc-finger nuclease architecture for highly specific genome editing. *Nat Biotechnol,* 25, 778-85.

MILLER, J. C., TAN, S., QIAO, G., BARLOW, K. A., WANG, J., XIA, D. F., MENG, X., PASCHON, D. E., LEUNG, E., HINKLEY, S. J., DULAY, G. P., HUA, K. L., ANKOUDINOVA, I., COST, G. J., URNOV, F. D., ZHANG, H. S., HOLMES, M. C., ZHANG, L., GREGORY, P. D. & REBAR, E. J. 2011. A TALE nuclease architecture for efficient genome editing. *Nat Biotechnol,* 29, 143-8.

MIYAWAKI, A. 2005. Innovations in the imaging of brain functions using fluorescent proteins. *Neuron,* 48, 189-99.

MIYAWAKI, A., GRIESBECK, O., HEIM, R. & TSIEN, R. Y. 1999. Dynamic and quantitative Ca2+ measurements using improved cameleons. *Proc Natl Acad Sci U S A,* 96, 2135-40.

MIYAWAKI, A., LLOPIS, J., HEIM, R., MCCAFFERY, J. M., ADAMS, J. A., IKURA, M. & TSIEN, R. Y. 1997. Fluorescent indicators for Ca2+ based on green fluorescent proteins and calmodulin. *Nature,* 388, 882-7.

MOGENSEN, J., PERROT, A., ANDERSEN, P. S., HAVNDRUP, O., KLAUSEN, I. C., CHRISTIANSEN, M., BROSS, P., EGEBLAD, H., BUNDGAARD, H., OSTERZIEL, K. J., HALTERN, G., LAPP, H., REINECKE, P., GREGERSEN, N. & BØRGLUM, A. D. 2004. Clinical and genetic characteristics of α cardiac actin gene mutations in hypertrophic cardiomyopathy. *Journal of Medical Genetics,* 41, e10-e10.

MOLKENTIN, J. D. 2004. Calcineurin-NFAT signaling regulates the cardiac hypertrophic response in coordination with the MAPKs. *Cardiovasc Res,* 63, 467-75.

MONSERRAT, L., HERMIDA-PRIETO, M., FERNANDEZ, X., RODRIGUEZ, I., DUMONT, C., CAZON, L., CUESTA, M. G., GONZALEZ-JUANATEY, C., PETEIRO, J., ALVAREZ, N., PENAS-LADO, M. & CASTRO-BEIRAS, A. 2007. Mutation in the alpha-cardiac actin gene associated with apical hypertrophic cardiomyopathy, left ventricular non-compaction, and septal defects. *Eur Heart J,* 28, 1953-61.

MOSCOU, M. J. & BOGDANOVE, A. J. 2009. A simple cipher governs DNA recognition by TAL effectors. *Science,* 326, 1501.

MOSQUEIRA, D., MANNHARDT, I., BHAGWAN, J. R., LIS-SLIMAK, K., KATILI, P., SCOTT, E., HASSAN, M., PRONDZYNSKI, M., HARMER, S. C., TINKER, A., SMITH, J. G. W., CARRIER, L., WILLIAMS, P. M., GAFFNEY, D., ESCHENHAGEN, T., HANSEN, A. & DENNING, C. 2018. CRISPR/Cas9 editing in human pluripotent stem cell-cardiomyocytes highlights arrhythmias, hypocontractility, and energy depletion as potential therapeutic targets for hypertrophic cardiomyopathy. *Eur Heart J.*

MULLER, M., BAMANN, C., BAMBERG, E. & KUHLBRANDT, W. 2011. Projection structure of channelrhodopsin-2 at 6 A resolution by electron crystallography. *J Mol Biol,* 414, 86-95.

MUSCHOL, M., DASGUPTA, B. R. & SALZBERG, B. M. 1999. Caffeine interaction with fluorescent calcium indicator dyes. *Biophys J,* 77, 577-86.

MUSSOLINO, C., MORBITZER, R., LUTGE, F., DANNEMANN, N., LAHAYE, T. & CATHOMEN, T. 2011. A novel TALE nuclease scaffold enables high genome editing activity in combination with low toxicity. *Nucleic Acids Res,* 39**,** 9283-93.

NAGAI, T., SAWANO, A., PARK, E. S. & MIYAWAKI, A. 2001. Circularly permuted green fluorescent proteins engineered to sense Ca2+. *Proc Natl Acad Sci U S A,* 98**,** 3197-202.

NAGEL, G., SZELLAS, T., HUHN, W., KATERIYA, S., ADEISHVILI, N., BERTHOLD, P., OLLIG, D., HEGEMANN, P. & BAMBERG, E. 2003. Channelrhodopsin-2, a directly light-gated cation-selective membrane channel. *Proc Natl Acad Sci U S A,* 100**,** 13940-5.

NAKAI, J., OHKURA, M. & IMOTO, K. 2001. A high signal-to-noise Ca2+ probe composed of a single green fluorescent protein. *Nat Biotech,* 19**,** 137-141.

NAPOLITANO, C. & ANTZELEVITCH, C. 2011. Phenotypical manifestations of mutations in the genes encoding subunits of the cardiac voltage-dependent L-type calcium channel. *Circ Res,* 108**,** 607-18.

NG, M., ROORDA, R. D., LIMA, S. Q., ZEMELMAN, B. V., MORCILLO, P. & MIESENBOCK, G. 2002. Transmission of olfactory information between three populations of neurons in the antennal lobe of the fly. *Neuron,* 36**,** 463-74.

NG, W. A., GRUPP, I. L., SUBRAMANIAM, A. & ROBBINS, J. 1991. Cardiac myosin heavy chain mRNA expression and myocardial function in the mouse heart. *Circ Res,* 68**,** 1742-50.

NIELSEN, J., MATZ, J., MITTOUX, A., POLCWIARTEK, C., STRUIJK, J. J., TOFT, E., KANTERS, J. K. & GRAFF, C. 2015. Cardiac effects of sertindole and quetiapine: analysis of ECGs from a randomized double-blind study in patients with schizophrenia. *Eur Neuropsychopharmacol,* 25**,** 303-11.

NISHIMURA, R. A., OMMEN, S. R. & TAJIK, A. J. 2003. Cardiology patient page. Hypertrophic cardiomyopathy: a patient perspective. *Circulation,* 108**,** e133-5.

NIWA, H., YAMAMURA, K. & MIYAZAKI, J. 1991. Efficient selection for high-expression transfectants with a novel eukaryotic vector. *Gene,* 108**,** 193-9.

OCEGUERA-YANEZ, F., KIM, S. I., MATSUMOTO, T., TAN, G. W., XIANG, L., HATANI, T., KONDO, T., IKEYA, M., YOSHIDA, Y., INOUE, H. & WOLTJEN, K. 2016. Engineering the AAVS1 locus for consistent and scalable transgene expression in human iPSCs and their differentiated derivatives. *Methods,* 101**,** 43-55.

OGATA, T., KOZUKA, T. & KANDA, T. 2003. Identification of an insulator in AAVS1, a preferred region for integration of adeno-associated virus DNA. *J Virol,* 77**,** 9000-7.

OHEIM, M., VAN 'T HOFF, M., FELTZ, A., ZAMALEEVA, A., MALLET, J. M. & COLLOT, M. 2014. New red-fluorescent calcium indicators for optogenetics, photoactivation and multi-color imaging. *Biochim Biophys Acta,* 1843**,** 2284-306.

OJALA, M., PRAJAPATI, C., POLONEN, R. P., RAJALA, K., PEKKANEN-MATTILA, M., RASKU, J., LARSSON, K. & AALTO-SETALA, K. 2016. Mutation-Specific Phenotypes in hiPSC-Derived Cardiomyocytes Carrying Either Myosin-Binding Protein C Or alpha-Tropomyosin Mutation for Hypertrophic Cardiomyopathy. *Stem Cells Int,* 2016**,** 1684792.

OKUDA, S., SUFU-SHIMIZU, Y., KATO, T., FUKUDA, M., NISHIMURA, S., ODA, T., KOBAYASHI, S., YAMAMOTO, T., MORIMOTO, S. & YANO, M. 2018. CaMKII-mediated phosphorylation of RyR2 plays a crucial role in aberrant Ca(2+)

release as an arrhythmogenic substrate in cardiac troponin T-related familial hypertrophic cardiomyopathy. *Biochem Biophys Res Commun,* 496**,** 1250-1256.

OLSON, T. M., DOAN, T. P., KISHIMOTO, N. Y., WHITBY, F. G., ACKERMAN, M. J. & FANANAPAZIR, L. 2000. Inherited and de novo mutations in the cardiac actin gene cause hypertrophic cardiomyopathy. *J Mol Cell Cardiol,* 32**,** 1687-94.

OO, Y. W., GOMEZ-HURTADO, N., WALWEEL, K., VAN HELDEN, D. F., IMTIAZ, M. S., KNOLLMANN, B. C. & LAVER, D. R. 2015. Essential Role of Calmodulin in RyR Inhibition by Dantrolene. *Mol Pharmacol,* 88**,** 57-63.

ORDOVAS, L., BOON, R., PISTONI, M., CHEN, Y., WOLFS, E., GUO, W., SAMBATHKUMAR, R., BOBIS-WOZOWICZ, S., HELSEN, N., VANHOVE, J., BERCKMANS, P., CAI, Q., VANUYTSEL, K., EGGERMONT, K., VANSLEMBROUCK, V., SCHMIDT, B. Z., RAITANO, S., VAN DEN BOSCH, L., NAHMIAS, Y., CATHOMEN, T., STRUYS, T. & VERFAILLIE, C. M. 2015. Efficient Recombinase-Mediated Cassette Exchange in hPSCs to Study the Hepatocyte Lineage Reveals AAVS1 Locus-Mediated Transgene Inhibition. *Stem Cell Reports,* 5**,** 918-31.

ÖSTMAN-SMITH, I. 2014. Beta-Blockers in Pediatric Hypertrophic Cardiomyopathies. *Rev Recent Clin Trials,* 9**,** 82-5.

PALMER, B. M., FISHBAUGHER, D. E., SCHMITT, J. P., WANG, Y., ALPERT, N. R., SEIDMAN, C. E., SEIDMAN, J. G., VANBUREN, P. & MAUGHAN, D. W. 2004. Differential cross-bridge kinetics of FHC myosin mutations R403Q and R453C in heterozygous mouse myocardium. *Am J Physiol Heart Circ Physiol,* 287**,** H91-9.

PAPAPETROU, E. P. & SCHAMBACH, A. 2016. Gene Insertion Into Genomic Safe Harbors for Human Gene Therapy. *Mol Ther,* 24**,** 678-84.

PAREDES, R. M., ETZLER, J. C., WATTS, L. T., ZHENG, W. & LECHLEITER, J. D. 2008. Chemical calcium indicators. *Methods,* 46**,** 143-51.

PARIKH, S. S., BLACKWELL, D. J., GOMEZ-HURTADO, N., FRISK, M., WANG, L., KIM, K., DAHL, C. P., FIANE, A., TONNESSEN, T., KRYSHTAL, D. O., LOUCH, W. E. & KNOLLMANN, B. C. 2017. Thyroid and Glucocorticoid Hormones Promote Functional T-Tubule Development in Human-Induced Pluripotent Stem Cell-Derived Cardiomyocytes. *Circ Res,* 121**,** 1323-1330.

PASSIER, R., ZENG, H., FREY, N., NAYA, F. J., NICOL, R. L., MCKINSEY, T. A., OVERBEEK, P., RICHARDSON, J. A., GRANT, S. R. & OLSON, E. N. 2000. CaM kinase signaling induces cardiac hypertrophy and activates the MEF2 transcription factor in vivo. *J Clin Invest,* 105**,** 1395-406.

PAVLOVA, S. V., PEROVSKII, P. P., CHEPELEVA, E. V., MALAKHOVA, A. A., DEMENT'EVA, E. V., POKUSHALOV, E. A., SUKHIKH, G. T. & ZAKIYAN, S. M. 2013. Characteristics of cardiac cell cultures derived from human myocardial explants. *Bull Exp Biol Med,* 156**,** 127-35.

PEI, Y., SIERRA, G., SIVAPATHAM, R., SWISTOWSKI, A., RAO, M. S. & ZENG, X. 2015. A platform for rapid generation of single and multiplexed reporters in human iPSC lines. *Sci Rep,* 5**,** 9205.

PENG, R., LIN, G. & LI, J. 2016. Potential pitfalls of CRISPR/Cas9-mediated genome editing. *Febs j,* 283**,** 1218-31.

PEREZ, E. E., WANG, J., MILLER, J. C., JOUVENOT, Y., KIM, K. A., LIU, O., WANG, N., LEE, G., BARTSEVICH, V. V., LEE, Y.-L., GUSCHIN, D. Y., RUPNIEWSKI, I., WAITE, A. J., CARPENITO, C., CARROLL, R. G., S ORANGE, J., URNOV, F. D., REBAR, E. J., ANDO, D., GREGORY, P. D., RILEY, J. L., HOLMES, M. C. & JUNE, C. H. 2008. Establishment of HIV-1 resistance in CD4+ T cells by genome editing using zinc-finger nucleases. *Nature Biotechnology,* 26**,** 808.

PEREZ KOLDENKOVA, V. & NAGAI, T. 2013. Genetically encoded Ca(2+) indicators: properties and evaluation. *Biochim Biophys Acta,* 1833**,** 1787-97.

PERIASAMY, M. & KALYANASUNDARAM, A. 2007. SERCA pump isoforms: their role in calcium transport and disease. *Muscle Nerve,* 35**,** 430-42.

PINNELL, J., TURNER, S. & HOWELL, S. 2007. Cardiac muscle physiology. *Continuing Education in Anaesthesia Critical Care & Pain,* 7**,** 85-88.

POINTON, A., HARMER, A. R., DALE, I. L., ABI-GERGES, N., BOWES, J., POLLARD, C. & GARSIDE, H. 2015. Assessment of cardiomyocyte contraction in human-induced pluripotent stem cell-derived cardiomyocytes. *Toxicol Sci,* 144**,** 227-37.

POLOGRUTO, T. A., YASUDA, R. & SVOBODA, K. 2004. Monitoring neural activity and [Ca2+] with genetically encoded Ca2+ indicators. *J Neurosci,* 24**,** 9572-9.

PRATYUSH, D. D., TIWARI, S., KUMAR, A. & SINGH, S. K. 2012. A new approach to touch down method using betaine as co-solvent for increased specificity and intensity of GC rich gene amplification. *Gene,* 497**,** 269-72.

PROTZE, S. I., LIU, J., NUSSINOVITCH, U., OHANA, L., BACKX, P. H., GEPSTEIN, L. & KELLER, G. M. 2017. Sinoatrial node cardiomyocytes derived from human pluripotent cells function as a biological pacemaker. *Nat Biotechnol,* 35**,** 56-68.

QUIGLEY, E. M. M. 2011. Cisapride: What can we learn from the rise and fall of a prokinetic? *Journal of Digestive Diseases,* 12**,** 147-156.

RAJALA, K., LINDROOS, B., HUSSEIN, S. M., LAPPALAINEN, R. S., PEKKANEN-MATTILA, M., INZUNZA, J., ROZELL, B., MIETTINEN, S., NARKILAHTI, S., KERKELA, E., AALTO-SETALA, K., OTONKOSKI, T., SUURONEN, R., HOVATTA, O. & SKOTTMAN, H. 2010. A defined and xeno-free culture method enabling the establishment of clinical-grade human embryonic, induced pluripotent and adipose stem cells. *PLoS One,* 5**,** e10246.

RAMIREZ, C. L., FOLEY, J. E., WRIGHT, D. A., MULLER-LERCH, F., RAHMAN, S. H., CORNU, T. I., WINFREY, R. J., SANDER, J. D., FU, F., TOWNSEND, J. A., CATHOMEN, T., VOYTAS, D. F. & JOUNG, J. K. 2008. Unexpected failure rates for modular assembly of engineered zinc fingers. *Nat Methods,* 5**,** 374-5.

RAN, F. A., CONG, L., YAN, W. X., SCOTT, D. A., GOOTENBERG, J. S., KRIZ, A. J., ZETSCHE, B., SHALEM, O., WU, X., MAKAROVA, K. S., KOONIN, E. V., SHARP, P. A. & ZHANG, F. 2015. In vivo genome editing using Staphylococcus aureus Cas9. *Nature,* 520**,** 186.

RAN, F. A., HSU, P. D., LIN, C. Y., GOOTENBERG, J. S., KONERMANN, S., TREVINO, A. E., SCOTT, D. A., INOUE, A., MATOBA, S., ZHANG, Y. & ZHANG, F. 2013a. Double nicking by RNA-guided CRISPR Cas9 for enhanced genome editing specificity. *Cell,* 154**,** 1380-9.

RAN, F. A., HSU, P. D., WRIGHT, J., AGARWALA, V., SCOTT, D. A. & ZHANG, F. 2013b. Genome engineering using the CRISPR-Cas9 system. *Nat Protoc,* 8**,** 2281-2308.

RAO, A., LUO, C. & HOGAN, P. G. 1997. TRANSCRIPTION FACTORS OF THE NFAT FAMILY:Regulation and Function. *Annual Review of Immunology,* 15**,** 707-747.

RAPTI, K., STILLITANO, F., KARAKIKES, I., NONNENMACHER, M., WEBER, T., HULOT, J. S. & HAJJAR, R. J. 2015. Effectiveness of gene delivery systems for pluripotent and differentiated cells. *Mol Ther Methods Clin Dev,* 2**,** 14067.

RAYNER-HARTLEY, E. & SEDLAK, T. 2016. Ranolazine: A Contemporary Review. *J Am Heart Assoc,* 5**,** e003196.

REISER, P. J., PORTMAN, M. A., NING, X. H. & SCHOMISCH MORAVEC, C. 2001. Human cardiac myosin heavy chain isoforms in fetal and failing adult atria and ventricles. *Am J Physiol Heart Circ Physiol,* 280**,** H1814-20.

REN, X., HENSLEY, N., BRADY, M. B. & GAO, W. D. 2017. The Genetic and Molecular Bases for Hypertrophic Cardiomyopathy: The Role for Calcium Sensitization. *J Cardiothorac Vasc Anesth*.

RICHARD, P., CHARRON, P., CARRIER, L., LEDEUIL, C., CHEAV, T., PICHEREAU, C., BENAICHE, A., ISNARD, R., DUBOURG, O., BURBAN, M., GUEFFET, J. P., MILLAIRE, A., DESNOS, M., SCHWARTZ, K., HAINQUE, B. & KOMAJDA, M. 2003. Hypertrophic cardiomyopathy: distribution of disease genes, spectrum of mutations, and implications for a molecular diagnosis strategy. *Circulation,* 107**,** 2227-32.

ROGERS, E. F., KONIUSZY, F. R. & ET AL. 1948. Plant insecticides; ryanodine, a new alkaloid from Ryania speciosa Vahl. *J Am Chem Soc,* 70**,** 3086-8.

ROMA-RODRIGUES, C. & FERNANDES, A. R. 2014. Genetics of hypertrophic cardiomyopathy: advances and pitfalls in molecular diagnosis and therapy. *The Application of Clinical Genetics,* 7**,** 195-208.

ROSE, T., GOLTSTEIN, P. M., PORTUGUES, R. & GRIESBECK, O. 2014. Putting a finishing touch on GECIs. *Frontiers in Molecular Neuroscience,* 7**,** 88.

ROTH, G. A., JOHNSON, C., ABAJOBIR, A., ABD-ALLAH, F., ABERA, S. F., ABYU, G., AHMED, M., AKSUT, B., ALAM, T., ALAM, K., ALLA, F., ALVIS-GUZMAN, N., AMROCK, S., ANSARI, H., ÄRNLÖV, J., ASAYESH, H., ATEY, T. M., AVILA-BURGOS, L., AWASTHI, A., BANERJEE, A., BARAC, A., BÄRNIGHAUSEN, T., BARREGARD, L., BEDI, N., BELAY KETEMA, E., BENNETT, D., BERHE, G., BHUTTA, Z., BITEW, S., CARAPETIS, J., CARRERO, J. J., MALTA, D. C., CASTAÑEDA-ORJUELA, C. A., CASTILLO-RIVAS, J., CATALÁ-LÓPEZ, F., CHOI, J.-Y., CHRISTENSEN, H., CIRILLO, M., COOPER, L., CRIQUI, M., CUNDIFF, D., DAMASCENO, A., DANDONA, L., DANDONA, R., DAVLETOV, K., DHARMARATNE, S., DORAIRAJ, P., DUBEY, M., EHRENKRANZ, R., EL SAYED ZAKI, M., FARAON, E. J. A., ESTEGHAMATI, A., FARID, T., FARVID, M., FEIGIN, V., DING, E. L., FOWKES, G., GEBREHIWOT, T., GILLUM, R., GOLD, A., GONA, P., GUPTA, R., HABTEWOLD, T. D., HAFEZI-NEJAD, N., HAILU, T., HAILU, G. B., HANKEY, G., HASSEN, H. Y., ABATE, K. H., HAVMOELLER, R., HAY, S. I., HORINO, M., HOTEZ, P. J., JACOBSEN, K., JAMES, S., JAVANBAKHT, M., JEEMON, P., JOHN, D., JONAS, J., KALKONDE, Y., KARIMKHANI, C., KASAEIAN, A., KHADER, Y., KHAN, A., KHANG, Y.-H., KHERA, S., KHOJA, A. T., KHUBCHANDANI, J., KIM, D., KOLTE, D., KOSEN, S., KROHN, K. J., KUMAR, G. A., KWAN, G. F., LAL, D. K., LARSSON, A., LINN, S., LOPEZ, A., LOTUFO, P. A., EL RAZEK, H. M. A., et al. 2017. Global, Regional, and National Burden of Cardiovascular Diseases for 10 Causes, 1990 to 2015. *Journal of the American College of Cardiology,* 70**,** 1-25.

ROUSSEAU, E. & MEISSNER, G. 1989. Single cardiac sarcoplasmic reticulum Ca2+-release channel: activation by caffeine. *Am J Physiol,* 256**,** H328-33.

RUBENSTEIN, P. A. & MARTIN, D. J. 1983. NH2-terminal processing of Drosophila melanogaster actin. Sequential removal of two amino acids. *J Biol Chem,* 258**,** 11354-60.

SADAYAPPAN, S. & DE TOMBE, P. P. 2012. Cardiac myosin binding protein-C: redefining its structure and function. *Biophysical Reviews,* 4**,** 93-106.

SADELAIN, M., PAPAPETROU, E. P. & BUSHMAN, F. D. 2011. Safe harbours for the integration of new DNA in the human genome. *Nat Rev Cancer,* 12**,** 51-8.

SAMULSKI, R. J., ZHU, X., XIAO, X., BROOK, J. D., HOUSMAN, D. E., EPSTEIN, N. & HUNTER, L. A. 1991. Targeted integration of adeno-associated virus (AAV) into human chromosome 19. *Embo j,* 10**,** 3941-50.

SANDER, J. D. & JOUNG, J. K. 2014. CRISPR-Cas systems for editing, regulating and targeting genomes. *Nat Biotechnol,* 32**,** 347-55.

SATIN, J., ITZHAKI, I., RAPOPORT, S., SCHRODER, E. A., IZU, L., ARBEL, G., BEYAR, R., BALKE, C. W., SCHILLER, J. & GEPSTEIN, L. 2008. Calcium handling in human embryonic stem cell-derived cardiomyocytes. *Stem Cells,* 26**,** 1961-72.

SATIN, J., KEHAT, I., CASPI, O., HUBER, I., ARBEL, G., ITZHAKI, I., MAGYAR, J., SCHRODER, E. A., PERLMAN, I. & GEPSTEIN, L. 2004. Mechanism of spontaneous excitability in human embryonic stem cell derived cardiomyocytes. *J Physiol,* 559**,** 479-96.

SCHULTZ, C., VAJANAPHANICH, M., HAROOTUNIAN, A. T., SAMMAK, P. J., BARRETT, K. E. & TSIEN, R. Y. 1993. Acetoxymethyl esters of phosphates, enhancement of the permeability and potency of cAMP. *J Biol Chem,* 268**,** 6316-22.

SEN-CHOWDHRY, S., JACOBY, D., MOON, J. C. & MCKENNA, W. J. 2016. Update on hypertrophic cardiomyopathy and a guide to the guidelines. *Nature Reviews Cardiology,* 13**,** 651.

SHALEM, O., SANJANA, N. E., HARTENIAN, E., SHI, X., SCOTT, D. A., MIKKELSON, T., HECKL, D., EBERT, B. L., ROOT, D. E., DOENCH, J. G. & ZHANG, F. 2014. Genome-scale CRISPR-Cas9 knockout screening in human cells. *Science,* 343**,** 84-87.

SHAN, Q., WANG, Y., LI, J., ZHANG, Y., CHEN, K., LIANG, Z., ZHANG, K., LIU, J., XI, J. J., QIU, J. L. & GAO, C. 2013. Targeted genome modification of crop plants using a CRISPR-Cas system. *Nat Biotechnol,* 31**,** 686-8.

SHANG, W., LU, F., SUN, T., XU, J., LI, L.-L., WANG, Y., WANG, G., CHEN, L., WANG, X., CANNELL, M. B., WANG, S.-Q. & CHENG, H. 2014. Imaging Ca2+ Nanosparks in Heart With a New Targeted Biosensor. *Circulation Research,* 114**,** 412-420.

SHEN, Y., DANA, H., ABDELFATTAH, A. S., PATEL, R., SHEA, J., MOLINA, R. S., RAWAL, B., RANCIC, V., CHANG, Y. F., WU, L., CHEN, Y., QIAN, Y., WIENS, M. D., HAMBLETON, N., BALLANYI, K., HUGHES, T. E., DROBIZHEV, M., KIM, D. S., KOYAMA, M., SCHREITER, E. R. & CAMPBELL, R. E. 2018. A genetically encoded Ca(2+) indicator based on circularly permutated sea anemone red fluorescent protein eqFP578. *BMC Biol,* 16**,** 9.

SHIBA, Y., FERNANDES, S., ZHU, W. Z., FILICE, D., MUSKHELI, V., KIM, J., PALPANT, N. J., GANTZ, J., MOYES, K. W., REINECKE, H., VAN BIBER, B., DARDAS, T., MIGNONE, J. L., IZAWA, A., HANNA, R., VISWANATHAN, M., GOLD, J. D., KOTLIKOFF, M. I., SARVAZYAN, N., KAY, M. W., MURRY, C. E. & LAFLAMME, M. A. 2012. Human ES-cell-derived cardiomyocytes electrically couple and suppress arrhythmias in injured hearts. *Nature,* 489**,** 322-5.

SHIGETOMI, E., BUSHONG, E. A., HAUSTEIN, M. D., TONG, X., JACKSON-WEAVER, O., KRACUN, S., XU, J., SOFRONIEW, M. V., ELLISMAN, M. H. & KHAKH, B. S. 2013. Imaging calcium microdomains within entire astrocyte territories and endfeet with GCaMPs expressed using adeno-associated viruses. *J Gen Physiol,* 141**,** 633-47.

SHIMADA, Y. J., PASSERI, J. J., BAGGISH, A. L., O'CALLAGHAN, C., LOWRY, P. A., YANNEKIS, G., ABBARA, S., GHOSHHAJRA, B. B., ROTHMAN, R. D., HO, C. Y., JANUZZI, J. L., SEIDMAN, C. E. & FIFER, M. A. 2013. Effects of losartan on left ventricular hypertrophy and fibrosis in patients with nonobstructive hypertrophic cardiomyopathy. *JACC Heart Fail,* 1**,** 480-7.

SIRENKO, O., CRITTENDEN, C., CALLAMARAS, N., HESLEY, J., CHEN, Y. W., FUNES, C., RUSYN, I., ANSON, B. & CROMWELL, E. F. 2013. Multiparameter in vitro assessment of compound effects on cardiomyocyte physiology using iPSC cells. *J Biomol Screen,* 18**,** 39-53.

SNIR, M., KEHAT, I., GEPSTEIN, A., COLEMAN, R., ITSKOVITZ-ELDOR, J., LIVNE, E. & GEPSTEIN, L. 2003. Assessment of the ultrastructural and proliferative properties of human embryonic stem cell-derived cardiomyocytes. *Am J Physiol Heart Circ Physiol,* 285**,** H2355-63.

SOMMESE, R. F., SUNG, J., NAG, S., SUTTON, S., DEACON, J. C., CHOE, E., LEINWAND, L. A., RUPPEL, K. & SPUDICH, J. A. 2013. Molecular consequences of the R453C hypertrophic cardiomyopathy mutation on human ß-cardiac myosin motor function. *Proceedings of the National Academy of Sciences,* 110**,** 12607-12612.

SONG, W., DYER, E., STUCKEY, D. J., COPELAND, O., LEUNG, M. C., BAYLISS, C., MESSER, A., WILKINSON, R., TREMOLEDA, J. L., SCHNEIDER, M. D., HARDING, S. E., REDWOOD, C. S., CLARKE, K., NOWAK, K., MONSERRAT, L., WELLS, D. & MARSTON, S. B. 2011. Molecular mechanism of the E99K mutation in cardiac actin (ACTC Gene) that causes apical hypertrophy in man and mouse. *J Biol Chem,* 286**,** 27582-93.

SORIANO, P. 1999. Generalized lacZ expression with the ROSA26 Cre reporter strain. *Nat Genet,* 21**,** 70-1.

SPATER, D., HANSSON, E. M., ZANGI, L. & CHIEN, K. R. 2014. How to make a cardiomyocyte. *Development,* 141**,** 4418-31.

SPOLADORE, R., MARON, M. S., D'AMATO, R., CAMICI, P. G. & OLIVOTTO, I. 2012. Pharmacological treatment options for hypertrophic cardiomyopathy: high time for evidence. *European Heart Journal,* 33**,** 1724-1733.

STAUFFER, B. L., WESTBY, C. M. & DESOUZA, C. A. 2008. Endothelin-1, aging and hypertension. *Current opinion in cardiology,* 23**,** 350-355.

STERN, J. A., MARKOVA, S., UEDA, Y., KIM, J. B., PASCOE, P. J., EVANCHIK, M. J., GREEN, E. M. & HARRIS, S. P. 2016. A Small Molecule Inhibitor of Sarcomere Contractility Acutely Relieves Left Ventricular Outflow Tract Obstruction in Feline Hypertrophic Cardiomyopathy. *PLoS One,* 11**,** e0168407.

STILLITANO, F., TURNBULL, I. C., KARAKIKES, I., NONNENMACHER, M., BACKERIS, P., HULOT, J. S., KRANIAS, E. G., HAJJAR, R. J. & COSTA, K. D. 2016. Genomic correction of familial cardiomyopathy in human engineered cardiac tissues. *Eur Heart J,* 37**,** 3282-3284.

STRIESSNIG, J., ORTNER, N. J. & PINGGERA, A. 2015. Pharmacology of L-type Calcium Channels: Novel Drugs for Old Targets? *Curr Mol Pharmacol,* 8**,** 110-22.

STRIESSNIG, J., PINGGERA, A., KAUR, G., BOCK, G. & TULUC, P. 2014. L-type Ca(2+) channels in heart and brain. *Wiley Interdiscip Rev Membr Transp Signal,* 3**,** 15-38.

SUZUKI, J., KANEMARU, K. & IINO, M. 2016. Genetically Encoded Fluorescent Indicators for Organellar Calcium Imaging. *Biophysical Journal,* 111**,** 1119-1131.

SUZUKI, J., KANEMARU, K., ISHII, K., OHKURA, M., OKUBO, Y. & IINO, M. 2014. Imaging intraorganellar Ca2+ at subcellular resolution using CEPIA. *Nat Commun,* 5**,** 4153.

TAKAHASHI, K., TANABE, K., OHNUKI, M., NARITA, M., ICHISAKA, T., TOMODA, K. & YAMANAKA, S. 2007. Induction of Pluripotent Stem Cells from Adult Human Fibroblasts by Defined Factors. *Cell,* 131**,** 861-872.

TALBERT, D. R., DOHERTY, K. R., TRUSK, P. B., MORAN, D. M., SHELL, S. A. & BACUS, S. 2015. A Multi-parameter In Vitro Screen in Human Stem Cell-Derived Cardiomyocytes Identifies Ponatinib-Induced Structural and Functional Cardiac Toxicity. *Toxicological Sciences,* 143**,** 147-155.

TALLINI, Y. N., OHKURA, M., CHOI, B. R., JI, G., IMOTO, K., DORAN, R., LEE, J., PLAN, P., WILSON, J., XIN, H. B., SANBE, A., GULICK, J., MATHAI, J., ROBBINS, J., SALAMA, G., NAKAI, J. & KOTLIKOFF, M. I. 2006. Imaging cellular signals in the heart in vivo: Cardiac expression of the high-signal Ca2+ indicator GCaMP2. *Proc Natl Acad Sci U S A,* 103**,** 4753-8.

TANAKA, A., YUASA, S., MEARINI, G., EGASHIRA, T., SEKI, T., KODAIRA, M., KUSUMOTO, D., KURODA, Y., OKATA, S., SUZUKI, T., INOHARA, T., ARIMURA, T., MAKINO, S., KIMURA, K., KIMURA, A., FURUKAWA, T., CARRIER, L., NODE, K. & FUKUDA, K. 2014. Endothelin-1 induces myofibrillar disarray and contractile vector variability in hypertrophic cardiomyopathy-induced pluripotent stem cell-derived cardiomyocytes. *J Am Heart Assoc,* 3**,** e001263.

TENDERA, M., WYCISK, A., SCHNEEWEISS, A., POLONSKI, L. & WODNIECKI, J. 1993. Effect of sotalol on arrhythmias and exercise tolerance in patients with hypertrophic cardiomyopathy. *Cardiology,* 82**,** 335-42.

TERRACCIANO, C. M., PHILIPSON, K. D. & MACLEOD, K. T. 2001. Overexpression of the Na(+)/Ca(2+) exchanger and inhibition of the sarcoplasmic reticulum Ca(2+)-ATPase in ventricular myocytes from transgenic mice. *Cardiovasc Res,* 49**,** 38-47.

THOMAS, D., TOVEY, S. C., COLLINS, T. J., BOOTMAN, M. D., BERRIDGE, M. J. & LIPP, P. 2000. A comparison of fluorescent Ca2+ indicator properties and their use in measuring elementary and global Ca2+ signals. *Cell Calcium,* 28**,** 213-23.

THOMPSON, K., DOCKERY, P. & HOROBIN, R. W. 2012. Predicting and avoiding subcellular compartmentalization artifacts arising from acetoxymethyl ester calcium imaging probes. The case of fluo-3 AM and a general account of the phenomenon including a problem avoidance chart. *Biotech Histochem,* 87**,** 468-83.

THOMSON, J. A., ITSKOVITZ-ELDOR, J., SHAPIRO, S. S., WAKNITZ, M. A., SWIERGIEL, J. J., MARSHALL, V. S. & JONES, J. M. 1998. Embryonic Stem Cell Lines Derived from Human Blastocysts. *Science,* 282**,** 1145-1147.

TIBURCY, M., HUDSON, J. E., BALFANZ, P., SCHLICK, S., MEYER, T., CHANG LIAO, M. L., LEVENT, E., RAAD, F., ZEIDLER, S., WINGENDER, E., RIEGLER, J., WANG, M., GOLD, J. D., KEHAT, I., WETTWER, E., RAVENS, U., DIERICKX, P., VAN LAAKE, L. W., GOUMANS, M. J., KHADJEH, S., TOISCHER, K., HASENFUSS, G., COUTURE, L. A., UNGER, A., LINKE, W. A., ARAKI, T., NEEL, B., KELLER, G., GEPSTEIN, L., WU, J. C. & ZIMMERMANN, W. H. 2017. Defined Engineered Human Myocardium With Advanced Maturation for Applications in Heart Failure Modeling and Repair. *Circulation,* 135**,** 1832-1847.

TSIEN, R. Y. & MIYAWAKI, A. 1998. Seeing the machinery of live cells. *Science,* 280**,** 1954-5.

URNOV, F. D., MILLER, J. C., LEE, Y. L., BEAUSEJOUR, C. M., ROCK, J. M., AUGUSTUS, S., JAMIESON, A. C., PORTEUS, M. H., GREGORY, P. D. & HOLMES, M. C. 2005. Highly efficient endogenous human gene correction using designed zinc-finger nucleases. *Nature,* 435**,** 646-51.

VAN DEN BERG, C. W., ELLIOTT, D. A., BRAAM, S. R., MUMMERY, C. L. & DAVIS, R. P. 2016. Differentiation of Human Pluripotent Stem Cells to Cardiomyocytes Under Defined Conditions. *Methods Mol Biol,* 1353**,** 163-80.

VAN DER VELDEN, J., HO, C. Y., TARDIFF, J. C., OLIVOTTO, I., KNOLLMANN, B. C. & CARRIER, L. 2015. Research priorities in sarcomeric cardiomyopathies. *Cardiovasc Res,* 105, 449-56.

VAN DER WERF, C. & WILDE, A. A. 2013. Catecholaminergic polymorphic ventricular tachycardia: from bench to bedside. *Heart,* 99, 497-504.

VAN RENSBURG, R., BEYER, I., YAO, X. Y., WANG, H., DENISENKO, O., LI, Z. Y., RUSSELL, D. W., MILLER, D. G., GREGORY, P., HOLMES, M., BOMSZTYK, K. & LIEBER, A. 2013. Chromatin structure of two genomic sites for targeted transgene integration in induced pluripotent stem cells and hematopoietic stem cells. *Gene Ther,* 20, 201-14.

VANAMEE, E. S., SANTAGATA, S. & AGGARWAL, A. K. 2001. FokI requires two specific DNA sites for cleavage. *J Mol Biol,* 309, 69-78.

VASILEVA, A. & JESSBERGER, R. 2005. Precise hit: adeno-associated virus in gene targeting. *Nat Rev Microbiol,* 3, 837-47.

VERLINDEN, N. J. & COONS, J. C. 2015. Disopyramide for Hypertrophic Cardiomyopathy: A Pragmatic Reappraisal of an Old Drug. *Pharmacotherapy,* 35, 1164-72.

VILLA-DIAZ, L. G., ROSS, A. M., LAHANN, J. & KREBSBACH, P. H. 2013. Concise review: The evolution of human pluripotent stem cell culture: from feeder cells to synthetic coatings. *Stem Cells,* 31, 1-7.

VORMBERGE, T., HOFFMANN, M. & HIMMEL, H. 2006. Safety pharmacology assessment of drug-induced QT-prolongation in dogs with reduced repolarization reserve. *J Pharmacol Toxicol Methods,* 54, 130-40.

WAGNER, S., MAIER, L. S. & BERS, D. M. 2015. Role of sodium and calcium dysregulation in tachyarrhythmias in sudden cardiac death. *Circ Res,* 116, 1956-70.

WANG, G., MCCAIN, M. L., YANG, L., HE, A., PASQUALINI, F. S., AGARWAL, A., YUAN, H., JIANG, D., ZHANG, D., ZANGI, L., GEVA, J., ROBERTS, A. E., MA, Q., DING, J., CHEN, J., WANG, D.-Z., LI, K., WANG, J., WANDERS, R. J. A., KULIK, W., VAZ, F. M., LAFLAMME, M. A., MURRY, C. E., CHIEN, K. R., KELLEY, R. I., CHURCH, G. M., PARKER, K. K. & PU, W. T. 2014. Modeling the mitochondrial cardiomyopathy of Barth syndrome with induced pluripotent stem cell and heart-on-chip technologies. *Nature Medicine,* 20, 616.

WANG, G., YANG, L., GRISHIN, D., RIOS, X., YE, L. Y., HU, Y., LI, K., ZHANG, D., CHURCH, G. M. & PU, W. T. 2017. Efficient, footprint-free human iPSC genome editing by consolidation of Cas9/CRISPR and piggyBac technologies. *Nat Protoc,* 12, 88-103.

WANG, H., LA RUSSA, M. & QI, L. S. 2016a. CRISPR/Cas9 in Genome Editing and Beyond. *Annu Rev Biochem,* 85, 227-64.

WANG, H., YANG, H., SHIVALILA, C. S., DAWLATY, M. M., CHENG, A. W., ZHANG, F. & JAENISCH, R. 2013. One-step generation of mice carrying mutations in multiple genes by CRISPR/Cas-mediated genome engineering. *Cell,* 153, 910-8.

WANG, J., DECLERCQ, J. J., HAYWARD, S. B., LI, P. W., SHIVAK, D. A., GREGORY, P. D., LEE, G. & HOLMES, M. C. 2016b. Highly efficient homology-driven genome editing in human T cells by combining zinc-finger nuclease mRNA and AAV6 donor delivery. *Nucleic Acids Res,* 44, e30.

WANG, J., XIE, J., LU, H., CHEN, L., HAUCK, B., SAMULSKI, R. J. & XIAO, W. 2007. Existence of transient functional double-stranded DNA intermediates during recombinant AAV transduction. *Proc Natl Acad Sci U S A,* 104, 13104-9.

WANG, Q., SHUI, B., KOTLIKOFF, M. I. & SONDERMANN, H. 2008. Structural basis for calcium sensing by GCaMP2. *Structure,* 16**,** 1817-27.

WARREN, L., MANOS, P. D., AHFELDT, T., LOH, Y. H., LI, H., LAU, F., EBINA, W., MANDAL, P. K., SMITH, Z. D., MEISSNER, A., DALEY, G. Q., BRACK, A. S., COLLINS, J. J., COWAN, C., SCHLAEGER, T. M. & ROSSI, D. J. 2010. Highly efficient reprogramming to pluripotency and directed differentiation of human cells with synthetic modified mRNA. *Cell Stem Cell,* 7**,** 618-30.

WATANABE, K., UENO, M., KAMIYA, D., NISHIYAMA, A., MATSUMURA, M., WATAYA, T., TAKAHASHI, J. B., NISHIKAWA, S., NISHIKAWA, S., MUGURUMA, K. & SASAI, Y. 2007. A ROCK inhibitor permits survival of dissociated human embryonic stem cells. *Nat Biotechnol,* 25**,** 681-6.

WATKINS, H., ROSENZWEIG, A., HWANG, D. S., LEVI, T., MCKENNA, W., SEIDMAN, C. E. & SEIDMAN, J. G. 1992. Characteristics and prognostic implications of myosin missense mutations in familial hypertrophic cardiomyopathy. *N Engl J Med,* 326**,** 1108-14.

WHITAKER, M. 2010. Genetically encoded probes for measurement of intracellular calcium. *Methods Cell Biol,* 99**,** 153-82.

WILLIAMS, A., HARKER, N., KTISTAKI, E., VEIGA-FERNANDES, H., RODERICK, K., TOLAINI, M., NORTON, T., WILLIAMS, K. & KIOUSSIS, D. 2008. Position effect variegation and imprinting of transgenes in lymphocytes. *Nucleic Acids Res,* 36**,** 2320-9.

WITJAS-PAALBERENDS, E. R., PIRODDI, N., STAM, K., VAN DIJK, S. J., OLIVIERA, V. S., FERRARA, C., SCELLINI, B., HAZEBROEK, M., TEN CATE, F. J., VAN SLEGTENHORST, M., DOS REMEDIOS, C., NIESSEN, H. W., TESI, C., STIENEN, G. J., HEYMANS, S., MICHELS, M., POGGESI, C. & VAN DER VELDEN, J. 2013. Mutations in MYH7 reduce the force generating capacity of sarcomeres in human familial hypertrophic cardiomyopathy. *Cardiovasc Res,* 99**,** 432-41.

WOO, A., RAKOWSKI, H., LIEW, J. C., ZHAO, M., LIEW, C., PARKER, T. G., ZELLER, M., WIGLE, E. D. & SOLE, M. J. 2003. Mutations of the ß myosin heavy chain gene in hypertrophic cardiomyopathy: critical functional sites determine prognosis. *Heart,* 89**,** 1179-85.

WU, H., LEE, J., VINCENT, L. G., WANG, Q., GU, M., LAN, F., CHURKO, J., SALLAM, K., MATSA, E., SHARMA, A., GOLD, J. D., ENGLER, A. J., XIANG, Y. K., BERS, D. M. & WU, J. C. 2015. Epigenetic Regulation of Phosphodiesterases 2A and 3A Underlies Compromised ß-adrenergic Signaling in an iPSC Model of Dilated Cardiomyopathy. *Cell Stem Cell,* 17**,** 89-100.

WU, J., LIU, L., MATSUDA, T., ZHAO, Y., REBANE, A., DROBIZHEV, M., CHANG, Y.-F., ARAKI, S., ARAI, Y., MARCH, K., HUGHES, T. E., SAGOU, K., MIYATA, T., NAGAI, T., LI, W.-H. & CAMPBELL, R. E. 2013. Improved Orange and Red Ca2+ Indicators and Photophysical Considerations for Optogenetic Applications. *ACS Chemical Neuroscience,* 4**,** 963-972.

XU, C., MA, H., INESI, G., AL-SHAWI, M. K. & TOYOSHIMA, C. 2004. Specific structural requirements for the inhibitory effect of thapsigargin on the Ca2+ ATPase SERCA. *J Biol Chem,* 279**,** 17973-9.

YANG, W., LI, Y., HE, F. & WU, H. 2015. Microarray profiling of long non-coding RNA (lncRNA) associated with hypertrophic cardiomyopathy. *BMC Cardiovasc Disord,* 15.

YANG, X., PABON, L. & MURRY, C. E. 2014. Engineering adolescence: maturation of human pluripotent stem cell-derived cardiomyocytes. *Circ Res,* 114**,** 511-23.

YANG, Y., ZHANG, X., YI, L., HOU, Z., CHEN, J., KOU, X., ZHAO, Y., WANG, H., SUN, X. F., JIANG, C., WANG, Y. & GAO, S. 2016. Naive Induced Pluripotent Stem Cells Generated From beta-Thalassemia Fibroblasts Allow Efficient Gene Correction With CRISPR/Cas9. *Stem Cells Transl Med,* 5**,** 8-19.

YAZAWA, M., HSUEH, B., JIA, X., PASCA, A. M., BERNSTEIN, J. A., HALLMAYER, J. & DOLMETSCH, R. E. 2011. Using induced pluripotent stem cells to investigate cardiac phenotypes in Timothy syndrome. *Nature,* 471**,** 230-4.

YIN, Z., KONG, Q. R., ZHAO, Z. P., WU, M. L., MU, Y. S., HU, K. & LIU, Z. H. 2012. Position effect variegation and epigenetic modification of a transgene in a pig model. *Genet Mol Res,* 11**,** 355-69.

YONEMOTO, I. T. & WEYMAN, P. D. 2017. Facile Site-Directed Mutagenesis of Large Constructs Using Gibson Isothermal DNA Assembly. *Methods Mol Biol,* 1498**,** 359-366.

YU, C., LIU, Y., MA, T., LIU, K., XU, S., ZHANG, Y., LIU, H., LA RUSSA, M., XIE, M., DING, S. & QI, L. S. 2015. Small molecules enhance CRISPR genome editing in pluripotent stem cells. *Cell Stem Cell,* 16**,** 142-7.

YU, J. & THOMSON, J. A. 2008. Pluripotent stem cell lines. *Genes Dev,* 22**,** 1987-97.

YU, Z., REN, M., WANG, Z., ZHANG, B., RONG, Y. S., JIAO, R. & GAO, G. 2013. Highly efficient genome modifications mediated by CRISPR/Cas9 in Drosophila. *Genetics,* 195**,** 289-91.

ZAMBROWICZ, B. P., IMAMOTO, A., FIERING, S., HERZENBERG, L. A., KERR, W. G. & SORIANO, P. 1997. Disruption of overlapping transcripts in the ROSA beta geo 26 gene trap strain leads to widespread expression of beta-galactosidase in mouse embryos and hematopoietic cells. *Proc Natl Acad Sci U S A,* 94**,** 3789-94.

ZAMPONI, G. W., STRIESSNIG, J., KOSCHAK, A. & DOLPHIN, A. C. 2015. The Physiology, Pathology, and Pharmacology of Voltage-Gated Calcium Channels and Their Future Therapeutic Potential. *Pharmacol Rev,* 67**,** 821-70.

ZHAI, J., SCHMIDT, A. G., HOIT, B. D., KIMURA, Y., MACLENNAN, D. H. & KRANIAS, E. G. 2000. Cardiac-specific overexpression of a superinhibitory pentameric phospholamban mutant enhances inhibition of cardiac function in vivo. *J Biol Chem,* 275**,** 10538-44.

ZHANG, J., KLOS, M., WILSON, G. F., HERMAN, A. M., LIAN, X., RAVAL, K. K., BARRON, M. R., HOU, L., SOERENS, A. G., YU, J., PALECEK, S. P., LYONS, G. E., THOMSON, J. A., HERRON, T. J., JALIFE, J. & KAMP, T. J. 2012. Extracellular matrix promotes highly efficient cardiac differentiation of human pluripotent stem cells: the matrix sandwich method. *Circ Res,* 111**,** 1125-36.

ZHANG, S., ZHOU, Z., GONG, Q., MAKIELSKI, J. C. & JANUARY, C. T. 1999. Mechanism of block and identification of the verapamil binding domain to HERG potassium channels. *Circ Res,* 84**,** 989-98.

ZHANG, T., KOHLHAAS, M., BACKS, J., MISHRA, S., PHILLIPS, W., DYBKOVA, N., CHANG, S., LING, H., BERS, D. M., MAIER, L. S., OLSON, E. N. & BROWN, J. H. 2007. CaMKIIdelta isoforms differentially affect calcium handling but similarly regulate HDAC/MEF2 transcriptional responses. *J Biol Chem,* 282**,** 35078-87.

ZHAO, M., HOLLINGWORTH, S. & BAYLOR, S. M. 1997. AM-loading of fluorescent Ca2+ indicators into intact single fibers of frog muscle. *Biophys J,* 72**,** 2736-47.

ZHAO, Y., ARAKI, S., WU, J., TERAMOTO, T., CHANG, Y.-F., NAKANO, M., ABDELFATTAH, A. S., FUJIWARA, M., ISHIHARA, T., NAGAI, T. & CAMPBELL, R. E. 2011a. An Expanded Palette of Genetically Encoded Ca(2+) Indicators. *Science (New York, N.Y.),* 333**,** 1888-1891.

ZHAO, Y., ARAKI, S., WU, J., TERAMOTO, T., CHANG, Y. F., NAKANO, M., ABDELFATTAH, A. S., FUJIWARA, M., ISHIHARA, T., NAGAI, T. & CAMPBELL, R. E. 2011b. An expanded palette of genetically encoded Ca(2)(+) indicators. *Science,* 333**,** 1888-91.

ZHU, W. Z., SANTANA, L. F. & LAFLAMME, M. A. 2009. Local control of excitation-contraction coupling in human embryonic stem cell-derived cardiomyocytes. *PLoS One,* 4**,** e5407.

ZISCHEWSKI, J., FISCHER, R. & BORTESI, L. 2017. Detection of on-target and off-target mutations generated by CRISPR/Cas9 and other sequence-specific nucleases. *Biotechnol Adv,* 35**,** 95-104.

Appendix I – Publications

Articles

Smith J.G.W., Owen T., **Bhagwan J.**, Mosqueira D., Mannhardt I., Patel A., Barriales-Villa R., Monserrat L., Hansen A., Eschenhagen T., Marston S., Harding S., Denning C. (2018) A hiPSC model reveals the *ACTC1* E99K mutation as necessary but not sufficient in the development of specific cardiomyopathy phenotypes. (Manuscript in preparation)

Mosqueira D., Mannhardt I., **Bhagwan J.**, Lis-Slimak K., Katili P., Scott E., Hassan M., Prondzynski M., Harmer S.C., Tinker A., Smith J.G.W., Carrier L., Williams P.M., Gaffney D., Eschenhagen T., Hansen A., Denning C. (2018) CRISPR/Cas9 editing in hPSC-cardiomyocytes highlights arrhythmias, hypocontractility and energy depletion as potential therapeutic targets for HCM. (*European Heart Journal* IF: 20.21)

Kondrashov A., Hoang M.D., Smith J.G.W., **Bhagwan J.**, Duncan G., Mosqueira D., Munoz M.B., Nguyen V.T., Denning C. (2018) Simplified footprint-free Cas9/CRISPR editing of cardiac-associated genes in human pluripotent stem cells. (*Stem Cells and Development* IF: 3.56)

Conference abstracts

Bhagwan J., Smith J.G.W., Duncan G., Borgdorff V., Denning C. (2015) Targeted gene editing of human induced pluripotent stem cells using CRISPR-Cas9 to generate calcium reporter lines to investigate cardiomyopathies. *Annual Conference of the British Society for Gene and Cell Therapy and the British Society for Cardiovascular Research, Volume 26*, Glasgow, UK. September 2015.

Appendix II – Predicted off-target locations for *AAVS1* targeting

Table 1. Guide RNA sequences and predicted off-target locations

AAVS1 guide RNA 1 - CACCCCACAGTGGGGCCACTAGG				
Sequence	Number of mismatches	Score	Ontarget	Gene
CACCCCACAGTGGGGCCACTAGG	0	100	True	None
CACTCCACACTGGGGCCACTGGG	2	6.16162	False	None
CTGCCCACTGTGGGGCCACTCAG	3	1.570161	False	None
CACCACTCACTGGGGCCACTAAG	3	1.562329	False	None
GACACCACAGAGGGGCCACTGGG	3	1.562222	False	None
GACCCCACAACGGGGCCACTGGG	3	1.438807	False	None
CACAGCACAGTGGGGCCACGAGG	3	1.397354	False	SCARA3
GTCACCAGAGTGGGGCCACTCGG	4	1.386187	False	None
CATGCCACAGTGGGGCCATTTAG	3	1.040778	False	None
AGACCCTCAGTGGGGCCACTCAG	4	0.919204	False	None
CACCCCACAGTGGGGCTACAGGG	2	0.918782	False	None
CACATCCTAGTGGGGCCACTGGG	4	0.904531	False	None
CAGCCCCTATTGGGGCCACTGGG	4	0.859763	False	None
CTCCTCAAGGTGGGGCCACTGGG	4	0.84696	False	None
TACCCCAAAGTGGGCCCACTAAG	3	0.844444	False	None
AACACAAGAGTGGGGCCACTGAG	4	0.838643	False	None
CAGTTCACCGTGGGGCCACTTGG	4	0.822304	False	FLNB
TGCCCCACTATGGGGCCACTGGG	4	0.805112	False	None
CCCCCCAACCTGGGGCCACTGGG	4	0.792383	False	None
CACAGCACTTTGGGGCCACTCAG	4	0.768095	False	None

Appendix II – Predicted off-target locations for AAVS1 targeting

Table 2. Guide RNA sequences and predicted off-target locations

AAVS1 guide RNA 2 - GGGGCCACTAGGGACAGGATTGG				
Sequence	Number of mismatches	Score	Ontarget	Gene
GGGGCCACTAGGGACAGGATTGG	0	100	True	None
GGAGACATTAGGGACAGGATAAG	3	2.448889	False	None
GGGGCCAGTAGGGAGAGGATAGG	2	1.9	False	None
GAGGGCTCTAGGGACAGGATGAG	3	1.69634	False	None
GGGACCATCAGGGACAGGATGGG	3	1.517516	False	None
GGCCCCACTAGGGACAGGACGAG	3	1.422965	False	None
CAGGGCACTGGGGACAGGATCAG	4	1.317696	False	None
GGGGCCAATTAGGACAGGATGGG	3	1.212478	False	None
GGGGCCAGTGGGGACAGGAGCAG	3	1.141954	False	None
GGGGCCAGTGGGGACAGGAAGGG	3	1.141954	False	None
GGGGTCACTGGGGACAAGATTGG	3	1.054322	False	None
GGGACCACTGGGCACAGGATCGG	3	0.977217	False	None
GGGGATGCTAGGGACAGGATGAG	3	0.958618	False	None
ACTGCCTCTAGGGACAGGATAGG	4	0.919204	False	None
TCGCCCACCAGGGACAGGATCAG	4	0.860351	False	RHOT2
TGGGCCACTATGGACAGGAATGG	3	0.857167	False	None
AGTGCCAACAGGGACAGGATGGG	4	0.848306	False	None
GTGTCCAAGAGGGACAGGATGGG	4	0.84696	False	None
GAGGGCAGCAGGGACAGGATGGG	4	0.84696	False	None
GCAGCCAGGAGGGACAGGATGGG	4	0.835103	False	FAIM2

Appendix II – Predicted off-target locations for AAVS1 targeting

Table 3. Guide RNA sequences and predicted off-target locations

AAVS1 guide RNA 3 - AGAACCAGAGCCACATTAACCGG				
Sequence	Number of mismatches	Score	Ontarget	Gene
AGAACCAGAGCCACATTAACCGG	0	100	True	None
AAAAGCAAAGCCACATTAACAGG	3	2.543507	False	None
AATTCCAGAGCCACATTAACCAG	3	2.287424	False	None
AATTCCAGAGCCACATTAACCAG	3	2.287424	False	None
AACTCCAGAGCCACATTAACCAG	3	2.287424	False	None
AGGAACAGAGCCACATTAATCAG	3	1.422965	False	None
AGAACCAAAGCCACAGTAACGAG	2	1.296825	False	None
AACTCCAGATCCACATTAACCAG	4	1.278707	False	None
AGAACCACACCCCCATTAACCAG	3	0.885244	False	None
GCAAACAGGGCCACATTAACAAG	4	0.860351	False	None
TGAGCCACTGCCACATTAACAGG	4	0.860351	False	None
ATAAACAATGCCACATTAACGAG	4	0.84696	False	None
AAAAAGAGATCCACATTAACTAG	4	0.784602	False	None
AAAACCAGAGTTACATTAACTAG	3	0.768613	False	None
CCAAACAGAGCCACATTAATCAG	4	0.710795	False	None
AGTAGCACAGCAACATTAACGGG	4	0.694061	False	SENP6
AATACCAAAGCCACATTAAAGGG	4	0.687683	False	None
TGAACCAAAACAACATTAACGAG	4	0.669827	False	None
CCAAGCAGAGCCACATCAACAGG	4	0.620617	False	None
AGACCCAAACCCACATTAATAGG	4	0.619096	False	None